



Terms and Conditions of Use of Digitised Theses from Trinity College Library Dublin

Copyright statement

All material supplied by Trinity College Library is protected by copyright (under the Copyright and Related Rights Act, 2000 as amended) and other relevant Intellectual Property Rights. By accessing and using a Digitised Thesis from Trinity College Library you acknowledge that all Intellectual Property Rights in any Works supplied are the sole and exclusive property of the copyright and/or other IPR holder. Specific copyright holders may not be explicitly identified. Use of materials from other sources within a thesis should not be construed as a claim over them.

A non-exclusive, non-transferable licence is hereby granted to those using or reproducing, in whole or in part, the material for valid purposes, providing the copyright owners are acknowledged using the normal conventions. Where specific permission to use material is required, this is identified and such permission must be sought from the copyright holder or agency cited.

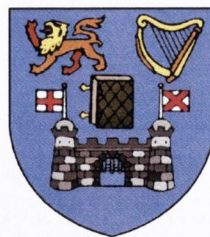
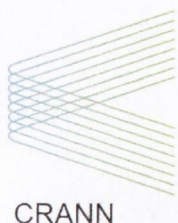
Liability statement

By using a Digitised Thesis, I accept that Trinity College Dublin bears no legal responsibility for the accuracy, legality or comprehensiveness of materials contained within the thesis, and that Trinity College Dublin accepts no liability for indirect, consequential, or incidental, damages or losses arising from use of the thesis for whatever reason. Information located in a thesis may be subject to specific use constraints, details of which may not be explicitly described. It is the responsibility of potential and actual users to be aware of such constraints and to abide by them. By making use of material from a digitised thesis, you accept these copyright and disclaimer provisions. Where it is brought to the attention of Trinity College Library that there may be a breach of copyright or other restraint, it is the policy to withdraw or take down access to a thesis while the issue is being resolved.

Access Agreement

By using a Digitised Thesis from Trinity College Library you are bound by the following Terms & Conditions. Please read them carefully.

I have read and I understand the following statement: All material supplied via a Digitised Thesis from Trinity College Library is protected by copyright and other intellectual property rights, and duplication or sale of all or part of any of a thesis is not permitted, except that material may be duplicated by you for your research use or for educational purposes in electronic or print form providing the copyright owners are acknowledged using the normal conventions. You must obtain permission for any other use. Electronic or print copies may not be offered, whether for sale or otherwise to anyone. This copy has been supplied on the understanding that it is copyright material and that no quotation from the thesis may be published without proper acknowledgement.



A Microcantilever-Based, Dual-Mode, Quantitative Sensing Platform for the Investigation of Biological Interactions

Thesis submitted to the
University of Dublin
for the degree of
Doctor in Philosophy

Jason Jensen

Supervisor:

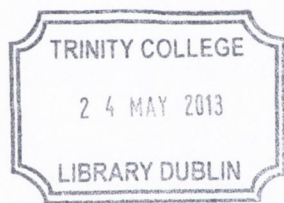
Prof. Martin Hegner

School of Physics,
Trinity College Dublin

and

Centre for Research on Adaptive
Nanostructures and Nanodevices

February 2013

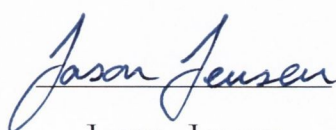


Thesis 9975

Declaration

I declare that this thesis has not been submitted as an exercise for a degree at this or any other university and it is entirely my own work.

I agree to deposit this thesis in the University's open access institutional repository or allow the Library to do so on my behalf, subject to Irish Copyright Legislation and Trinity College Library conditions of use and acknowledgement.

A handwritten signature in blue ink that reads "Jason Jensen". The signature is written in a cursive style with a horizontal line underneath the name.

Jason Jensen
February 1, 2013

Summary

Since the introduction of the atomic force microscope (AFM) and the subsequent availability of high-quality cantilevers the interest in the application of microcantilevers as biosensors has increased year-on-year. Much of the work using these sensors involves working in either the static or the dynamic mode, however there is little work described in the literature involving the use of the two modes in parallel. This thesis describes the development of a dual-mode microcantilever-based sensing platform for applications of quantitative biosensing in a liquid. Due to the large damping of the liquid the application of the dual-mode device for the detection of small biomolecules in low concentration requires the use of a mass label which can increase the sensitivity of the device.

Dual-mode cantilever array device

This section describes the development of a cantilever-based sensing platform capable of the measurement of both the static and dynamic responses of a cantilever array containing eight cantilevers with a length of 500 μm , a width of 100 μm , and a centre-to-centre spacing of 250 μm in a physiological liquid environment. The device incorporates a laser mounted on a 2D automatic translation stage which provides readout from the eight cantilevers sequentially by the optical beam deflection technique. The resolution of the static mode is on the order of 1 - 2 nm and in the dynamic mode it is possible to measure up to the 19th flexural resonance mode of vibration. The entire device is controlled and managed via a user-friendly LabVIEW environment.

Compressible fluid model verification

The qualitative agreement between the predictions of the compressible fluid model developed by Van Eysden and Sader and experimental observations of the flexural resonance frequencies and Q factors of 2 and 7 μm thick cantilevers vibrated in air is presented. The prediction that the Q factor of a vibrating cantilever can decrease after a specified critical resonance mode is verified. The observed resonance frequencies and Q factors were lower than the predicted values and this is attributed to the design of the hinged section of the cantilevers.

Protein aggregation and Parkinson's disease

Using the dynamic mode it was possible to detect the aggregation of the protein α -synuclein, which is a protein relevant in neurodegenerative diseases such as Parkinson's Disease, on the surface of a 1 μm thick cantilever in a quantitative and label-free manner. A total mass of 6 ng of α -synuclein was detected over nine hours on the surface of the cantilever. The result is compared to conventional fluorescence measurements of α -synuclein aggregation under similar conditions. It is found that the label-free cantilever detection method requires a concentration of protein 50 times smaller than that of the current method and indicated potential for significantly faster response times.

Mass label experiments

Initial experiments with mass labels and oligonucleotides (oligos) demonstrated the successful detection of oligo-functionalised nanoparticles (NPs) with diameters of 12.3 nm and 50 nm with total mass uptakes on the surface of the cantilever of 12 ± 3.5 ng and 1.5 ± 0.3 ng respectively. The successful detection of the hybridisation of biotinylated oligos using the static mode and the subsequent detection of the binding of streptavidin-functionalised polystyrene beads to the hybridised biotinylated oligos resulting in an average mass uptake of 1.1 ± 0.2 ng on the cantilevers is also described. Boundary streaming on the surface of the vibrating cantilevers is found to affect the resonance frequency shift observed depending on the size of the mass label used.

The detection of binding of anti-biotin antibody-functionalised magnetic beads to a biotin self-assembled monolayer (SAM) on an Au coated cantilever array resulting in an average mass increase of 3.0 ± 0.3 ng is presented. This measurement represents the final step towards the development of a full assay for the detection of inflammation proteins from liquid samples using antibody-functionalised magnetic beads and cantilever arrays.

Acknowledgements

I would like to give special thanks my supervisor Prof. Martin Hegner for all his wisdom, guidance and support; for providing the excellent working conditions which I enjoy; and finally for bringing together such a great interdisciplinary team to work with.

Thanks to Prof. Javier Tamayo and Dr. Eric Finch for taking the time to review my work and for making the *viva voce* exam an enjoyable process.

Thanks to the members of the Nanobiotech group for all of their help and general support over the last four years, Christian Steinbring, Dorothea Brüggemann, Florian Wruck, Gyöngyi Lukács, Michael Walther, Niall Maloney, Rohit Mishra, Sarah-Louise Ball, Sinead Cullen, and Vivek Jadhav.

Thanks to Rohit who has been sitting beside me from the start, for his general help and advice regarding the static mode and for proof reading. Thanks to Niall for all of his help and discussions regarding various aspects of the dynamic mode, his good humour and for proof reading. Michael for all of his help and support with the device and his good lab manner. Gyöngyi for her help with the biological aspects of the work.

Thanks also to former group members Dr. Wilfried Grange, for his advice regarding LabVIEW and his help with the development of the new dynamic mode device; Dr. Hélène Gaussier, for her wisdom regarding everything biological and especially for her help with the protein preparations; Dr. Thomas Braun and Kasper Renggli, for their help during the beginning of my Ph.D.; Margherita Farina for work with the protein aggregation; undergraduate students Niall Mc Laughlin and Larry O' Connell for their time working on the Au nanoparticle experiments.

Thanks to Dr. John Elie Sader and his student Anthony Van Eysden for discussions regarding their cantilever dynamics models and the interactions of fluids and cantilevers in general.

Thanks to Dave O' Mahony, Gordon, Paddy and Dave from the mechanical workshop for their help and for fabrication of various pieces which were implemented in the device. Jean Pierre Ramseyer, for useful discussions regarding the cantilever holder and device design principles.

Thanks to the School of Pharmacy and Pharmaceutical Sciences, Trinity College Dublin for the use of the FLUOstar Optima microplate multi-detection reader during the work on the protein aggregation.

Thanks to Cathal McCauley and Dermot Daly for training on the SEM. The SEM images were taken in the Advanced Microscopy Laboratory, Trinity Technology and Enterprise Campus, Dublin 2, Ireland under the framework of the INSPIRE program, funded by the Irish Government's Programme for Research in Third Level Institutions, Cycle 4, National Development Plan 2007-2013.

This work was supported by Science Foundation Ireland under the CSET scheme SFI08/CE/I1432 and PI scheme SFI/09IN/1B2623.

A big thanks to Aisling for her love and support which keeps me going, and for putting up with me during the last few years of work. Finally, a big thanks to my parents, Anne and Bruno, and my sister Keri for their constant love and support, without which I would not be where I am today.

Contents

| | |
|--|-----------|
| Declaration | iii |
| Summary | v |
| Acknowledgements | vii |
| Contents | xii |
| Abbreviations and Acronyms | xiii |
| Symbols | xv |
| 1 Introduction | 1 |
| 1.1 Nanomechanical Sensors | 1 |
| 1.1.1 Nanomechanical Biosensors | 3 |
| 1.1.2 Competing Technologies | 4 |
| 1.2 Static Mode | 5 |
| 1.2.1 Static-Mode Detection | 5 |
| 1.3 Dynamic Mode | 8 |
| 1.3.1 Quality Factor | 9 |
| 1.3.2 Mass Detection in a Liquid Environment | 10 |
| 1.3.3 Higher Resonance Modes | 12 |
| 1.3.4 Dynamic-Mode Detection | 13 |
| 1.4 Scope of Thesis | 13 |
| References | 16 |
| 2 Dual-Mode Device | 23 |
| 2.1 Existing Dynamic-Mode Device | 23 |
| 2.1.1 Problems with the Existing Device | 24 |
| 2.2 Instrumentation | 25 |
| 2.2.1 Fluid Chamber | 25 |
| 2.2.2 Optics and Laser Positioning System | 28 |
| 2.2.3 Position Sensitive Detector | 32 |

| | | |
|----------|---|-----------|
| 2.2.4 | Temperature Control | 34 |
| 2.2.5 | Fluidic System | 36 |
| 2.2.6 | The Assembled Dual-Mode Device | 38 |
| 2.3 | LabVIEW Programming | 41 |
| 2.3.1 | The Main Program | 41 |
| 2.3.2 | Measurement Procedure | 45 |
| 2.4 | Results and Discussion | 50 |
| 2.4.1 | Performance of Dual-Mode Device | 50 |
| 2.4.2 | Line Scan of Cantilever Vibrating in Air | 52 |
| 2.4.3 | Response to Heat Pulse | 53 |
| 2.4.4 | Syringe Pump vs. Pressure Flow | 55 |
| | References | 59 |
| 3 | General Cantilever Preparation Techniques | 61 |
| 3.1 | Cantilever Cleaning | 61 |
| 3.2 | Metal Coating | 62 |
| 3.2.1 | BOC Edwards | 62 |
| 3.2.2 | Temescal | 63 |
| 3.3 | UV Cleaning | 64 |
| 3.4 | Cantilever Functionalisation | 64 |
| | References | 66 |
| 4 | Compressible Fluid Model Verification | 67 |
| 4.1 | Introduction | 67 |
| 4.2 | Materials and Methods | 69 |
| 4.3 | Comparison Between Theory and Experiment | 72 |
| 4.3.1 | 7 μm Thick Cantilevers | 72 |
| 4.3.2 | 2 μm Thick Cantilevers | 75 |
| 4.4 | Discussion | 76 |
| | References | 78 |
| 5 | Protein Aggregation and Parkinson's Disease | 81 |
| 5.1 | Introduction | 81 |
| 5.1.1 | Parkinson's Disease and α -Synuclein | 82 |
| 5.1.2 | Investigating Protein Aggregation | 83 |
| 5.2 | Materials and Methods | 85 |
| 5.2.1 | Cantilever Functionalisation | 85 |
| 5.2.2 | Cantilever Measurements | 86 |
| 5.2.3 | Thioflavin T Measurements | 87 |
| 5.2.4 | Data Handling | 88 |

| | | |
|----------|---|------------|
| 5.3 | Results | 88 |
| 5.3.1 | Cantilever Measurements | 88 |
| 5.3.2 | Fluorescence Measurements | 89 |
| 5.4 | Discussion | 90 |
| | References | 92 |
| 6 | Oligonucleotides and Mass Labels | 97 |
| 6.1 | Introduction | 97 |
| 6.1.1 | Mass Labels | 98 |
| 6.1.2 | Au Nanoparticle Synthesis | 98 |
| 6.2 | Materials and Methods | 99 |
| 6.2.1 | Laser-Ablated Au Nanoparticles | 99 |
| 6.2.2 | Citrate-Reduction Au Nanoparticles | 100 |
| 6.2.3 | Streptavidin-Coated Polystyrene Beads | 102 |
| 6.3 | Results | 104 |
| 6.3.1 | Laser-Ablated Au Nanoparticles | 104 |
| 6.3.2 | Citrate-Reduction Au Nanoparticles | 106 |
| 6.3.3 | Streptavidin-Coated Polystyrene Beads | 109 |
| 6.4 | Discussion | 115 |
| | References | 118 |
| 7 | Antibodies and Magnetic Mass Labels | 121 |
| 7.1 | Introduction | 121 |
| 7.1.1 | Magnetic Nanoparticles | 121 |
| 7.1.2 | ELISA | 123 |
| 7.2 | Materials and Methods | 123 |
| 7.3 | Results | 124 |
| 7.4 | Discussion | 127 |
| | References | 128 |
| 8 | Conclusions and Outlook | 129 |
| 8.1 | Conclusions | 129 |
| 8.2 | Outlook | 130 |
| 8.2.1 | Instrumentation | 130 |
| 8.2.2 | Experimental | 131 |
| | References | 133 |
| | Appendices | 135 |

| | | |
|----------|--|------------|
| A | Supplementary Information | 137 |
| A.1 | Calculation of Phase Shift | 137 |
| A.2 | f vs n for Example Spectrum | 138 |
| A.3 | Heat Pulse | 140 |
| A.4 | Protein Aggregation Cantilever Measurements | 143 |
| A.5 | Oligo-Functionalised Au Nanoparticles Measurements | 145 |
| A.6 | Dulbecco's PBS | 148 |
| A.7 | SEM Images of Au Nanoparticles on Cantilever Surface | 149 |
| A.8 | Heat Pulse for Calibration of Static-Mode Oligo Hybridisation Test . . | 150 |
| A.9 | Biotinylated Oligos with Streptavidin Beads | 151 |
| | References | 152 |
| B | Protocols | 153 |
| B.1 | Piranha Cleaning of Cantilever Arrays | 153 |
| B.2 | Plasma Cleaning of Cantilever Arrays | 155 |
| B.3 | UV Cleaning of Cantilever Arrays | 156 |
| B.4 | PEG Silane Functionalisation | 157 |
| B.5 | Oligonucleotide Preparation | 158 |
| B.6 | Functionalised Au Nanoparticle Buffer Transfer Protocol | 159 |
| B.7 | Au Nanoparticle-DNA Conjugation | 161 |
| B.8 | Antibody Binding to Protein G Magnetic Beads | 163 |
| B.9 | Biotin SAM Formation | 165 |
| | References | 166 |
| C | Mathematica Source Code | 167 |
| C.1 | Matrix Size Convergence Test | 167 |
| C.2 | Compressible Fluid Model | 170 |
| C.3 | Extended Viscous Model | 173 |
| | References | 176 |
| D | List of Publications and Presentations | 177 |
| | List of Figures | 179 |
| | List of Tables | 183 |
| | Glossary | 185 |

Abbreviations and Acronyms

AFM atomic force microscope.

bp base pair.

BSA bovine serum albumin.

CD circular dichroism.

DAQ data acquisition board.

DI deionised.

DLS dynamic light scattering.

DNA deoxyribonucleic acid.

DPBS Dulbecco's phosphate-buffered saline.

DSU dithiobis(succinimidyl undecanoate).

DTT dithiothreitol.

ELISA enzyme-linked immunosorbent assay.

FTIR Fourier transform infrared spectroscopy.

FWHM full width at half maximum.

HCP hexagonal close-packed.

LabVIEW Laboratory Virtual Instrumentation Engineering Workbench.

MW molecular weight.

ND neutral density.

NMR nuclear magnetic resonance.

NP nanoparticle.

oligo oligonucleotide.

PBS phosphate-buffered saline.

PEEK polyether-ether-ketone.

PEG polyethylene glycol.

PSD position sensitive detector.

QCM quartz crystal microbalance.

RMS root mean square.

RT room temperature.

SAM self-assembled monolayer.

SEM scanning electron microscope.

SHO simple harmonic oscillator.

ssDNA single-stranded deoxyribonucleic acid.

TEAA triethylammonium acetate.

VCSEL vertical-cavity surface-emitting laser.

VI virtual instrument.

Symbols

β angle between the incident laser and the cantilever normal.

$\Gamma(f_n, n)$ dimensionless hydrodynamic function.

γ damping factor.

Δf frequency shift *or* change in frequency.

Δm change in mass.

Δs change in the position of the spot on the position sensitive detector (PSD).

Δz deflection.

δ Stokes boundary layer thickness.

δf bandwidth of a resonator.

Θ angle of deflection.

λ wavelength.

ν kinematic viscosity.

ρ_{Au} density of gold (19,300 kg/m³ at room temperature (RT)).

ρ_{air} density of air (1.1839 kg/m³ at RT).

ρ_{poly} density of polystyrene (1,060 kg/m³ at RT).

ρ_{Si} density of silicon (2,330 kg/m³ at RT).

ϕ phase.

ω radial frequency.

A amplitude.

A_0 zero frequency amplitude.

A_{bl} baseline amplitude.

b width.

C_0 intrinsic damping coefficient per unit length.

C_v dissipation coefficient.

D_c critical bead diameter.

D_{cl} diameter of the laser spot on the cantilever.

D_{coll} diameter of the collimated laser beam.

d_{PSD} distance between the cantilever and the PSD.

DOF depth of focus.

E Young's modulus.

F driving force.

f frequency.

f_0^* fundamental eigenfrequency in a vacuum in the absence of damping with the mass concentrated at one point.

f_{0n} eigenfrequency of mode n of a cantilever with a distributed mass in the absence of damping.

f_c centre frequency of a peak.

f_{lens} focal length of the lens.

f_n resonance frequency of mode n .

$f_{vac,n}$ vacuum resonance frequency of mode n .

G calibration factor.

g acceleration due to gravity (9.8 m s^{-2}).

h thickness.

I moment of inertia.

I_1 current from contact 1 on PSD.

I_2 current from contact 2 on PSD.

k spring constant.

L cantilever length.

L_{PSD} active length of the PSD.

M bending moment.

m slope.

m_c cantilever mass.

m_l mass of liquid.

m_{total} total mass.

n mode number.

n_c critical mode number.

Q quality factor.

Q_n quality factor at mode n .

R_{PSD} response measured by the PSD.

S sensitivity.

s position of laser spot on the PSD.

T temperature.

t time.

$u(x, t)$ deflection of the cantilever perpendicular to its surface.

V voltage.

x coordinate along the cantilever.

z coordinate perpendicular to the surface of the straight cantilever.

$z(x)$ bending profile of the cantilever.

Chapter 1

Introduction

The improvement of silicon fabrication technologies over the last few decades and the introduction of the atomic force microscope (AFM) [1] created the availability of high-quality, reproducible, and relatively inexpensive silicon cantilevers. Starting in the mid 1990s [2–6] the interest in applying these micron-scale cantilevers in sensing applications other than AFM has increased year-on-year. The versatility and sensitivity of these sensors has led to a broad range of sensing applications as described recently in several excellent review papers [7, 8]. The use of cantilevers as transducers in biosensors provides many interesting and potentially lucrative applications in clinical and industrial settings.

1.1 Nanomechanical Sensors

Nanomechanical sensors, and cantilevers in particular, have found applications in many areas including mass, chemical (liquid and vapour), and humidity sensing in addition to surface stress and thermal effect measurements among others [9, 10].

The cantilevers used most frequently are fabricated from silicon because the manufacturing technology is well established by the semiconductor industry and allows for reproducible, high precision fabrication. The size of the cantilevers used range from sub-micron to hundreds of microns in length with a similar range of thicknesses, in single or arrayed format. Fig. 1.1 shows a typical array of eight silicon cantilevers used in the work presented here. The resonance frequencies of the cantilevers in this type of array vary by only 0.5% [9] and they can be manufactured in bulk to reduce the cost per array significantly.

The use of a reference in sensing applications involving cantilevers is essential. As suggested above, the cantilever can respond to virtually any stimulus and the careful preparation of reference cantilevers is required if the correct deductions are to be taken from the recorded response. The use of an array such as the one shown in Fig. 1.1 allows the inclusion of multiple tests and *in situ* references in one experiment. This greatly

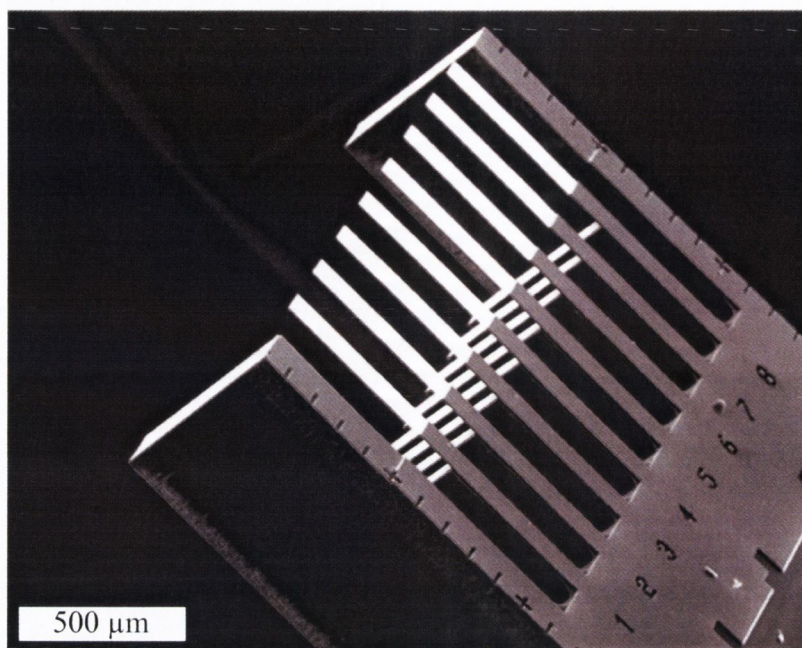


Figure 1.1. A typical cantilever array used in the work presented here. The arrays are fabricated from silicon in the IBM Research Laboratory at Rüschlikon, Zurich. The array contains eight cantilevers with a length of 500 μm , width of 100 μm and a thickness of 1 μm . The centre-to-centre spacing of the cantilevers is 250 μm . The arrays are available with or without protective sidebars. The arrays can be fabricated with a range of cantilever thicknesses between 500 nm and 7 μm depending on the desired sensing application. Multiple cantilevers in an array allows for several experiments with *in situ* references to be performed simultaneously on the same small sample volume. Image adapted from [11].

increases throughput and ensures that unwanted responses of the test cantilevers can be accounted for (e.g. thermal drift).

There are two basic operational modes of a cantilever based sensor, the static mode and the dynamic mode which will be described in detail in Section 1.2 and Section 1.3. Most applications deal with only one of the modes of operation; however sensing devices have been designed that can provide readout from both modes simultaneously [11–13].

Laser beam deflection [14] was introduced quickly after the development of the AFM as a method to measure the response of a cantilever and is the most common detection method in use today. There are, however, many other possible methods that allow the monitoring of the response of a cantilever including interferometry [15], capacitive [16], and piezoresistive [17].

1.1.1 Nanomechanical Biosensors

Nanomechanical cantilever sensors have been widely applied in the field of biology due to their versatility and easy functionalisation with a broad range of chemical and biological molecules. The sensor can be operated in liquid [18] which allows detection of the target molecules in a physiological environment, providing useful insights into biological processes.

Within a short time of the initial work using cantilevers as sensors Fritz *et al.* showed that it was possible to detect a single base pair (bp) mismatch between two 12-mer oligonucleotides (oligos) in a label-free manner using a cantilever array operated in the static mode [19]. This sensitivity combined with the potential for easily upscaling the number of cantilevers in an array has led to widespread interest in the area of DNA-binding and genomics involving cantilevers [20–25] with the vast majority of the applications using the static mode.

The label-free capabilities of microcantilever based detection offer an attractive advantage over many other detection methods employed in more traditional or standard biological assays such as fluorescence based methods which require the target to be marked with a label. In this manner cantilevers are used in applications for the detection of proteins [26], as immunosensors [27], and for the investigation of membrane protein-ligand interactions [28].

Another biological area where cantilevers have found an application includes the detection of micro-organisms such as viruses [29, 30] and bacteria [31, 32]. It is also possible to perform bacterial and fungal growth detection measurements using cantilever arrays [33–36]. Here the cantilever is coated with a thin layer of agarose which is loaded with nutrients in the same way as a standard petri dish. The growth of the fungal spores and the resulting mycelium along the cantilever affect the resonance properties of the cantilever and allow the growth to be detected quickly in a quantitative manner [36].

The biological applications of cantilevers mentioned above are just a few examples of what is possible. The versatility of functionalisation of the cantilever array allows detection or measurement of virtually any biomolecule once a suitable functionalisation is possible. With applications in biology on the rise for cantilevers it is worth noting that special care must be made to employ one or more suitable reference and control cantilevers in the measurement or detection scheme if the correct deductions are to be made from the signals obtained. Also, the passing of the functionalised cantilever through a liquid-to-air interface should be avoided if the aim of the measurement is to investigate the interaction between biological molecules as the functionality or conformation of the molecules may be altered or damaged. In addition, passing the cantilever from a salt-buffered solution to air will invariably lead to the formation of

salt crystals on the surface of the cantilever which may lead to misinterpretation of the results obtained. Thus, the ‘dip and dry’ method should be avoided.

1.1.2 Competing Technologies

There are many different types of nanomechanical sensors which operate under more or less the same basic principles as the cantilever sensor. These include trampoline-shaped resonators [37], paddle-shaped levers [38, 38], membrane resonators [39], doubly-clamped beams [40], and nanowires [41, 42] amongst others.

A novel approach to overcome the challenges associated with operating a cantilever in a liquid environment for biological applications has been developed by the Manalis research group at MIT whereby the liquid is flowed through a channel in a vacuum packed cantilever. The suspended microchannel resonator combines microfluidics with resonating detection to allow impressive mass resolution of 1 fg in a 1 Hz bandwidth [43] with label-free biodetection possible [44]. The suspended microchannel resonator allows a series of measurements to be performed on individual cells in an automated manner (like flow cytometry) providing information such as the weight [43], and density [45] of the cells. Density measurements of individual cells has applications in distinguishing between unhealthy and healthy cells for various diseases including sickle-cell anemia and leukemia [45]. Direct monitoring of the growth of mammalian cells over multiple generations is also possible [46].

Despite the range of other available nanomechanical sensors, many of them have similar advantages and disadvantages as the cantilever-based sensor. With the exception of the suspended microchannel resonator all of the devices will suffer from additional damping if working in a liquid environment. For resonating detection the limit of detection is related to the total mass of the sensor, so as with cantilever based sensors moving to a smaller size will increase the sensitivity of the sensor. The overall sensitivity of some of these sensors can be impressive in vacuum, with mass sensitivity approaching that of an individual proton ($1.7 \text{ yg} = 1.7 \times 10^{-24} \text{ g}$) using a carbon nanotube resonator [47]. However, relatively little work has been performed with these resonators in liquid. The cantilever array allows easy functionalisation of individual cantilevers via capillary immersion (discussed in more detail in Section 3.4) whereas for doubly-clamped beams or nanowires individual functionalisation may not prove to be as trivial.

The main rival to nanomechanical sensors in general is the quartz crystal microbalance (QCM) [48] which has already achieved commercial success with more than twenty different devices available from eleven manufacturers in 2010 [49]. As QCM has become more accepted as a standard measurement device the number of publications relating to QCM listed per year on the ISI Web of Science has risen from

just under 100 in 2001 to well over 500 in 2010 [49].

The QCM is a mechanical resonator with a size on the centimeter scale which is capable of mass sensing. As the name suggests the device is based on the piezoelectric properties of a quartz crystal and when an AC voltage is applied to the crystal a standing shear wave is established. QCM derives its sensitivity from the high frequency and Q factors associated with the shear motion which is only weakly coupled to the surroundings and so suffers from little damping effects.

While QCM has its origins with gas sensing and thin-film deposition it has been increasingly applied to the biosciences as the increase in the number of biology related QCM publications indicates [49], with much of the work involving small molecules, protein adsorption, and immunoassays.

The sensitivity of the QCM to protein adsorption is in the nM range when operated in liquid [50, 51]. This can be improved to fM sensitivity by using ‘dip and dry’ methods [50]. This compares favourably with cantilever based sensors which have reported sensitivity down to 0.3 pM in liquid [50, 52]. Thus, cantilever based sensors are potentially more sensitive than the more well-established QCM, but work must be done in order to establish cantilever sensors as a commonly used tool in biology, as described in the review by Calleja *et al.* [8].

1.2 Static Mode

In the static mode the deflection of the cantilever, caused by a differential surface stress, is measured with respect to time. The cantilever is typically coated with a functional monolayer on one side and passivated against the target molecule on the opposite side. The bending is induced by adsorption of the target molecule onto the functional layer [9]. The bending response of the cantilever is caused by stress at the interface between the adsorbed and functional layers [9, 10]. This stress can be generated by a number of interactions including volume expansion of the functional layer, steric hindrance, changes in the structure of the functional layer, charge effects, or a combination of these effects. The cantilevers used in static mode experiments are fabricated with a very low elastic spring constant to ensure that the smallest forces possible are detectable.

1.2.1 Static-Mode Detection

There are two main types of static measurement that can be recorded using the laser beam deflection method [14]. The first and most common method is to record the deflection of the cantilever by taking a single measurement of the deflection at the tip of the cantilever. The other is to take multiple measurements, or a scan, along the

length of the cantilever to establish the full bending profile of the cantilever.

Measurement from the Tip of the Cantilever

The tip method has the advantage that it is very fast and allows more measurements to be obtained in a shorter period of time and is thus suitable for monitoring the bending of the cantilever in experiments where a fast interaction between the cantilever and the target is expected. The speed of this method typically allows a greater number of samples of the bending to be taken during each measurement which reduces the noise of the measurement. However, this method does make the assumption that the cantilever bends with a uniform curvature.

Laser beam deflection is used to measure the bending from the tip of the cantilever as shown in Fig. 1.2 and the deflection of the laser beam on the surface of the position sensitive detector (PSD) can be related to the bending of the cantilever by a calibration factor G based on the geometry of the path of the laser beam.

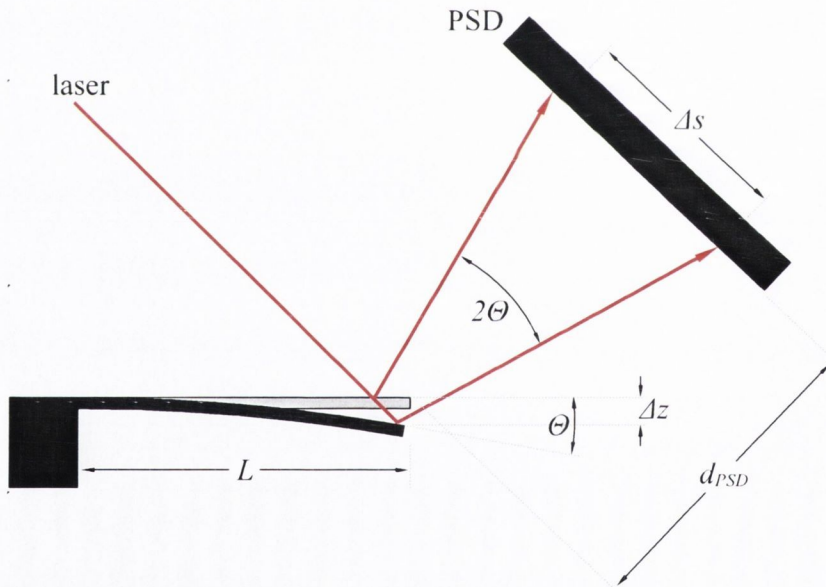


Figure 1.2. A schematic of the static-mode bending of a cantilever and readout using laser beam deflection. The laser beam is deflected from the surface of the cantilever and a small change in the bending of the cantilever results in a change in the position of the laser spot on the surface of the PSD. The change in the bending Δz can be related to the change in the spot position Δs by a calculation based on the geometry of the laser path.

The application of a bending moment M to the free end of the cantilever causes a small deflection of the cantilever by an amount Δz , through an angle Θ , which can be defined by [53]

$$\Theta = \frac{ML}{EI} \quad (1.1)$$

and

$$\Delta z = \frac{ML^2}{2EI} \quad (1.2)$$

where L is the length of the cantilever, E is the Young's modulus, and I is the moment of inertia of the cantilever. By combining Eq. 1.1 and Eq. 1.2 the small deflection Δz becomes

$$\Delta z = \frac{\Theta L}{2}. \quad (1.3)$$

If the bending angle Θ of the cantilever is small then the angular deflection of the laser beam will be equal to twice the angular change of the cantilever, and

$$2\Theta = \frac{\Delta s}{d_{PSD}} \quad (1.4)$$

where Δs is the change in the position of the spot on the PSD and d_{PSD} is the distance between the cantilever and the PSD as shown in Fig. 1.2.

When Eq. 1.2 and Eq. 1.4 are combined a relation between the change in the spot position on the PSD, Δs , and the bending of the cantilever, Δz , is obtained

$$\Delta z = \frac{L}{4d_{PSD}} \Delta s = G \Delta s \quad (1.5)$$

where $G = L/4d_{PSD}$ is the calibration factor.

Thus, the bending of the cantilever can be easily obtained from the motion of the spot on the surface of the PSD. This calibration factor is based entirely on the geometry of the path of the laser and requires accurate measurement of the distances and angles involved. It is possible to find the calibration factor by obtaining a thermal noise power spectrum from the cantilever and using the equipartition theorem to relate the total potential energy of the cantilever to the mean square deflection of the cantilever caused by the thermal vibrations [54]. This allows an easy measurement of G for a given geometry, provided the spring constant of the cantilever is well known.

Measurement of the Line Profile of the Cantilever

This method has the advantage that more information about the local strain on the surface of the cantilever and the true bending of the cantilever surface can be obtained. However, the method is typically significantly slower than the tip measurement method as more measurements per cantilever are required to establish the profile. This method also requires a laser which is moveable in two directions in order to obtain the bending profile of several cantilevers in an array.

As shown in Fig. 1.3 the laser is scanned along the length of the cantilever in the x direction. The bending profile of the cantilever in the z direction, $z(x)$, can be obtained by relating the local slope of the cantilever surface to the position of the laser spot on

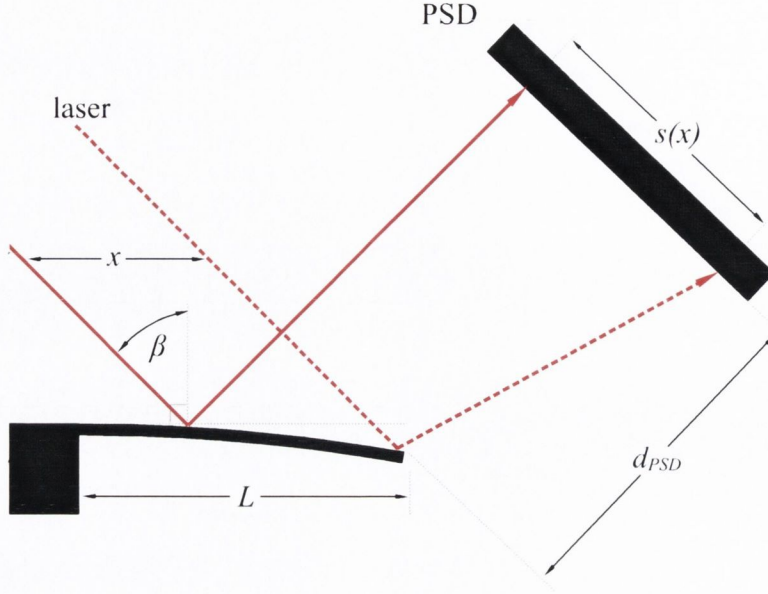


Figure 1.3. A schematic of the static mode bending of a cantilever and line profile readout using laser beam deflection. The laser beam is scanned along the length of the cantilever in the x direction resulting in a change in the spot position on the PSD $s(x)$. The bending profile of the cantilever $z(x)$ can be derived from the change in spot position $s(x)$.

the surface of the PSD, $s(x)$ [55].

The local slope of the cantilever surface causes a change in the position of the laser spot on the surface of the PSD, however the motion of the laser along the length of the cantilever also contributes to the change in the position of the spot, thus [55]

$$s(x) \cong 2d_{PSD} \frac{dz(x)}{dx} + x \cos \beta \quad (1.6)$$

where β is the angle between the incident laser beam and the normal to the cantilever when it is straight. The second term in the above equation accounts for the motion of the laser during the profile measurement. Hence, the cantilever profile can be obtained by integration of Eq. 1.6,

$$z(x) = \frac{1}{2d_{PSD}} \int_0^x s(x') dx' - \frac{1}{4} \frac{x^2}{d_{PSD}} \cos \beta. \quad (1.7)$$

1.3 Dynamic Mode

In the dynamic mode changes in the resonance frequency of the cantilever, due to changes in the physical properties of the cantilever or surrounding medium, are measured with respect to time. Typically the cantilever is vibrated at one of its

resonance frequencies and can be used as a very fine microbalance. The eigenfrequencies (the free vibrational frequencies in vacuum, different from the resonance frequency, see Section 1.3.2) of a cantilever depend on the mass of the cantilever and the mass bound to it. The cantilever is typically coated with a functional layer on one or both sides. Therefore, as material binds to the functional layer a change in the properties of the cantilever occurs which is reflected in the frequency observed. Detection of mass changes of as little as 1 ag have been reported [29].

In addition to mass sensing, a cantilever operated in dynamic mode can be used to characterise Newtonian fluids [56]. The resonance frequency of a cantilever depends on not only the mass bound to the cantilever, but also the viscosity and density of the fluid in which it is vibrating. Any change in these factors results in a change of the resonance frequency (shifts or damping).

The majority of the work presented here involves the vibration of cantilevers in a liquid environment, where both the surrounding fluid and the target can affect the properties of the cantilever. There are many known challenges when operating a cantilever sensor in a liquid environment, especially in dynamic mode. In particular the large damping caused by the liquid causes low Q factors (see Section 1.3.1) and thus lowers the sensitivity. The added mass of the liquid co-moved with the cantilever when it vibrates causes the effective mass of the cantilever to increase, and thus also lowers the sensitivity of the sensor. However, by operating the cantilever at its higher resonance modes some of the sensitivity can be regained, as discussed in Section 1.3.3.

1.3.1 Quality Factor

The quality factor or Q factor is a dimensionless parameter that is used to describe the damping of a resonator, or equivalently, to characterise the bandwidth of a resonator relative to its centre frequency.

For a damped resonator, such as a cantilever or an RLC circuit, the Q factor can be defined as [57]

$$Q = 2\pi \frac{\text{Energy stored}}{\text{Energy lost per cycle}}. \quad (1.8)$$

The Q factor can be equivalently defined as the ratio of the centre frequency, f_c , and the bandwidth, δf , for high Q factors [57]

$$Q = \frac{f_c}{\delta f} \quad (1.9)$$

which can be measured from the amplitude-frequency spectrum of the vibration.

From the bandwidth definition of the Q factor, it is obvious that the higher the Q factor of a resonator the sharper the amplitude response and thus a sharper resonance

peak is formed in the frequency spectrum. For applications that involve tracking the frequency of the resonator this simplifies the feedback control electronics, minimises the perturbing effect of the drive electronics, and provides a high resolution [58]. A high Q factor also indicates that the resonator is weakly coupled its surroundings which gives high accuracy and long-term stability [58].

In order to understand how the Q factor of a cantilever can be affected it is useful to consider the dissipation, which is defined as the ratio of energy lost per cycle to the energy stored i.e. $1/Q$. The dissipation can be described as the sum of various contributions of energy dissipation in the system [7, 58–60], as follows

$$\frac{1}{Q} = \sum_i \frac{1}{Q_i} = \frac{1}{Q_{clamp}} + \frac{1}{Q_{vis}} + \frac{1}{Q_{mat}} + \frac{1}{Q_{thermo}} + \frac{1}{Q_{other}} \quad (1.10)$$

where $1/Q_{clamp}$ is the energy dissipation into the base due to the clamping of the cantilever [58, 61], $1/Q_{vis}$ is the dissipation due to viscous and acoustic effects with the surrounding medium [58, 62], $1/Q_{mat}$ is the dissipation due to internal material damping [58, 59], $1/Q_{thermo}$ is the dissipation due to thermo-elastic damping [58, 60, 63, 64], and $1/Q_{other}$ is the dissipation due to other effects.

1.3.2 Mass Detection in a Liquid Environment

The dynamics of microcantilevers operating in liquid are well documented in the literature both theoretically [62, 65–71] and experimentally [56, 67, 72] due to the importance of understanding their behaviour for use with AFM. The model, upon which the data analysis software NOSEtools [73–75] used in this project is based, is described in detail in Braun *et al.*, 2005 [67]. An outline of the model will be presented here.

The equation of motion of a cantilever in a vacuum is given by (modified from reference [76], see also reference [67])

$$EI \frac{\partial^4 u(x, t)}{\partial x^4} + C_0 \frac{\partial u(x, t)}{\partial t} + \frac{m_c}{L} \frac{\partial^2 u(x, t)}{\partial t^2} = 0 \quad (1.11)$$

where E is Young's modulus, I is the moment of inertia, C_0 is the intrinsic damping coefficient per unit length, m_c is the mass of the cantilever, L is the length of the cantilever, $u(x, t)$ is the deflection of the cantilever perpendicular to its surface, x is the coordinate along the cantilever, and t is time.

When a cantilever is vibrated in a liquid there are several factors which are not present in a vacuum that must be taken into account. The first is that when the cantilever is driven it is no longer only the mass of the cantilever which must be accelerated, a specific mass of liquid (m_l) will also be accelerated with the cantilever

beam. This results in an additional inertial force acting on the cantilever. The second is that because the liquid is not an ideal fluid the cantilever will experience a dissipative force per unit length that is proportional to the velocity of the cantilever.

When these additional forces, and the driving force applied by the piezoelectric actuator ($F(x, t)$), are taken into account the equation of motion of the cantilever is

$$EI \frac{\partial^4 u(x, t)}{\partial x^4} + (C_0 + C_v) \frac{\partial u(x, t)}{\partial t} + \frac{m_c + m_l}{L} \frac{\partial^2 u(x, t)}{\partial t^2} = F(x, t) \quad (1.12)$$

where C_v is the dissipation coefficient.

In order to solve the equation of motion completely m_l and C_v must be determined. By letting

$$u(t) = u_0 e^{i2\pi f_n t} \quad (1.13)$$

the resonance frequencies, f_n , can be determined from the complex solutions of Eq. 1.11.

$$f_n = \frac{1}{2\pi} \left(\sqrt{\alpha_n^4 (2\pi f_0^*)^2 - \gamma^2 + i\gamma} \right) \quad (1.14)$$

where the damping factor, γ (with dimension of inverse time), is defined by

$$\gamma = \frac{C_0 + C_v}{(2/L)(m_c + m_l)} \quad (1.15)$$

and f_0^* is the fundamental eigenfrequency in a vacuum in the absence of damping, with the mass concentrated at one point (like a simple harmonic oscillator).¹

The f_n are equal to the resonance frequencies of a damped harmonic oscillator except for the α_n term. α_n is the n th positive root of $1 + \cos \alpha_n \cosh \alpha_n = 0$ and is related to the eigenvalues of the modes ($\alpha_1 = 1.875$, $\alpha_2 = 4.694$, \dots , $\alpha_n = \pi(n - 0.5)$).

When the rectangular shape of the cantilevers is taken into account, the eigenfrequencies of a cantilever with a distributed mass in the absence of damping are given by

$$f_{0n} = \frac{\alpha_n^2}{2\pi} \sqrt{\frac{k}{3(m_c + m_l)}} \quad (1.16)$$

where $k = 3EI/L^3$ is the spring constant.

The resonance frequency, f_n , measured as the maximum of the amplitude response in dependence on driving frequency (the resonance peak) can be related to f_{0n} by

$$f_n = \sqrt{f_{0n}^2 - \frac{\gamma^2}{2\pi}}. \quad (1.17)$$

¹The eigenfrequency is the free vibration of the cantilever in the absence of damping given by Eq. 1.16, whereas the resonance frequency refers to the maximum of the amplitude response of the cantilever when vibrated in the liquid.

If extra mass (Δm) binds to the surface of the cantilever uniformly then the total mass (m_{total}) is given by

$$m_{total} = m_c + m_l + \Delta m \quad (1.18)$$

Assuming the spring constant, k , does not change then Eq. 1.16 can be modified to become

$$f'_{0n} = \frac{\alpha_n}{2\pi} \sqrt{\frac{k}{3(m_c + m_l + \Delta m)}}. \quad (1.19)$$

If $\Delta m \ll m_c + m_l$ then the following approximation can be made

$$f'_{0n} \approx f_{0n} \left(1 - \frac{1}{2} \frac{\Delta m}{m_c + m_l} \right). \quad (1.20)$$

Thus

$$\Delta m = \frac{2(m_c + m_l) \Delta f}{f_{0n}} \quad (1.21)$$

where $\Delta f = f_{0n} - f'_{0n}$.

The sensitivity, S , of the cantilever can be defined as

$$S = \frac{\Delta f}{\Delta m} = \frac{f_{0n}}{2(m_c + m_l)} \quad (1.22)$$

which indicates that the sensitivity of a mass loaded cantilever increases with mode number. This is a valid measure of sensitivity because the accuracy of the measurement of Δf is independent of the eigenfrequencies.

This calculation of the added mass from the frequency shift makes the assumption that the added mass is uniformly distributed on the surface in a thin layer and that the spring constant remains unchanged by the adsorption of the added mass. Thus, care should be taken when using such a method as the adsorbed molecules can affect the spring constant of the cantilever in some cases where the thickness of the adsorbed layer is non-negligible [77].

The position of the adsorbed layer of mass can also play a role in the response of the cantilever as shown by the varied response of a microcantilever to the adsorption of bacteria on the surface of the cantilever [78]. This effect is shown to be even more position dependent when higher resonance modes are used [79]. The positioning of individual or several point masses on the surface of the cantilever can also have varied effects on the resonance frequency [80, 81].

1.3.3 Higher Resonance Modes

In order to overcome some of the lost sensitivity due to working in a liquid environment it is possible to vibrate the cantilever at one or more of its higher resonance modes. It

has been shown that the Q factor of the cantilever increases with mode number [18, 82] as predicted by several models [65, 66, 70]. The Q factor increases approximately (excluding internal damping) as [83]

$$Q_n = \frac{f_n}{f_1} Q_1 \quad (1.23)$$

where Q_n is the Q factor at mode n and f_n is the frequency of mode n . Increasing the mode number to increase the Q factor works in general for most applications, however there are cases where this does not apply [62, 71] as discussed in detail in Chapter 4.

The sensitivity of a resonating cantilever beam increases as the mode number of the resonance increases. It has been shown that for a microcantilever vibrating in air the sensitivity of the cantilever increases linearly with the square of the mode number n [82]. The effect of moving to higher modes increasing sensitivity has been well established with microcantilever resonators [84, 85].

It has been shown that the amount of liquid that is co-moved (m_l) with the cantilever decreases asymptotically with increasing mode number n [18]. This is due to the smaller amplitude of the vibrations of the cantilever as the mode number increases. It can be easily determined from Eq. 1.22 that as the mass of co-moved liquid m_l decreases the sensitivity increases. Thus, by vibrating the cantilever at its higher resonance modes it is possible to regain some of the sensitivity that is lost by working in a liquid environment.

1.3.4 Dynamic-Mode Detection

Laser beam deflection is commonly used in AFM devices to measure the response of vibrating cantilevers. When the cantilever is vibrated at a higher resonance mode there are several nodes and antinodes of vibration established along the length of the cantilever. Laser beam deflection is very sensitive to the change in the slope of the cantilever and not so sensitive to the amplitude of the vibration of the cantilever, which can be on the order of a nanometer when using higher modes in a liquid. Thus, as shown in Fig. 1.4, for the maximum signal the laser must be focused at, or near to, a node of the resonance mode where the change in the slope of the cantilever surface during vibration is largest.

1.4 Scope of Thesis

Despite the large number of devices noted in the literature designed to use cantilever sensor arrays, very few devices are capable of the readout of both the static and dynamic response of the cantilever array. The work presented within this thesis details the

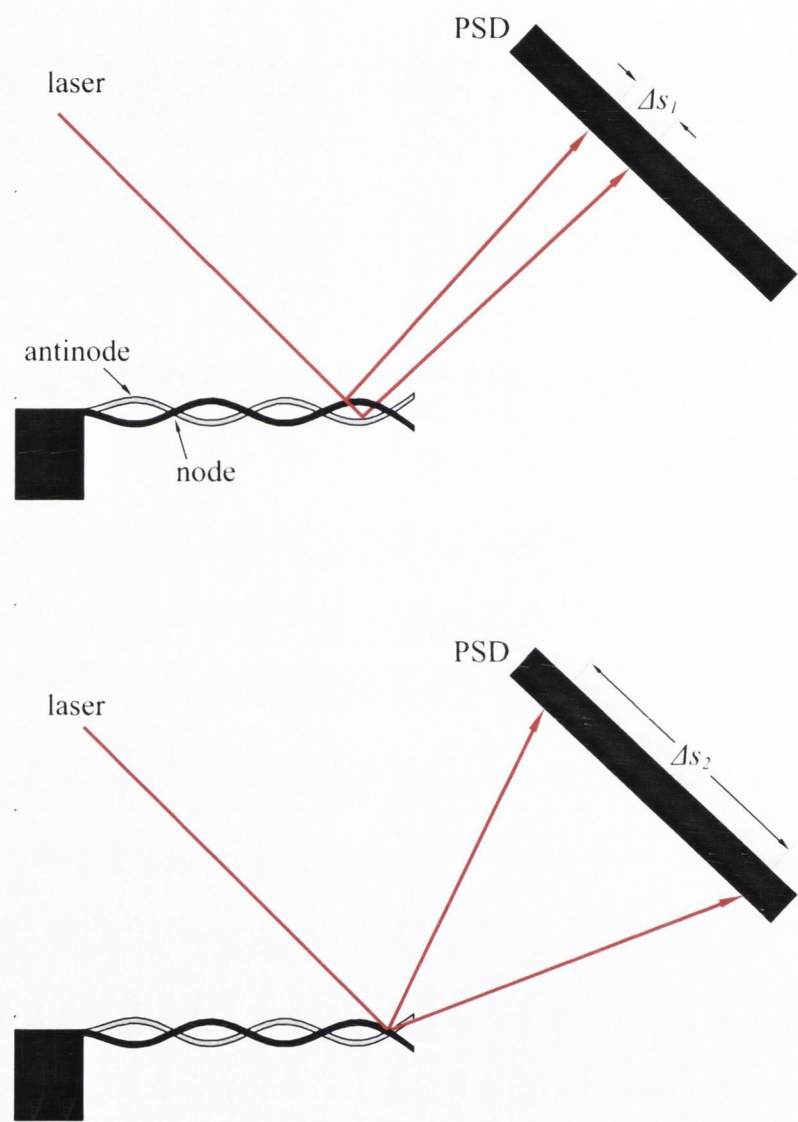


Figure 1.4. Schematics showing the readout of the dynamic response of the cantilever vibrating at the fifth resonance mode using optical beam deflection. When the laser is focused near the antinode of the resonance there is only a small signal (Δs_1) observed on the PSD. When the laser is focused near the node of the resonance there is a large signal (Δs_2) observed on the PSD.

upgrade and development of a dual-mode cantilever-based sensing platform capable of the readout of both the static and dynamic response of the cantilevers in a liquid environment. The application of the dual-mode device is geared towards biological measurements in liquid environments which present their own unique set of challenges.

Due to the varied nature of the work involved in the development of the dual-mode device for biological measurements the main body of the thesis has been split into several distinct sections with the more physics and engineering related material appearing in the early chapters and the application of the developed device to biological detection appearing in the later chapters.

Chapter 2 details the development of the dual-mode device with a brief description of the original dynamic-mode device, and detailed discussion of the instrumentation and programming involved in the development of the dual-mode device. Several initial measurements and demonstrations of various capabilities of the device are presented in the results section of the chapter.

Chapter 3 describes the general preparation techniques that are applied to the cantilever array for most experiments.

Chapter 4 presents verification of the compressible fluid model described by Van Eysden and Sader in air using 2 μm and 7 μm thick cantilevers.

Chapter 5 describes work performed on the detection of the aggregation of the protein α -synuclein which is involved in Parkinson's disease.

Chapter 6 describes initial work on the use of nanoparticles (NPs) and microparticles as a mass label to increase the sensitivity of the device to small molecules which are below the limit of detection alone. A link between the size of the label used and the resulting response of the cantilever is discussed.

Chapter 7 expands on the work in the previous chapter and presents a final step towards the development of a full assay using antibody-functionalised magnetic particles as a mass label in conjunction with cantilever based sensing.

Chapter 8 draws conclusions and provides an outlook for future work.

The Appendices of the thesis are split into sections relating to supplementary information, experimental protocols, and Mathematica source code. A list of presentations and publications by the author is given after the main appendices. A full list of figures and tables contained within the thesis is also given after the appendices. A glossary of terms which may not be familiar to the reader is included at the very back of the volume.

References

- [1] G. Binnig, C. Quate, and C. Gerber, "Atomic force microscope," *Physical Review Letters*, vol. 56, pp. 930–933, 1986.
- [2] J. Gimzewski, C. Gerber, E. Meyer, and R. Schlittler, "Observation of a chemical reaction using a micromechanical sensor," *Chemical Physics Letters*, vol. 217, pp. 589–594, 1994.
- [3] J. R. Barnes, R. J. Stephenson, M. E. Welland, C. Gerber, and J. K. Gimzewski, "Photothermal spectroscopy with femtojoule sensitivity using a micromechanical device," *Nature*, vol. 372, no. 6501, pp. 79–81, 1994.
- [4] T. Thundat, R. Warmack, G. Chen, and D. Allison, "Thermal and ambient-induced deflections of scanning force microscope cantilevers," *Applied Physics Letters*, vol. 64, no. 21, pp. 2894–2896, 1994.
- [5] T. Thundat, E. A. Wachter, S. L. Sharp, and R. J. Warmack, "Detection of mercury vapor using resonating microcantilevers," *Applied Physics Letters*, vol. 66, no. 13, pp. 1695–1697, 1995.
- [6] T. Thundat, G. Y. Chen, R. J. Warmack, D. P. Allison, and E. A. Wachter, "Vapor detection using resonating microcantilevers," *Analytical Chemistry*, vol. 67, no. 3, pp. 519–521, 1995.
- [7] A. Boisen, S. Dohn, S. S. Keller, S. Schmid, and M. Tenje, "Cantilever-like micromechanical sensors," *Reports on Progress in Physics*, vol. 74, no. 3, p. 036101, 2011.
- [8] M. Calleja, P. M. Kosaka, A. San Paulo, and J. Tamayo, "Challenges for nanomechanical sensors in biological detection," *Nanoscale*, vol. 4, no. 16, pp. 4925–4938, 2012.
- [9] H. P. Lang, M. Hegner, and C. Gerber, *Springer Handbook of Nanotechnology*. Berlin, New York, Heidelberg: Springer Verlag, 2006, ch. 16, pp. 443–450.
- [10] H. P. Lang, M. Hegner, and C. Gerber, "Cantilever array sensors," *Materials Today*, vol. 8, pp. 30–36, 2005.
- [11] M. K. Ghatkesar, H. P. Lang, C. Gerber, M. Hegner, and T. Braun, "Comprehensive characterization of molecular interactions based on nanomechanics," *PLoS ONE*, vol. 3, no. 11, p. e3610, 2008.
- [12] F. Battiston, J. Ramseyer, H. Lang, M. Baller, C. Gerber, J. Gimzewski, E. Meyer, and H. Güntherodt, "A chemical sensor based on a microfabricated cantilever array with simultaneous resonance-frequency and bending readout," *Sensors and Actuators B: Chemical*, vol. 77, pp. 121–131, 2001.
- [13] K. Nieradka, T. P. Gotszalk, and G. Schroeder, "A novel method for simultaneous readout of static bending and multimode resonance-frequency of microcantilever-based biochemical sensors," *Sensors and Actuators B: Chemical*, vol. 170, pp.

- 172–175, 2012.
- [14] G. Meyer and N. Amer, “Novel optical approach to atomic force microscopy,” *Applied Physics Letters*, vol. 53, no. 12, pp. 1045–1047, 1988.
- [15] M. Reinstaedtler, U. Rabe, V. Scherer, J. A. Turner, and W. Arnold, “Imaging of flexural and torsional resonance modes of atomic force microscopy cantilevers using optical interferometry,” *Surface Science*, vol. 532–535, pp. 1152–1158, 2003.
- [16] N. Blanc, J. Brugger, N. deRooij, and U. Durig, “Scanning force microscopy in the dynamic mode using microfabricated capacitive sensors,” *Journal of Vacuum Science & Technology B*, vol. 14, no. 2, pp. 901–905, 1996, 8th International Conference on Scanning Tunneling Microscopy and Related Methods (STM 95), SNOWMASS, CO, JUL 25–29, 1995.
- [17] R. Mukhopadhyay, V. V. Sumbayev, M. Lorentzen, J. Kjems, P. A. Andreasen, and F. Besenbacher, “Cantilever sensor for nanomechanical detection of specific protein conformations,” *Nano Letters*, vol. 5, no. 12, pp. 2385–2388, 2005.
- [18] M. K. Ghatkesar, T. Braun, V. Barwich, C. Gerber, M. Hegner, and H.-P. Lang, “Resonating modes of vibrating microcantilevers in liquid,” *Applied Physics Letters*, vol. 92, p. 043106, 2008.
- [19] J. Fritz, M. Baller, H. Lang, H. Rothuizen, P. Vettiger, E. Meyer, H. Güntherodt, C. Gerber, and J. Gimzewski, “Translating biomolecular recognition into nanomechanics,” *Science*, vol. 288, pp. 316–318, 2000.
- [20] R. McKendry, J. Y. Zhang, Y. Arntz, T. Strunz, M. Hegner, H. P. Lang, M. K. Baller, U. Certa, E. Meyer, H. J. Guntherodt, and C. Gerber, “Multiple label-free biodetection and quantitative dna-binding assays on a nanomechanical cantilever array,” *Proceedings of the National Academy of Sciences of the United States of America*, vol. 99, no. 15, pp. 9783–9788, 2002.
- [21] F. Huber, M. Hegner, C. Gerber, H. J. Guntherodt, and H. P. Lang, “Label free analysis of transcription factors using microcantilever arrays,” *Biosensors and Bioelectronics*, vol. 21, no. 8, pp. 1599–1605, 2006.
- [22] J. Zhang, H. P. Lang, F. Huber, A. Bietsch, W. Grange, U. Certa, R. McKendry, H. J. Guntgerodt, M. Hegner, and C. Gerber, “Rapid and label-free nanomechanical detection of biomarker transcripts in human rna,” *Nature Nanotechnology*, vol. 1, no. 3, pp. 214–220, 2006.
- [23] L. M. Lechuga, J. Tamayo, M. Álvarez, L. G. Carrascosa, A. Yufera, R. Doldán, E. Peralías, A. Rueda, J. A. Plaza, K. Zinoviev, C. Domínguez, A. Zaballos, M. Moreno, C. Martínez-A, D. Wenn, N. Harris, C. Bringer, V. Bardinal, T. Camps, C. Vergnenègre, C. Fontaine, V. Díaz, and A. Bernad, “A highly sensitive microsystem based on nanomechanical biosensors for genomics applications,” *Sensors and Actuators B: Chemical*, vol. 118, no. 1–2, pp. 2–10, 2006.

- [24] J. Mertens, C. Rogero, M. Calleja, D. Ramos, J. Martín-Gago, C. Briones, and J. Tamayo, "Label-free detection of DNA hybridization based on hydration-induced tension in nucleic acid films," *Nature Nanotechnology*, vol. 3, pp. 301–307, 2008.
- [25] D. Ramos, M. Arroyo-Hernández, E. Gil-Santos, H. D. Tong, C. V. Rijn, M. Calleja, and J. Tamayo, "Arrays of dual nanomechanical resonators for selective biological detection," *Analytical Chemistry*, vol. 81, no. 6, pp. 2274–2279, 2009.
- [26] G. A. Campbell and R. Mutharasan, "Detection and quantification of proteins using self-excited PZT-glass millimeter-sized cantilever," *Biosensors and Bioelectronics*, vol. 21, no. 4, pp. 597–607, 2005.
- [27] N. Backmann, C. Zahnd, F. Huber, A. Bietsch, A. Pluckthun, H. P. Lang, H. J. Guntherodt, M. Hegner, and C. Gerber, "A label-free immunosensor array using single-chain antibody fragments," *Proceedings of the National Academy of Sciences of the United States of America*, vol. 102, no. 41, pp. 14 587–14 592, 2005.
- [28] T. Braun, M. Ghatkesar, N. Backmann, W. Grange, P. Boulanger, L. Letellier, H. Lang, A. Bietsch, C. Gerber, and M. Hegner, "Quantitative time-resolved measurement of membrane protein-ligand interactions using microcantilever array sensors," *Nature Nanotechnology*, vol. 4, pp. 179–185, 2009.
- [29] B. Ilic, Y. Yang, and H. Craighead, "Virus detection using nanoelectromechanical devices," *Applied Physics Letters*, vol. 85, no. 13, pp. 2604–2606, 2004.
- [30] A. Gupta, D. Akin, and R. Bashir, "Single virus particle mass detection using microresonators with nanoscale thickness," *Applied Physics Letters*, vol. 84, no. 11, pp. 1976–1978, 2004.
- [31] G. A. Campbell and R. Mutharasan, "Detection of pathogen escherichia coli o157:h7 using self-excited pzt-glass microcantilevers," *Biosensors and Bioelectronics*, vol. 21, no. 3, pp. 462–473, 2005.
- [32] D. Ramos, J. Tamayo, J. Mertens, L. Villanueva, and A. Zaballos, "Detection of bacteria based on the thermomechanical noise of a nanomechanical resonator: origin of the response and detection limits," *Nanotechnology*, vol. 19, p. 035503, 2008.
- [33] K. Y. Gfeller, N. Nugaeva, and M. Hegner, "Micromechanical oscillators as rapid biosensor for the detection of active growth of escherichia coli," *Biosensors and Bioelectronics*, vol. 21, no. 3, pp. 528–533, 2005.
- [34] K. Y. Gfeller, N. Nugaeva, and M. Hegner, "Rapid biosensor for detection of antibiotic-selective growth of escherichia coli," *Applied and Environmental Microbiology*, vol. 71, no. 5, pp. 2626–2631, 2005.
- [35] N. Nugaeva, K. Gfeller, N. Backmann, H. Lang, M. Düggelin, and M. Hegner, "Micromechanical cantilever array sensors for selective fungal immobilization and fast growth detection," *Biosensors and Bioelectronics*, vol. 21, pp. 849–856, 2005.

- [36] N. Maloney, G. Lukacs, N. Nugaeva, W. Grange, J. P. Ramseyer, J. Jensen, , and M. Hegner, “Fibre optic readout of microcantilever arrays for fast microorganism growth detection,” *Journal of Sensors*, vol. 2012, p. 405281, 2012.
- [37] P. S. Waggoner, M. Varshney, and H. G. Craighead, “Detection of prostate specific antigen with nanomechanical resonators,” *Lab on a Chip*, vol. 9, no. 21, pp. 3095–3099, 2009.
- [38] M. Varshney, P. S. Waggoner, C. P. Tan, K. Aubin, R. A. Montagna, and H. G. Craighead, “Prion protein detection using nanomechanical resonator arrays and secondary mass labeling,” *Analytical Chemistry*, vol. 80, p. 2141, 2008.
- [39] L. Nicu, M. Guirardel, F. Chambosse, P. Rougerie, S. Hinh, E. Trevisiol, J.-M. Francois, J.-P. Majoral, A.-M. Caminade, E. Cattani, and C. Bergaud, “Resonating piezoelectric membranes for microelectromechanically based bioassay: detection of streptavidin-gold nanoparticles interaction with biotinylated dna,” *Sensors and Actuators B: Chemical*, vol. 110, no. 1, pp. 125–136, 2005.
- [40] A. N. Cleland, M. Pophristic, and I. Ferguson, “Single-crystal aluminum nitride nanomechanical resonators,” *Applied Physics Letters*, vol. 79, no. 13, pp. 2070–2072, 2001.
- [41] E. Stern, J. F. Klemic, D. A. Routenberg, P. N. Wyrembak, D. B. Turner-Evans, A. D. Hamilton, D. A. LaVan, T. M. Fahmy, and M. A. Reed, “Label-free immunodetection with cmos-compatible semiconducting nanowires,” *Nature*, vol. 445, no. 7127, pp. 519–522, 2007.
- [42] D. Ramos, E. Gil-Santos, V. Pini, J. M. Llorens, M. Fernández-Regúlez, A. San Paulo, M. Calleja, and J. Tamayo, “Optomechanics with silicon nanowires by harnessing confined electromagnetic modes,” *Nano Lett.*, vol. 12, no. 2, pp. 932–937, 2012.
- [43] T. P. Burg, M. Godin, S. M. Knudsen, W. Shen, G. Carlson, J. S. Foster, K. Babcock, and S. R. Manalis, “Weighing of biomolecules, single cells and single nanoparticles in fluid,” *Nature*, vol. 446, no. 7139, pp. 1066–1069, 2007.
- [44] M. G. von Muhlen, N. D. Brault, S. M. Knudsen, S. Jiang, and S. R. Manalis, “Label-Free Biomarker Sensing in Undiluted Serum with Suspended Microchannel Resonators,” *Analytical Chemistry*, vol. 82, no. 5, pp. 1905–1910, 2010.
- [45] W. H. Grover, A. K. Bryan, M. Diez-Silva, S. Suresh, J. M. Higgins, and S. R. Manalis, “Measuring single-cell density,” *Proceedings of the National Academy of Sciences of the United States of America*, vol. 108, no. 27, pp. 10 992–10 996, 2011.
- [46] S. Son, A. Tzur, Y. Weng, P. Jorgensen, J. Kim, M. W. Kirschner, and S. R. Manalis, “Direct observation of mammalian cell growth and size regulation,” *Nature Methods*, vol. advance online publication, pp. –, 2012.
- [47] J. Chaste, A. Eichler, J. Moser, G. Ceballos, R. Rurali, and A. Bachtold, “A nanomechanical mass sensor with yoctogram resolution,” *Nature Nanotechnology*,

- vol. 7, no. 5, pp. 301–304, 2012.
- [48] W. H. King, “Piezoelectric sorption detector,” *Analytical Chemistry*, vol. 36, no. 9, pp. 1735–1739, 1964.
- [49] R. E. Speight and M. A. Cooper, “A survey of the 2010 quartz crystal microbalance literature,” *Journal of Molecular Recognition*, vol. 25, no. 9, pp. 451–473, 2012.
- [50] J. Arlett, E. Myers, and M. Roukes, “Comparative advantages of mechanical biosensors,” *Nature Nanotechnology*, vol. 6, no. 4, pp. 203–215, 2011.
- [51] N. Kim, D.-K. Kim, and Y.-J. Cho, “Development of indirect-competitive quartz crystal microbalance immunosensor for c-reactive protein,” *Sensors and Actuators B: Chemical*, vol. 143, no. 1, pp. 444–448, 2009.
- [52] K. S. Hwang, J. H. Lee, J. Park, D. S. Yoon, J. H. Park, and T. S. Kim, “In-situ quantitative analysis of a prostate-specific antigen (psa) using a nanomechanical PZT cantilever,” *Lab Chip*, vol. 4, no. 6, pp. 547–552, 2004.
- [53] T. Miyatani and M. Fujihira, “Calibration of surface stress measurements with atomic force microscopy,” *Journal of Applied Physics*, vol. 81, no. 11, p. 7099, 1997.
- [54] R. Mishra, W. Grange, and M. Hegner, “Rapid and reliable calibration of laser beam deflection system for microcantilever-based sensor setups,” *Journal of Sensors*, vol. 2012, p. 617386, 2012.
- [55] J. Mertens, M. Álvarez, and J. Tamayo, “Real-time profile of microcantilevers for sensing applications,” *Applied Physics Letters*, vol. 87, no. 23, p. 234102, 2005.
- [56] M. K. Ghatkesar, E. Rakhmatullina, H.-P. Lang, C. Gerber, M. Hegner, and T. Braun, “Multi-parameter microcantilever sensor for comprehensive characterization of Newtonian fluids,” *Sensors and Actuators B: Chemical*, vol. 135, pp. 133–138, 2008.
- [57] H. J. Pain, *The physics of vibrations and waves*, 6th ed. John Wiley & Sons, Inc., 2005.
- [58] G. Stemme, “Resonant silicon sensors,” *Journal of Micromechanics and Microengineering*, vol. 1, pp. 113–125, 1991.
- [59] R. Sandberg, K. Mølhave, A. Boisen, and W. Svendsen, “Effect of gold coating on the Q -factor of a resonant cantilever,” *Journal of Micromechanics and Microengineering*, vol. 15, no. 12, p. 2249, 2005.
- [60] K. Yasumura, T. Stowe, E. Chow, T. Pfafman, T. Kenny, B. Stipe, and D. Rugar, “Quality factors in micron- and submicron-thick cantilevers,” *Microelectromechanical Systems, Journal of*, vol. 9, no. 1, pp. 117–125, 2000.
- [61] D. M. Photiadis and J. A. Judge, “Attachment losses of high Q oscillators,” *Applied Physics Letters*, vol. 85, no. 3, pp. 482–484, 2004.
- [62] C. A. Van Eysden and J. E. Sader, “Frequency response of cantilever beams immersed in compressible fluids with applications to the atomic force microscope.”

- Journal of Applied Physics*, vol. 106, p. 094904, 2009.
- [63] R. Lifshitz and M. L. Roukes, "Thermoelastic damping in micro- and nanomechanical systems," *Physical Review B*, vol. 61, no. 8, pp. 5600–5609, 2000.
- [64] S. Schmid and C. Hierold, "Damping mechanisms of single-clamped and prestressed double-clamped resonant polymer microbeams," *Journal of Applied Physics*, vol. 104, no. 9, p. 093516, 2008.
- [65] F.-J. Elmer and M. Dreier, "Eigenfrequencies of a rectangular atomic force microscope cantilever in a medium," *Journal of Applied Physics*, vol. 81, no. 12, pp. 7709–7713, 1997.
- [66] J. E. Sader, "Frequency response of cantilever beams immersed in viscous fluids with applications to the atomic force microscope," *Journal of Applied Physics*, vol. 84, no. 1, pp. 64–76, 1998.
- [67] T. Braun, V. Barwich, M. Ghatkesar, A. Bredekamp, C. Gerber, M. Hegner, and H. Lang, "Micromechanical mass sensors for biomolecular detection in a physiological environment," *Physical Review E*, vol. 72, no. 031907, p. 031907, 2005.
- [68] C. A. Van Eysden and J. E. Sader, "Resonant frequencies of a rectangular cantilever beam immersed in a fluid," *Journal of Applied Physics*, vol. 100, p. 114916, 2006.
- [69] C. A. Van Eysden and J. E. Sader, "Small amplitude oscillations of a flexible thin blade in a viscous fluid: Exact analytical solution," *Physics of Fluids*, vol. 18, p. 123102, 2006.
- [70] C. A. Van Eysden and J. E. Sader, "Frequency response of cantilever beams immersed in viscous fluids with applications to the atomic force microscope: Arbitrary mode order," *Journal of Applied Physics*, vol. 101, p. 044908, 2007.
- [71] C. A. Van Eysden and J. E. Sader, "Compressible viscous flows generated by oscillating flexible cylinders," *Physics of Fluids*, vol. 21, p. 013104, 2009.
- [72] S. Kim and K. Kihm, "Experimental verification of the temperature effects on Sader's model for multilayered cantilevers immersed in an aqueous medium," *Applied Physics Letters*, vol. 89, p. 061918, 2006.
- [73] T. Braun, M. K. Ghatkesar, V. Barwich, N. Backmann, F. Huber, W. Grange, N. Nugaeva, H. Lang, J. Ramseyer, C. Gerber, and M. Hegner, "Digital processing of multi-mode nano-mechanical cantilever data," *Journal of Physics: Conference Series*, vol. 61, pp. 341–345, 2007.
- [74] T. Braun, F. Huber, M. K. Ghatkesar, N. Backmann, H. P. Lang, C. Gerber, and M. Hegner, "Processing of kinetic microarray signals," *Sensors and Actuators B-Chemical*, vol. 128, no. 1, pp. 75–82, 2007.
- [75] T. Braun, "Nosetools homepage," accessed 1st Mar 2010, NOSEtools Version 7.2 (rev 438) is available to download free from the NOSEtools Homepage.

- The software is copyrighted by Thomas Braun 2008, 2009, University of Basel, Switzerland. [Online]. Available: <http://web.me.com/brunobraun/NOSEtools/Home.html>
- [76] L. Landau and E. Lifshitz, *Theory of Elasticity*. Oxford: Pergamon, 1970.
 - [77] J. Tamayo, D. Ramos, J. Mertens, and M. Calleja, "Effect of the adsorbate stiffness on the resonance response of microcantilever sensors," *Applied Physics Letters*, vol. 89, no. 22, p. 224104, 2006.
 - [78] D. Ramos, J. Tamayo, J. Mertens, and M. Calleja, "Origin of the response of nanomechanical resonator to bacteria adsorption," *Journal of Applied Physics*, vol. 100, p. 106105, 2006.
 - [79] D. Ramos, M. Calleja, J. Mertens, A. Zaballo, and J. Tamayo, "Measurement of the mass and rigidity of adsorbates on a microcantilever sensor," *Sensors*, vol. 7, no. 9, pp. 1834–1845, 2007.
 - [80] S. Dohn, W. Svendsen, A. Boisen, and O. Hansen, "Mass and position determination of attached particles on cantilever based mass sensors," *Review of Scientific Instruments*, vol. 78, no. 10, pp. 103303–3, 2007.
 - [81] S. Dohn, S. Schmid, F. Amiot, and A. Boisen, "Position and mass determination of multiple particles using cantilever based mass sensors," *Applied Physics Letters*, vol. 97, no. 4, p. 044103, 2010.
 - [82] M. K. Ghatkesar, V. Barwich, T. Braun, J. P. Ramseyer, C. Gerber, M. Hegner, H. P. Lang, U. Drechsler, and M. Despont, "Higher modes of vibration increase mass sensitivity in nanomechanical microcantilevers," *Nanotechnology*, vol. 18, p. 445502, 2007.
 - [83] R. Garcia and E. T. Herruzo, "The emergence of multifrequency force microscopy," *Nature Nanotechnology*, vol. 7, no. 4, pp. 217–226, 2012.
 - [84] S. Dohn, R. Sandberg, W. Svendsen, and A. Boisen, "Enhanced functionality of cantilever based mass sensors using higher modes," *Applied Physics Letters*, vol. 86, no. 23, p. 233501, 2005.
 - [85] D. Then, A. Vidic, and C. Ziegler, "A highly sensitive self-oscillating cantilever array for the quantitative and qualitative analysis of organic vapor mixtures," *Sensors and Actuators B: Chemical*, vol. 117, no. 1, pp. 1–9, 2006.

Chapter 2

Dual-Mode Device

This chapter will describe the development of an experimental device capable of the measurement of the static and dynamic responses of a micron-scale cantilever array in a physiological liquid environment. Firstly the dynamic-mode device existing at the start of my studies will be briefly described to provide a reference point from which the development of the current generation of the device began. The main components of the current dual-mode device, including the fluid chamber, optics, laser positioning system, PSD, temperature control, and the fluidic system will be described in detail. A brief description of the measurement procedure and the main considerations in the Laboratory Virtual Instrumentation Engineering Workbench (LabVIEW) programming behind the device will be given. Finally some measurements of the frequency spectrum and response of a gold coated cantilever array to a heat pulse will be shown to demonstrate the working device. The improvements of flowing fluid using the pressure flow system compared to the syringe pump will be highlighted.

2.1 Existing Dynamic-Mode Device

The existing device used an optical beam deflection method to read out the response of the each cantilever during the experiment. An array of eight vertical-cavity surface-emitting lasers (VCSELs) (Avalon Photonics) were used in a time-multiplexed manner to provide read out from each of the eight cantilevers in the array. The VCSELs had a wavelength of 760 nm. The cone of light produced from a VCSEL has an angle of divergence that depends on the aperture size. For the VCSELs used here the solid angle was 13° at full width at half maximum (FWHM). The output power of the VCSELs when operated at 5 mA was 1.2 mW.

The VCSELs were focused onto the surface of the cantilevers using an external focusing system. The focusing system consisted of two 12.5 mm diameter convex lenses (Edmund Scientific) each with a focal length of 45 mm placed next to each other. The VCSELs were located at the focal point of one of the lenses and the lens system was

moved so that the cantilever array was at the focal point of the other. The pitch of the VCSEL array matched that of the cantilever array with the idea being that using one-to-one optics ensured that the laser spot from each VCSEL was focused onto the surface of the corresponding cantilever. The VCSEL array and the focusing system were mounted on a lockable stage on a dove tail rail, which could be moved in one dimension to allow the positioning of the cantilever array at the focal point.

The PSD was mounted on a stack of translation and rotation stages which allowed the PSD to be moved in three dimensions in addition to being rotated about the vertical axis.

Fluid was pumped through the chamber using a syringe pump (Kent Scientific). Polyether-ether-ketone (PEEK) tubing was used to bring the liquid from the syringe to the fluid chamber.

The device was housed inside a small refrigeration unit (Intertronic) which provided a temperature stable environment. A small CCD camera was mounted in the box to aid in the alignment of the VCSELs on the surface of the cantilevers.

2.1.1 Problems with the Existing Device

The VCSEL array and focusing system were fixed on a sliding dove tail mount with a screw to fix the position. This sliding mount was used to position the VCSELs relative to the cantilever array, which was mounted separately. This sliding mount did not allow fine positioning of the VCSELs which made it difficult to position the focus of the laser on the surface of the cantilever. The locking screw was applied from one side of the rail only and could move the beam off axis when applied, causing major difficulty in the alignment of the beam. In addition, the VCSEL array and focusing system were mounted on an XY translation platform which allowed only a coarse adjustment of the spot position on the cantilever surface. The VCSEL array was mounted in a tube which was rotatable for aligning the array of VCSELs with the array of cantilevers. This rotation was done coarsely by hand and alignment of the two arrays could only be performed by tedious sequential switching on and off of the VCSELs.

The wavelength of the VCSELs was partially in the infra-red and so it was difficult to observe when the laser spot was properly focused on the surface of the cantilever. The small CCD camera saturated easily when the VCSELs were turned on and did not have sufficient resolution to show if the correct focus had been achieved. It was sufficient to tell if the laser was hitting the cantilever, but not more than that.

The difficulty in focusing and moving the VCSEL spot accurately on the cantilever surface leads to a lack of sensitivity (increase in optical noise) for measuring higher resonance modes of the cantilever which give a better sensitivity for mass change [1] (see Section 1.3.3).

Another problem with the existing device was that the VCSEL array was located in the same tube that held the focusing system. This did not allow for the VCSEL array to be temperature regulated, which could lead to instability of the VCSEL output. Instability in the laser output can lead to an additional source of noise in experiments and could potentially shorten the lifespan of the VCSELs (which are no longer available as an ‘off the shelf’ component and must be fabricated to order at a significantly higher price than when the device was originally developed).

The optics technique used in the focusing system created small differences in the optical path length between each VCSEL and its corresponding cantilever. While these path differences were indeed very small, it has been shown that small differences in the optical path can lead to different calibration factors of the device [2], and so for high-quality precision measurements differences in the path should be avoided.

The many degrees of freedom of the PSD motion and alignment of the VCSELs caused the initial setup of each experiment to be painstaking and lead to small differences in the setup for each experiment. The time taken for alignment could vary significantly and was not suited for measurements where the quality of the functionalisation of the cantilever surface was time sensitive.

2.2 Instrumentation

2.2.1 Fluid Chamber

The chamber which houses the cantilever array is comprised of two halves which are precision machined from PEEK and are screwed together using M4 screws. The chamber has a single inlet and outlet which couple to standard 1/16” tubing and is designed such that the flow of liquid is directed from the side and across the cantilevers in the array and minimises dead volume and areas of poor mixing. The total volume of the chamber is approximately 6 μl which is small enough to allow efficient changing of fluids (e.g. during sample injection) and minimise the amount of sample required. The entire chamber is shown in Fig.2.1.a.

The thermal motion of the cantilevers when immersed in liquid does not provide sufficient amplitudes of motion to allow measurement beyond the first few resonance modes to the higher resonance modes of the cantilevers. In order to obtain the higher resonance modes the cantilevers are driven using a piezoelectric actuator (EBL Products Inc., East Hartford, CT 06108, USA). The cantilever array body is clamped on top of the piezoelectric actuator to allow coupling of the cantilevers and the actuator (Fig. 2.1.b). The piezoelectric actuator does not create any non-flexural peaks in the frequency spectrum of the actuated cantilever (as shown in Fig. 2.2).

The piezoelectric actuator is separated from the liquid chamber by a 180 μm thick

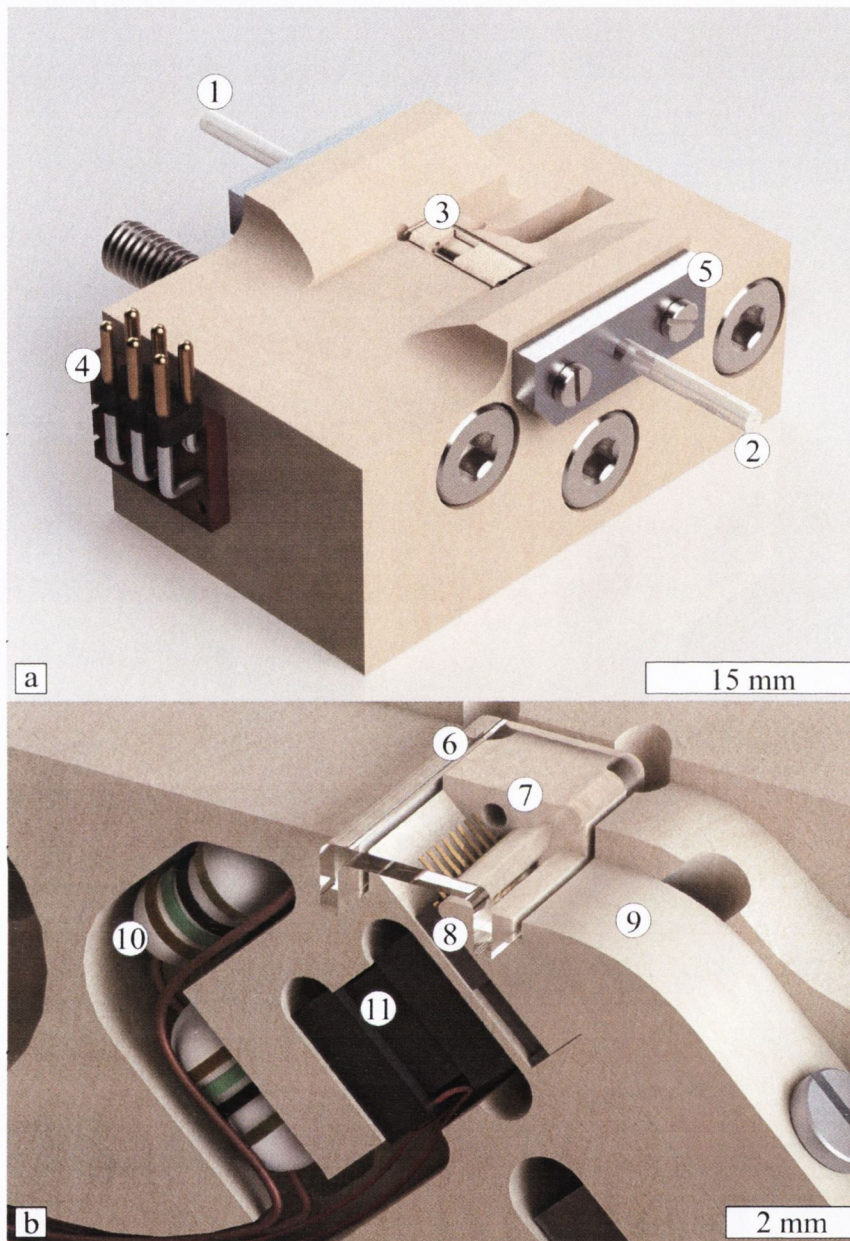


Figure 2.1. The fluid chamber and close up view. **a) The fluid chamber.** The chamber is precision machined from PEEK and is comprised of two halves which are screwed together by three M4 screws. The excess screws protruding from the side of the chamber are used to mount the chamber in its holder. **1.** Fluid inlet: 1/16" teflon tubing. **2.** Fluid outlet. **3.** Location of cantilever array. **4.** Electrical connections to the piezoelectric actuator and the two 15 Ω resistors. **5.** Seal for the fluid inlet/outlet with o-ring hidden. **b) Close up view of the fluid chamber.** The chamber contains an actuator which is separated from the fluid by a 180 μm thick membrane which is thin enough to allow coupling of the cantilevers and the actuator, but thick enough to be mechanically stable and long lasting. The resistors are used to provide a heat pulse to the chamber. The electronic components are surrounded by Torsel in the finished piece to provide further insulation from the fluid. **6.** Custom borosilicate glass cover slip. **7.** Inlet for the fluid. **8.** Cantilever array. **9.** PEEK clamp to hold the array in place. **10.** Two 15 Ω resistors. **11.** Piezoelectric stack.

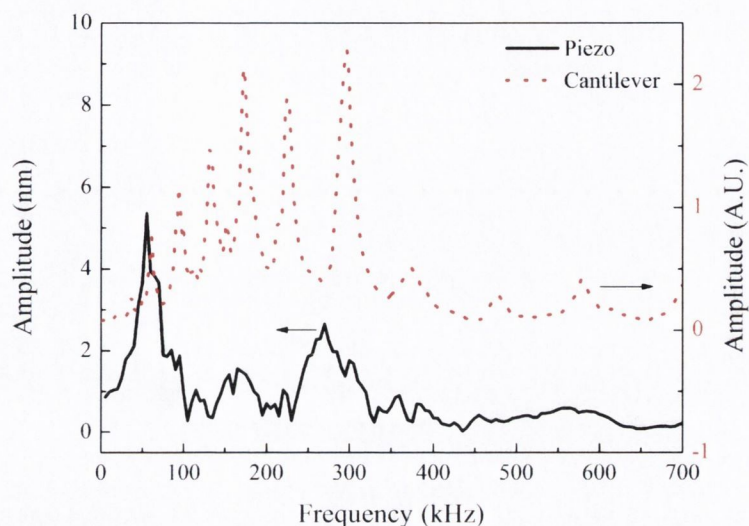


Figure 2.2. Comparison between the amplitude of the piezoelectric actuator and the actuated cantilever vs. frequency. It is clear from the overlay that the actuation of the cantilever does not create any non-flexural peaks in the response of the cantilever. The amplitude of the actuator vibration was measured using a laser Doppler vibrometer (Polytec Fiber Vibrometer OFV-552, Polytec Ltd., Lambda House, Batford Mill, Harpenden Hertfordshire, AL5 5BZ, UK).

membrane which provides a barrier between the liquid and the piezoelectric actuator to avoid shorting and damage. The membrane is thin enough to allow for efficient coupling of energy from the piezoelectric actuator to the cantilevers, but thick enough to be mechanically stable and long lasting.

The cantilever array is positioned at an angle of 45° to the edges of the chamber to avoid the creation of interference in the frequency spectra due to the formation of standing waves in the liquid or reflections from the walls of the chamber. In addition, the base of the cantilever array is sufficiently thick to avoid any squeeze film effects between the cantilevers and the membrane.

The custom borosilicate glass cover (VitroCom, Mountain Lakes, New Jersey 07046) and positioning of the cantilever array allows the laser light to enter and leave the chamber at 90° to the liquid/glass interface and thus avoids any divergence of the beams due to refractive index changes.

A heat pulse can be applied to the fluid chamber by passing a current through two $15\ \Omega$ resistors connected in series and located below the fluid chamber. This allows calibration of the response of the individual cantilevers in the array and results in comparable measurements between the cantilevers.

The electronic components below the fluid chamber are all covered with a layer of Torseal which is allowed to dry before being machined flat on the surface. This

provides further isolation of the components from the liquid in the chamber.

2.2.2 Optics and Laser Positioning System

A single-wavelength fibre-coupled diode laser (632.99 nm \pm 1.5 pm, free space power >2.4 mW, linewidth <200 kHz, SWL 7504-P; New Focus, Newport, CA 92606, USA) with controller (SWL-7500 ECDL controller, New Focus) is used to replace the VCSEL array. The laser current and diode temperature can be controlled via a serial connection from a PC to the controller. For optimal stability and performance the laser is operated at the recommended factory settings which are unique to each laser. For the laser used here the laser current is 85 mA and the diode temperature is 21.3 °C. The laser has a very stable output (power is stable to within 1% once it has been turned on for 20 minutes) and the temperature control avoids any changes in power that can be observed when using an array of VCSELs for readout.

The beam is collimated into a 3.45 mm diameter beam using a fibre collimation package (F280 APC-B; Thorlabs, Cambridgeshire, CB7 4EX, UK). The package is prealigned to collimate the beam propagating from the tip of the connected fibre with diffraction limited performance. The divergence of the collimated beam is 0.014° when used at the alignment wavelength of 635 nm. The receptacle of the package is angled to ensure that the collimated beam is aligned with the mechanical axis of the package.

The intensity of the laser when reflected from the surface of a gold coated cantilever is sufficient to saturate the PSD which has a maximum output of 10 V. The output of the laser was attenuated using an absorptive neutral density (ND) filter (OD 1.3 NE513B; Thorlabs, Cambridgeshire, CB7 4EX, UK) with a transmission of 5%. For initial focusing and alignment of the laser a stronger ND filter was used (OD 6.0 NE560B) with a transmission of 0.0001% to avoid eye damage.

The beam is focused into a spot on the surface of the cantilever using a 50 mm focal-length doublet (AC254-050-A1-ML; Thorlabs, Cambridgeshire, CB7 4EX, UK). The lens is achromatic and can be used to achieve a diffraction limited spot when combined with a monochromatic source.

The spot size of the laser on the surface of the cantilever can be calculated using the basic optics formula for beam diameter at the waist of the beam [3].

$$D_{cl} = \left(\frac{4\lambda}{\pi} \right) \left(\frac{f_{lens}}{D_{coll}} \right) \quad (2.1)$$

where D_{cl} is the diameter of the spot on the cantilever, λ is the wavelength of the laser, f_{lens} is the focal length of the lens, and D_{coll} is the collimated beam diameter. Using the values mentioned above the spot size on the cantilever can be calculated to be $\sim 12 \mu\text{m}$.

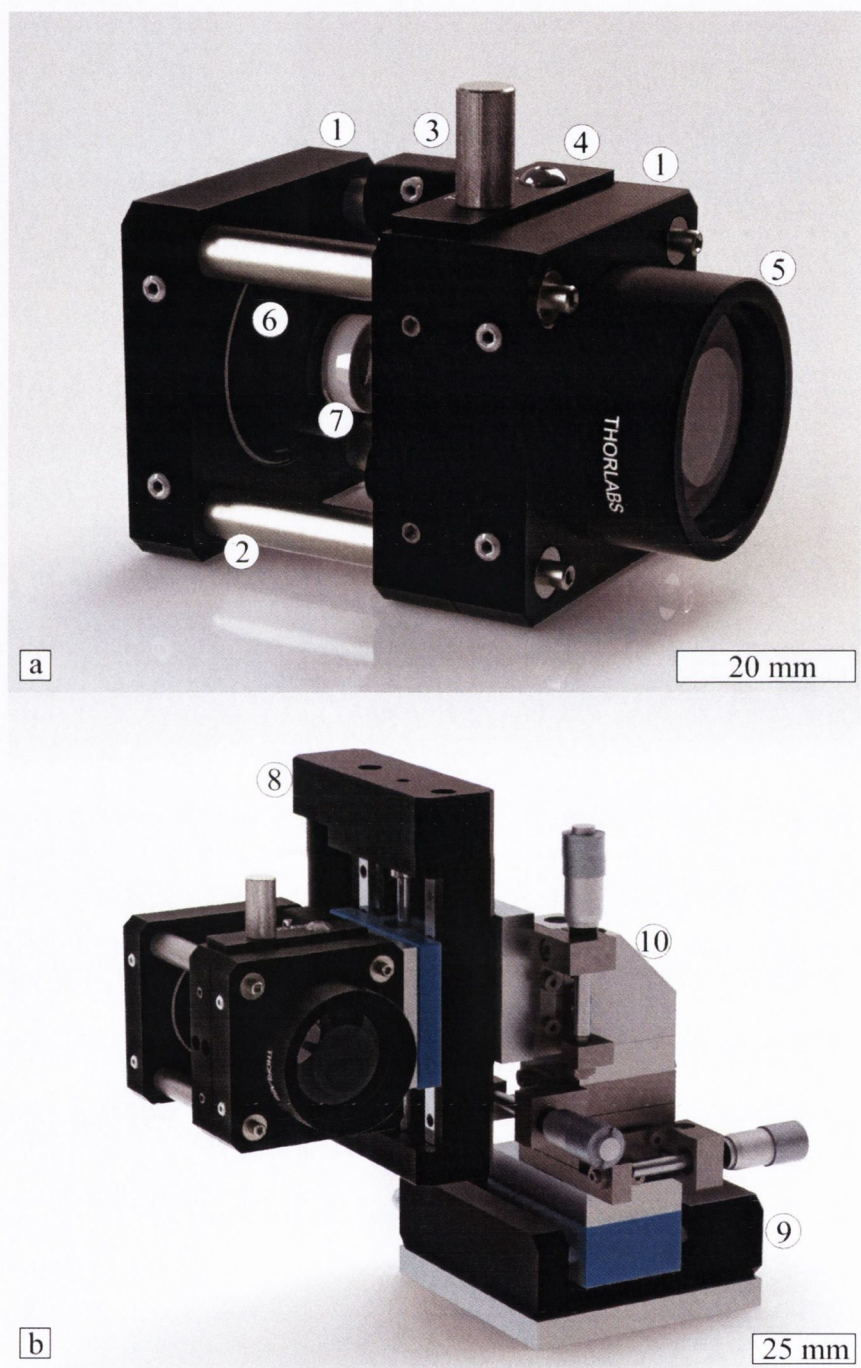


Figure 2.3. The optic cage and laser positioning system. **a) The optic cage.** The cage system keeps the optic axis of the system aligned. **1.** Cage plates. **2.** Cage rods. **3.** Cage mounting adapter **4.** Filter holder with switchable ND filter. **5.** 50 mm focal-length achromatic doublet. **6.** Mounting adapter for collimator package. **7.** Aspheric collimator package. **b) Laser positioning system.** The positioning system allows movement of the laser spot between and along the length of the cantilevers via the motion of two automated stages. Initial focusing of the laser spot on the cantilever is achieved using the XYZ translation stage **8.** M-122.2DG precision micro-translation stage. **9.** M11.1DG precision micro-translation stage. **10.** Micro-translation XYZ translation stage.

The depth of focus (DOF) of is given by [3]

$$DOF = \left(\frac{8\lambda}{\pi} \right) \left(\frac{f_{lens}}{D_{coll}} \right)^2. \quad (2.2)$$

The depth of focus can be calculated to be $\sim 340 \mu\text{m}$, which shows the tolerance of the focus positioning and also gives the limits of the movement of the laser beam with respect to the cantilever.

The optic axis of the system is maintained using a cage system shown in Fig. 2.3.a [30 mm Cage mounting adapter: CP02B; Collimator Mounting adapter: AD11F; Cage Plate: CP02/M; Rods: ER2; Filter Holder: NE513B] (Thorlabs, Cambridgeshire, CB7 4EX, UK).

Two automated translation stages (M110.1DG and M122.2DD; Physik Instrumente, Bedford, MK43 0AN, UK) allow the sequential readout of the response from the eight cantilevers in the array (Fig. 2.3.b). The stages are aligned at right angles to each other to provide movement between the cantilevers and also along the length of each cantilever. The positioning stages facilitate rapid movement between cantilevers (max travel speeds 1 and 20 mm/s respectively), with very repeatable positioning of the spot on the surface as shown in Fig. 2.4.

The spot position repeatability was measured by rotating the PSD by 90° and measuring the static response of the cantilever as the translation stage moved the spot from cantilever to cantilever repeatedly over a two hour period. As a result the position of the spot on the surface of the cantilever (and not the bending of the cantilever) was measured. The spot position repeatability using the M110.1DG stage has a spread of $\sim 2 \text{ nm}$ at the ‘home’ position on cantilever 1 and shows little drift. On cantilever 5 there is a similar spread in the position, which a slight drift of $\sim 3.5 \text{ nm/hr}$. This is well within the stated positional repeatability of the stage and will not contribute significant levels of noise to the static signal. The M122.2DG shows a similar response, with the spread being $\sim 10 \text{ nm}$ and similar drifts (data not shown). Thus, the motion of the stages will not contribute significantly to the noise levels in the static and dynamic response of the cantilevers.

The two automated stages are connected to a lockable xyz micro-translation stage (Gothic Arch 9061-XYZ-M; Newport, CA 92606, USA) which allows fine focusing of the laser spot on the surface of the cantilever.

The motion of the stages is controlled via the main LabVIEW program (see Section 2.3.2) and two Mercury C863 DC Motor Controllers (Physik Instrumente). As shown in Fig. 2.5 the laser spot is positioned at the tip of cantilever 1 at the start of the experiment using the xyz micro-translation stage. The M110.1DG stage is then used to place the spot at the position which gives the best dynamic signal (see Section 1.3.4). The M122.2DD stage is used to move the laser spot between cantilevers at a speed of

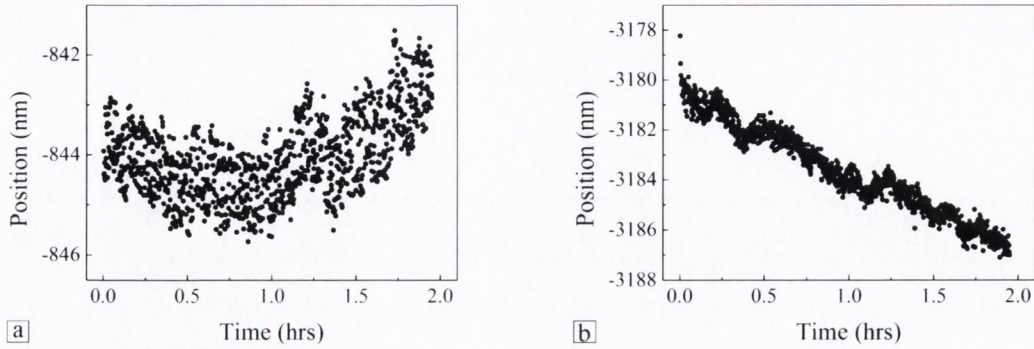


Figure 2.4. The position of the laser spot on the surface of the cantilever was measured as the spot was moved repeatedly from cantilever to cantilever over a two hour period using the M110.1DG stage and measuring the static response of the cantilever with the PSD rotated 90°. This allows the position of the spot on the cantilever (not the bending of the cantilever) to be measured. **a)** The spot position on cantilever 1 has a spread of ~ 2 nm and very little drift. **b)** The spot position on cantilever 5 also has a spread of ~ 2 nm but has a drift of ~ 3.5 nm/hr. The motion of the stages should not contribute significantly to the noise levels in the static or dynamic response of the cantilevers.

10 mm/s, and then the M110.1DG is used to move the spot along the cantilever at a speed of 1 mm/s to the best position. Following the movement there is a short 50 ms wait before the dynamic measurement is taken to ensure that there is no effect of the movement on the measured cantilever response.

The second positioning stage combined with the small spot size of the laser allows the best position for readout of each dynamic mode to be found on each cantilever in the array. The maximum signal in the dynamic mode is achieved when the laser is positioned at a node of the resonance resulting in the largest angular deflection of the beam (see Section 1.3.4). Individual positioning along each cantilever compensates for small differences between the cantilevers and as a result more cantilevers in the array can be read out successfully during each experiment. Previously, with a VCSEL array or a single translation stage, it was not always possible to have low noise/high amplitude readings from all cantilevers in the array because the higher resonance nodes are not necessarily at exactly the same distance from the tip of each cantilever. The second automated stage also provides easy use of arrays containing different numbers of cantilevers, different length cantilevers (harp-shaped arrays), or cantilevers with different properties (e.g. thickness, width).

The stable optical system allows for ease of use of the device. Once the laser has been aligned, the array and the fluid chamber can be removed and replaced many times without any need for adjustment of the optics. The focus of the laser has not needed adjustment since the initial alignment (>1 year).

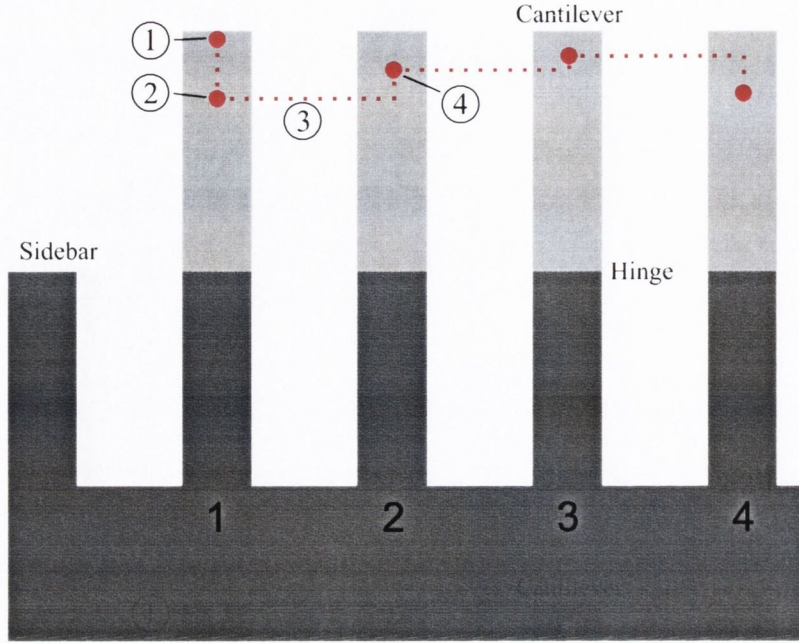


Figure 2.5. Schematic showing the movement of the laser spot between cantilevers. The M110.1DG stage is used for moving along the cantilever and the M122.2DD stage is used for moving between cantilevers. **1.** The laser spot is positioned at the tip of cantilever number 1, with the xyz micro-translation stage, at the start of the experiment. **2.** The laser spot is moved to the best position for dynamic measurement on cantilever 1 using the M110.1DG stage at a speed of 1 mm/s. **3.** The laser spot is moved to cantilever 2 using the M122.2DD stage at a speed of 10 mm/s. **4.** Once the spot is on cantilever 2 it is then moved along the cantilever to the best position for dynamic measurement using the M110.1DG stage. Once the laser spot has moved there is a 50 ms pause before the measurement of the dynamic signal to ensure there is no effect of the movement on the response of the cantilever. The movements along the length of the cantilever are greatly exaggerated in the image as an example.

2.2.3 Position Sensitive Detector

A PSD is usually a PIN diode device (a layered semiconductor device consisting of a lightly doped intrinsic semiconductor region sandwiched between p-type and n-type semiconductor regions) operated in reverse bias. A simple example of a PSD structure is shown in Fig. 2.6.a. The PSD can measure the position of a spot of light based on the amount of current generated at each contact caused by the formation of carriers in the depletion region by the incident light. The position of the spot (s), measured from the centre line, on a 1D PSD can be calculated using the following formula [4, 5]

$$s = \frac{I_1 - I_2}{I_1 + I_2} \frac{L_{PSD}}{2} \quad (2.3)$$

where I_1 and I_2 are the currents from the contacts on the PSD, and L_{PSD} is the active length of the PSD. The position of the spot calculated does not depend on the intensity

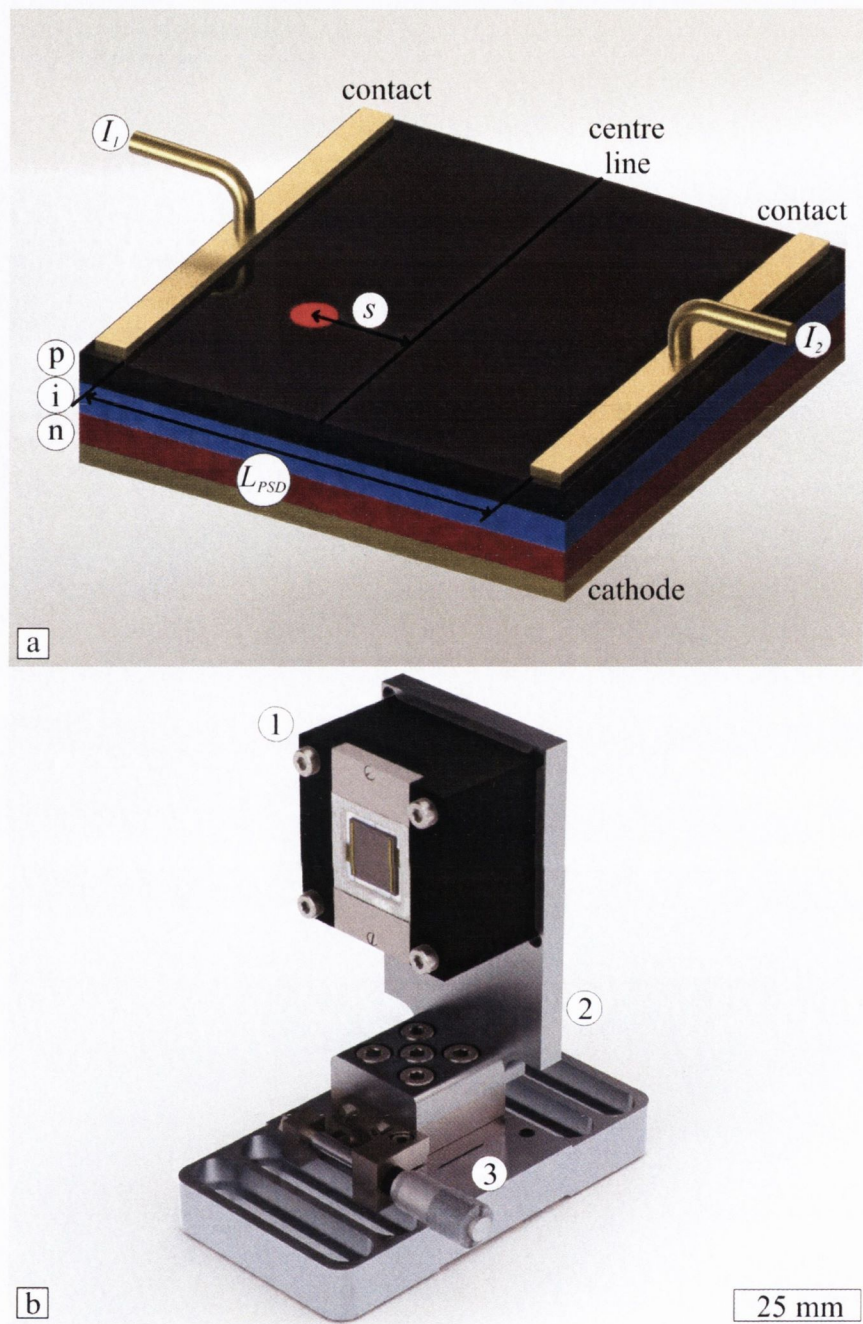


Figure 2.6. **a)** The PSD is a PIN diode operated in reverse bias. The device consists of three layers, a p-type semiconductor, an n-type semiconductor, and a lightly doped intrinsic layer sandwiched between the other two layers. The metal contact on the backside of the device is the cathode and a bias voltage of 15 V is applied across the device. The two metal contacts on the top surface are used for measuring the currents I_1 and I_2 which are used to calculate the position, s , of the laser spot on the surface of the PSD. **b)** The PSD is mounted in a custom machined aluminium holder on a linear translation stage. The stage has a small range of movement which allows the PSD to be moved such that the reflected laser beam strikes the PSD at the centre. This compensates for any small initial bending of the cantilever prior to the start of the experiment. **1.** The PSD and electronics in housing. **2.** Custom machined aluminium holder. **3.** Linear translation stage.

of the light incident on the detector and the position obtained is a centre of gravity position meaning that the measurement is relatively insensitive to the shape of the spot.

The PSD used in the current device is a 1D PSD (1L10-10-ASU15, Sitek, Sweden) mounted in a custom machined housing containing an electronics board to convert the currents to voltages and op-amps to amplify the signal. The PSD has three contacts, two on the front side for measuring the currents and a cathode on the backside for applying the bias voltage (5-30 V range with typical value of 15 V). The rise time of the PSD is typically 60 ns with a maximum of 110 ns. The linearity of the response of the PSD between the two electrodes is excellent (data not shown). The bandwidth of the PSD is 2 MHz.

A 1D PSD, as opposed to a 2D PSD, was chosen because the flexural resonance modes of the cantilever are of interest. By aligning the axis of the PSD with the plane of motion of the laser beam induced by the flexural modes, the effect of the torsional modes of resonance can be removed from the measured response.

An image of the mounted PSD and holder is shown in Fig. 2.6.b. The custom PSD holder is mounted on a one dimensional micro-translation stage (Low profile gothic-arch translation stage, 25×25 mm platform, 12.7 mm travel, New Focus) which allows the the PSD to be moved to account for any small initial bending of the cantilevers and positioning of the spot at the centre line of the PSD.

2.2.4 Temperature Control

A steady temperature is essential when working with cantilevers which are coated on one side with a metal. Any change in temperature in the system will induce a bending in the cantilevers due to the difference in thermal expansion coefficients of the metal and the silicon. To avoid this the entire device is housed inside a small refrigeration unit (Intertronic, Interdiscount, Switzerland) which is capable of heating and cooling. The temperature is maintained at a constant temperature of 23.0 ± 0.1 °C via a power supply (Agilent E3614A DC power supply, Agilent Technologies Ireland Ltd., Unit 3, Euro House, Euro Business Park, Little Island, Cork, Ireland) and a fuzzy logic routine implemented in the main LabVIEW program.

The temperatures from the room and the refrigeration unit are recorded using three thermocouples (one in the room and two at different heights within the unit). The voltages from the thermocouples are measured by the data acquisition board (DAQ) (NI PCI 6221, National Instruments, Texas, USA) and an input/output board (BNC 2110, National Instruments) which is connected to the DAQ and is housed in the chassis.

In order to have a reliable reading of the temperature the thermocouples were

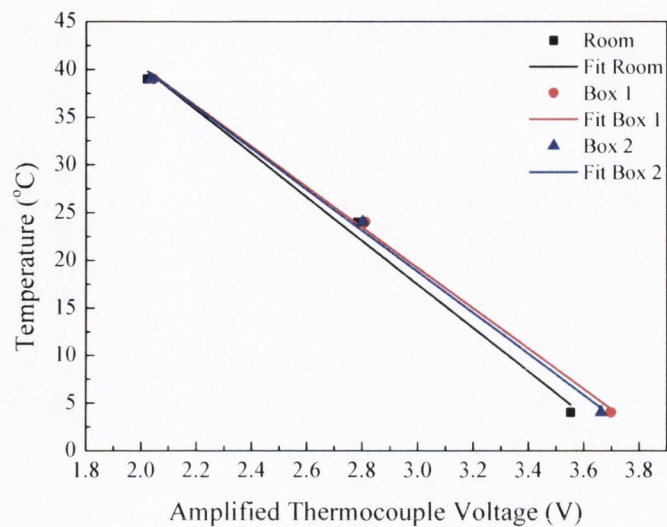


Figure 2.7. The three thermocouples used in the temperature regulation system were calibrated by measuring the amplified thermocouple voltage at three temperatures (4, 25 and 39 °C) and fitting with the equation $T = aV + b$ to determine the constants for the linear response of the thermocouple around room temperature. The constants for the three thermocouples are given in Table 2.1. A mercury thermometer was used as a reference for the calibration.

Table 2.1. The constants for the calibration of the three thermocouples.

| Thermocouple | a (°C/V) | b (°C) |
|--------------|-----------------|----------------|
| Room | -22.8 ± 1.8 | 86.0 ± 5.3 |
| Box 1 | -21.2 ± 0.8 | 82.8 ± 2.5 |
| Box 2 | -21.6 ± 1.0 | 83.5 ± 3.0 |

calibrated by placing them in a standard refrigerator (4 °C) and an incubator (25 °C and 39 °C). A mercury thermometer was used as an analogue reference during the calibration. The linear response of the thermocouples was then determined by fitting the data with the equation $T = aV + b$, where T is the temperature in Celsius, V is the thermocouple voltage, and a and b are constants. The fit of the data is shown in Fig. 2.7 and the constants for each thermocouple are given in Table 2.1.

The refrigeration unit contains a heat sink at the rear of the box which is aided by a fan that was connected to the main power of the unit. The unit is heated and cooled by varying the voltage applied to the unit, and thus the fan would not run at a steady rate if it remained connected to the main power. The fan could also create a small vibration in the system when it was running at full speed. To remove these problems the old fan was replaced with a ‘silent’ 15 cm PC case fan with a separate switchable power supply (0, 5 or 12 V). The new fan creates virtually no vibration in the system

when running at 12 V and the temperature in the system can be maintained at a stable level even when the fan speed is reduced to 5 V.

To aid the smooth heating and cooling of the air inside the unit a 9 cm 'silent' PC case fan was positioned on a side wall inside the unit. This fan also has a separate switchable power supply and significantly decreases the time taken to reach a stable temperature inside the system. The rotation of the fan inside the unit does not affect the noise levels in the static or dynamic response of the cantilevers.

2.2.5 Fluidic System

The fluid can be pumped through the chamber in a number of ways. For quick measurements it is possible to use a syringe pump (Kent Scientific Corporation, Connecticut 06790 USA). However, cantilever arrays are very sensitive to changes in the pressure and flow rate of the fluid passing through the fluid chamber. When using a syringe pump it is possible that there will be a frequency response of the cantilever to small changes in the flow rate. Therefore, for sensitive measurements, it is preferred to use an air pressure driven flow which will provide a continuous steady flow even at low flow rates.

An air pressure driven fluid flow system was implemented to replace the syringe pump (Fig. 2.8). The bottles are standard Pyrex media bottles (borosilicate glass, ISO 4796 25 ml or 50 ml, Fisher Scientific Ireland Ltd., 30 Herbert St., Dublin 2, Dublin, Ireland) modified by a glass blower to have an air inlet at the top and a liquid outlet from the centre of the base of the bottle. A 0.2 μm pore size filter is placed below the bottle as a connection to the standard 1/16" O.D. teflon fluid tubing (0.3 mm I.D.). The fluid is then caused to flow through the chamber by applying pressure to the bottle.

The pressure is monitored using a pressure sensor (140 PCB, Sensor Technics, McGowan House, 66C Somers Road, Rugby, Warwickshire CV22 7DH, United Kingdom) for each fluid bottle. The pressure sensors are calibrated and temperature compensated by the manufacturer. The output signal is amplified and is in the range 0 - 6 V with 3 V set to atmospheric pressure. The flow rate and sensor voltage are shown for a range of pressures in Fig. 2.9. The response of the pressure sensors is linear for small changes of the pressure in the system.

The flow of air to and from the bottles is controlled by switching valves (EV2 & EV3, Clippard, Parc Scientifique Einstein, Rue du Bosquet, 6, B-1348 Louvain-la-Neuve-Sud, Belgium). The switching of the valves is controlled via the main LabVIEW program and a mechanical relay board (NI PCI-6520, National Instruments, Texas, USA).

The pressure applied to the bottles can be either positive (pushed flow) or negative (pulled flow) depending on setting of the valves and the connection to the compressed

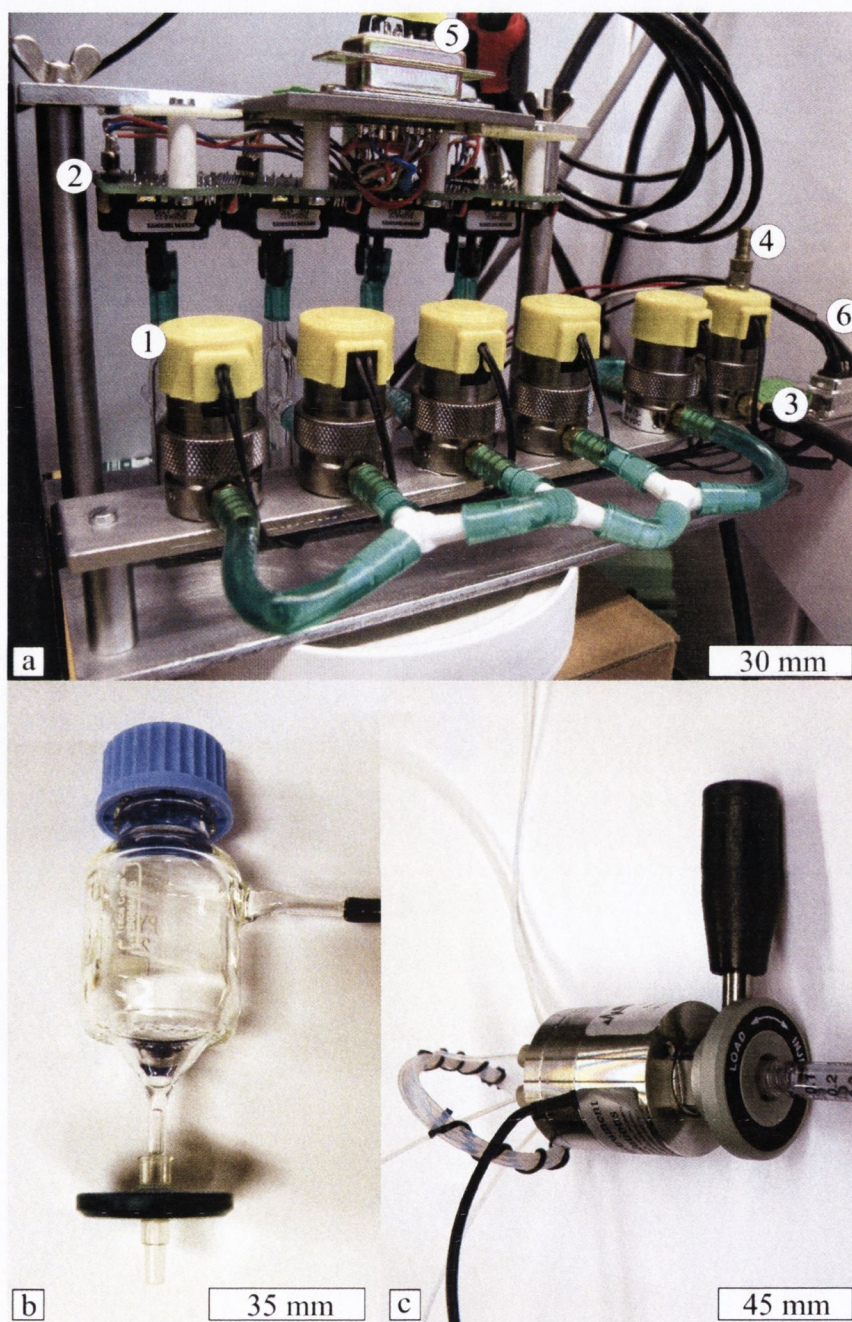


Figure 2.8. The various components of the fluidic system (the pressure regulator is not shown). **a)** The pressure valve and sensor rack. Air pressure can be applied to up to four bottles simultaneously. **1.** Switching valves. **2.** Pressure sensors. **3.** Connection to regulated compressed air. **4.** Connection to vacuum pump. **5.** Connection to BNC 2110, DAQ and LabVIEW. **6.** Connection to relay board NI PCI 6520. **b)** Customised glass bottles. The bottles are semi filled with the buffer and the inlet at the top allows the air pressure in the bottle to be changed causing flow of the liquid in to (or out of) the bottle. A $0.2\ \mu\text{m}$ pore size filter is placed below the bottle as a connection to the fluid lines. The black tube connects to the glass fittings visible behind the valves in photograph (a). **c)** Manual switching injection valve. The injection loop volume can be changed to suit the experiment. The loop is filled via the needle port at the front of the tube when the switch is in the load position.

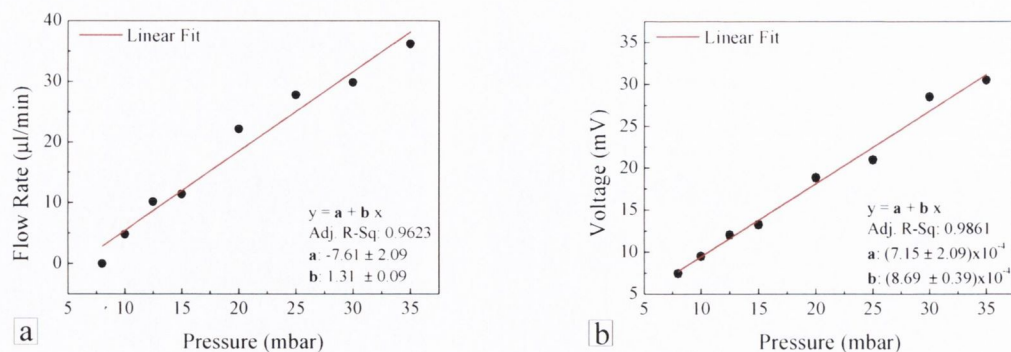


Figure 2.9. Calibration plots for pressure sensors and the flow rate of nanopure water into the fluid chamber for an applied pressure. **a)** The flow rate (µl/min) vs applied pressure (mbar). The valve was in the load position for the measurements of flow rate. When in the inject position the resulting tube length is longer, and thus the flow rate will be correspondingly lower for a given applied pressure. **b)** Voltage (mV) vs applied pressure (mbar) for the pressure sensors. The response of the pressure sensors is linear for small changes in pressure in the system.

air regulator (0 - 50 mbar ,U33, Spectrotec, Spectron Gas Control Systems GmbH, Fritz-Klatte-Str. 8, D-65933 Frankfurt) or a vacuum pump.

For the injection of small samples of rare or expensive molecules into the fluid chamber an injection loop (changeable size depending on experiment) and switching valve (Analytical Injection Loop D Uni, ECOM spol. s r.o., Americka 3, CZ12035 Praha 2, Czech Republic) has been incorporated into the fluidic system. The injection loop can be filled via a needle port of the front of the valve when the valve is in the load position. The loop can be filled during the experiment with no effect on the flow of buffer to the fluid chamber. Switching the valve does not show any effect on the measured response of the cantilevers. The flow rates measured in Fig 2.9.a were measured with the bottle at the same height as the inlet for the fluid chamber and the valve in the load position. When the valve is in the inject position the total tube length of the fluidic system is increased and thus the corresponding flow rate for a given applied pressure is lower. For most buffer solutions used for experiments the flow rate at 50 mbar applied pressure is 42 µl/min when the valve is in the inject position and 80 µl/min when in the load position for a 100 µl loop..

The effect of flowing the fluid using the syringe pump compared to the pressure flow system will be demonstrated in Section 2.4.4.

2.2.6 The Assembled Dual-Mode Device

The main components of the optical beam deflection system are assembled on a breadboard (Thorlabs) such that the distance from the midplane of the doublet to

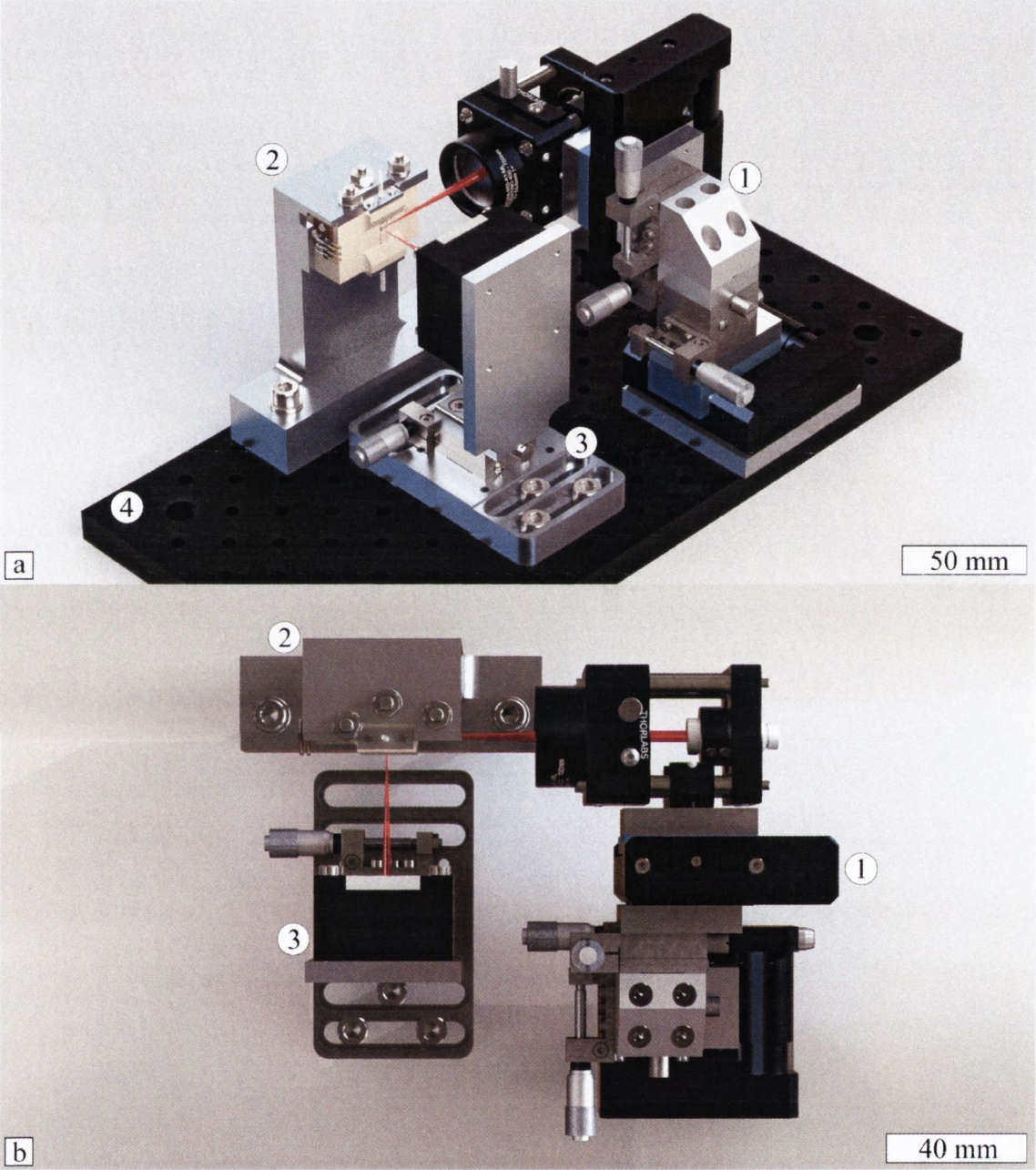


Figure 2.10. The assembled dual-mode device optical deflection system. The device is assembled on a breadboard. The custom machined aluminium mounts and connectors are designed such that the distance from the lens to the cantilever is 50 mm and the distance from the cantilever to the PSD is 40 mm. The XYZ and linear translation stages allow small adjustments to be made to ensure a sharp focus of the laser on the cantilever surface and that the laser reflects onto the centre of the PSD. The path of the laser beam is indicated in red, and represents the calculated beam shape. **a) Isometric view.** Shown without cables for clarity. **1.** Optic cage and laser positioning system. **2.** Fluid chamber and holder. **3.** PSD and holder. **4.** Breadboard. **b) Plan view.** The breadboard is omitted from the plan view for clarity.

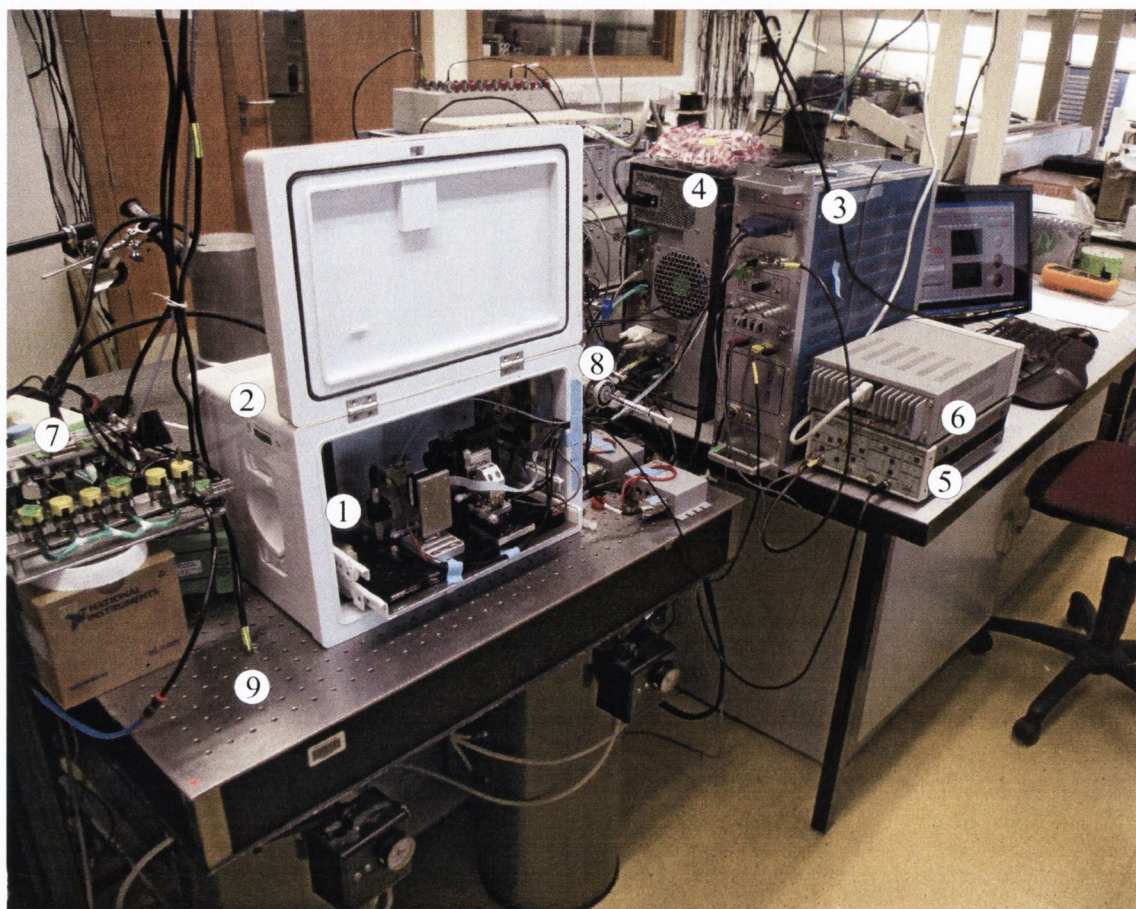


Figure 2.11. Photograph of the entire assembled device including peripheral components. **1.** The main components of the optical deflection readout system as shown in Fig. 2.10. **2.** Temperature regulated enclosure. **3.** Chassis containing connections to LabVIEW DAQ (BNC 2110) and power supply for the PSD. **4.** PC containing the National Instruments boards and the main LabVIEW program. **5.** Amplifier. **6.** Power supply for temperature control and heat pulse. **7.** Fluidic system valve and pressure sensor rack. **8.** Injection valve. **9.** Air cushioned optical table to isolate the device from external vibrations.

the cantilever array is 50 mm and the distance from the cantilever array to the front plane of the PSD is 40 mm. The custom adapter and mounting pieces were designed to achieve these distances. The laser beam was aligned to be level horizontal before being focused on the surface of a test cantilever array in nanopure water. The assembled device is shown in Fig. 2.10. The path of the laser beam is shown in red in the figure and shows the calculated focusing and divergence of the beam.

As shown in Fig. 2.11 the optical beam deflection system is mounted inside the temperature regulated box, which has a small entrance on the right hand side for all cables and tubing to enter the box. The box is placed on an optical table (NRC Pneumatic Isolating Mount, type XL-G, Newport Corporation) to isolate the device from external vibrations. This is more of an issue for the static mode, for dynamic

mode the measured frequencies are too high to be affected by any of the external sources of noise.

The automated stage controllers, fluidic system, injection valve, the laser, and the laser controller are all mounted on the optical table to help avoid passing external vibrations along their connections to the optical deflection system and the fluid chamber. The PC, chassis containing connections to LabVIEW DAQ (BNC 2110) and power supply for the PSD, power supply, and amplifier (SR560 Low-Noise Preamplifier; Stanford Research Systems, CA 94089, USA) are placed as near as possible to the temperature regulated box to keep all electrical connections as short as possible to reduce electrical noise.

The optical table is grounded to earth, with everything placed on the table grounded to the table. The breadboard is also connected to the table via a wire to stop any build up of static electricity due to the motion of the automated stages.

2.3 LabVIEW Programming

LabVIEW is a proprietary platform for the visual programming language “G” developed by National Instruments. Each LabVIEW program is essentially a virtual instrument (VI), e.g. a multimeter or an oscilloscope as a simple case, which can be easily customised to meet the needs of the programmer. LabVIEW allows the creation of a user interface (front panel) and a corresponding code ‘behind’ the front panel on the block diagram. The front panel can be considered to be similar to the front panel of any physical instrument while the block diagram is analogous to the electronics inside the physical instrument. The block diagram contains the source code of any LabVIEW program and focuses on the flow of data between different nodes on the diagram which are connected by drawing wires between them. The compiler contained in LabVIEW, which translates the source code into native code for the CPU, automatically incorporates parallel processing, which makes it very easy to take advantage of the multiple cores available in modern CPUs. Each LabVIEW program can be used as a standalone program, or placed as a subroutine inside another LabVIEW program via the use of the connector panel and in this way complicated instruments capable of many different tasks can be assembled virtually and interfaced with the outside world via PCI boards mounted in a PC.

2.3.1 The Main Program

The whole dual-mode device is managed by a single LabVIEW VI which forms the core of the dual-mode device as shown in the schematic in Fig. 2.12. The main VI gives the user control over the device via the front panel shown in Fig. 2.13. The front

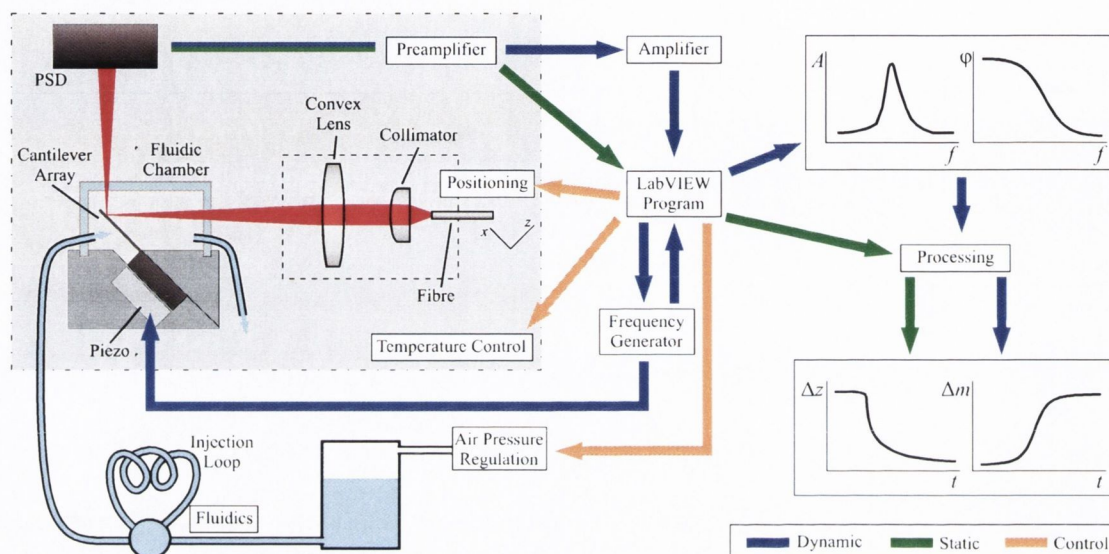


Figure 2.12. Schematic of dual-mode device control and measurement procedure. The main LabVIEW program controls all aspects of the device and the acquisition of data. Using the device it is possible to record both the dynamic and the static response of the cantilever. The LabVIEW program uses fuzzy logic to control the heating and cooling of the box containing the device to maintain a stable temperature to within $\pm 0.1^\circ\text{C}$. The flow of liquid through the fluid chamber via air pressure is also controlled using the LabVIEW program. To obtain the dynamic signal (blue arrows on the schematic) the laser spot is moved to the position on the cantilever that gives the best response for the resonance mode of interest. The LabVIEW program controls the frequency generation board which applies a sinusoidal frequency signal to the piezoelectric actuator. The cantilever is excited at a number of frequencies (f) in a linear range and the response from the cantilever is detected using the optical beam deflection technique. The signal from the PSD is then amplified before being processed by the LabVIEW program which creates amplitude (A) and phase (ϕ) frequency spectra. To obtain the static signal (green arrows on the schematic) the laser spot is moved to the tip of the cantilever and then the differential and sum signals from the PSD are sampled and passed to the LabVIEW program which then determines the bending of the cantilever. The resonance modes and bending of each cantilever are obtained sequentially before moving to the next cantilever in the array. The dynamic and static data can then be processed using NOSEtools or a similar routine to obtain the change in mass (Δm) and the change in bending (Δz) or surface stress of the cantilever with respect to time (t).

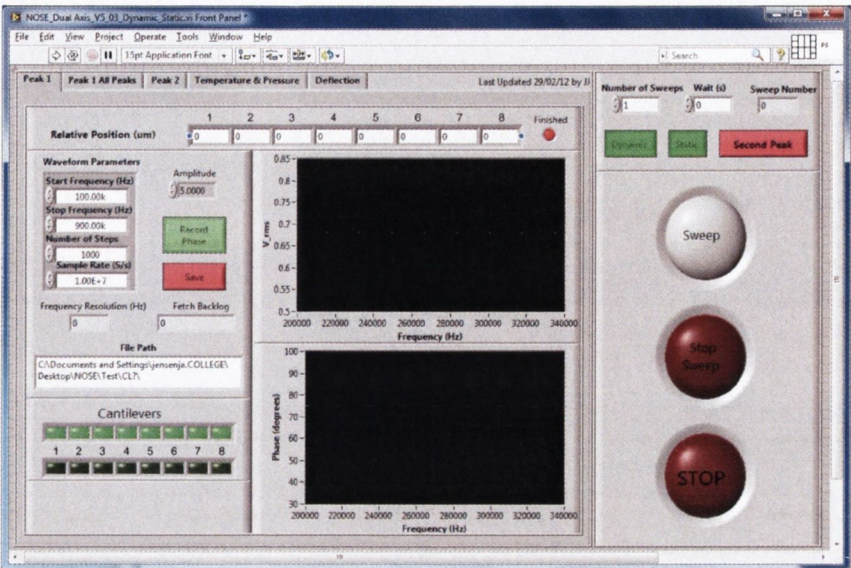


Figure 2.13. The front panel of the dual-mode device provides the user with a simple interface for control of the device an monitoring of data. It is split into several tabs which correspond broadly to dynamic mode, static mode, and control of temperature and fluid flow.

panel contains several tabs which correspond roughly to the several tasks and types of data required by the user. It is possible to record from two different, non-adjacent, frequency ranges in the dynamic mode and each range has a tab for control and viewing of the data ('Peak 1' and 'Peak 2'). The distance along the cantilever from which the dynamic data should be recorded from each cantilever can be set for each frequency range. The 'Deflection' tab contains the static-mode data plots. The 'Temperature and Pressure' tab gives control of the set point of the temperature regulated box, the heat pulse to the chamber, and the pressure applied to each fluid bottle and hence the flow of liquid through the chamber. When using the front panel it is possible for the user to select the mode of operation of the device i.e. dynamic (one or two frequency ranges), static, or dual mode. The user can also select which cantilevers will be investigated for each mode.

The block diagram for the main program is shown in Fig. 2.14. There are three more or less independent sub-parts in the main program which run simultaneously and can also share information if needed (e.g. whether a certain input or output channel is currently in use). The first main component is a large while loop responsible for the movement of the stages, acquisition and processing of the data, and saving of relevant data in a way that can be processed easily after the experiment. The core subroutine of this component will be described in more detail in Section 2.3.2.

The second main component is related to the recording and regulation of the temperature, implementation of the fuzzy logic routine, and applying the heat pulse

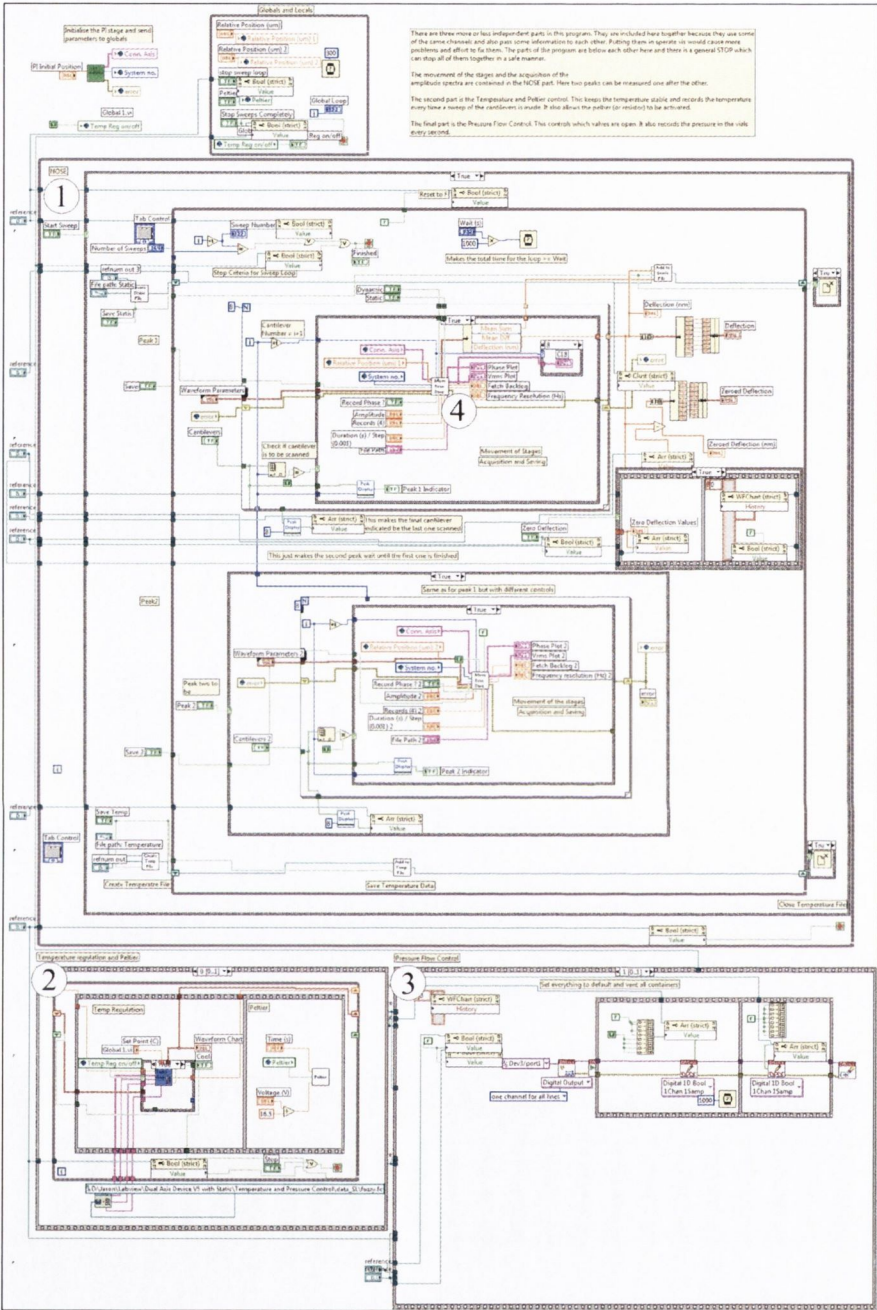


Figure 2.14. The block diagram of the main program. This is a large piece of code which contains three more or less independent components which run simultaneously. **1.** A large while loop responsible for the movement of the stages in addition to the acquisition, processing, and saving of data. **2.** A sequence detailing the control and regulation of the temperature inside the box, implementation of the fuzzy logic routine, and the application of a heat pulse to the fluid chamber. **3.** A sequence detailing the switching of valves and control of the air pressure inside the bottles. **4.** This subVI implements the measurement procedure described in detail in Section 2.3.2 and is shown in Fig. 2.16.

to the chamber (see also Section 2.2.1 and Section 2.2.4). Most of the interactions of this component are via the DAQ board (NI PCI 6221), which is also used during the static measurement. The static measurement is very short, so it does not affect the stability of the device if this component is temporarily set to not update or change status while the static measurement takes place. The temporary pause is achieved by passing information between the two VIs using a global variable. Similarly, the same power supply is used to regulate the box and apply the heat pulse to the chamber so both operations cannot be run concurrently, and the temperature regulation is temporarily suspended while the heat pulse is applied. This does not have any effect on the temperature stability of the device due to the short time of the suspension.

The third main component deals with the regulation of the flow of liquid through the fluidic system described in Section 2.2.5, monitoring of the pressures and switching of the valves via the mechanical relay boards NI PCI 6520.

2.3.2 Measurement Procedure

As shown in the schematic in Fig. 2.12 the response of the cantilevers is obtained using optical beam deflection readout. The position of the reflected beam is measured using the linear PSD described in Section 2.2.3. The measurement procedure program, as shown in Fig. 2.15, can be broken down into three steps with a subVI for each step. The laser spot is moved to the cantilever of interest, then the resonance modes and bending of each cantilever are obtained sequentially with a short pause between each measurement. The wait time before obtaining the bending is significantly longer than the damping time of the vibration of the cantilever and therefore there is no additional noise in the static signal due to the dynamic readout.

Movement The movement of the automated translation stages is controlled by several small VIs. The commands for each stage are very similar so only the movement of Stage 1, the M110.1DG stage, will be described in detail. The stages are initialised when the main VI is switched on. Briefly, the initialisation checks that the range of movement is OK, sets the travel velocities of the two stages, and sends them to their starting positions near the middle of the range of motion (the ‘Home’ position). The laser spot is placed at the tip of cantilever 1 with the XYZ stage prior to starting the experiment.

When the measurement procedure is started for a cantilever several pieces of information about the stages are required (Connected Axis, System Number, Error Status) which are all passed into the Move VI (shown in Fig. 2.16.a) from the Global memory. The VI then picks the Axis for Stage 1 and passes all of the information to a lower level VI (Move Stage 1, Fig. 2.16.b) that communicates directly with the stage.

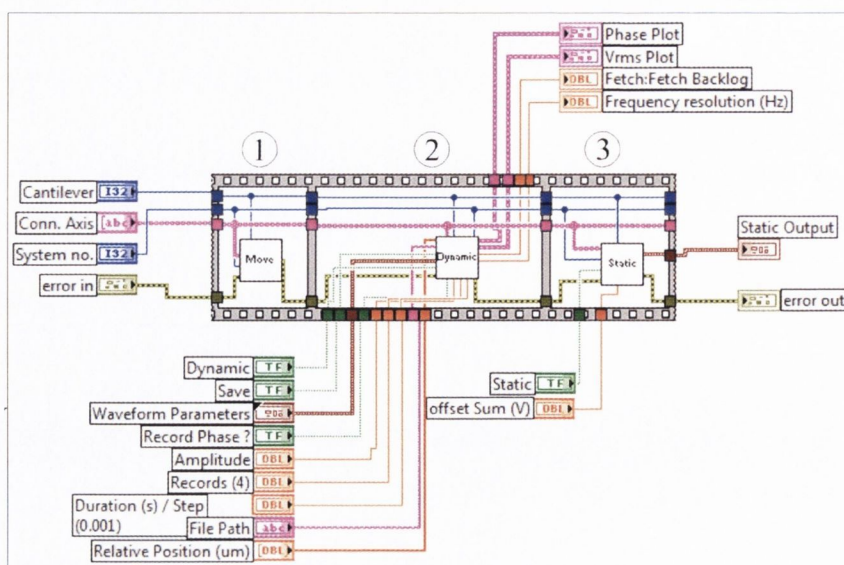


Figure 2.15. The subVI highlighted in Fig. 2.14 which implements the measurement procedure in the dual-mode device. The measurement procedure can be broken down into three steps and hence three sub VIs. **1.** Movement of the laser spot to the cantilever of interest. **2.** Measurement of dynamic signal. **3.** Measurement of static signal. The three subVIs are shown in detail in Fig. 2.16, Fig. 2.17, and Fig. 2.18.

Depending on the cantilever number that the measurement procedure is targeting, the Move Stage 1 VI will implement in one of two ways. For cantilever 1, *Cantilever Number* = 1 and the instruction to the stage will be “Go Home”. If the cantilever number is not 1, then the instruction to the stage will be to move to the location $(\text{Cantilever Number} - 1) \times 250 \mu\text{m}$ from ‘Home’. The VI then implements a procedure whereby it continuously queries whether the stage is moving, which runs until the stage is no longer moving. The VI then ends and passes the Error Status out.

The only main difference in the motion of Stage 2, the M122.2DG stage, is that the distance moved is chosen by the user, and it is scaled to account for the 45° angle between the plane of motion of the stage and the plane of the surface of the cantilever.

Dynamic Signal The acquisition, processing and saving of the dynamic-mode data during the measurement procedure is handled by the Dynamic VI, shown in Fig. 2.17.a. Firstly the laser spot is moved to the predetermined position along the cantilever that gives the best signal for the mode(s) being investigated. This movement is handled by the Move Stage 2 subVI, which operates in a similar way to the Move Stage 1 VI described above. After a 50 ms pause the dynamic signal is then recorded by the Dynamic Measurement subVI, which is shown in detail in Fig. 2.17.b.

The Dynamic Measurement VI is a rather complicated procedure that communicates with two PCI boards (the frequency generator, NI PCI 5406, and the high speed digitiser, NI PCI 5112), and contains several further subVIs (many of

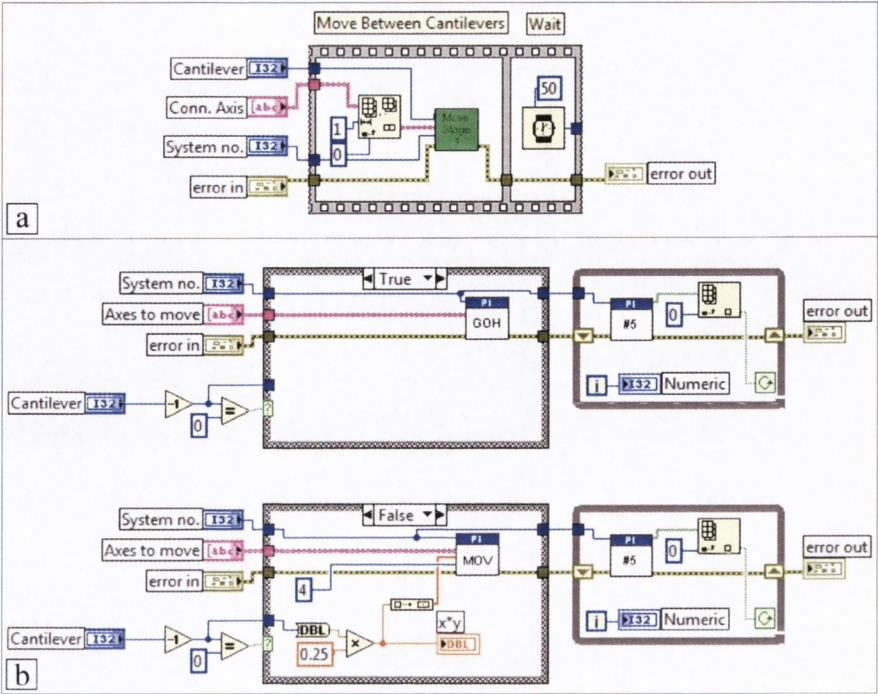


Figure 2.16. The block diagram of the movement subVI shown in Fig. 2.15 and the subVI contained within it. This VI sends a signal to the M122.2DG stage to move to the designated cantilever. **a)** The block diagram. **b)** The ‘Move Stage 1’ subVI block diagram has two different instructions depending on the cantilever number. Cantilever 1 is chosen as the ‘Home’ cantilever, so if *CantileverNumber* = 1, then the instruction is to “Go Home”. If the cantilever is not 1, then the instruction is to move to the location $(CantileverNumber - 1) \times 250 \mu\text{m}$ from ‘Home’. The while loop on the right hand side queries the stage to check if it is still moving and waits for the stage to stop moving before ending the subVI.

which contain even further subVIs) and so the procedure will not be described in full detail.

The frequency generation board requires a list of frequencies and corresponding durations in order to actuate the cantilever. These are calculated from the Waveform Parameters given by the user on the front panel. The frequency generation board and the digitiser are then configured by sub VIs. The digitiser starts recording the signal from the PSD to its buffer and then the frequency generation board starts to generate the actuation signal. At this point a large loop starts to work which simultaneously pulls data from the circular buffer of the digitiser to temporary memory on the PC while also analysing data already on the PC memory.

Because the digitiser starts recording a continuous stream of data ($10^7 \text{ samples s}^{-1}$) from two channels before the signal is generated it is necessary to find the start of the interesting, relevant data. This is handled by a subVI in the loop. Once the start position (Zero) of the relevant data is found it can then be broken into the separate channels (from the PSD and the frequency generator). The data from the two channels

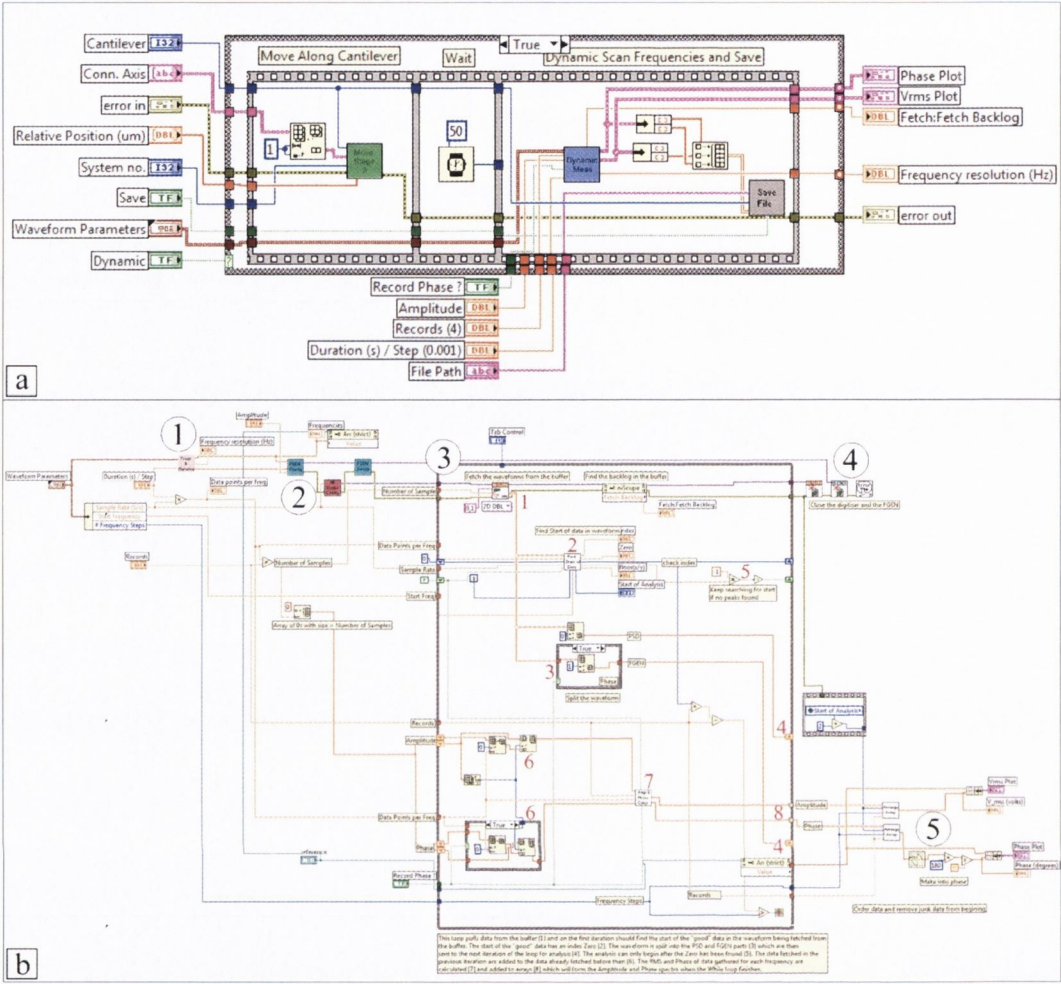


Figure 2.17. Block diagram of the dynamic subVI shown in Fig. 2.15 and details of dynamic measurement subVI contained within it. **a)** The block diagram of the ‘Dynamic’ subVI first instructs the M110.1DG stage to move to the predetermined position along the cantilever (‘Move Stage 2’), then a brief 50 ms pause before measuring the dynamic response of the cantilever and then saving the data to an individual file on the hard drive of the PC. **b)** The dynamic measurement subVI is a complicated routine involving several main pieces. **1.** Calculate the list of frequencies and durations of actuation. **2.** Configure the frequency generation, configure and start recording from the PSD with the digitiser, then start the actuation of the frequency list. **3.** This large loop has several pieces which are indicated with red numbers in the figure. This loop pulls data from the circular buffer (1) and then searches the data for the start of the response of the cantilever to the actuation. This point has the label ‘Zero’ (2). The waveform is then split into the components from the PSD and from the frequency generation board (3) which are then sent to the next iteration of the loop for analysis (4). The analysis can only begin after the ‘Zero’ has been found. The data fetched in the previous iteration are added to the data fetched in the iterations before that (6). The mean amplitude and phase of chunks of the data corresponding to one frequency are calculated (7) and passed out of the loop (8). **4.** After the loop has ended the digitiser and frequency generation tasks are closed. **5.** The data passed from the loop are arranged into the amplitude and phase arrays that will be sent to the front panel and saved after the subVI ends.

is sent to the next iteration of the loop for analysis (which can only begin after the Zero is found). The data fetched in the previous iteration of the loop is added to the data fetched in the iterations before that. The data is then split into smaller chunks that correspond to each separate frequency in the list and the amplitude and phase of the response is then calculated and passed out of the loop.

The amplitude is calculated as the root mean square (RMS) of the amplitude of the response waveform for each frequency of the actuation. The phase is calculated from the waveforms from the PSD and the frequency generation board using the method outlined in Appendix A.1.

The loop continues until all the relevant data is split and processed or the data being written to the circular buffer ‘catches up’ with the data that has not yet been pulled to the computer memory.

After the loop ends the digitiser and frequency generation tasks are closed. The amplitude and phase data are then arranged into arrays that correspond to the amplitude and phase spectra are sent out of the VI when it ends.

The spectra are then sent to the front panel as plots and are saved to the hard disk of the PC for post experiment analysis.

Static Signal The acquisition of the static-mode data during the measurement procedure is handled by the Static subVI, shown in Fig. 2.18.a. The laser spot is moved to the tip of the cantilever which is managed by the Move Stage 2 subVI. The temperature regulation of the box is switched off to clear the DAQ board for use in the static measurement. A 150 ms wait is then enforced to give the DAQ board (Ni PCI 6221) time to clear and to also ensure that the cantilever is no longer vibrating from the measurement of the dynamic mode. Following the wait the static response is recorded by the Static Measurement subVI shown in Fig. 2.18.b.

The DAQ board is configured to read a differential voltage from two channels corresponding to the difference (diff, $I_1 - I_2$) and sum ($I_1 + I_2$) signals from the PSD. The sample number, rate, and timing of the measurement are set and then the measurement is taken before closing the DAQ task. The signals are digitally DC filtered to remove any vibration component of the signal due to thermal motion of the cantilever. The mean diff and sum (2,500 samples at a rate of 10^5 samples s^{-1}) are then used to calculate the bending (Δz) of the cantilever using Eq. 1.5. The deflection and some of the other quantities are then sent out of the subVI as it ends.

After a 50 ms wait the temperature regulation is turned back on and the static data is sent to the front panel for observation during the experiment and will be added to a static save file following the measurement of the static signal from all cantilevers of interest.

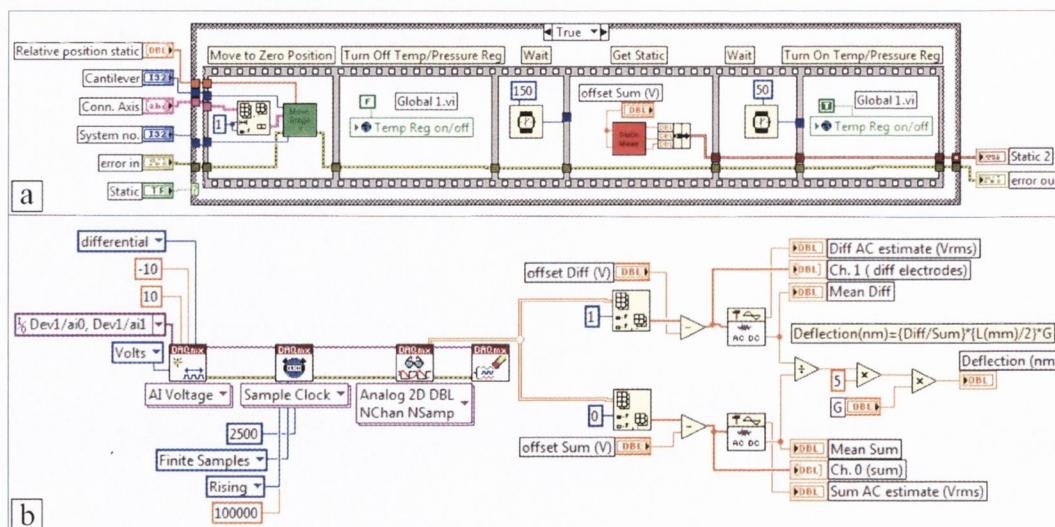


Figure 2.18. Block diagram of the static subVI shown in Fig. 2.15 and details of static measurement subVI contained within it. **a)** The block diagram of the ‘Static’ subVI first instructs the M110.1DG stage to move to the tip of the cantilever (‘Move Stage 2’). The temperature regulation is switched off to clear the DAQ board for the static measurement. A pause of 150 ms gives time to clear the DAQ and ensure that the cantilever has stopped vibrating following the dynamic measurement. The static response of the cantilever is then measured and after a 50 ms wait the temperature regulation is turned back on. **b)** The static measurement subVI block diagram. The DAQ board is configured to a differential voltage measurement on two channels. The number of sample and the rate are then set before the measurement is taken. The data from the two channels is then DC filtered to remove any vibration effects of the cantilever. The deflection can then be calculated from the difference and sum information measured on the two channels using Eq. 1.5.

2.4 Results and Discussion

2.4.1 Performance of Dual-Mode Device

The new dual-mode device contains several electronics upgrades compared to the older dynamic-mode device which help improve the overall performance of the device. The SRS SR560 Low-Noise amplifier replacing the Tektronix TM502A (Oplink solutions) allows a high-pass, low-pass, or band-pass filter to be applied to the output from the PSD prior to the digitiser and provides a better boosting of the resonance peaks with respect to the noise levels. The National Instruments frequency generation board (NI PCI 5406), which only outputs certain waveforms, replaced the arbitrary waveform generator (NI PCI 5412) which reduces the amount of information that needs to be stored and generated for the actuation of the cantilevers. This means larger frequency spans can be actuated with a higher resolution than previously was possible.

The readout of the dynamic signal has been optimised using a circular buffer to allow measurement of >3,000 data points in each spectrum for eight cantilevers in ~30

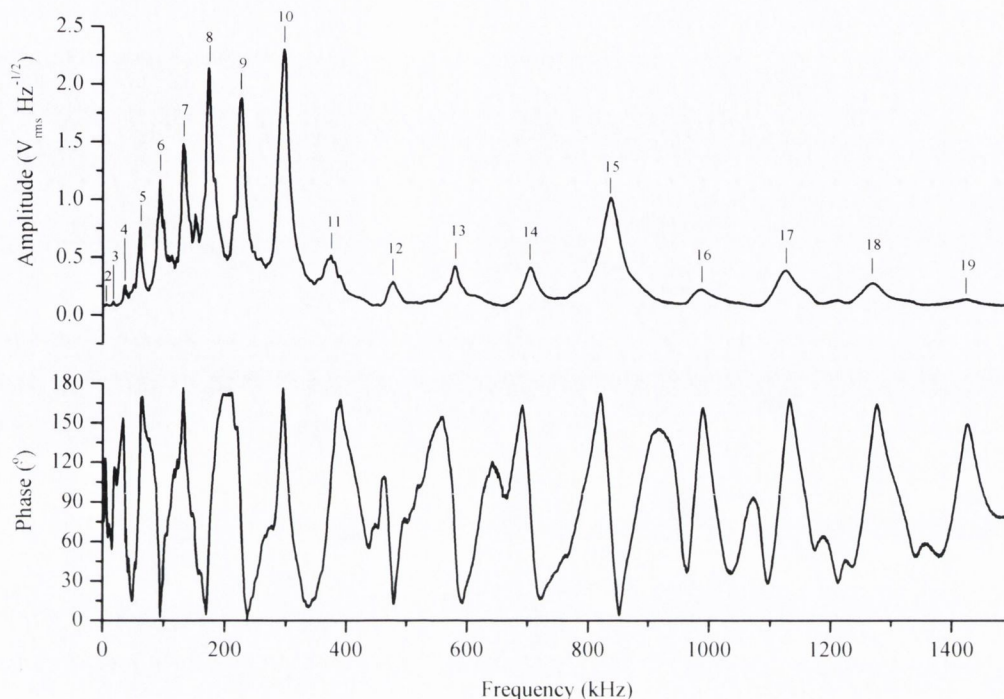


Figure 2.19. The amplitude and phase spectra of a typical 1 μm thick cantilever between 1 kHz and 1.5 MHz. The resonance modes from 2 up to 19 are clearly visible. The entire spectrum was obtained, as shown, in one measurement. The spectrum contains 3,000 data points. Each point is the average of 10,000 samples taken at a frequency of 10^7 samples s^{-1} over 1 ms.

s (including travel between cantilevers). The sampling rate is set to 10^7 samples s^{-1} to satisfy Nyquist's theorem and avoid aliasing. Each data point in the spectrum is the average of 10^4 samples. When only the static signal is being recorded it is possible to read out from all eight cantilevers once every 6 - 7 seconds, and once every 30 seconds when the dual mode is used.

Programming changes implemented to process the data while still acquiring data lead to reduction in the data stored by a factor 10^4 and when combined with the implementation of the circular buffer and the new frequency generation board means an improvement in the frequency resolution of the dynamic signal of a factor ten compared to the initial dynamic-mode device over the same range. e.g. for a 150 kHz window the frequency resolution of the dual-mode device is 42.8 Hz compared to 375 Hz for the dynamic-mode device.

As an example of the capability of the dynamic part of the device a frequency spectrum of a gold coated 1 μm thick cantilever (in liquid) from a typical array used in experiments is shown in Fig. 2.19. The spectrum clearly shows the flexural resonance modes from mode 2 to mode 19. The resonance mode frequencies follow an approximate

squared increase with increasing mode number, which indicates that they are all flexural modes (Appendix A.2). The frequency range spans 1 kHz to 1.5 MHz and contains 3,000 data points. The spectrum was recorded, processed and saved in three seconds. Each data point in the spectrum is the average of 10,000 samples taken at a frequency of 10^7 samples s^{-1} .

Previously to obtain a spectrum such as this one it would be necessary to take multiple measurements at different positions on the cantilever surface to obtain all of the resonance modes and then stitch them together during post processing. This spectrum shows the advantage the new device performance and of having the fine positioning system and small spot size for obtaining high-quality resonance spectra. During actual experiments 18 resonance modes are not monitored, as the frequency resolution would not be optimal, however it is possible to monitor several resonance modes in each frequency range specified by the user with good resolution in time and frequency.

It was not within the scope of the thesis to perform upgrades to the fluid chamber. As such the chamber presented is from the existing device. The chamber allows for high-quality measurements in a liquid environment, however there can be a small leak from one end of the chamber which can cause problems during stop flow experiments. Occasionally a small bubble can form in the chamber due to the leak which can interfere with the readout from one or more of the cantilevers.

2.4.2 Line Scan of Cantilever Vibrating in Air

To demonstrate the sensitivity of the dynamic mode to the positioning of the laser spot on the surface of the cantilever a scan along the longitudinal axis of a typical bare silicon 1 μm thick cantilever was performed with measurements taken every 5 μm . For the dynamic measurements the cantilever was excited at its 5th flexural resonance mode in air and the resonance spectra were fitted with a simple harmonic oscillator (SHO) model to determine the amplitude of the signal.

The static bending profile was obtained from the PSD signal using Eq. 1.7. The profiles are shown in Fig. 2.20. The nodes and antinodes of the resonance are clearly reflected in the dynamic response, with the maximum amplitude of the resonance peak obtained at the nodes of resonance as indicated by Fig. 1.4 in Section 1.3.4. The bending profile shows a 3 μm upwards bend of the cantilever indicating a small residual tensile stress from the fabrication process. The bending profile was calibrated using the thick side bar as a reference to account for any tilt of the cantilever in the holder.

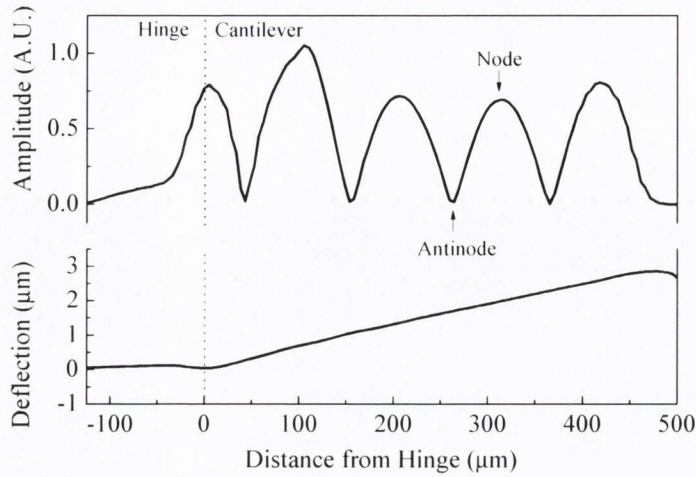


Figure 2.20. Measurement of the amplitude of the 5th resonance mode in air and the bending of a typical cantilever from the array. The data was obtained by taking a dynamic measurement followed by a static measurement at 5 μm intervals along the length of the cantilever and the bending profile can be established using Eq. 1.7. The 120 μm long and ~ 3 μm thick hinged portion of the cantilever has some flexibility as indicated by the reduced amplitude of vibration observed [6].

2.4.3 Response to Heat Pulse

To demonstrate the sensitivity of the device to both dynamic and static response of the cantilever array a heat pulse was applied to the fluid chamber (2 V, 250 s). This caused a trough to be formed in the static signal (as shown in Fig. 2.21 and Appendix A.3, Fig. A.3) which can be used to calibrate the response of the individual cantilevers in the array and allow for comparable measurements between the cantilevers [7]. The downward bending is caused by the different thermal expansion coefficients of the silicon cantilever and the gold layer on the upper surface of the cantilever ($3 \times 10^{-6} \text{ }^\circ\text{C}^{-1}$ for Si and $14 \times 10^{-6} \text{ }^\circ\text{C}^{-1}$ for Au).

The flexural resonance modes 8 to 10 were recorded during the heat pulse and their response is shown in Fig. 2.22. The shift in resonance frequency is due to the change in properties of the cantilevers and the surrounding fluid with increase in temperature. It would be expected that the fluid is less dense at the higher temperature and therefore the mass of the liquid that is moved with the cantilever as it vibrates is less, thus increasing the resonance frequency. The higher modes of resonance are more sensitive to the change in mass of the water as expected [8] and as shown in Appendix A.3, Fig. A.4. The change in mass corresponds to an average of $\sim 6 \pm 0.5$ ng of co-moved water following analysis in NOSEtools [9, 10] as shown in Appendix A.3, Fig. A.5. It should be noted that this analysis assumes that the spring constant of the cantilever remains unchanged during the experiment, which may not be true. A total increase in stress

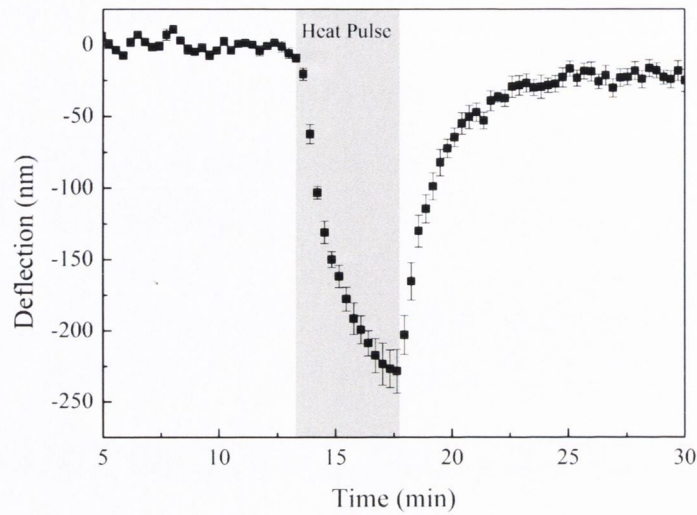


Figure 2.21. Average static response of the eight cantilevers in the array to the 250 s heat pulse. The cantilevers showed an average bending of 230 nm by the end of the heat pulse.

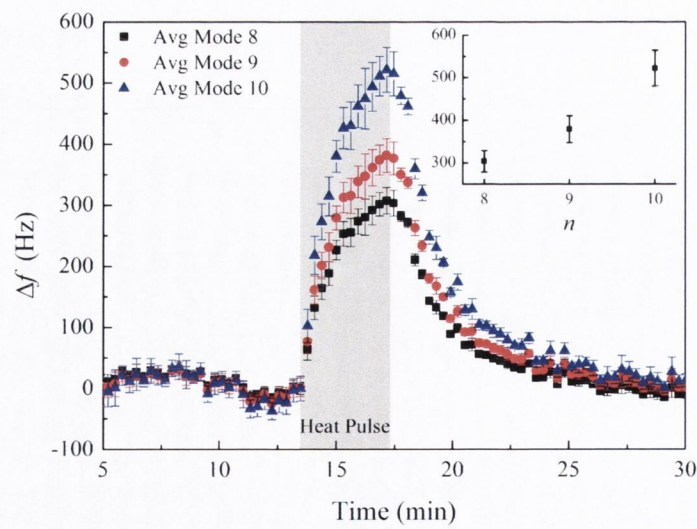


Figure 2.22. Average frequency response of the flexural resonance modes 8 to 10 to the 250 s heat pulse. **Inset:** The maximum frequency shift (Δf) vs. mode number (n). It is clear that the higher resonance modes are more sensitive to an applied stimulus.

on the cantilever, as caused by the heat induced bending can cause a change in spring constant, and hence a change in resonance frequency [11, 12].

2.4.4 Syringe Pump vs. Pressure Flow

During some continuous flow experiments it was noticed that there was a clear periodic signal superimposed on the frequency response of the cantilever. It was usually possible to remove the effect by box filtering of the data, or during reference subtraction the effect would be removed. The fact that the effect was occurring on all cantilevers with similar magnitude simultaneously indicated that the cause was in the environment of the cantilever. The temperature of the box, and hence the liquid in the chamber) was constant and so was not causing the periodic effect. The effect was found to be absent during stopped flow experiments.

The effect of causing liquid to flow through the fluid chamber using the syringe pump compared to using the air pressure driven flow was investigated. Nanopure water was passed through the fluid chamber at various flow rates using the syringe pump and the frequency response was recorded at mode 14 from a number of cantilevers in the chamber. The resonance peak was fitted with the SHO amplitude equation with added terms to account for any baseline in the spectrum,

$$A = A_{bl} + mf + \sqrt{\frac{A_0^2 f_c^4}{(f^2 - f_c^2)^2 + \frac{f_c^2 f_c^2}{Q^2}}} \quad (2.4)$$

where A is the amplitude, A_{bl} is the intersection of the baseline amplitude, m is the slope of the baseline, A_0 is the zero frequency amplitude, f is the frequency, f_c is the centre frequency of the peak, and Q is the quality factor of the peak. The peak was fitted to find A_{bl} , m , A_0 , f_c , and Q using a Levenberg-Marquardt fitting algorithm implemented in a custom LabVIEW VI. The centre frequency was then plotted versus time to determine if any effect on the response was induced by the fluid flow. The baseline corrected frequency response of three cantilevers to two different syringe pump speeds are shown in Fig. 2.23. There is an obvious periodic effect visible in the frequency response.

Following the introduction of the pressure driven flow system described in Section 2.2.5, nanopure water was caused to flow continuously through the fluid chamber by applying different pressures to the bottles. The frequency response at mode 14 of three cantilevers at two different applied pressures are shown in Fig. 2.24. There is no periodic effect obvious to the eye.

The frequency responses were baseline corrected and a fast Fourier transform (FFT) was performed on the data to determine the period of the effect on the frequency response. There is a clear periodic response of the syringe pumped flow data which

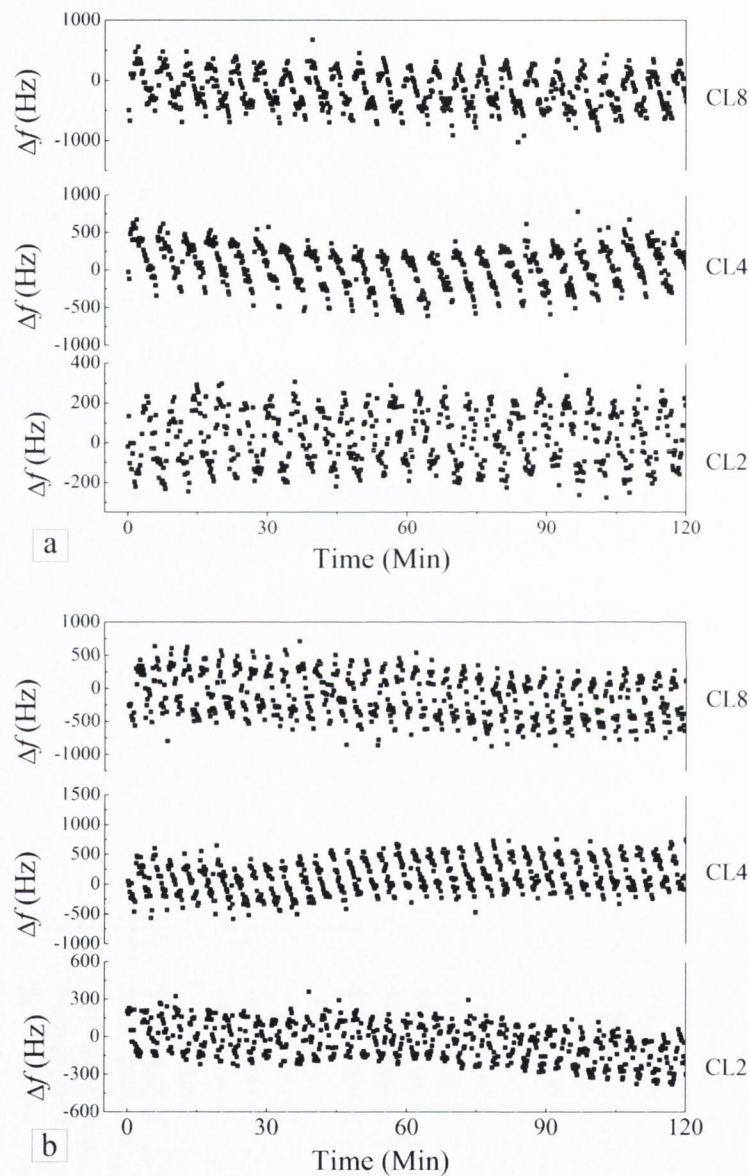


Figure 2.23. The frequency response of mode 14 of three cantilevers at two different pumping speeds of the syringe pump. It is clear that there is a periodic response of the cantilever frequency. **a)** Response to continuous flow at 10 $\mu\text{l/min}$ **b)** Response to continuous flow at 15 $\mu\text{l/min}$.

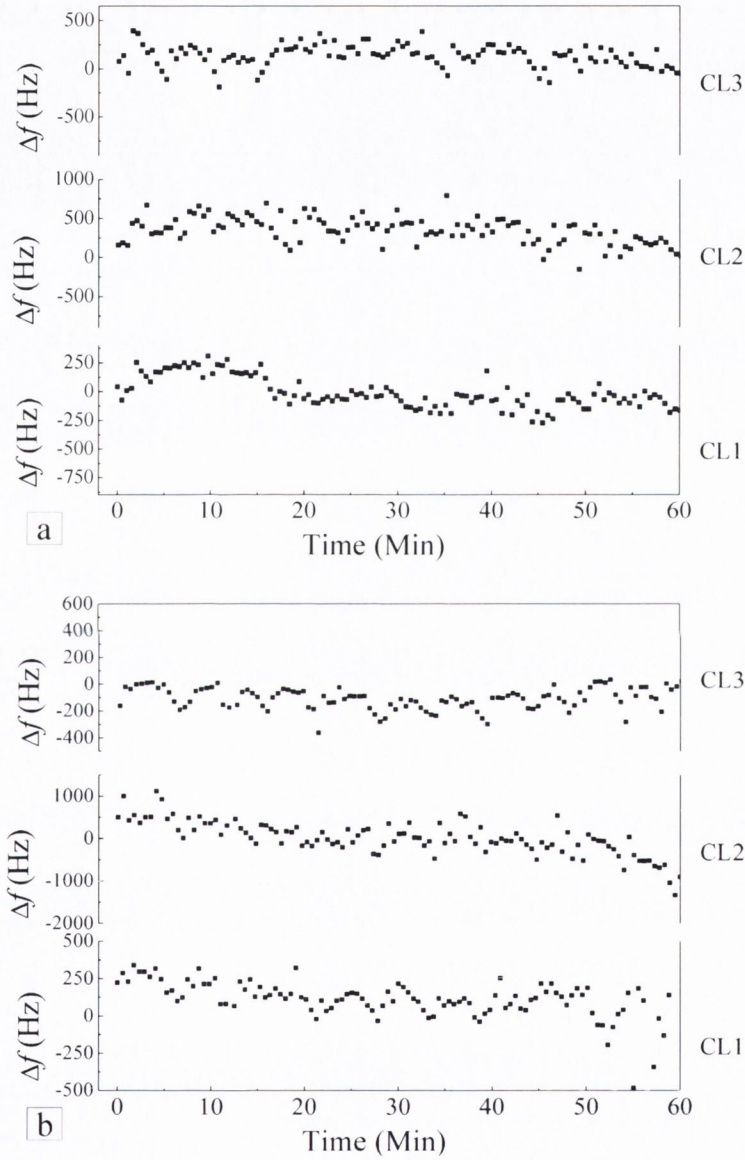


Figure 2.24. The frequency response of mode 14 of three cantilevers at two different pressure induced flow rates. It is clear that there is no periodic response of the cantilever frequency. **a)** Response to continuous flow at 10 mbar applied pressure **b)** Response to continuous flow at 15 mbar applied pressure.

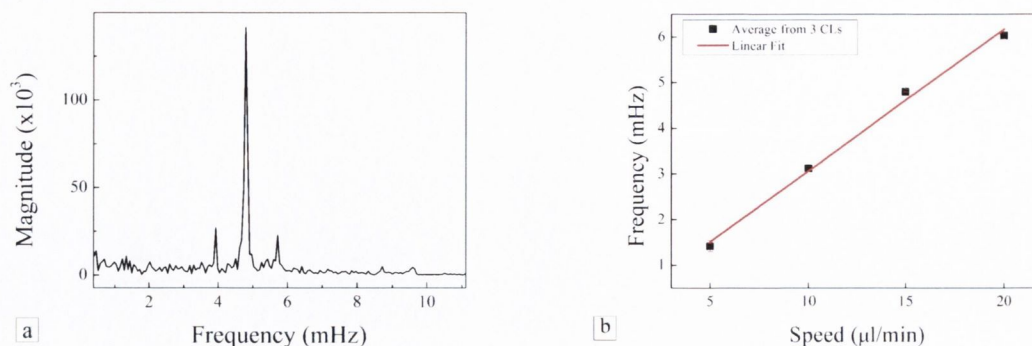


Figure 2.25. **a)** The FFT magnitude of the frequency response of cantilever 4 at 15 $\mu\text{l/min}$ shows a clear peak indicating that there is a definite periodic response of the cantilever. The other cantilevers show similar responses at all pump speeds. **b)** A plot of the frequency of the oscillations vs. the pump speed shows a definite linear trend, indicating that the periodic response of the cantilever is related to the pumping speed of the syringe pump.

results in a peak in the FFT magnitude obtained from the data (Fig. 2.25.a). The period frequency indicated by the peak in the FFT was averaged over the cantilevers for each pumping speed.

A plot of the period frequency vs. pumping speed (Fig. 2.25.b) clearly shows a linear trend which indicates that the periodic response of the frequency is related to the pumping speed of the syringe.

The absence of the effect during pressure induced flow and the linear response of the frequency of the effect with pumping speed indicates that the effect was caused by the flow of the liquid induced by the syringe pump. The cause of the effect within the syringe pump is less clear. Cleaning and greasing of the pump did not remove the effect. The effect is unlikely to be due to stick/slip of the syringe due to the very even effect on the frequency of the cantilever. With stick/slip of the syringe random slips of different sizes would be expected and so would not lead to a definite peak in the FFT.

The effect could be due to the axle of the pump being slightly misaligned and thus an even pumping speed is not achieved and so the flow rate would vary periodically with time.

Another possible cause is that at very low pumping speeds of the pump, combined with a larger volume syringe, the pumping is not continuous as there is a minimum rotation of the screw drive in the pump. Thus, the average flow though the chamber would match the desired target flow rate, but the flow speed would not be steady, or may even be pulsed.

As a result it is preferred to use the pressure induced flow of liquid though the chamber during experiments, especially those with low flow rates, or where a small response of the cantilever is expected.

References

- [1] T. Braun, V. Barwich, M. Ghatkesar, A. Bredekamp, C. Gerber, M. Hegner, and H. Lang, "Micromechanical mass sensors for biomolecular detection in a physiological environment," *Physical Review E*, vol. 72, no. 031907, p. 031907, 2005.
- [2] R. Mishra, W. Grange, and M. Hegner, "Rapid and reliable calibration of laser beam deflection system for microcantilever-based sensor setups," *Journal of Sensors*, vol. 2012, p. 617386, 2012.
- [3] Newport Corporation, "Gaussian beam optics tutorial," World Wide Web, accessed 26th Feb 2010. [Online]. Available: <http://www.newport.com/seervicesupport/Tutorials/default.aspx?id=112>
- [4] "Characteristic and use of PSD," Hamamatsu Photonics UK, Tech. Rep., Accessed: 17/07/2012. [Online]. Available: http://sales.hamamatsu.com/assets/pdf/catsandguides/psd_technical_information.pdf
- [5] H. Andersson, "Position sensitive detectors - device technology and applications in spectroscopy," Ph.D. Thesis, Electronics Design Division in Dept. of Information Technology and Media, Mid Sweden University, Sweden, 2008.
- [6] J. Jensen and M. Hegner, "Predictions of the compressible fluid model and its comparison to experimental measurements of Q factors and flexural resonance frequencies for microcantilevers," *Journal of Sensors*, vol. 2012, p. 258381, 2012.
- [7] T. Braun, F. Huber, M. K. Ghatkesar, N. Backmann, H. P. Lang, C. Gerber, and M. Hegner, "Processing of kinetic microarray signals," *Sensors and Actuators B-Chemical*, vol. 128, no. 1, pp. 75–82, 2007.
- [8] M. K. Ghatkesar, V. Barwich, T. Braun, J. P. Ramseyer, C. Gerber, M. Hegner, H. P. Lang, U. Drechsler, and M. Despont, "Higher modes of vibration increase mass sensitivity in nanomechanical microcantilevers," *Nanotechnology*, vol. 18, p. 445502, 2007.
- [9] T. Braun, "Nosetools homepage," accessed 1st Mar 2010, NOSEtools Version 7.2 (rev 438) is available to download free from the NOSEtools Homepage. The software is copyrighted by Thomas Braun 2008, 2009, University of Basel, Switzerland. [Online]. Available: <http://web.me.com/brunobraun/NOSEtools/Home.html>
- [10] T. Braun, M. K. Ghatkesar, V. Barwich, N. Backmann, F. Huber, W. Grange, N. Nugaeva, H. Lang, J. Ramseyer, C. Gerber, and M. Hegner, "Digital processing of multi-mode nano-mechanical cantilever data," *Journal of Physics: Conference Series*, vol. 61, pp. 341–345, 2007.
- [11] M. J. Lachut and J. E. Sader, "Effect of surface stress on the stiffness of cantilever plates," *Physical Review Letters*, vol. 99, no. 20, p. 085440, 2007.

- [12] M. J. Lachut and J. E. Sader, “Effect of surface stress on the stiffness of thin elastic plates and beams,” *Physical Review B*, vol. 85, no. 8, pp. 085 440–, 2012.

Chapter 3

General Cantilever Preparation Techniques

In order to build a biosensor from a cantilever array it is necessary to attach a bio-recognition layer to the surface of the cantilever. The cantilever acts as the mechanical transducer while the surface coating is the recognition element. The performance of the sensor depends on the interface between the sensing layer and the cantilever. The reproducibility of the sensor will only be as good as the reproducibility of this layer.

Cantilevers can respond to virtually any stimulus. Therefore careful preparation of the cantilever array is essential in order to create a sensor that is both sensitive and specific to a particular target molecule. In all of the biological experiments presented in this thesis the basic preparation of the sensor follows the same steps. Firstly the cantilever array is cleaned to remove any residue from manufacturing, transport and storage. The clean cantilever array is then coated with a thin Au layer. The Au surface is cleaned after storage and then thiol chemistry is used to bind the probe molecules to the Au surface. The steps involved in the preparation of the cantilever array are discussed in detail below.

3.1 Cantilever Cleaning

Initially the cantilever arrays were precleaned prior to metal coating using a piranha solution. Piranha solution is a strong oxidiser which is effective at removing organics and hydroxylates from the Si surface, leaving it hydrophilic. Piranha cleaning is often used as a first step to clean gross organic materials from the surface of Si wafers in the semiconductor industry [1]. The protocol for piranha cleaning of cantilever arrays is presented in Appendix B.1. However, the cleaning process required many rinsing steps with deionised (DI) H₂O to remove the detergent used at the start of the protocol, and to fully rinse the piranha solution from the chip and avoid leaving sulphur, S, residues

on the silicon, Si, surface [1].

This method was replaced by an O₂ plasma cleaning process because it is a safer technique which yields similar results and does not require multiple steps or leave any residue on the surface. The UV light generated by the plasma breaks organic bonds of contaminants on the Si surface. In addition the oxygen species generated react with the organic contaminants to form e.g. H₂O and CO₂ [1] which are then pumped out of the vacuum chamber. The protocol for plasma cleaning of cantilever arrays is presented in Appendix B.2

3.2 Metal Coating

The cantilever arrays were coated with Ti and Au for most experiments to provide a substrate for thiol binding of the probe molecules to the cantilever surface. The quality of the surface has a direct impact on the binding of the probe molecules and hence the performance of the sensors. The reproducibility of the metal coating will therefore impact directly on the reproducibility of the sensors.

The Au layer has the added advantage of increasing the reflectivity of the surface which aids in the optical beam deflection. In addition, when only one side of the array is coated with the metal, a convenient mechanical calibration of the sensor response can be performed by applying a heat pulse to the array.

The metal coating was initially performed using the BOC Edwards Auto 500 evaporation system before it was replaced with the Temescal FC-2000 Evaporation system for better reproducibility and ease of use. The deposition rates and thicknesses were optimised and the final Au surfaces had a RMS roughness of ~ 0.8 nm, with a grain size of ~ 35 nm [2].

3.2.1 BOC Edwards

The initial metal depositions were performed using the BOC Edwards Auto 500 evaporation system. This system is manually operated by the user and requires constant small adjustments to yield consistent depositions. The settings used for the depositions are given in Table 3.1. The Ti deposition was performed by e-beam evaporation and the Au deposition was performed by thermal evaporation using a tungsten boat.

The distance from the sample to the target in the BOC Edwards Auto 500 system is ~ 20 cm. Using thermal evaporation for the deposition of the Au layer generated radiative heating of the arrays and combined with the short distance could cause the cantilevers to bend significantly and become unusable in further experiments.

The time taken to reach the base pressure of $\sim 4.3 \times 10^{-7}$ Torr was on the order of

Table 3.1. The settings used for metal coating of the cantilever arrays using the BOC Edwards Auto 500 evaporation system. The base pressure before deposition was $\sim 4.3 \times 10^{-7}$ Torr.

| | Ti | Au |
|-----------------|----------------------|--------------------|
| Method | E-Beam | Thermal |
| Pressure (Torr) | 1.4×10^{-6} | 5×10^{-5} |
| Current (mA) | 47 | 10 |
| Rate (nm/s) | 0.02 | 0.02 |
| Thickness (nm) | 2 | 20 |

hours and usually resulted in an overnight pump down of the deposition chamber. If a coating of both sides of the array was required it was necessary to break the vacuum and manually rotate the arrays, resulting in a ~ 40 hour time period for a metal deposition.

3.2.2 Temescal

The Temescal FC-2000 Evaporation System was used for the metal deposition as a replacement for the BOC Edwards system. The Temescal provides an automated approach to the metal deposition yielding more reproducible results when properly maintained. The system uses e-beam for both the Ti and the Au evaporations, with a larger sample-target distance (~ 50 cm) than the Edwards system. The deposition settings for the Temescal are given in Table 3.2.

Table 3.2. The settings used for metal coating of the cantilever arrays using the Temescal FC 2000 evaporation system. The base pressure before deposition was 2×10^{-6} Torr.

| | Ti | Au |
|-----------------|----------------------|----------------------|
| Method | E-Beam | E-Beam |
| Pressure (Torr) | $< 2 \times 10^{-6}$ | $< 2 \times 10^{-6}$ |
| Rate (nm/s) | 0.02 | 0.05 |
| Thickness (nm) | 2 | 21 |

The larger distance between the sample and the target leads to less (or no) bending of the cantilevers. Precision control of the deposition rates and deposition pressure yields more reproducible depositions.

The system uses an interlock for the loading of the samples which gives significantly lower deposition times. A flippable mount can be used in the Temescal which allows coating of both sides of the array without breaking the vacuum. As a result, with the Temescal it is possible to load the arrays and coat both sides of the array in under two hours.

3.3 UV Cleaning

An Au surface will quickly foul at ambient laboratory conditions [3] and this contamination could potentially affect the functionalisation of the cantilevers. A quick UV/ozone cleaning of the surface is thus performed immediately prior to the functionalisation procedure [4]. The UV cleaning uses UV radiation to remove organic contaminants from the surface via an oxidative process. The contaminants can react with oxygen species generated by the UV radiation from oxygen present in the system to form products that desorb from the surface. The protocol for UV cleaning of the coated cantilever arrays is presented in Appendix B.3.

3.4 Cantilever Functionalisation

The functionalisation step is the point at which the cantilever array is transformed into a biosensor. The eight cantilevers in each array allow several different molecules to be immobilised on the surface to act as test or references for the particular interaction being investigated. The cantilevers are sensitive to a range of effects which can interfere with the biological measurement (e.g temperature changes, flow rate changes, environmental noise, etc...) in addition to non-specific interactions with the target molecules, and so a proper *in situ* reference is essential if the correct interpretations are to be drawn from the data obtained.

For all of the biological experiments presented in this thesis thiol chemistry is used to form self-assembled monolayers (SAMs) of the the probe and reference molecules on the surface of the cantilevers [5]. The functional group on the molecule deprotonates upon adsorption to the Au surface to form a strong thiol bond.



There are several possible methods for functionalisation of individual cantilevers within an array, the most popular being immersion of the cantilever in a capillary [6, 7] or inkjet spotting of drops onto the surface of the cantilever [7–9]. The method used for functionalisation of the arrays used in the experiments presented in this thesis is the capillary immersion technique.

For the capillary functionalisation a custom device is used which allows the precise insertion of the cantilevers in the array into precisely arranged glass capillaries (OD $240 \pm 10 \mu\text{m}$, ID $180 \pm 10 \mu\text{m}$, length 75 mm, King Precision Glass Inc, California, USA). The capillaries are arranged such that the spacing between their centres matches the spacing between the cantilevers in the array. A microscope mounted on the device allows the user to guide the cantilevers into the capillaries using micro translation stages, as shown in Fig. 3.1.a.

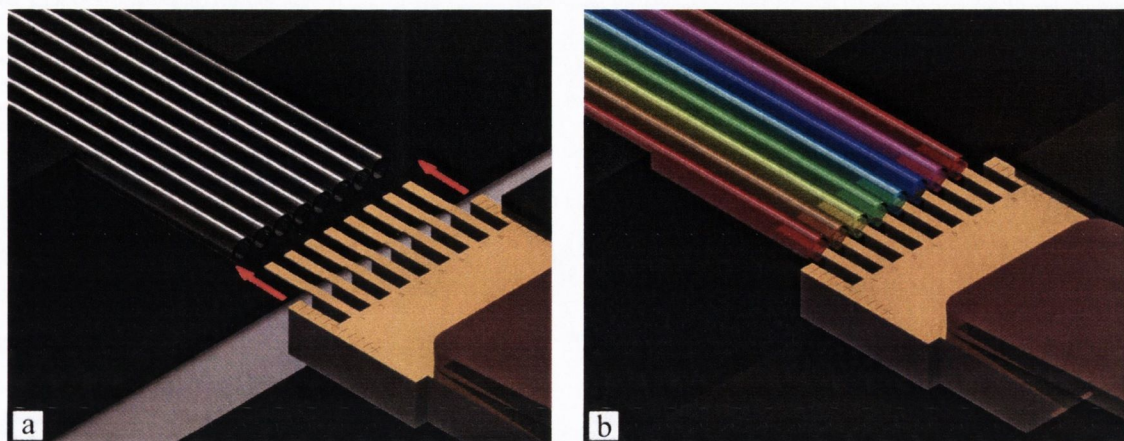


Figure 3.1. The individual cantilevers in the array are functionalised using the capillary immersion technique. The size and spacing of the capillaries are chosen to match the cantilever array. Individual reservoirs for each capillary allow each cantilever to be given a unique functionalisation, providing the capacity for multiple tests and references to be included in each experiment. **a)** The cantilevers are inserted into the arranged capillaries using a set of microtranslation stages and a microscope. **b)** The capillaries are back filled from the reservoirs with the individual functionalisation solutions.

The other end of the capillaries are placed in small individual reservoirs where the functionalisation solutions can be placed. Flow of the solution from the reservoir to the cantilever compensates for any loss of liquid due to evaporation (Fig. 3.1.b) Incubation times of up to two hours are possible using this device. If longer times are required the device can be placed in a humid chamber to stop evaporation of the functionalisation solutions.

Prior to use the glass capillaries are plasma cleaned for eight minutes (using the same settings as in Appendix B.2) followed by a bath in HPLC grade ethanol for a minimum of ten minutes. The capillaries are dried on filter paper on a hot plate (100 °C) immediately prior to use. This is done to remove any small debris from the capillaries, and to remove any oils etc left over from the fabrication process. The cleaning process was observed to increase the flow rate of liquid from the reservoir to the cantilevers and results in less cases of the fluid stopping in the capillaries before reaching the cantilevers.

References

- [1] K. A. Reinhardt and W. Kern, *Handbook of Silicon Wafer Cleaning Technology (2nd Edition)*. William Andrew Publishing, NY USA, 2008.
- [2] R. Mishra, "Selective gene fishing in complex genomic environments using microcantilevers: Applications in RNAi therapy," Ph.D. dissertation, Centre for Research on Adaptive Nanostructures and Nanodevices, and the School of Physics, Trinity College Dublin, Dublin, Ireland, 2012.
- [3] T. Smith, "The hydrophilic nature of a clean gold surface," *Journal of Colloid and Interface Science*, vol. 75, no. 1, pp. 51–55, 1980.
- [4] H. Ron, S. Matlis, and I. Rubinstein, "Self-assembled monolayers on oxidized metals. 2. gold surface oxidative pretreatment, monolayer properties, and depression formation," *Langmuir*, vol. 14, no. 5, pp. 1116–1121, 1998.
- [5] C. D. Bain, E. B. Troughton, Y. T. Tao, J. Evall, G. M. Whitesides, and R. G. Nuzzo, "Formation of monolayer films by the spontaneous assembly of organic thiols from solution onto gold," *J. Am. Chem. Soc.*, vol. 111, no. 1, pp. 321–335, 1989.
- [6] R. McKendry, J. Y. Zhang, Y. Arntz, T. Strunz, M. Hegner, H. P. Lang, M. K. Baller, U. Certa, E. Meyer, H. J. Guntherodt, and C. Gerber, "Multiple label-free biodetection and quantitative dna-binding assays on a nanomechanical cantilever array," *Proceedings of the National Academy of Sciences of the United States of America*, vol. 99, no. 15, pp. 9783–9788, 2002.
- [7] A. Bietsch, J. Y. Zhang, M. Hegner, H. P. Lang, and C. Gerber, "Rapid functionalization of cantilever array sensors by inkjet printing," *Nanotechnology*, vol. 15, no. 8, pp. 873–880, 2004.
- [8] A. Bietsch, M. Hegner, H. P. Lang, and C. Gerber, "Inkjet deposition of alkanethiolate monolayers and DNA oligonucleotides on gold: Evaluation of spot uniformity by wet etching," *Langmuir*, vol. 20, no. 12, pp. 5119–5122, 2004.
- [9] G. Lukacs, N. Maloney, and M. Hegner, "Ink-jet printing: Perfect tool for cantilever array sensor preparation for microbial growth detection," *Journal of Sensors*, vol. 2012, p. 561256, 2012.

Chapter 4

Compressible Fluid Model Verification

This chapter describes the qualitative agreement between experimental measurements of the Q factors and flexural resonance frequencies in air of microcantilevers and calculations based on the compressible fluid model of Van Eysden and Sader [1]. The Q factors and resonance frequencies observed on two sets of cantilever arrays were slightly lower than those predicted by the model. This is attributed to the individual design and geometry of the microfabricated hinged end of the cantilever beams in the array. Some of the contents of this chapter are published in reference [2] by Jensen and Hegner, *Journal of Sensors*, 2011.

4.1 Introduction

Applications for micron-scale cantilevers as a sensing tool have been found in the fields of genomics [3–8], proteomics [9–11], microbiology [12–17], and many others. Many of these applications make use of the micro-cantilever as a sensitive mass detector. It has been shown that operating the cantilever at higher resonance modes increases the mass sensitivity of the device [18]. This increase in the sensitivity is linked to the increased Q factor observed for the higher flexural resonance modes of the cantilever [18].

Along with increased interest in possible applications came the need for improved understanding of the dynamics of cantilevers on this scale and models which can predict their behaviour in a range of situations. In general the higher the Q factor of the resonance peak the smaller the minimum observable frequency shift is. Thus it is desirable to obtain the highest Q factor possible during experiments to maximise the sensitivity of the experiment. Models indicating the dynamics of the cantilever are useful when planning such experiments and determining the expected minimum response required for successful detection of the target.

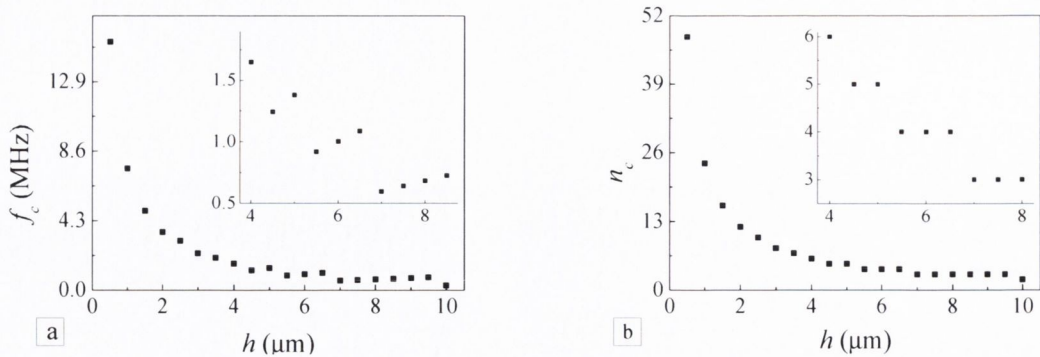


Figure 4.1. **a)** The critical frequency f_c and **b)** the critical mode n_c vs the thickness h of the cantilever as predicted by the scaling analysis presented in [1]. There should be a turning point at the $n_c = 3$ mode which occurs below 1 MHz for a $7 \mu\text{m}$ thick cantilever. For a $2 \mu\text{m}$ thick cantilever of the same size the predicted mode is much higher ($n_c = 12$) and occurs around 3.6 MHz.

Many models detailing the behaviour of microcantilevers have been proposed, including the Elmer-Dreier model [19] and Sader's viscous [20] and extended viscous models [21]. Sader's extended model includes the 3D flow field of the fluid around the cantilever beam and can be applied for arbitrary mode number.

The models mentioned above assume that the fluid in which the cantilever is vibrating is incompressible, and in general have good agreement with experimental results [22]. However, recent papers by Van Eysden and Sader [1, 23] which detail a model for a cantilever beam vibrating in a compressible fluid indicate that this unbounded increase of the quality factor is not always valid. They predict that as the mode number increases and passes a coincidence point (which is determined by the thickness to length ratio of the cantilever and the fluid in which the cantilever is vibrating) the Q factor will begin to decrease.

This coincidence point occurs when the length scale of spatial vibrations of the cantilever beam reduces to a point where it is comparable with the acoustic wavelength of the media in which the cantilever is vibrating. At this point it is possible that energy can be dissipated by the generation of acoustic waves.

For practical applications of microcantilevers (such as mass sensing) this is not an issue when operating the cantilever in liquid. However, if the cantilever is vibrated in air then it can be possible to observe this effect at higher modes. For a cantilever which is $100 \mu\text{m}$ wide, $500 \mu\text{m}$ long and $7 \mu\text{m}$ thick the scaling analysis from the compressible fluid model [1] predicts that there should be a turning point at the $n_c = 3$ mode which occurs below 1 MHz as shown in Fig. 4.1. For a $2 \mu\text{m}$ thick cantilever of the same size the predicted mode is much higher ($n_c = 12$) and occurs around 3.6 MHz.

4.2 Materials and Methods

The thickness of the cantilevers was measured in a scanning electron microscope (SEM) (Zeiss Ultra, Cambridge, UK) and were found to be $7.2 \pm 0.5 \mu\text{m}$ and $1.972 \pm 0.005 \mu\text{m}$ thick (Fig. 4.2). The variation in the thicknesses of the cantilevers was shown to depend on their position on the production wafer. As shown in Fig. 4.2 the cantilevers are connected to the main body of the chip via a $120 \mu\text{m}$ long segment which is approximately twice as thick as the cantilever itself for the $7 \mu\text{m}$ thick cantilevers and three times the thickness for the $2 \mu\text{m}$ thick cantilevers. This design was implemented to facilitate better definition between the hinge (clamping point) of the cantilever and the main body of the array.

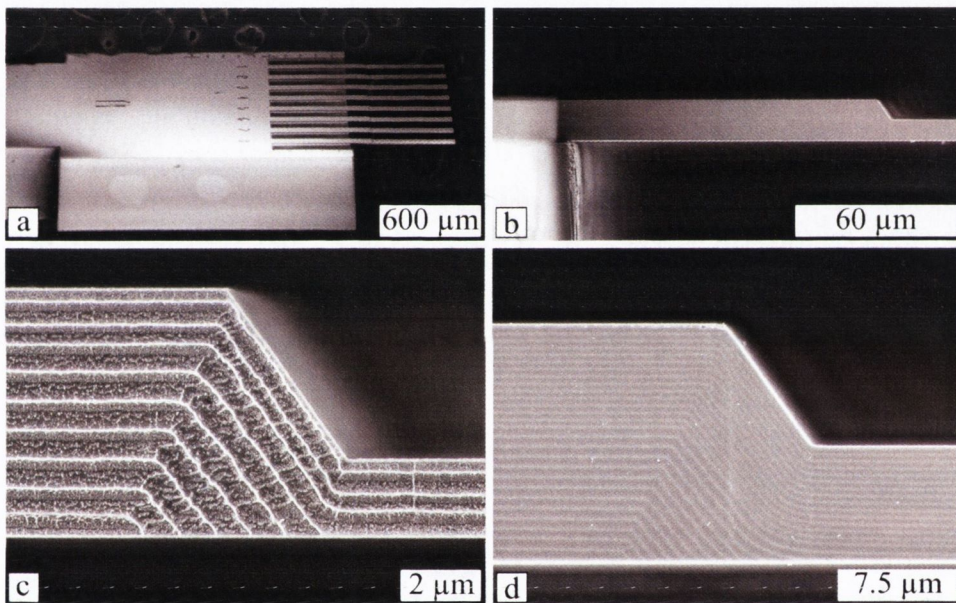


Figure 4.2. **a)** SEM image of typical cantilever array used for these measurements. **b)** Closer view of the hinged end of one of the $7 \mu\text{m}$ thick cantilever showing the $120 \mu\text{m}$ long hinged design that connects the cantilever with the main body of the array. **c)** and **d)** Two closer views of the hinged portion of the 2 and $7 \mu\text{m}$ thick cantilevers respectively. The hinge is approximately twice the thickness of the cantilever for the $7 \mu\text{m}$ thick cantilevers and approximately three times the thickness on the $2 \mu\text{m}$ thick cantilevers.

Cantilever arrays were taken at random from the production wafers and multiple measurements of the first four flexural resonance modes were taken for the $7 \mu\text{m}$ thick cantilevers (Fig. 4.3) and of the first seven modes of the $2 \mu\text{m}$ thick cantilevers (Fig. 4.4). The resonance peaks obtained can be described by a SHO model [24]

$$A(f) = A_{bl} + \frac{A_0 f_n^2}{\sqrt{(f^2 - f_n^2)^2 + \frac{f^2 f_n^2}{Q^2}}} \quad (4.1)$$

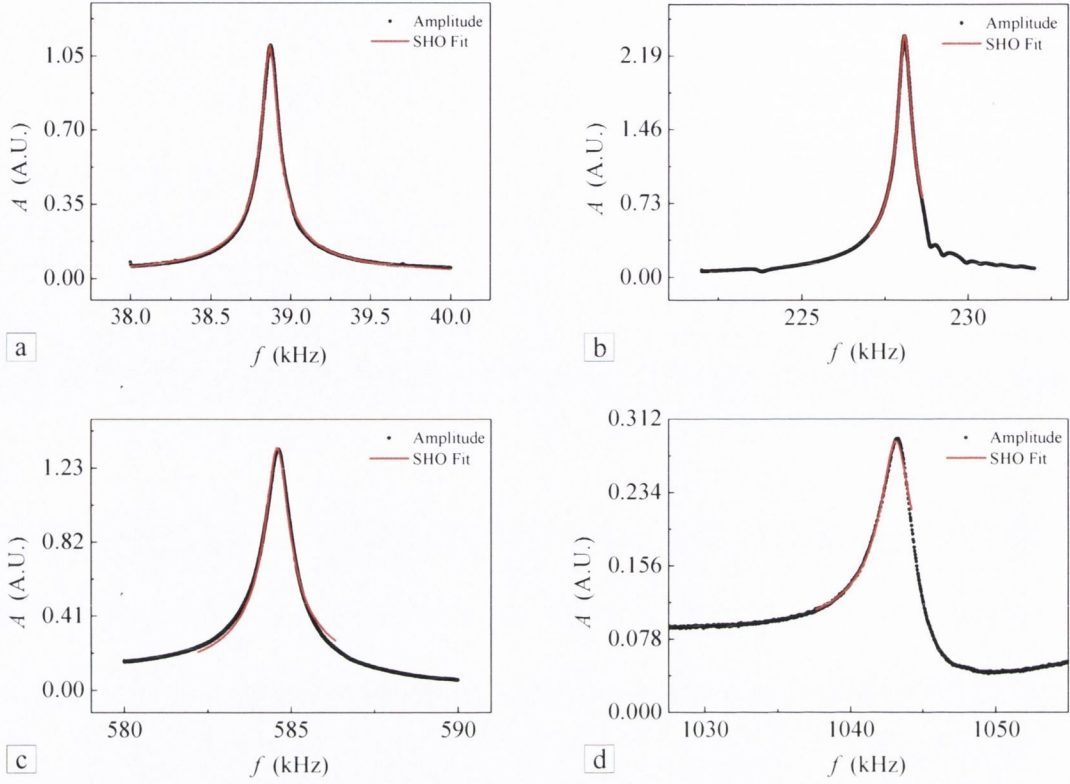


Figure 4.3. Sample of the four resonance modes examined for the 7 μm thick cantilevers using one clamping position. The modes were fitted using Eq. 4.1 to find the centre frequency and the Q factor. Ten measurements of each mode were recorded. **a)** Mode 1 at 38.87 kHz. **b)** Mode 2 at 228.09 kHz. **c)** Mode 3 at 584.60 kHz. **d)** Mode 4 at 1043.20 kHz.

where A_{bl} is the amplitude of the baseline, A_0 is the zero frequency amplitude, f is the frequency, f_n is the resonance frequency of mode n , and Q is the quality factor. The Q factor and resonance frequencies were extracted from the best fit of the resonance peaks with the above model using a Levenberg-Marquardt algorithm [25]. The mean and standard deviation of the resonance frequencies and Q factors of each of the modes were then calculated from the fitted data.

Van Eysden and Sader's extended viscous [21] and compressible fluid models [1] were used to predict the resonance frequency and Q factor of modes of the 7 μm thick cantilevers which were below 2 MHz and the modes of the 2 μm thick cantilevers below 1 MHz. The compressible fluid model is very sensitive to the thickness of the cantilever for a given length. As shown above the thickness of the cantilevers in the array can vary significantly across the production wafer. As a result of the variation of thicknesses observed the models were used to predict the Q factors and resonance frequencies predicted for the middle and the limits of the range of thicknesses ($7.2 \pm 0.5 \mu\text{m}$ for the 7 μm thick cantilevers and $1.972 \pm 0.005 \mu\text{m}$ for the 2 μm thick cantilevers).

The material and fluid properties were chosen to match the experimental conditions.

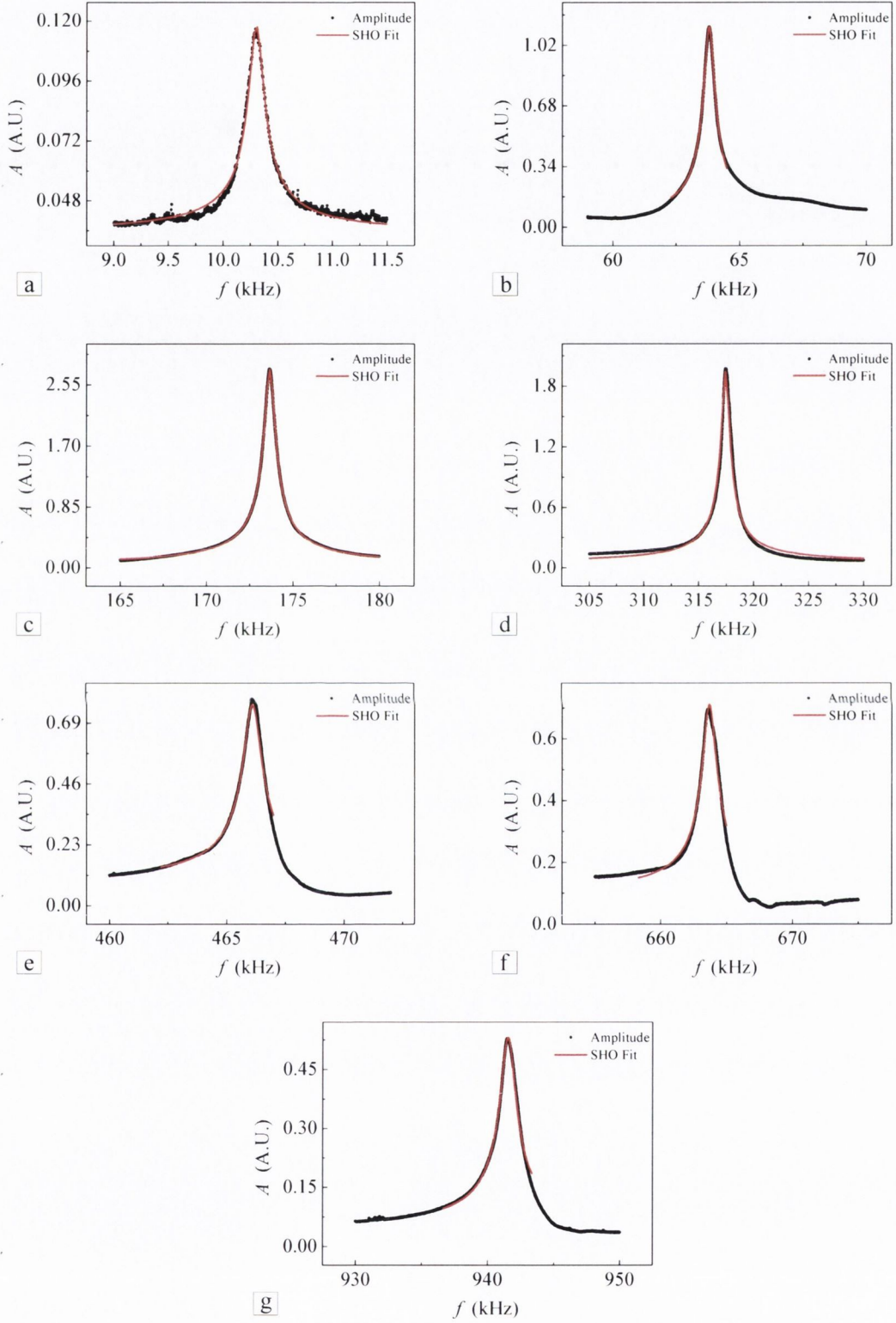


Figure 4.4. Sample of the seven resonance modes examined for the 2 μm thick cantilevers using one clamping position. The modes were fitted using Eq. 4.1 to find the centre frequency and the Q factor. Ten measurements of each mode were recorded. **a)** Mode 1 at 10.30 kHz. **b)** Mode 2 at 63.81 kHz. **c)** Mode 3 at 173.63 kHz. **d)** Mode 4 at 317.43 kHz. **e)** Mode 5 at 466.10 kHz. **f)** Mode 6 at 663.71 kHz. **g)** Mode 7 at 941.51 kHz.

Young's Modulus of Si: 169 GPa; density of Si (ρ_{Si}): 2330 kg/m³; density of air (ρ_{air}) (at room temperature (RT)): 1.18 kg/m³; viscosity of air (at RT): 1.78 kg/(m s); speed of sound in air (at RT): 346 m/s.

The general equations for the resonance frequency and Q factor of a given mode are [1, 21]

$$f_n = \frac{f_{vac,n}}{\sqrt{\frac{1+(\pi\rho_{air}b)}{4\rho_{Si}h}\Gamma_r(f_n,n)}} \quad (4.2)$$

$$Q = \frac{\frac{4\rho_{Si}h}{\pi\rho_{air}b} + \Gamma_r(f_n,n)}{\Gamma_i(f_n,n)} \quad (4.3)$$

where h is the thickness of the cantilever, b is the width of the cantilever, $f_{vac,n}$ is the vacuum resonance frequency of mode n of the cantilever, and $\Gamma(f_n,n)$ is the dimensionless hydrodynamic function and the subscripts r and i refer to the real and imaginary components respectively.

The calculations of the Q factor and resonance frequencies required finding the hydrodynamic function for each of the models (it is this term that the compressibility of the fluid affects). This involved solving the systems of linear equations given in Eq. 11 of reference [21] and in Eq. 7 of reference [1]. The integer M described in the models was chosen to be 36 and was shown to provide sufficient convergence of the solution for the higher modes of vibration as shown in Fig. 4.5. For further information on the characteristics of these functions and their convergence see references [1, 21, 26]. Mathematica 8.0 was used to perform the calculations, and the source code for all calculations is contained in Appendix C.

4.3 Comparison Between Theory and Experiment

4.3.1 7 μ m Thick Cantilevers

It was found that there was a decrease in the Q factor of the seven cantilever beams between the third and fourth modes which agrees with the prediction of the scaling analysis mentioned above that the “coincidence point” is the $n_c = 3$ mode. This decrease in Q factor can be clearly seen in Fig. 4.6. The large error bars of the experimental data shown in Fig. 4.6 correspond to the statistical standard deviation of the Q factor as measured from five experiments where the cantilever was unclamped and re-clamped between experiments and is an indication of the coupling between the piezo and the cantilever. The statistical standard deviation of the resonance frequencies measured for each cantilever were on the order of 0.001%. There was a difference of ~ 400 Hz in the fundamental frequency between cantilever 1 and cantilever 7. A similar decrease was also noted in the higher modes of the cantilevers and is an indication that there is a noticeable difference in thickness of the

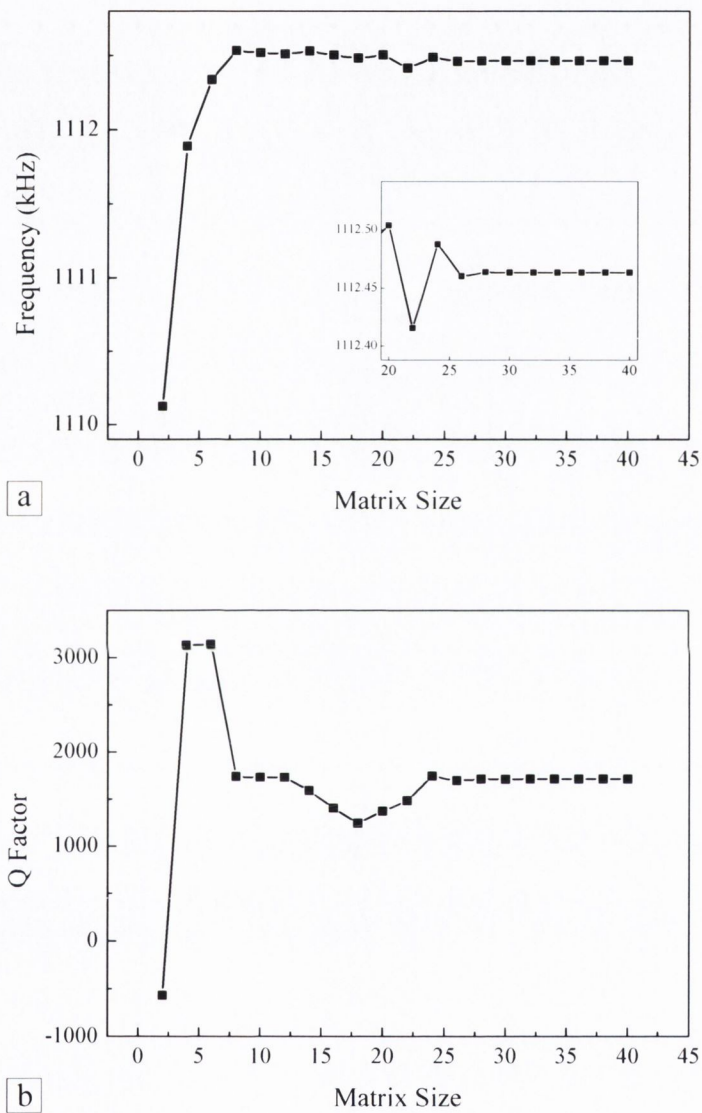


Figure 4.5. The predicted resonance frequency and Q factor becomes more reliable as the size of the matrix used to calculate them increases. **a)** The resonance frequency of mode 4 in air of a 6.723 μm thick cantilever vs. the matrix size. **Inset:** Zoom to show stability of predicted frequency above $M = 30$ **b)** The Q factor of the resonance peak vs. matrix size. Based on these graphs a matrix size of 36×36 was chosen for all calculations.

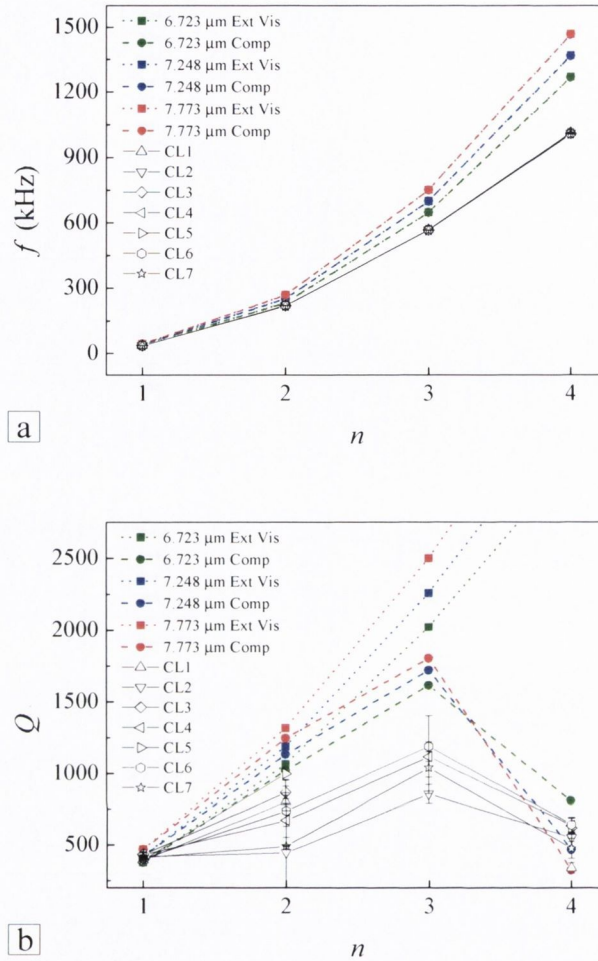


Figure 4.6. Resonance frequency and Q factor vs. mode number comparison between theory and experiment for the 7 μm thick cantilevers. The solid square symbols with dotted lines correspond to the extended viscous model, while the solid circles with dashed lines correspond to the compressible fluid model. The open symbols with solid lines correspond to the experimental data. In the frequency plot the experimental data are overlapping.

cantilevers within the array.

The resonance frequencies measured experimentally at the first mode agreed well with the models, however as the mode number increased the measured frequencies were increasingly lower than those predicted by the models. The lower frequencies observed are consistent with a cantilever which is longer than the cantilevers used here, but shorter than the cantilever and hinge section added together ($\sim 620 \mu\text{m}$ total length, data not shown). The strong dependence of the predictions of the compressible fluid model on the thickness of the cantilever can be observed in Fig. 4.6.

A repeat of the experiment where the cantilever was not removed from the holder

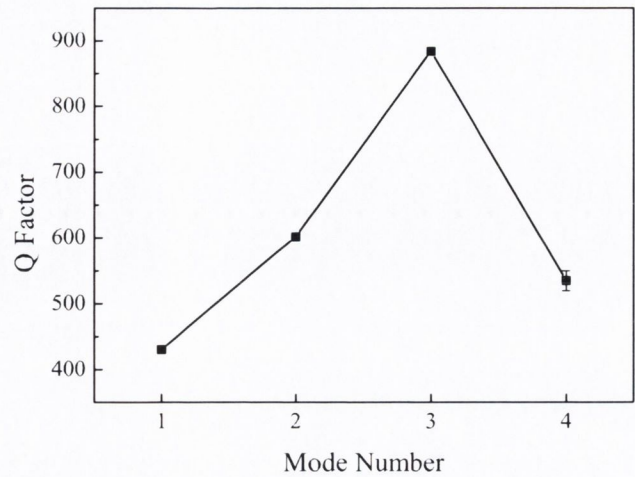


Figure 4.7. Repeated measurement of the Q factor vs. mode number for a single cantilever without removing the array between measurements. The statistical standard deviation of the Q factors for modes 1 - 3 is 0.003% and the statistical standard deviation for mode 4 is 0.02%. This indicated that the previously observed larger standard deviations were due to differences in the coupling between the cantilever and the piezo between experiments.

between measurements is shown in Fig. 4.7. Here ten measurements were taken and it should be noted that the standard deviation is considerably smaller.

4.3.2 2 μm Thick Cantilevers

The “coincidence point” predicted for a 2 μm thick cantilever was mode 12 with a resonance frequency of 3.6 MHz. Using the current device it is not possible to observe the flexural resonance modes at such a high frequency, and therefore only the modes up to 1 MHz were observed. The hinge portion of the array is relatively thicker for these arrays than for the 7 μm thick cantilever arrays and as such should have less of an effect on the dynamics of the cantilever.

Fig. 4.8 shows the comparison between the experimental data and the predictions of the extended viscous and compressible fluid models. It is clear that the resonance frequencies are still below those predicted by the models; however they match better than for the 7 μm thick cantilever array (16% compared to 29% difference at mode 4). This is an indication that the comparatively thinner hinge portion of the array is making a significant contribution to the dynamics of the 7 μm thick cantilever arrays.

It is clear from Fig. 4.8 that there are differences in the predicted Q factors of the two models well below the “coincidence point”. The experimental values match well with those predicted by the compressible fluid model (20% lower for the compressible fluid model compared to 75% lower for the extended viscous model at mode 7).

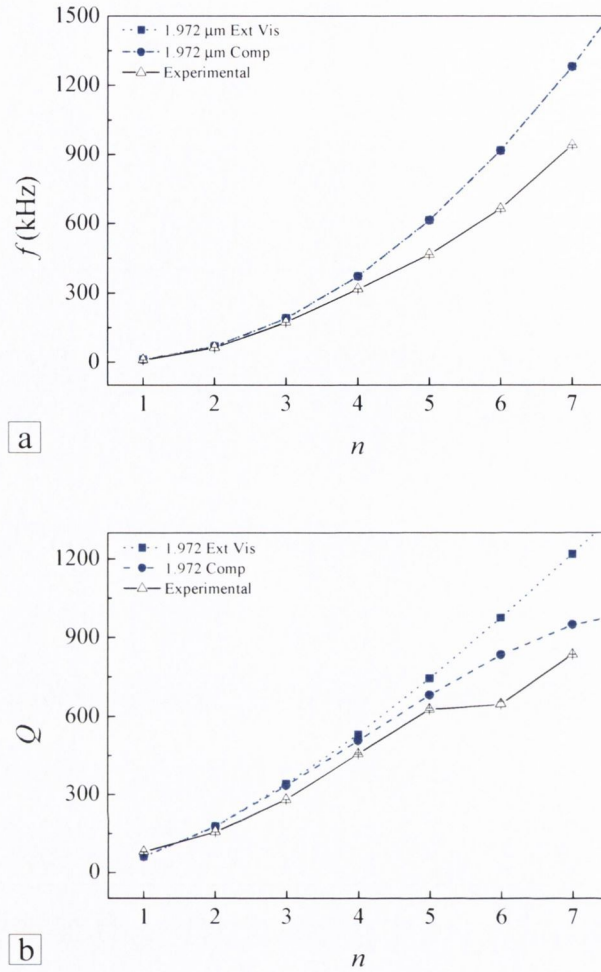


Figure 4.8. Resonance frequency and Q factor vs. mode number comparison between theory and experiment for the 2 μm thick cantilever. The solid square symbols with dotted lines correspond to the extended viscous model, while the solid circles with dashed lines correspond to the compressible fluid model. The open symbols with solid lines correspond to the experimental data.

4.4 Discussion

It is clear that the experimental data agrees qualitatively with the predictions of the compressible fluid model of Van Eysden and Sader, but that absolute quantitative agreement is not demonstrated here. Deviations of the resonance frequency and Q factors of the cantilevers between the predictions from the compressible fluid model and the experimental findings could be due to the hinge of the cantilever being only approximately twice or three times the thickness of the cantilever (Fig. 4.2). This may not provide a sufficiently stiff support and there may be some degree of mechanical coupling between the hinge and the cantilever beam as shown in Fig. 2.20 in Section

2.4.2. This is significantly more noticeable for the 7 μm thick cantilevers where the hinge is comparatively thinner and as such is an indication that the hinge is the cause of the observed deviations from the compressible fluid model predictions. The models are based on an ideal cantilever extending from a fixed support and as such should not be expected to predict exactly the behaviour of cantilevers with a hinge design such as the one used here, however theoretical geometric assumptions are not always translatable into physical microfabricated devices.

Another possible reason for a qualitative and not a quantitative result could be that the model is based on thermal actuation of the cantilever beam and here a piezo actuator is used to amplify the motion of the cantilever, and while efforts are made to keep the cantilever operating within the linear regime of the vibrations, this may not be 100% successful. It should also be noted that the model is valid for cantilevers with a large aspect ratio and here the cantilevers used to conduct the experiment have a ratio of 5 which places them very near the boundary for which the theory is valid.

References

- [1] C. A. Van Eysden and J. E. Sader, "Frequency response of cantilever beams immersed in compressible fluids with applications to the atomic force microscope," *Journal of Applied Physics*, vol. 106, p. 094904, 2009.
- [2] J. Jensen and M. Hegner, "Predictions of the compressible fluid model and its comparison to experimental measurements of Q factors and flexural resonance frequencies for microcantilevers," *Journal of Sensors*, vol. 2012, p. 258381, 2012.
- [3] J. Fritz, M. Baller, H. Lang, H. Rothuizen, P. Vettiger, E. Meyer, H. Güntherodt, C. Gerber, and J. Gimzewski, "Translating biomolecular recognition into nanomechanics," *Science*, vol. 288, pp. 316–318, 2000.
- [4] R. McKendry, J. Y. Zhang, Y. Arntz, T. Strunz, M. Hegner, H. P. Lang, M. K. Baller, U. Certa, E. Meyer, H. J. Guntherodt, and C. Gerber, "Multiple label-free biodetection and quantitative dna-binding assays on a nanomechanical cantilever array," *Proceedings of the National Academy of Sciences of the United States of America*, vol. 99, no. 15, pp. 9783–9788, 2002.
- [5] F. Huber, M. Hegner, C. Gerber, H. J. Guntherodt, and H. P. Lang, "Label free analysis of transcription factors using microcantilever arrays," *Biosensors and Bioelectronics*, vol. 21, no. 8, pp. 1599–1605, 2006.
- [6] L. M. Lechuga, J. Tamayo, M. Álvarez, L. G. Carrascosa, A. Yufera, R. Doldán, E. Peralías, A. Rueda, J. A. Plaza, K. Zinoviev, C. Domínguez, A. Zaballos, M. Moreno, C. Martínez-A, D. Wenn, N. Harris, C. Bringer, V. Bardinal, T. Camps, C. Vergnenègre, C. Fontaine, V. Díaz, and A. Bernad, "A highly sensitive microsystem based on nanomechanical biosensors for genomics applications," *Sensors and Actuators B: Chemical*, vol. 118, no. 1-2, pp. 2–10, 2006.
- [7] J. Mertens, M. Álvarez, and J. Tamayo, "Real-time profile of microcantilevers for sensing applications," *Applied Physics Letters*, vol. 87, no. 23, p. 234102, 2005.
- [8] D. Ramos, M. Arroyo-Hernández, E. Gil-Santos, H. D. Tong, C. V. Rijn, M. Calleja, and J. Tamayo, "Arrays of dual nanomechanical resonators for selective biological detection," *Analytical Chemistry*, vol. 81, no. 6, pp. 2274–2279, 2009.
- [9] N. Backmann, C. Zahnd, F. Huber, A. Bietsch, A. Pluckthun, H. P. Lang, H. J. Guntherodt, M. Hegner, and C. Gerber, "A label-free immunosensor array using single-chain antibody fragments," *Proceedings of the National Academy of Sciences of the United States of America*, vol. 102, no. 41, pp. 14 587–14 592, 2005.
- [10] P. S. Waggoner, M. Varshney, and H. G. Craighead, "Detection of prostate specific antigen with nanomechanical resonators," *Lab on a Chip*, vol. 9, no. 21, pp. 3095–3099, 2009.
- [11] T. Braun, M. Ghatkesar, N. Backmann, W. Grange, P. Boulanger, L. Letellier,

- H. Lang, A. Bietsch, C. Gerber, and M. Hegner, "Quantitative time-resolved measurement of membrane protein-ligand interactions using microcantilever array sensors," *Nature Nanotechnology*, vol. 4, pp. 179–185, 2009.
- [12] B. Ilic, Y. Yang, and H. Craighead, "Virus detection using nanoelectromechanical devices," *Applied Physics Letters*, vol. 85, no. 13, pp. 2604–2606, 2004.
- [13] N. Nugaeva, K. Gfeller, N. Backmann, H. Lang, M. Düggelin, and M. Hegner, "Micromechanical cantilever array sensors for selective fungal immobilization and fast growth detection," *Biosensors and Bioelectronics*, vol. 21, pp. 849–856, 2005.
- [14] K. Y. Gfeller, N. Nugaeva, and M. Hegner, "Micromechanical oscillators as rapid biosensor for the detection of active growth of escherichia coli," *Biosensors and Bioelectronics*, vol. 21, no. 3, pp. 528–533, 2005.
- [15] K. Y. Gfeller, N. Nugaeva, and M. Hegner, "Rapid biosensor for detection of antibiotic-selective growth of escherichia coli," *Applied and Environmental Microbiology*, vol. 71, no. 5, pp. 2626–2631, 2005.
- [16] D. Ramos, J. Tamayo, J. Mertens, L. Villanueva, and A. Zaballos, "Detection of bacteria based on the thermomechanical noise of a nanomechanical resonator: origin of the response and detection limits," *Nanotechnology*, vol. 19, p. 035503, 2008.
- [17] N. Maloney, G. Lukacs, N. Nugaeva, W. Grange, J. P. Ramseyer, J. Jensen, , and M. Hegner, "Fibre optic readout of microcantilever arrays for fast microorganism growth detection," *Journal of Sensors*, vol. 2012, p. 405281, 2012.
- [18] M. K. Ghatkesar, V. Barwich, T. Braun, J. P. Ramseyer, C. Gerber, M. Hegner, H. P. Lang, U. Drechsler, and M. Despont, "Higher modes of vibration increase mass sensitivity in nanomechanical microcantilevers," *Nanotechnology*, vol. 18, p. 445502, 2007.
- [19] F.-J. Elmer and M. Dreier, "Eigenfrequencies of a rectangular atomic force microscope cantilever in a medium," *Journal of Applied Physics*, vol. 81, no. 12, pp. 7709–7713, 1997.
- [20] J. E. Sader, "Frequency response of cantilever beams immersed in viscous fluids with applications to the atomic force microscope," *Journal of Applied Physics*, vol. 84, no. 1, pp. 64–76, 1998.
- [21] C. A. Van Eysden and J. E. Sader, "Frequency response of cantilever beams immersed in viscous fluids with applications to the atomic force microscope: Arbitrary mode order," *Journal of Applied Physics*, vol. 101, p. 044908, 2007.
- [22] M. K. Ghatkesar, T. Braun, V. Barwich, C. Gerber, M. Hegner, and H.-P. Lang, "Resonating modes of vibrating microcantilevers in liquid," *Applied Physics Letters*, vol. 92, p. 043106, 2008.
- [23] C. A. Van Eysden and J. E. Sader, "Compressible viscous flows generated by oscillating flexible cylinders," *Physics of Fluids*, vol. 21, p. 013104, 2009.

-
- [24] J. W. M. Chon, P. Mulvaney, and J. E. Sader, "Experimental validation of theoretical models for the frequency response of atomic force microscope cantilever beams immersed in fluids," *Journal of Applied Physics*, vol. 87, no. 8, pp. 3978–3988, 2000.
 - [25] K. Levenberg, "A method for the solution of certain problems in least squares," *Quarterly of Applied Mathematics*, vol. 2, pp. 164–168, 1944.
 - [26] C. A. Van Eysden and J. E. Sader, "Resonant frequencies of a rectangular cantilever beam immersed in a fluid," *Journal of Applied Physics*, vol. 100, p. 114916, 2006.

Chapter 5

Protein Aggregation and Parkinson's Disease

This chapter describes the successful detection of the aggregation of the protein α -synuclein in a quantitative, label-free manner by functionalising a microcantilever with α -synuclein monomers and operating it in dynamic mode in the presence of α -synuclein monomers in solution. A total mass of 6 ng of α -synuclein was detected over nine hours on the surface of the cantilever. The result is compared to conventional fluorescence measurements of α -synuclein aggregation under similar conditions. It is found that the label-free cantilever detection method requires a concentration of protein 50 times smaller than that of the current method and indicated potential for significantly faster response times. Some of the contents of this chapter are published in “Quantitative, label-free detection of the aggregation of α -synuclein using microcantilever arrays operated in a liquid environment” by Jensen *et al.*, Journal of Sensors, 2011 [1].

5.1 Introduction

Parkinson's disease, first described in 1817 by James Parkinson [2], is the second most common neurodegenerative disorder (Alzheimer's disease is the most common) and the most common movement disorder. It affects 1-2% of the population over the age of 65 years [3]. It is a progressive, neurodegenerative disorder that is clinically diagnosed by muscle rigidity, resting tremor and bradykinesia [3, 4]. Some patients also present with postural imbalance and festinating gait [3, 4]. In later stages it can also cause cognitive impairment [3, 4]. The disease currently has no cure and treatment is only symptomatic (does nothing to stop the progression of the disease) and becomes less effective in later stages of the disease [3].

Parkinson's disease has been associated with mutations of the gene encoding for,

and aggregation of, the protein α -synuclein in the dopamine-containing neurons in the substantia nigra [3–7]. This brings the disease into the area where nanomechanical sensors can be used as a fast, efficient and reliable *in vitro* tool for the investigation of the self-interactions of the α -synuclein protein.

5.1.1 Parkinson's Disease and α -Synuclein

α -synuclein is a protein which is highly expressed in the dopaminergic neurons in the brain (the main source of dopamine in the mammalian central nervous system) where it is mainly concentrated in the pre-synaptic nerve terminals [8–11]. It contains 140 amino acid residues and is part of the group of natively unfolded proteins (proteins which display little secondary structure) [8, 9]. The exact role of α -synuclein within the dopaminergic neurons is still unknown.

Genetic evidence has directly implicated α -synuclein in the pathogenesis of Parkinson's disease. Several genetic mutations in the α -synuclein gene have been associated with the development of Parkinson's disease [5, 6, 12–14]. These mutations are associated with rare hereditary or 'early onset' Parkinson's disease. The majority of cases of Parkinson's disease are considered idiopathic (not caused by an inherited genetic mutation, but rather by an environmental factor).

The neuropathological feature of Parkinson's disease is the presence of cytoplasmic inclusions (fibrillar aggregates in the cytoplasm of the cell) called Lewy bodies and Lewy neurites. These cytoplasmic inclusions were first described by Friedrich H. Lewy in 1912 and were later named by Tretiakoff who showed that they are numerous in the substantia nigra [3].

Around the same time that the genetic links between α -synuclein and Parkinson's disease were established it was found that α -synuclein is a major component of Lewy bodies [15–17]. The α -synuclein found in the Lewy bodies is in the form of filaments 200–600 nm long and \sim 5–10 nm in diameter [3, 4, 7, 18].

Animal models have indicated that accumulation of α -synuclein may play a role in the loss of dopaminergic neurons in Parkinson's disease [19, 20]. An animal model using transgenic *Drosophila* that produce human α -synuclein was able to replicate several of the essential features of Parkinson's disease [21].

The findings mentioned above created two leading ideas of the disease pathway in Parkinson's disease which are outlined in Fig. 5.1. The first is that by either genetic or other factors there is a dysfunction in the α -synuclein protein. This leads to aggregation of the protein into protofibrils. The protofibrils then aggregate further into fibrils and finally the fibrils come together to form Lewy bodies. The Lewy bodies are then responsible for death of the dopaminergic neurons (the lack of dopamine is responsible for the clinical symptoms of the disease). The second (indicated by the dashed path

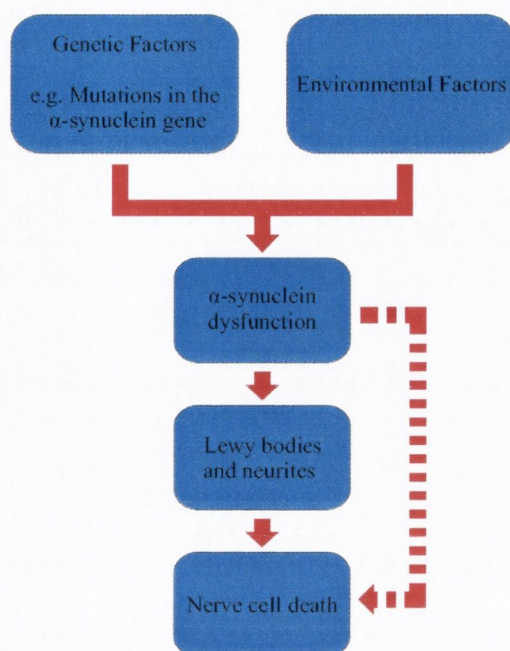


Figure 5.1. Genetic or environmental factors cause a dysfunction in the α -synuclein protein. This results in aggregation into Lewy bodies which then cause nerve cell death. Another possibility is that the the dysfunction in the α -synuclein protein causes the nerve cell death and the formation of Lewy bodies is a protective measure. Adapted from Goedert, 2001 [3].

in Fig. 5.1) is that it is the oligomers/protofibrils which are responsible for the death of the dopaminergic neurons and that the formation of fibrils and Lewy bodies is a protective action by the cell [3].

It has now become more likely that the oligomers and not the fibrils are cytotoxic, with a lot of evidence in favour of this theory [22]. It is clear that a better understanding of the aggregation of α -synuclein would be beneficial in determining the pathway of the disease and also possibly in the development of a cure for the disease.

5.1.2 Investigating Protein Aggregation

Several methods exist for investigating protein aggregates. They can be split into two groups, those which are used to characterise the protein aggregates post-aggregation and those which can be use to determine the kinetics and growth rates during aggregation.

Post-Aggregation Techniques The morphology of a protein aggregate or fibril can be determined using AFM [10, 23, 24]. Use of the AFM in force spectroscopy mode

allows some of the mechanical properties to be determined, such as elasticity or bending rigidity [25]. A modified form of AFM called scanning conductance microscopy can be used to determine the dielectric constants of different materials and has been used on several biological materials [26, 27]. SEM can also be used to determine the dimensions of the aggregate and determine if it is fibrillar in nature [28]. The structure of a fibril can also be determined using X-ray diffraction [29].

It is possible to determine the composition of a protein aggregate using nuclear magnetic resonance (NMR) spectroscopy [28]. This results in a spectrum, the peaks of which indicate the chemical components contained in the sample. The interactions between the different components can also be determined from the spectrum leading to structural information about the protein at the atomic level. However, this method cannot be applied to larger aggregates.

Another way of determining if a specific protein is contained in an aggregate (of unknown composition) is to use an immunolabeling technique in which primary antibodies are generated which bind to a specific epitope of the specific protein. If the protein is present in the sample the primary antibody binds to it. The primary antibody is then labeled with a secondary antibody with a tag attached (e.g. fluorescent label or gold nanoparticle). The sample is then viewed using a microscopy technique (SEM or fluorescent microscopy) to determine if the tag is present in the sample, giving information on the localisation of the target protein within the sample. This technique only indicates if a particular protein is present and does not give the full composition of the aggregate.

Real Time Techniques Dynamic light scattering (DLS) is a technique that can be used to determine the size distribution of particles in suspension. This technique can be applied to determine aggregation rates for proteins in solution [30]. DLS only tracks the change in size of the particles in solution and not their morphology, so one or more of the techniques previously mentioned should be used in addition to confirm the aggregation/fibrillation of the protein.

Several fluorescent labels are available which undergo a shift in their emission frequency upon binding to a protein or aggregation of proteins. Thioflavin T is a fluorescent label for α -synuclein which undergoes a shift in emission frequency upon aggregation of the protein [10, 31, 32]. By monitoring the intensity of the shifted emission frequency rates of aggregation of the protein can be determined [10]. However this technique requires knowledge of the label-fibril binding stoichiometries which can be variable depending on solution conditions or type of protein being investigated. α -synuclein aggregation rates determined using Thioflavin T show a strong dependence on solution conditions such as pH or salt concentration, with incubation times (at 37 °C) for achieving half the final intensity being ~ 80 hrs at pH

7 and as short as 70 minutes at pH 4 [10]. Typically large concentrations of the protein are also required to provide sufficient intensity for measurement. Also the presence of another molecule which interacts with the fibril can affect binding kinetics, therefore label-free detection techniques which do not affect the kinetics are preferable [33].

The kinetics and thermodynamics of protein aggregation can be determined using a QCM [24]. This method tracks the change in bound mass on the surface of the QCM with time by tracking the dynamic changes of the oscillator (frequency shifts, damping of the oscillation response). A problem with this technique is that there is no *in situ* reference during the experiment and several other experiments with different conditions must be conducted to act as a reference.

Transitions of the protein from one type of secondary structure to another (e.g. from random coil to β -pleated sheet conformation) can indicate fibrillation of the protein. The secondary structure of a protein can be tracked using Fourier transform infrared spectroscopy (FTIR) or circular dichroism (CD) as a function of environmental factors (e.g. time or temperature). This can be used to indicate if a protein is aggregating or likely to aggregate under certain conditions. However, only environmental factors, such as temperature, can be changed during the experiment. In order to investigate other conditions, such as pH or salt concentration, individual experiments must be conducted.

Detection of growth of amyloid fibrils by measuring the deflection of a microcantilever array has been reported [34]. However this method only reported the tracking of the deflection of the cantilever with time and the surface stress induced by the growth. The report did not give any indication of the rate of binding of the protein. Therefore the technique is better used as an indication that growth of the fibril is occurring, but is not suitable for determining the rate of growth or the kinetics of the interaction in a quantitative manner.

5.2 Materials and Methods

5.2.1 Cantilever Functionalisation

Prior to metal coating the cantilever was coated with polyethylene glycol (PEG), as described in Appendix B.4, to prevent unspecific binding of protein to the bare silicon during the experiment. The cantilever array was functionalised using the custom fabricated capillary functionalisation setup described in Section 3.4. The test cantilevers were first coated with a monolayer of dithiobis(succinimidyl undecanoate) (DSU) (NBS Biologicals) [35] by immersion in a solution of 0.5 mM DSU in dioxane 1,4 for 30 minutes. The DSU binds to the gold via a thiol group at one end. The

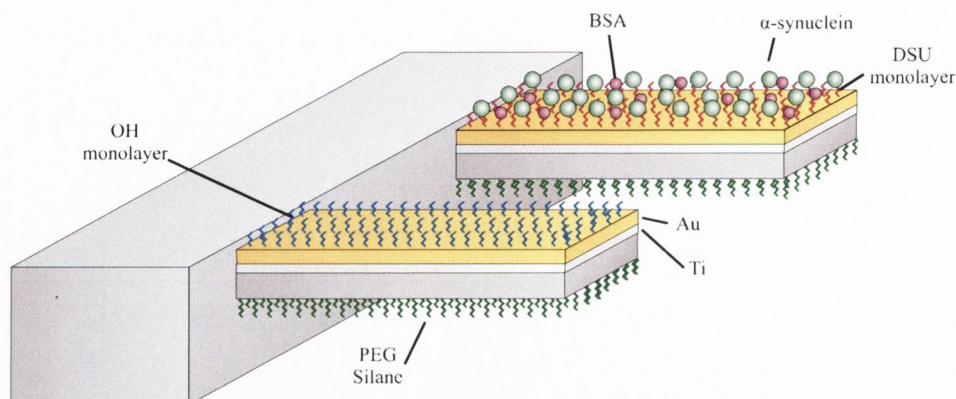


Figure 5.2. Schematic showing the functionalisation of the cantilever array. The backside of the cantilever is coated with a PEG silane monolayer to prevent non-specific adsorption of α -synuclein during the experiment. The array is coated with a Ti/Au layer to facilitate functionalisation using thiol chemistry. The reference cantilever is coated with a self-assembled OH monolayer. The test cantilever is coated with α -synuclein bound to a DSU monolayer. All remaining binding sites are blocked with BSA.

reference cantilevers were passivated against protein binding using a hydroxyl terminated monolayer. The layer was formed by immersing the cantilevers in a solution of 0.5 mM 11-mercapto-1-undecanol in EtOH for 30 minutes. The array was then rinsed in dioxane 1,4 for 5 minutes followed by EtOH for 3 minutes. The test cantilevers were then further functionalised with wild type α -synuclein protein (r-Peptide, Bogart, Georgia 30622, USA), which binds to the DSU, by immersion in 5 μ g/ml α -synuclein in sodium phosphate buffer (20 mM, pH 7) for 2 hours. This was followed by a rinse in the same buffer for 5 minutes. Any remaining binding sites on the cantilever array were blocked using bovine serum albumin (BSA) at a concentration of 0.1 mg/ml in phosphate buffer (20 mM, pH 7.0). The BSA solution was sonicated and filtered through a 0.2 μ m filter to remove any aggregates prior to immersion of the cantilever array in the solution. A final schematic of the functionalised test and reference cantilevers is shown in Fig. 5.2.

5.2.2 Cantilever Measurements

The array was loaded into the dynamic mode fluidic chamber and clamped on top of the piezo actuator. Sodium phosphate buffer (20 mM, pH 6.0) was passed through the chamber at a rate of 3.3 μ l/min for four hours to allow the α -synuclein on the surface of the cantilevers to equilibrate to the lower pH and also to establish a baseline from which the shift of resonance frequency could be measured.

α -synuclein lyophilised in Tris was resuspended in 18 M Ω nanopure water to a final concentration of 1 mg/ml α -synuclein in 10 mM Tris, pH 7.4. The α -synuclein was rebuffed in 20 mM sodium phosphate buffer, pH 6, using a protein desalting spin column (Pierce Protein Research Products, Fisher Scientific Ireland, Dublin, Ireland). The solution was then diluted down to a final concentration of 10 μ g/ml in the same buffer.

The α -synuclein monomers were passed through the fluidic chamber at a rate of 3.3 μ l/min. In total 1.8 ml of the monomer solution was passed over the array. Following the injection of the monomer solution phosphate buffer was passed through the chamber to check for any unbinding of protein from the surface of the cantilever.

5.2.3 Thioflavin T Measurements

The aggregation of the protein α -synuclein in solution was also measured using fluorescence measurements as a further control to be compared with the cantilever array measurement. The fluorescent marker Thioflavin T was used to indicate aggregation of the α -synuclein in solution.

Preparation of α -synuclein The α -synuclein lyophilised in Tris was resuspended in 18 M Ω nanopure water to a final concentration of 1 mg/ml α -synuclein in 10 mM Tris, pH 7.4. The protein was resuspended in 10 mM sodium phosphate buffer, pH 7.4 using a dialysis membrane (Slide-A-Lyzer Dialysis Cassette 3,500 MWCO, Pierce Protein Research Products, Fisher Scientific Ireland, Dublin, Ireland). The 1 ml of protein in Tris solution was injected into the membrane and placed in 800 ml of the sodium phosphate buffer for 30 hours and stored at 4 °C. The sodium phosphate buffer was replaced three times during the procedure.

Fluorescence Measurements A 96-well microtiter plate (Sterilin Ltd., Newport, NP11 3EF, England) was prepared with wells containing 30 μ l of 10 mM sodium phosphate buffer (pH 7.4), 10 μ l of 500 mM NaCl in 10 mM buffer, 50 μ l of α -synuclein 1mg/ml in 10 mM buffer, and 10 μ l of 100 μ M Thioflavin-T in 10 mM buffer for a final volume of 100 μ l in each well. Reference wells for Thioflavin T and blank measurements were also prepared. The reference well for Thioflavin T contained 80 μ l of 10 mM buffer, 10 μ l of 500 mM NaCl in 10 mM buffer, and 10 μ l of 100 μ M Thioflavin-T in 10 mM buffer. The blank reference wells contained 90 μ l of 10 mM buffer, and 10 μ l of 500 mM NaCl in 10 mM buffer. Two wells of each of the above were prepared at three time intervals 8 hrs apart to facilitate measurements of the aggregation at equally spaced time intervals.

The plates were incubated at 37 °C while shaking continuously at 150 RPM, with a diameter of 20 mm. The plates were removed from the incubator for intensity

measurements every 2.5 hours. The plates were covered at all times to avoid photo bleaching of the Thioflavin T. The fluorescence measurements were carried out in a FLUOstar Optima microplate multi-detection reader (BMG Labtech, Aylesbury, HP20 2QJ, UK) with excitation at 450 nm and emission intensity recorded at 520 nm.

5.2.4 Data Handling

The 14th flexural resonance mode of the cantilever (~ 640 kHz) was tracked during the experiment. The frequency range of each scan was 200 kHz, with 2000 steps in the range giving a frequency resolution of 100 Hz. Each frequency in the range was excited for 1 ms and the response from the PSD was sampled at a rate of 10^6 samples per second. The RMS value of the differential signal from the PSD was then calculated for each of the frequencies in the spectrum. The resonance mode was measured every 30 seconds for each cantilever in the array. The bound mass on the surface of the cantilevers was then extracted from the frequency spectra by post-processing of the data using NOSEtools software [36–38]. Samples of the spectra are given in Appendix A.4, Fig. A.6.

For the fluorescence measurements there were two wells measured at each time point for the test, reference and blank solutions. The mean of each type was taken and the test and reference measurements were then scaled by the blank measurement. The response from the reference wells could then be subtracted from the test wells to give the true response.

5.3 Results

5.3.1 Cantilever Measurements

The frequency spectra resulting from the cantilever measurements were post processed using NOSEtools software to determine the shift of the flexural resonance peak and hence the change in mass on the surface of the cantilever (Fig. 5.3). The reference cantilever demonstrated a small decrease in frequency during the experiment (data shown in Appendix A.4, Fig. A.7). The response from the reference cantilever was subtracted from that of the test cantilever to account for any non-specific adsorption of protein to the either side (PEG back side or OH-terminated top side) of the cantilever and to account for any drifts in the response. The only sites available for the α -synuclein monomers in solution to bind to the surface of the cantilever was by aggregating and starting its polymerisation with the protein already attached to the DSU monolayer on the surface. Approximately 6 ng of protein was aggregated on the surface of the cantilever over a 9 hour period. Following the injection of monomers buffer was passed

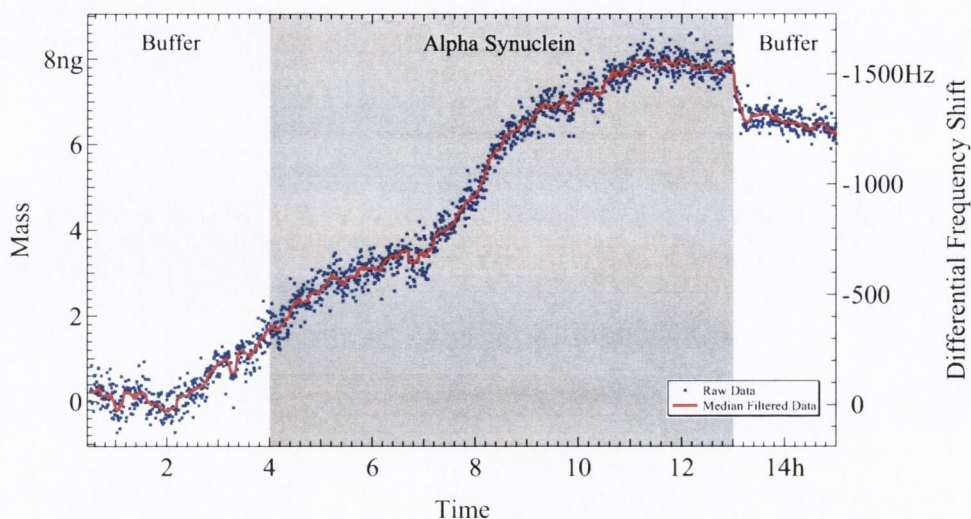


Figure 5.3. Graph of bound mass on the surface of the cantilever vs. time. The frequency spectra recorded during the experiment were post processed using NOSEtools software to obtain the resulting plot of bound mass vs. time. The blue scatter plot shows the raw data (with the reference cantilever subtracted) and the red line shows the median box filter of the raw data (box size 23). The left axis shows the bound mass on the surface of the cantilever and the right axis shows the corresponding differential frequency shift. The grey area indicates the period that 10 $\mu\text{g/ml}$ α -synuclein in 20 mM sodium phosphate buffer was flowing through the fluidic chamber at a rate of 3.3 $\mu\text{l/min}$.

through the chamber and a small amount of α -synuclein (~ 1 ng) was removed from the surface of the test cantilever.

The small amount of non-specific binding of the α -synuclein to the reference cantilever highlights the importance of the *in situ* reference when conducting experiments of this kind. The subtraction of the response of the reference cantilever from that of the test cantilever allows any non-specific binding of the protein to be subtracted from the measurement so that only the response from the protein-protein interactions are examined.

5.3.2 Fluorescence Measurements

The intensity of the emission from 10 μM Thioflavin T with 0.5 mg/ml α -synuclein at 520 nm was recorded for 23 hours. The intensities recorded for the fluorescence measurements were scaled by the intensity from the blank wells in order to account for changes in the input power of the laser in the microplate reader. The intensity from the reference wells was then subtracted from the test wells to show the change in intensity due to the aggregation of the α -synuclein. The experiment was carried out in duplicate and the data from each time point was averaged (Fig. 5.4). The error bars correspond to the result of the propagation of the standard error of the mean of

the intensities through the analysis outlined above. After an initial lag phase of seven hours there is a steady increase of the average intensity recorded. This indicates that there is aggregation of the α -synuclein during this time.

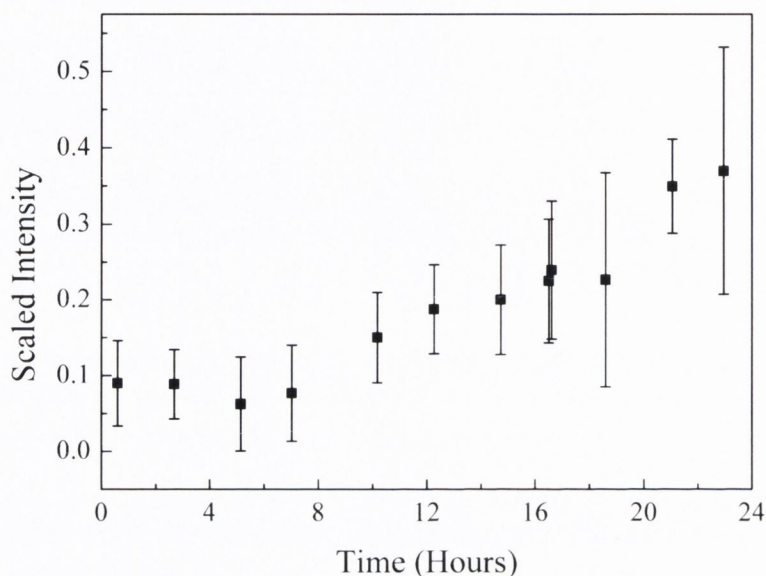


Figure 5.4. Scaled Intensity vs. Time for Thioflavin T intensity measurements. The intensity of the emission from 10 μ M Thioflavin T with 0.5 mg/ml α -synuclein at 520 nm was recorded for 23 hours. The intensity was scaled by the blank measurement and the Thioflavin T reference was subtracted from the test intensity measurement. The data shown is the average of the intensity from the two wells and the error bars correspond to the propagation of the standard error of the mean through the analysis.

5.4 Discussion

These experiments show that it is possible to detect the aggregation of the protein α -synuclein in a label-free manner using functionalised microcantilevers operating in dynamic mode in a physiological liquid environment. The concentration of protein required to detect the aggregation using the label free method is a factor 50 smaller than that used for the fluorescent method presented here. The total mass of protein required was also smaller despite the continuous flow method used for the cantilever measurements, with 50 μ g of protein being required per test well, while only 18 μ g of protein was passed through the cantilever fluidic chamber. In addition, no lag phase was observed during the cantilever measurements, whereas there was a seven hour lag phase observed in the fluorescence measurements.

The aggregation of the α -synuclein on the surface of the cantilever was reproducible, however the total mass of protein aggregated was heavily dependent on

the conformation and density of the initial seeded monomers on the surface of the cantilever (data not shown).

It should be noted that approximately 6 ng of the protein that was passed through the fluidic chamber was polymerised on the surface indicating that the continuous flow method is very wasteful. Employing a method where a smaller amount of α -synuclein is used and the flow is stopped when the protein is in the fluidic chamber (which has a volume of $\sim 6 \mu\text{l}$) a more efficient detection of the aggregation could be possible. However, if the aim is to determine the binding kinetics of the aggregation then such a stop flow situation could lead to incorrect conclusions as the rate that is obtained can heavily depend on the diffusion rate of the protein towards the surface of the cantilever within the fluidic chamber.

The sensitivity of a microcantilever for mass sensing allows detection of a very small mass of protein from the liquid flowed through the chamber (the current sensitivity of the device lies in the sub-nanogram regime in liquids). This can be advantageous when working with particularly expensive molecules or when the aim of the experiment is to detect molecules which are in very low concentrations in a natural, physiological environment. The method and results presented here show a quantitative measurement of aggregation of the protein α -synuclein on the surface of a microcantilever with an *in situ* reference in a physiological environment. This represents an improvement over other measurements of protein aggregation using microcantilevers reported in the literature [34]. As discussed in the introduction the static method is not suitable for determining the kinetics of the aggregation process.

References

- [1] J. Jensen, M. Farina, G. Zuccheri, W. Grange, and M. Hegner, "Quantitative, label-free detection of the aggregation of α -synuclein using microcantilever arrays operated in a liquid environment," *Journal of Sensors*, vol. 2012, p. 874086, 2012.
- [2] J. Parkinson, *An essay on the shaking palsy*. London: Sherwood, Neely and Jones, 1817.
- [3] M. Goedert, "Alpha-synuclein and neurodegenerative diseases," *Nature Reviews Neuroscience*, vol. 7, pp. 492–501, 2001.
- [4] J. Lotharius and P. Brundin, "Pathogenesis of parkinson's disease: dopamine, vesicles and [alpha]-synuclein," *Nature Reviews. Neuroscience*, vol. 3, no. 12, pp. 932–942, 2002.
- [5] L. I. Golbe, G. D. Iorio, V. Bonavita, D. C. Miller, and R. C. Duvoisin, "A large kindred with autosomal dominant parkinson's disease," *Annals of Neurology*, vol. 27, no. 3, pp. 276–82, 1990.
- [6] R. Krüger, W. Kuhn, T. Müller, D. Voitalla, M. Graeber, S. Kösel, H. Przuntek, J. Epplen, L. Schöls, and O. Riess, "Ala30Pro mutation in the gene encoding α -synuclein in Parkinson's disease," *Nature Genetics*, vol. 18, no. 2, pp. 106–108, 1998.
- [7] K. Wakabayashi, K. Tanji, F. Mori, and H. Takahashi, "The Lewy body in Parkinson's disease: Molecules implicated in the formation and degradation of α -synuclein aggregates," *Neuropathology*, vol. 27, pp. 494–506, 2007.
- [8] P. H. Weinreb, W. Zhen, A. W. Poon, K. A. Conway, and P. T. Lansbury, "Nacp, a protein implicated in alzheimer's disease and learning, is natively unfolded," *Biochemistry*, vol. 35, no. 43, pp. 13 709–13 715, 1996.
- [9] D. Eliezer, E. Kutlay, R. Bussell, Jr., and G. Browne, "Conformational properties of α -synuclein in its free and lipid associated states," *Journal of Molecular Biology*, vol. 307, pp. 1061–1073, 2001.
- [10] W. Hoyer, T. Antony, D. Cherny, G. Heim, T. Jovin, and V. Subramaniam, "Dependence of α -synuclein aggregate morphology on solution conditions," *Journal of Molecular Biology*, vol. 322, pp. 383–393, 2002.
- [11] Z. Qin, D. Hu, S. Han, D. Hong, and A. Fink, "Role of different regions of α -synuclein in the assembly of fibrils," *Biochemistry*, vol. 46, pp. 13 322–13 330, 2007.
- [12] M. Polymeropoulos, C. Lavedan, E. Leroy, S. Ide, A. Dehejia, A. Dutra, B. Pike, H. Root, J. Rubenstein, R. Boyer, E. Stenroos, S. Chandrasekharappa, A. Athanassiadou, T. Papapetropoulos, W. Johnson, A. Lazzarini, R. Duvoisin, G. Di-Iorio, Lawrence I. Golbe, and R. Nussbaum, "Mutation in the α -synuclein gene identified in families with Parkinson's disease," *Science*, vol. 276, pp. 2045–

- 2047, 1997.
- [13] J. Zarranz, J. Alegre, J. Gómez-Esteban, E. Lezcano, R. Ros, I. Ampuero, L. Vidal, J. Hoenicka, O. Rodriguez, B. Atarés, D. Muñoz, and J. de Yebenes, "The new mutation, E46K, of α -synuclein causes Parkinson and Lewy body dementia," *American Neurological Association*, vol. 55, pp. 164–172, 2003.
- [14] A. B. Singleton, M. Farrer, J. Johnson, A. Singleton, S. Hague, J. Kachergus, M. Hulihan, T. Peuralinna, A. Dutra, R. Nussbaum, S. Lincon, A. Crawley, M. Hanson, D. Maraganore, C. Adler, M. R. Cookson, M. Muentert, M. Baptista, D. Miller, J. Blancato, J. Hardy, and K. Gwinn-Hardy, " α -synuclein locus triplication causes Parkinson's disease," *Science*, vol. 302, p. 841, 2003.
- [15] M. G. Spillantini, M. L. Schmidt, V. M.-Y. Lee, J. Q. Trojanowski, R. Jakes, and M. Goedert, " α -synuclein in Lewy bodies," *Nature*, vol. 388, pp. 839–840, 1997.
- [16] M. Baba, S. Nakajo, P. Tu, T. Tomita, K. Nakaya, V. Lee, J. Trojanowski, and T. Iwatsubo, "Aggregation of alpha-synuclein in lewy bodies of sporadic parkinson's disease and dementia with lewy bodies," *American Journal of Pathology*, vol. 152, no. 4, pp. 879–884, 1998.
- [17] M. G. Spillantini, R. A. Crowther, R. Jakes, M. Hasegawa, and M. Goedert, " α -synuclein in filamentous inclusions of Lewy bodies from Parkinson's disease and dementia with Lewy bodies," *Proceedings of the National Academy of Sciences of the United States of America*, vol. 95, pp. 6469–6473, 1998.
- [18] R. Crowther, S. Daniel, and M. Goedert, "Characterisation of isolated α -synuclein filaments from substantia nigra of Parkinson's disease brain," *Neuroscience Letters*, vol. 292, pp. 128–130, 2000.
- [19] E. Masliah, E. Rockenstein, I. Veinbergs, M. Mallory, M. Hashimoto, A. Takeda, Y. Sagara, A. Sisk, and L. Mucke, "Dopaminergic loss and inclusion body formation in α -synuclein mice: implications for neurodegenerative disorders," *Science*, vol. 287, pp. 1265–1269, 2000.
- [20] E. Maries, B. Dass, T. Collier, J. Kordower, and K. Steece-Collier, "The role of α -synuclein in Parkinson's disease: insights from animal models," *Nature Reviews Neuroscience*, vol. 4, pp. 727–738, 2003.
- [21] M. Feany and W. Bender, "A *Drosophila* model of Parkinson's disease," *Nature*, vol. 404, pp. 394–398, 2000.
- [22] L. Breydo, J. W. Wu, and V. N. Uversky, " α -synuclein misfolding and parkinson's disease," *Biochimica et Biophysica Acta (BBA) - Molecular Basis of Disease*, vol. 1822, no. 2, pp. 261 – 285, 2012.
- [23] G. Binnig, C. Quate, and C. Gerber, "Atomic force microscope," *Physical Review Letters*, vol. 56, pp. 930–933, 1986.
- [24] T. Knowles, W. Shu, G. Devlin, S. Meehan, S. Auer, C. Dobson, and M. Welland, "Kinetics and thermodynamics of amyloid formation from direct measurements of

- fluctuations in fibril mass,” *Proceedings of the National Academy of Sciences of the United States of America*, vol. 104, no. 24, pp. 10 016–10 021, 2007.
- [25] J. F. Smith, T. P. J. Knowles, C. M. Dobson, C. E. MacPhee, and M. E. Welland, “Characterization of the nanoscale properties of individual amyloid fibrils,” *Proceedings of the National Academy of Sciences of the United States of America*, vol. 103, no. 43, pp. 15 806–15 811, 2006.
- [26] C. Clausen, J. Lange, L. Jensen, P. Shah, M. Dimaki, and W. Svendsen, “Scanning conductance microscopy investigations on fixed human chromosomes,” *Biotechniques*, vol. 44, no. 2, pp. 225–228, 2008.
- [27] C. Clausen, J. Jensen, J. Castillo, M. Dimaki, and W. Svendsen, “Qualitative mapping of structurally different dipeptide nanotubes,” *Nano Letters*, vol. 8, no. 11, pp. 4066–4069, 2008.
- [28] C. Jaroniec, C. MacPhee, N. Astrof, C. Dobson, and R. Griffin, “Molecular conformation of a peptide fragment of transthyretin in an amyloid fibril,” *Proceedings of the National Academy of Sciences of the United States of America*, vol. 99, no. 26, pp. 16 748–16 753, 2002.
- [29] R. Nelson, M. Sawaya, M. Balbirine, A. Madsen, C. Riek, R. Grothe, and D. Eisenberg, “Structure of the cross- β spine of amyloid-like fibrils,” *Nature*, vol. 435, pp. 773–777, 2005.
- [30] A. Lomakin, D. Chung, G. Benedek, D. Kirschner, and D. Teplow, “On the nucleation and growth of amyloid- β protein fibrils: Detection of nuclei and quantitation of rate constants,” *Proceedings of the National Academy of Sciences of the United States of America*, vol. 93, pp. 1125–1129, 1996.
- [31] H. Naiki, K. Higuchi, M. Hosokawa, and T. Takeda, “Fluorometric determination of amyloid fibrils in vitro using the fluorescent dye, thioflavine t,” *Analytical Biochemistry*, vol. 177, no. 2, pp. 244–249, 1989.
- [32] H. LeVine, “Quantification of β -sheet amyloid fibril structures with thioflavin t,” *Methods in Enzymology*, vol. 309, pp. 274–284, 1999.
- [33] R. Demaimay, J. Harper, H. Gordon, D. Weaver, B. Chesebro, and B. Caughey, “Structural aspects of congo red as an inhibitor of protease-resistant prion protein formation,” *Journal of Neurochemistry*, vol. 71, pp. 2534–2541, 1998.
- [34] T. P. J. Knowles, W. Shu, F. cois Huber, H. P. Lang, C. Gerber, C. M. Dobson, and M. E. Welland, “Label-free detection of amyloid growth with microcantilever sensors,” *Nanotechnology*, vol. 19, p. 384007, 2008.
- [35] P. Wagner, M. Hegner, P. Kern, F. Zaugg, and G. Semenza, “Covalent immobilization of native biomolecules onto au(111) via n-hydroxysuccinimide ester functionalized self-assembled monolayers for scanning probe microscopy,” *Biophysical Journal*, vol. 70, no. 5, pp. 2052–2066, 1996.
- [36] T. Braun, M. K. Ghatkesar, V. Barwich, N. Backmann, F. Huber, W. Grange,

- N. Nugaeva, H. Lang, J. Ramseyer, C. Gerber, and M. Hegner, "Digital processing of multi-mode nano-mechanical cantilever data," *Journal of Physics: Conference Series*, vol. 61, pp. 341–345, 2007.
- [37] T. Braun, "Nosetools homepage," accessed 1st Mar 2010, NOSEtools Version 7.2 (rev 438) is available to download free from the NOSEtools Homepage. The software is copyrighted by Thomas Braun 2008, 2009, University of Basel, Switzerland. [Online]. Available: <http://web.me.com/brunobraun/NOSEtools/Home.html>
- [38] T. Braun, F. Huber, M. K. Ghatkesar, N. Backmann, H. P. Lang, C. Gerber, and M. Hegner, "Processing of kinetic microarray signals," *Sensors and Actuators B-Chemical*, vol. 128, no. 1, pp. 75–82, 2007.

Chapter 6

Oligonucleotides and Mass Labels

The successful detection of small biomolecules in a liquid environment is especially challenging in the dynamic mode, however this is often the main aim of the development of the use of cantilever arrays as a diagnostic tool. As a result it can be necessary to add a mass label to the target to enhance the signal obtained from the binding events. This chapter describes the successful detection of oligo-functionalised NPs with diameters of 12.3 nm and 50 nm with total mass uptakes on the surface of the cantilever of 12 ± 3.5 ng and 1.5 ± 0.3 ng respectively. The successful detection of the hybridisation of biotinylated oligos using the static mode and the subsequent detection of the binding of streptavidin-functionalised polystyrene beads to the hybridised biotinylated oligos is also described. This resulted in an average mass uptake of 1.1 ± 0.2 ng on the cantilevers. The differences in the magnitude of the mass uptake in relation to the size of the mass label used is discussed. It is suggested that boundary streaming on the surface of the vibrating cantilevers and the diameter of the particles may play a role in the effectiveness of the mass labels used.

6.1 Introduction

There is a strong history of performance of static-mode applications of cantilever arrays in the field of genomics since the detection of a single base pair mismatch in the hybridisation of two 12-mer oligos [1]. Since then there have been several more reports of the use of the static mode for the detection of genomic material [2, 3]. There have been somewhat fewer reports of the detection of deoxyribonucleic acid (DNA) using the dynamic mode without the use of an additional label to increase the mass of the target [4]. The majority of the reports of resonating detection of DNA also report the use of an additional mass label to enhance the signal obtained (whether by QCM or cantilever) [5–7].

The strong background of research for the detection of oligos using static-mode microcantilever arrays provides a good platform for the testing of the effectiveness

of mass labels in the new dual-mode device with a biological interaction that is well understood and for which there are already good procedures for the preparation of the cantilever array for use during experiments.

6.1.1 Mass Labels

Micro- and nano-scale cantilevers are capable of detecting very small amounts of mass when operated in the dynamic mode, with detection limits in the attogram range reported using cantilevers [8] and as low as 1.7 yg recently reported [9] using a nanomechanical sensor. However, as discussed previously in Section 1.3 when working in a physiological liquid environment the sensitivity of the cantilever to small changes in mass is significantly lower than when working in vacuum or in air.

Many biological molecules that are of interest for sensing applications, such as proteins or small strands of DNA, have such a small mass that they would not be detectable using cantilever arrays operated in the dynamic mode in a liquid environment. It is possible to use an additional mass as a label to enhance the signal obtained from the binding of the molecule to the cantilever.

NPs, and Au NPs in particular, are a convenient choice for use as a mass label due to their high density (19.3 g/cm^3), relatively simple synthesis, and easy functionalisation using thiol chemistry. They have been reported as a mass label for the detection of various biological molecules including genomic material of *Escherichia coli* [5], DNA [6, 7], prion proteins [10], thrombin [11], and prostate specific antigen [12]. Using a QCM sensor and Au NP mass labels with oligo aptamers it is possible to detect Hg^{2+} ions from water samples [13, 14].

6.1.2 Au Nanoparticle Synthesis

The most common synthesis of Au NPs is by the reduction of chloroauric acid (HAuCl_4) in water [15, 16]. A commonly used reducing agent is trisodium citrate ($\text{Na}_3\text{C}_6\text{H}_5\text{O}_7$) which can be used to control the size of the NPs by changing the ratio of reducing agent added to the solution containing the chloroauric acid [17]. The trisodium citrate acts as both the reducing agent and the capping agent to prevent coagulation of the neutral Au NPs once they are formed from the Au^{3+} ions. These Au NPs can be functionalised later by replacing the capping molecules with the functional molecules of choice.

It is also possible to synthesise and functionalise Au NPs in one step using ultrashort pulsed laser ablation of an Au target in a liquid [18, 19] which also contains the functional molecules [20]. In this case the functional molecules are thiolated oligos which are then bound to the surface of the Au NPs via the thiol bond. The oligos act as the capping agent and prevent coagulation of the NPs.

6.2 Materials and Methods

All of the oligos used during the experiments presented were obtained from Microsynth (Microsynth AG, Schtzenstrasse 15, P.O. Box 9436, Balgach, Switzerland). Table 6.1 contains information about the oligos used during the experiments presented. The information includes their sequence, length in number of bps, their modification, and their molecular weight (MW).

Table 6.1. Information about the oligos used during the experiments. All of the oligos listed were synthesised by Microsynth and contain a (CH₂)₆ linker between the 5' end of the oligo and the functional modification.

| ID | Sequence | # bp | 5' Mod | MW g/mol |
|----------|----------------------------------|------|--------|-------------|
| Unspec12 | 5'-ACA CAC ACA CAC-3' | 12 | Thiol | 3552.2 |
| BioB2 | 5'-TCG TGT TTG AAG-3' | 12 | Thiol | 3887.7 |
| BioB2c | 5'-CTT CAA ACA GCA-3' | 12 | Thiol | 3794.4 |
| BioB3 | 5'-CCG GAA GAT TGC-3' | 12 | Thiol | 3886.4 |
| BioB3c | 5'-GCA ATC TTC CGG-3' | 12 | Thiol | 3817.5 |
| BioB4 | 5'-GGA AGC CGA GCG-3' | 12 | Thiol | 3916.2 |
| BioB4c | 5'-CGC TCG GCT TCC-3' | 12 | Thiol | 3769.5 |
| #930352 | 5'-TCG CTA CAG TGT GAT-3' | 15 | Thiol | 4737.0 |
| #930353 | 5'-ATC ACA CTG TAG CGA-3' | 15 | Thiol | 4614.8 |
| #930356 | 5'-AAA AAA TCA CAC TGT AGC GA-3' | 20 | Thiol | 6280.3 |
| #1234760 | 5'-TCG CTA CAG TGT GAT-3' | 15 | Biotin | 4998.0 |
| #1234761 | 5'-ATC ACA CTG TAG CGA-3' | 15 | Biotin | 4965.8 |

6.2.1 Laser-Ablated Au Nanoparticles

A 1 ml, 5 µM, oligo (#930352) solution in nanopure water was prepared using the protocol presented in Appendix B.5. The solution was sent to Particular GmbH for use in functionalising Au NPs prepared using the laser ablation technique. The initial request was for batches of Au NPs with diameters of 20–25 nm and 50 nm, however when SEM analysis was performed by Particular GmbH on the batch of functionalised NPs the average diameter was observed to be 12.32 nm and 42 ±20 nm nm respectively. The stock concentration of the 12.32 nm oligo-functionalised NPs was 13.78 nM and the *in situ* functionalisation resulted in an average of 29 oligos per NP. The stock concentration of the 42 nm oligo NPs was 222 fM (based on a diameter of 42 nm). The 12.32 nm oligo NPs were stored in nanopure water following synthesis and were transferred to a 10 mM sodium phosphate, 150 mM NaCl buffer using the protocol

presented in Appendix B.6. Despite many attempts it was not possible to resuspend the larger 42 nm oligo NPs in buffer solution. The larger particles appeared to become unstable and flocculate with even a small raise (2 mM sodium phosphate) in the salt concentration of the storage solution.

A cantilever array was prepared as described in Chapter 3 and functionalised with 10 μ M thiolated oligo (prepared as described in Appendix B.5) in 50 mM triethylammonium acetate (TEAA) (see Table. 6.2) for 20 minutes. The test cantilevers in the array were functionalised with the complement of the oligo on the NP. A longer complementary oligo with an additional five A bases at the 5' end was also used to check if the additional spacer provided an increase in binding of the NPs from solution. An unspecific oligo Unspec12 was used as a reference which would not hybridise with the oligo on the NPs. After functionalisation the array was rinsed in 50 mM TEAA for 5 minutes followed by rinsing in buffer for 5 minutes prior to loading into the fluid chamber.

Table 6.2. Functionalisation of cantilever array for laser-ablated nanoparticles experiment.

| Cantilever | Functionalisation |
|------------|-------------------|
| 1 | None |
| 2, 4, 6 | Unspec12 |
| 3, 5, 7 | #930353 |
| 5, 8 | #930356 |

Following loading of the array into the fluid chamber buffer was caused to flow through the chamber at a rate of 5 μ l/min using a syringe pump, this flow rate was maintained for the duration of the experiment. The system was allowed to equilibrate for 45 minutes prior to acquisition of a baseline for 125 minutes. A 100 μ l injection loop was used to inject 464 pM oligo NPs in buffer into the chamber at the 125 minute mark and again at the 205 minute mark (as a test of saturation of the cantilevers). A final baseline was acquired following the second injection.

Three resonance modes were recorded once per minute from each cantilever during the experiment between 560 kHz and 940 kHz, corresponding to the 14–16th flexural resonance modes, with 2,500 points per frequency sweep (frequency resolution 152 Hz). Samples of the resonance modes are shown in Appendix A.5, Fig. A.8. The data was processed using NOSEtools [21].

6.2.2 Citrate-Reduction Au Nanoparticles

Due to the large variation in size of the larger laser-ablated Au NPs and their lack of stability in buffer solutions, 50 nm diameter Au NPs (BBI Life Sciences) with a size

variation of $<8\%$ were functionalised with thiolated oligos using the protocol presented in Appendix B.7. The oligo-functionalised NPs were stored in 10 mM sodium phosphate pH 7.4 buffer which resulted in a better yield of NPs from the buffer transfer protocol than when higher salt concentrations were used. Dropping the NaCl concentration in the buffer lowered the melting temperature of a typical 15 mer oligo from 44 °C to around 30 °C depending on the exact sequence. This melting temperature is still sufficiently high that the bond between the 15 mer oligo and its complement will be stable at room temperature. The BioB2 oligo was used during the optimisation of the protocol, with DLS used to confirm an increase in size of the NP following functionalisation. The longer oligo #930356 was used for functionalisation of the 50 nm NPs for the dynamic mode experiments.

A cantilever array was prepared as described in Chapter 3 and functionalised with 10 μ M thiolated oligo (prepared as described in Appendix B.5) in 50 mM TEAA (see Table. 6.3) for 20 minutes. The test cantilevers were functionalised with the complement of the long oligo and the reference cantilevers were functionalised with an unspecific oligo which would not hybridise with the oligo on the NPs. After functionalisation the array was rinsed in 50 mM TEAA for 5 minutes followed by rinsing in buffer for 5 minutes prior to loading into the fluid chamber.

Table 6.3. Functionalisation of cantilever array for #930356-functionalised nanoparticles experiment.

| Cantilever | Functionalisation |
|------------|-------------------|
| 1, 8 | None |
| 2, 5, 7 | Unspec12 |
| 3, 4, 6 | #930352 |

Following loading of the array into the fluid chamber buffer (10 mM sodium phosphate, pH 7.4) was caused to flow through the chamber at a rate of 26 μ l/min using the pressure flow system, this flow rate was maintained during equilibration of the system, and was the flow rate used for the injection of the sample into the fluid chamber during the experiment. The system was allowed to equilibrate for 45 minutes prior to acquisition of a baseline for 45 minutes during which there was no flow of fluid through the chamber. The oligo NPs were injected into the chamber at a concentration of 4.5×10^9 /ml using a 100 μ l injection loop for 150 seconds and then the flow was stopped. The 150 second injection was timed to ensure that there was sufficient mixing within the fluid chamber and that the concentration of NPs within the chamber was stable. After 42.5 minutes the chamber was rinsed with buffer prior to obtaining a final baseline with no flow through the chamber.

Two resonance modes were recorded once per minute from each cantilever during

the experiment between 275 kHz and 425 kHz, corresponding to the 10th and 11th flexural resonance modes, with 1,000 points per frequency sweep (frequency resolution 150 Hz). Samples of the resonance modes are shown in Appendix A.5, Fig. A.9. The data was processed using NOSEtools [21].

6.2.3 Streptavidin-Coated Polystyrene Beads

In order to determine that the oligos on the NPs were hybridising with their complements on the cantilevers a two-step test using biotinylated oligos and streptavidin-coated polystyrene spheres (Spherotech) was performed. The initial step was a static mode experiment where the biotinylated oligos were injected into the chamber and the deflection of the cantilever caused by the hybridisation is detected. Following the hybridisation the streptavidin-coated beads were injected which could then bind with the biotin on the hybridised strands. This test has the advantage of confirming that the oligo SAMs were functional and not damaged and also provides a simple proof of concept test for the experiments presented in Chapter 7, using similar sized beads with the well understood and simpler biological interaction between biotin and streptavidin.

For these experiments Dulbecco’s phosphate-buffered saline (DPBS) was used as a buffer as it was determined that it provides a better static response of the cantilevers to hybridisation of oligos than regular phosphate-buffered saline (PBS) [22]. The formulation of DPBS is given in Appendix A.6.

Test of static response to biotinylated oligo hybridisation.

An initial static only experiment was performed to test the static response of the 1 µm thick cantilevers to the hybridisation of the two complementary 15 mer oligos with one of the oligos biotinylated on the 5’ end. A large concentration of oligo was injected to ensure a response from the cantilever. A cantilever array was prepared as described in Chapter 3 and functionalised with 10 µM thiolated oligo (prepared as described in Appendix B.5) in 50 mM TEAA (see Table. 6.4) for 25 minutes. After functionalisation the array was rinsed in 50 mM TEAA for 5 minutes followed by rinsing in DPBS for 5 minutes prior to loading into the fluid chamber.

Table 6.4. Functionalisation of cantilever array for static biotinylated oligos experiment.

| Cantilever | Functionalisation |
|------------|-------------------|
| 1, 2, 5, 6 | #930352 |
| 3, 4, 7 | Unspec12 |
| 8 | Broken |

Following loading the array into the fluid chamber DPBS was caused to flow through the fluid chamber at 42 $\mu\text{l}/\text{min}$ using the pressure flow system while the system was equilibrating. The flow was stopped and a short baseline was recorded from cantilevers 2–7 (a signal could not be obtained from cantilever 1). The deflection of the cantilevers was measured once every 6 seconds. Once a stable baseline was achieved a heat pulse was applied to the chamber by applying 2 V to the resistors below the chamber for 4 minutes. The system was allowed to return to equilibrium and then the chamber was rinsed for 5 minutes. The flow was stopped and the system was allowed to re-equilibrate and a baseline was recorded before injecting 100 nM oligo #1234761 for 90 seconds at a flow rate of 42 $\mu\text{l}/\text{min}$. After 45 minutes the chamber was rinsed with DPBS at 82 $\mu\text{l}/\text{min}$ for 5 minutes before a final baseline was recorded with no flow through the chamber.

Two-step experiment with biotinylated oligos and streptavidin beads.

The streptavidin beads obtained from Spherotech had a mean diameter of $1.87 \pm 0.046 \mu\text{m}$ and were stored in 0.016 M PBS, pH 7.4 with 0.02% sodium azide at a concentration of 2.78×10^6 beads μl^{-1} . They have a stated binding capacity of biotin of 0.56 nmol biotin-FITC to 1 mg of beads. The beads were rinsed three times by centrifuging at 3,000 g and removing the liquid and replacing with an equal volume of DPBS and resuspending. The beads were then diluted by to 0.182% of stock concentration (5,055 beads μl^{-1}) in DPBS for injection during the experiment.

A cantilever array was prepared as described in Chapter 3 and functionalised with 10 μM thiolated oligo (prepared as described in Appendix B.5) in 50 mM TEAA (see Table. 6.5) for 25 minutes. After functionalisation the array was rinsed in 50 mM TEAA for 5 minutes followed by rinsing in DPBS for 5 minutes prior to loading into the fluid chamber.

Table 6.5. Functionalisation of cantilever array for two-step biotinylated oligos with streptavidin beads experiment.

| Cantilever | Functionalisation |
|------------|-------------------|
| 1, 5,7 | #930353 |
| 3, 8 | #930356 |
| 2, 4, 6 | Unspec12 |

Following loading the array into the fluid chamber DPBS was caused to flow through the fluid chamber at 42 $\mu\text{l}/\text{min}$ using the pressure flow system while the system was equilibrating. The flow was stopped and a short baseline was recorded. The deflection of the cantilevers was measured once every 6 seconds. Once a stable baseline was achieved a heat pulse was applied to the chamber by applying 2 V to the resistors

below the chamber for 1 minute. The system was allowed to return to equilibrium and then the chamber was rinsed for 3 minutes. The flow was stopped and the system was allowed to settle and a baseline was recorded before injecting 20 nM oligo #1234760 in DPBS for 90 seconds at a flow rate of 42 $\mu\text{l}/\text{min}$. After 30 minutes the chamber was rinsed with DPBS for 10 minutes at a flow rate of 80 $\mu\text{l}/\text{min}$.

Once the system was settled the static and dynamic response of the cantilevers were recorded once per minute. A baseline was recorded for 30 minutes and then 1.87 μm diameter streptavidin-coated polystyrene beads were injected at a concentration of 5,055 beads micro l^{-1} for 90 seconds at a flow rate of 42 $\mu\text{l}/\text{min}$. The beads were left in the chamber with no flow for 45 minutes before a 20 minute rinse with DPBS at 80 $\mu\text{l}/\text{min}$. A final baseline was recorded after the rinse.

A single resonance mode was recorded between 210 and 250 kHz (mode 9), with 1,000 data points per frequency sweep (40 Hz frequency resolution). Samples of the resonance modes are shown in Appendix A.5, Fig. A.10. The data was processed using NOSEtools [21].

6.3 Results

6.3.1 Laser-Ablated Au Nanoparticles

The baseline corrected bound mass data from four of the cantilevers in the array is shown in Fig. 6.1. A large periodic noise is visible in the four sets of data and is particularly noticeable in the data corresponding to the cantilever which has the largest mass increase following injection of the 464 pM NP suspension. The periodic noise was found to be due to the continuous flow of the liquid through the chamber being driven by the syringe pump (see Section 2.4.4 for more details). The scatter due to the syringe pump flow can be smoothed by applying a median box filter to the data (box size 31).

The Unspec12-functionalised reference cantilever (red trace in Fig. 6.1) did not show any response to the injection of the functionalised NPs as expected. Thus, the reference SAM was formed correctly and protected the cantilever from any non-specific interactions with the NPs.

The cantilever functionalised with the longer complementary oligo #9030356 (light blue in Fig. 6.1) did not show any significant difference in response to the functionalised NP injection than the bare Au (unfunctionalised) reference cantilever (orange in Fig. 6.1). This suggests that the oligo SAM was not formed correctly and that the oligo was not in a position to hybridise with the complementary oligo on the NP. It is possible that the oligo on the surface of the cantilever did not form a full SAM and instead was in a lying down position instead of the preferred standing position.

The differential response of the cantilever functionalised with the complementary

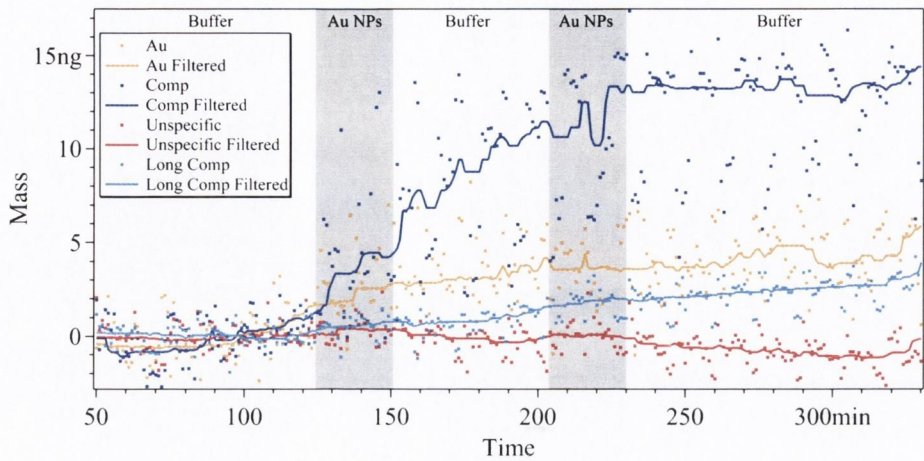


Figure 6.1. The blue plots show the data from the cantilever functionalised with complementary oligo #930353 (dark) and oligo #930356 (light), the red plots show the data from the reference cantilever functionalised with the unspecific oligo, and the orange plots show the cantilever with no functionalisation. The scatter plots show the raw baseline corrected data and the lines corresponds to the median box filtered data (box size 31). The grey area indicates the period that 464 pM Au NPs-functionalised with oligo #930352 in 10 mM sodium phosphate, 150 mM NaCl buffer was flowing through the chamber at a rate of 5 μ l/min.

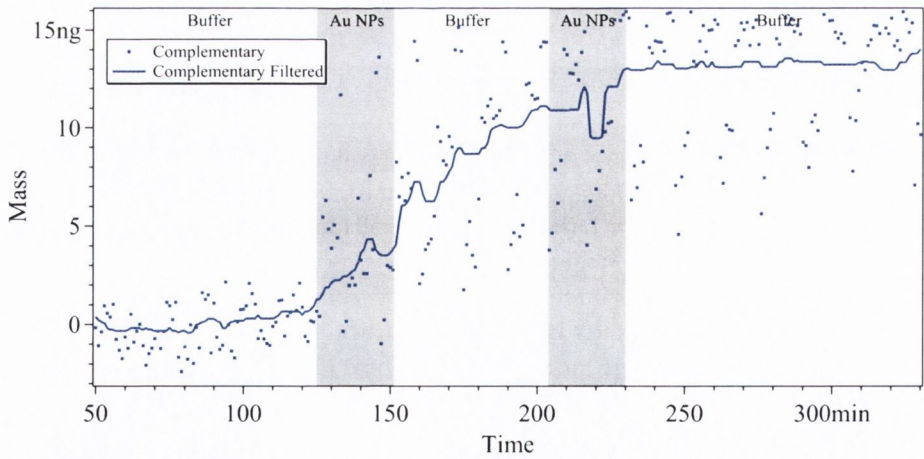


Figure 6.2. The scatter plot shows the reference corrected data and the line corresponds to the median box filtered data (box size 31). The grey area indicates the period that 464 pM oligo NPs in 10 mM sodium phosphate, 150 mM NaCl buffer was flowing through the fluidic chamber at a rate of 5 μ l/min. The scatter in the raw data is due to the pumping of the fluid using the syringe pump. There is a clear increase of mass on the cantilever of $\sim 12 \pm 3.5$ ng. The second injection of functionalised NPs was performed to test if the cantilever surface was saturated. No further increase in mass was observed during the second injection.

oligo #930353 is shown in Fig. 6.2. There is a significant increase of mass on the surface of the cantilever of 12 ± 3.5 ng if the full range of the scatter due to the pumping is taken into account. This corresponds to a surface coverage of $\sim 80\%$ of the cantilever with 12 nm diameter NPs.

6.3.2 Citrate-Reduction Au Nanoparticles

The BioB2 oligo was used during the optimisation of the Au NP functionalisation protocol. The concentration of oligo used for functionalisation was too low to measure the amount of oligo remaining in the supernatant following centrifugation of the functionalised NPs. Thus, the exact number of oligos per NP could not be confirmed, but it is assumed that the well-documented protocol by Mirkin (see Appendix B.7) is robust and provides a surface coverage in the region of what is predicted (35 pmol/cm^2). DLS used to confirm an increase in size of the NP following functionalisation (see Fig. 6.3) as a substitute for measuring the remaining oligo concentration following functionalisation.

There is a clear increase in the average diameter of the NPs of 9 nm, which is consistent with the expected length of the BioB2 12 mer. Single-stranded deoxyribonucleic acid (ssDNA) has a bp length of ~ 0.6 nm [23], so for 12 bps a full length of 7.2 nm is expected. The persistence length of ssDNA is 1–2 nm which causes the observed length of the oligos sticking out from the surface of the NPs to be somewhat less than the maximum of 7.2 nm predicted. Thus, an increase of diameter of 9 nm is consistent with a surface modification to the Au NPs with 12 mer oligos.

Initial tests using the BioB2-functionalised NPs during experiments resulted in very little or no hybridisation of the functionalised NPs with the complementary BioB2c strand on the cantilever. Similarly only small hybridisation of BioB3- and BioB4-functionalised NPs with their complements BioB3c and BioB4c were observed during measurements where the functionalised cantilever array was immersed in 70 μl of stock concentration ($\sim 2 \times 10^{10} \text{ ml}^{-1}$) functionalised NPs in 10 mM sodium phosphate buffer for 30 minutes, followed by a 30 second rinse in DI water. SEM was used to check for the presence of NPs on the surface of the cantilevers (data shown in Fig. A.11 in Appendix A.7). A large non-specific interaction between unfunctionalised Au NPs with unfunctionalised Au coated cantilevers was observed.

By using the longer oligo #930356 to functionalise the NPs it was possible to observe an increase of mass on the surface of the test cantilevers functionalised with the complementary oligo #930352 as shown in Fig. 6.4.a. The three test cantilevers showed a similar mass uptake, within 0.4 ng, and the average differential response (Fig. 6.4 b) was a mass uptake of 1.3 ± 0.3 ng by the end of the period that the functionalised NPs were present in the chamber. Each NP has a mass of 1.3 ± 0.3 fg, indicating that

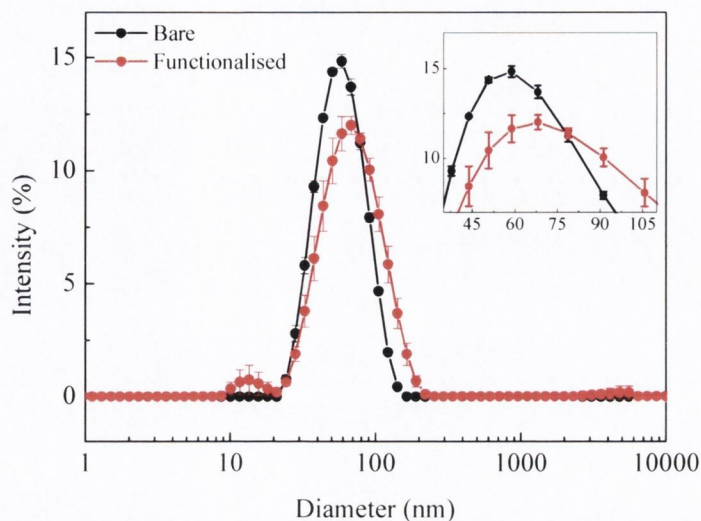


Figure 6.3. DLS was used to confirm functionalisation of the NPs with the 12 mer oligo BioB2 which was used during the optimisation of the functionalisation protocol. A clear increase of the diameter of the particles was observed with the average peak centre moving from 61.41 nm for the bare Au to 70.46 nm for the functionalised NPs.

there was an average of $(1.0 \pm 0.2) \times 10^6$ NPs hybridised to the surface of each cantilever. This corresponds to a surface coverage of 20 ± 4 NPs/ μm^2 .

It was found that the oligo NPs did not store well and were best used as soon as possible after functionalisation. DLS measurements of the Au NPs functionalised with the oligo #930356 following one week of storage at 4 °C in 10 mM sodium phosphate buffer at pH 7.4 revealed that there was no observable difference in the diameter of the bare NPs and the functionalised NPs as shown in Fig. 6.5. It is clear that the oligos were no longer attached to the NPs and therefore must be free in the solution. If experiments are performed with the functionalised NPs, even after a small period of time following the functionalisation, it is possible that the free oligos in solution would compete with the reaction between the functionalised NPs and the cantilevers, resulting in lower or no observed mass uptake during the experiment. As a result it is advised to rinse the functionalised NPs before each experiment and to use them as soon as possible after functionalisation for best results.

The finding that the oligos were dissociating from the Au NPs in a relatively short time span is in good agreement with Bhatt *et al.* [24] who conducted a systematic study of the stability of the thiol bond in DNA-functionalised Au NPs (17 bp long DNA with 13 nm diameter Au NPs). They found that while there was no degradation of the DNA there was spontaneous dissociation of the bond under all test conditions and that DNA-functionalised NPs should be freshly prepared and used within a day or two. They conclude that for storage of oligo NPs low temperature, low ionic strength,

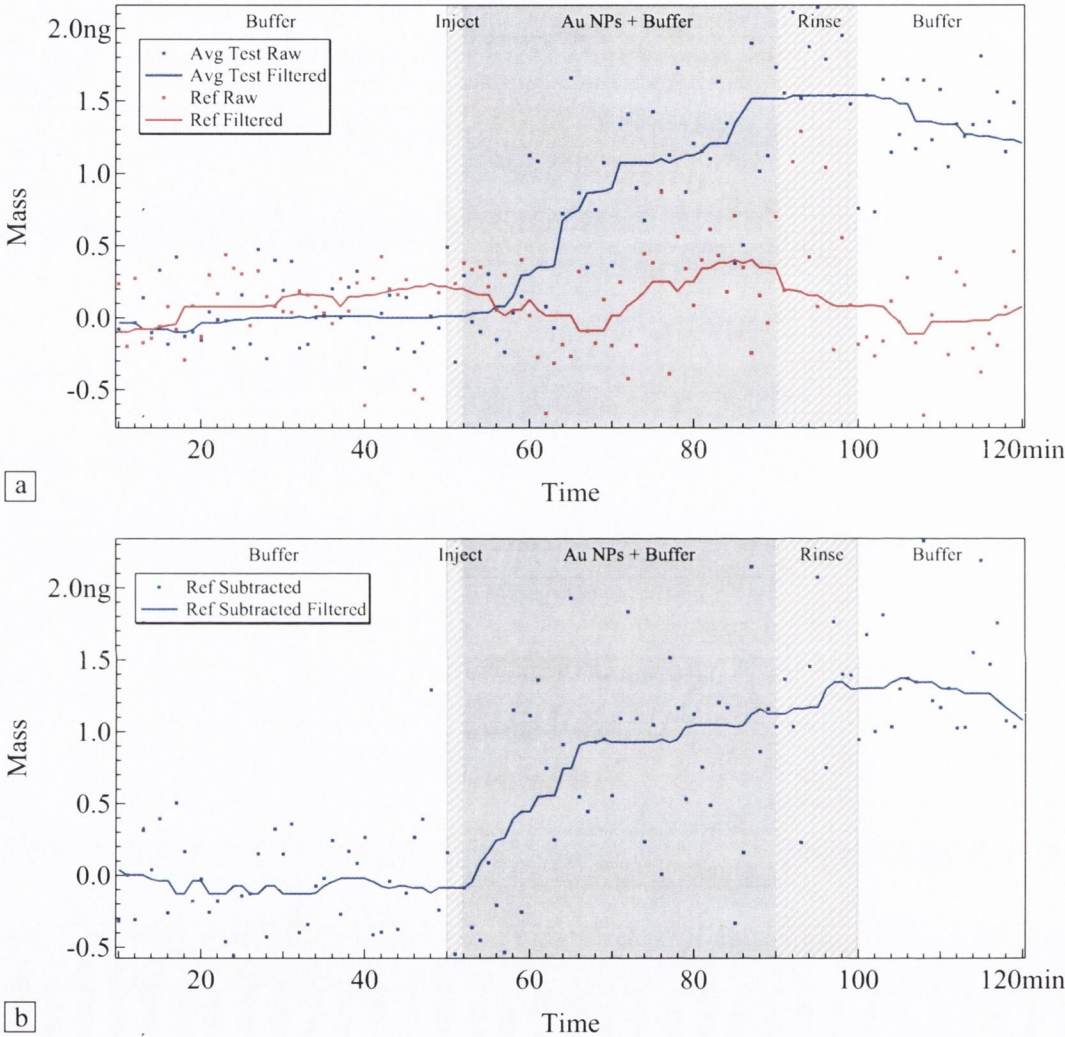


Figure 6.4. **a)** The baseline corrected average change in mass for the three test cantilevers (blue data) functionalised with the #930352 oligo and for one of the reference cantilevers (red data) functionalised with the Unspec12 oligo. **b)** The differential response of the average of the test cantilevers. There is an average change in mass of 1.3 ± 0.3 ng following the injection of the #930356-functionalised 50 nm NPs. The grey shaded area indicates the time during which there was functionalised NPs present in the chamber. The hatched areas indicate the time during which the buffer is flowing through the chamber i.e. during injection and rinsing.

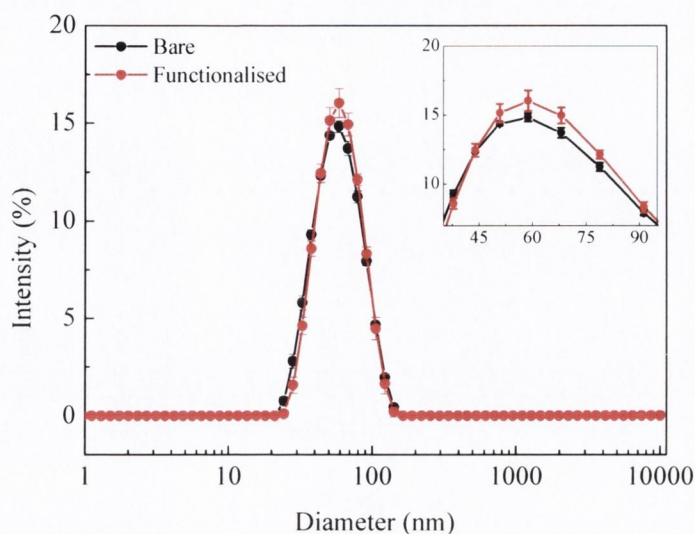


Figure 6.5. DLS was used to check the functionalisation of the NPs with the 20 mer oligo #9030356 following one week of storage at 4 °C. It is clear that there is no observable difference between the functionalised and bare NPs indicating that the majority of the oligos are no longer on the surface of the NPs.

and slightly acidic pH is best.

6.3.3 Streptavidin-Coated Polystyrene Beads

Test of static response to biotinylated oligo hybridisation.

The heat pulse applied to the chamber resulted in a large downward (away from the Au Layer) bending of the cantilever as shown in Fig. A.12.a in Appendix A.8. There was a 120 nm difference in the total deflection of the six cantilevers measured. The response from the cantilevers was calibrated by normalising the response of each cantilever to the mean of the maximum deflection of the six cantilevers during the heat pulse. As shown in Fig. A.12.b in Appendix A.8 the calibrated signal displays less spread in the response of the cantilevers to the heat pulse. The calibration factor for each cantilever was then used in all subsequent analysis of the bending during the rest of the experiment.

Fig. 6.6.a shows the baseline corrected and calibrated data from cantilevers 3 – 6. The data recorded from the other two cantilevers was too noisy and as such was disregarded from the rest of the analysis. There was a large downward bending of the cantilevers when the injection and rinsing stages of the experiment (the hatched areas in the Fig. 6.6.a). This bending is due to the positioning of the cantilevers slightly below the centre of the liquid inlet and the subsequent force applied to the top surface of the cantilever by the flowing liquid entering the chamber. If left for a sufficient amount of time with a steady flow rate the cantilevers would come to a stable position

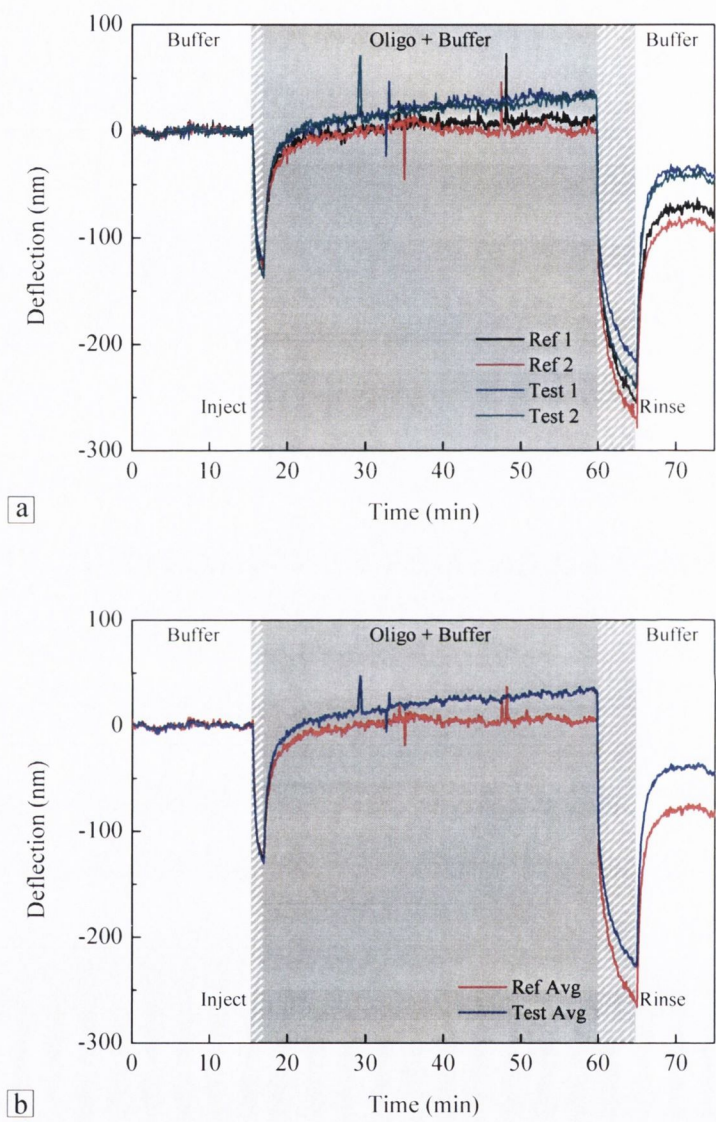


Figure 6.6. **a)** Baseline corrected and calibrated data for the two test cantilevers functionalised with the complementary oligo (#930352) and the reference cantilevers functionalised with Unspec12. **b)** The averaged response of the test and reference cantilevers. The hatched areas correspond to times when the liquid is flowing through the chamber for injection or rinsing, and the grey area corresponds to the period when the target biotinylated oligo is present in the chamber. The large downward bending observed is due to the flow of the liquid through the chamber.

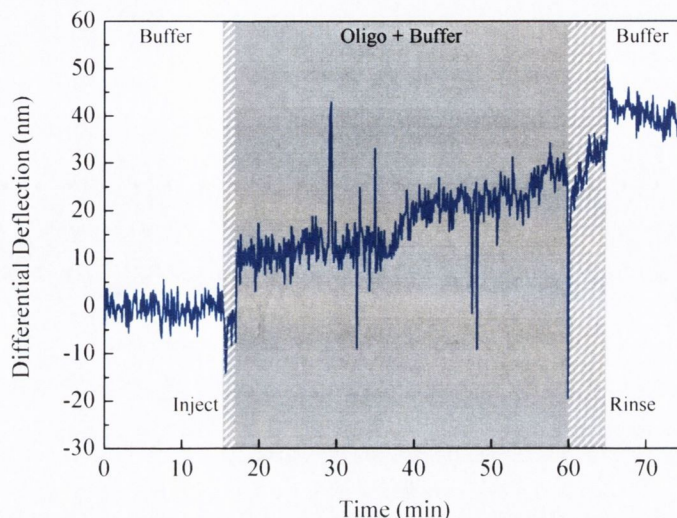


Figure 6.7. When the average reference response is removed from the test response, there is an average differential deflection of 40 ± 3 nm. The hatched areas correspond to times when the liquid is flowing through the chamber for injection or rinsing, and the grey area corresponds to the period when the target biotinylated oligo is present in the chamber.

within the stream.

The average response from the two test cantilevers functionalised with oligo #930532 and the two reference cantilevers coated with oligo Unspec12 is shown in Fig. 6.6.b. There is a clear difference in the response of the cantilevers to the injection of the 100 nM solution of the biotinylated oligo #1234761. The Unspec12-functionalised cantilevers show very little response to the injection as expected. The #350352-functionalised cantilevers show an upward bending (towards the Au layer). The upward bending of the cantilevers indicates that a tensile stress is formed on the surface of the cantilevers. This was unexpected as generally a compressive stress is formed upon hybridisation of oligos on the cantilevers [1], but can be explained by a change in configurational entropy in the SAM as hybridisation occurs, which depends on the state of the initial oligo monolayer [25]. It is also possible that the tensile stress formed is as a result of the biotin modification to the 5' end of the probe oligo.

As shown in Fig. 6.7 the differential deflection of the #930352-functionalised cantilevers is 40 ± 3 nm. The large bending signal observed during the injection and rinsing stages of the experiment is removed by the subtraction of the reference cantilever. Once the rinsing was complete the average difference in deflection between the test and the reference cantilevers was stable and there was no loss of hybridised oligos from the surface of the test cantilevers.

Two-step experiment with biotinylated oligos and streptavidin beads.

The calibrated and baseline corrected data from the static mode response to the injection of the 20 nM of oligo #1234760 again showed clear bands corresponding to the test cantilevers functionalised with the oligo #350353 and the reference cantilever functionalised with Unspec12. When the average of the response for the test and reference cantilevers was taken there was again an obvious upwards bending response of the test cantilevers to the injection of the biotinylated oligo when compared to the reference cantilevers. The calibrated and baseline corrected data for five of the cantilevers and the averaged response for the test and reference cantilevers are shown in Appendix A.9 Fig. A.13.

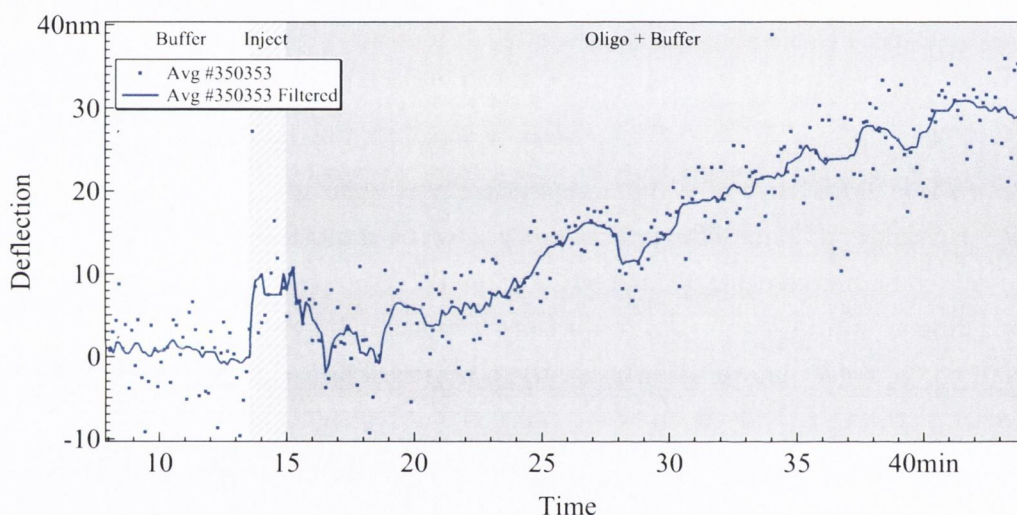


Figure 6.8. The differential response of the cantilevers functionalised with oligo #350353 to the injection of 20 nM oligo #1234760. There was an average upwards bending of the cantilevers when compared to the reference cantilevers of 30 ± 5 nm. The hatched area corresponds to the time when the liquid was flowing through the chamber for the injection of the biotinylated oligos and the shaded area corresponds to the time when the biotinylated oligos were present in the chamber.

As shown in Fig. 6.8 the differential response of the test cantilevers is 30 ± 5 nm. This response is smaller than the response previously observed, but is the result of a lower concentration injection over a shorter period of time, and so a similar magnitude was not expected. The tensile stress formed by the hybridisation with the biotinylated oligos is observed indicating that there were biotin molecules available for binding the streptavidin on the polystyrene beads.

Upon injection of the streptavidin-functionalised beads there was an increase in the scatter of the measured resonance frequency of the cantilevers, as can be seen in Fig. 6.9.a as scatter in the observed bound mass. The increase in the scatter is due to the streptavidin beads which have a diameter of $1.87 \mu\text{m}$ passing through the path of the

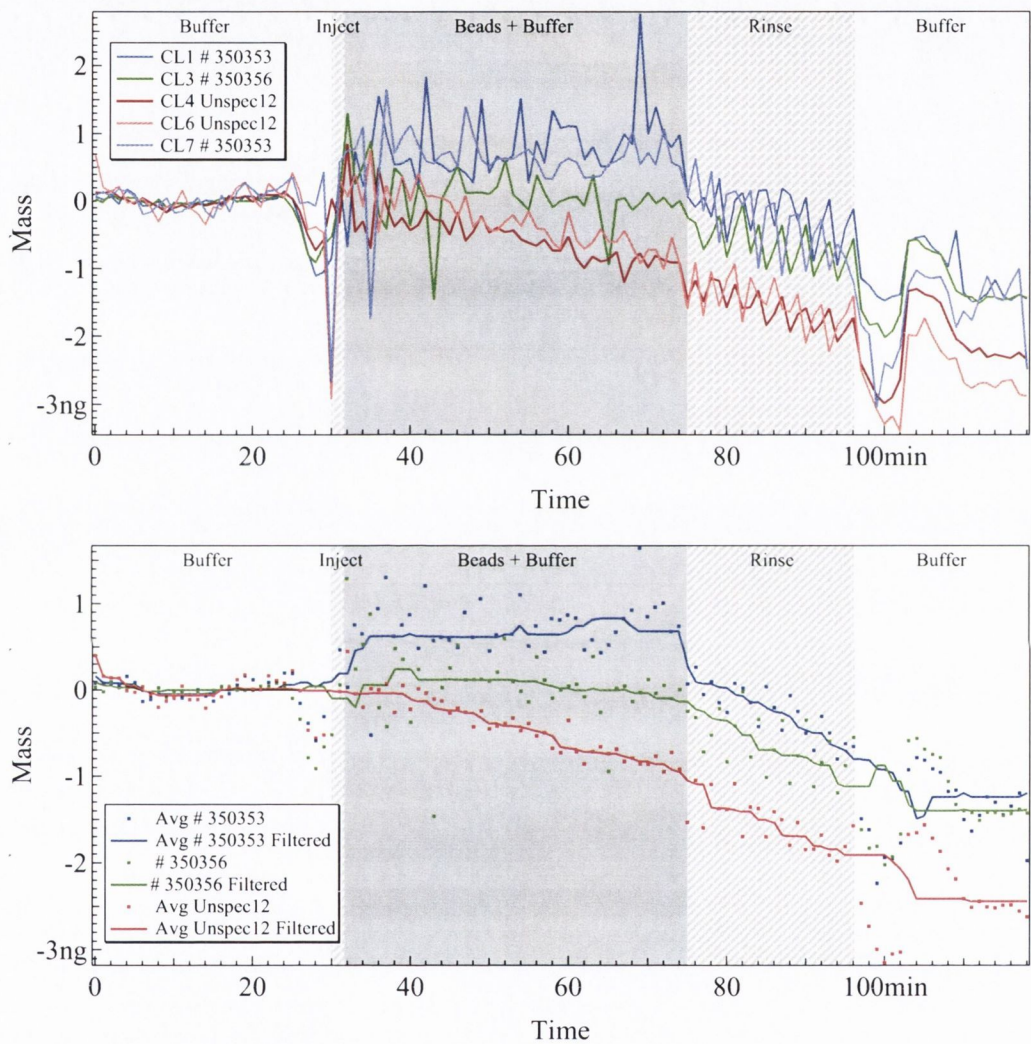


Figure 6.9. **a)** Baseline corrected data from the dynamic mode step of the experiment. **b)** Averaged data (dots) and median box filtered data (lines, box size 15). The colours of the lines correspond to the different functionalisations of the cantilevers: blue for oligo #930353, green for oligo #930356, and red for the Unspec12 oligo. The hatched areas indicate the times that liquid was flowing through the chamber for the injection of the beads and the rinsing of the chamber. The grey shaded area indicates the time that the beads were present in the chamber.

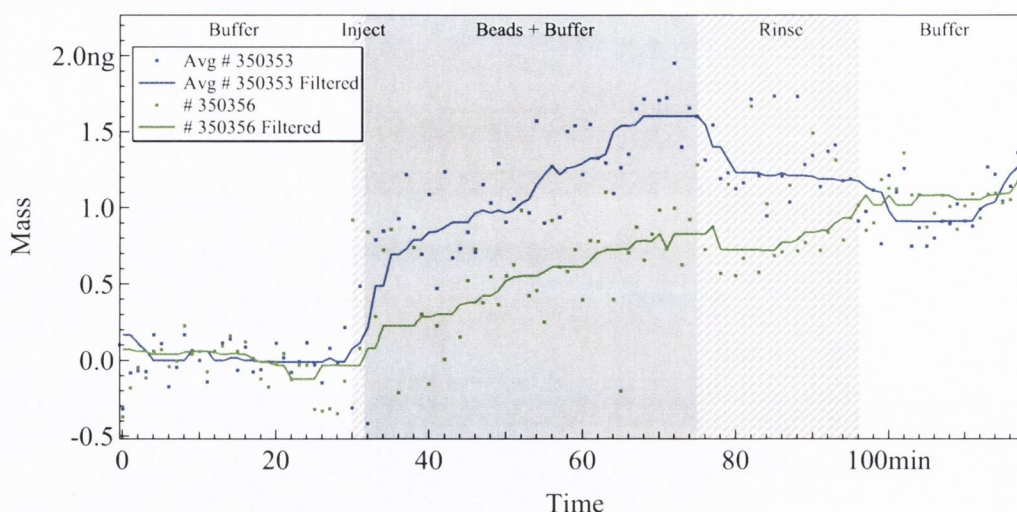


Figure 6.10. The average differential response of the test cantilevers during the dynamic mode step of the experiment. Both types of test cantilever showed an average increase of mass of 1.1 ± 0.2 ng. The colours of the lines correspond to the different functionalisations of the cantilevers: blue for oligo #930353 and green for oligo #930356. The hatched areas indicate the times that liquid was flowing through the chamber for the injection of the beads and the rinsing of the chamber. The grey shaded area indicates the time that the beads were present in the chamber.

laser as the resonance frequencies of the cantilevers were being measured. The scatter in the resonance frequencies reduced to a similar level to the baseline following the rinsing of the chamber.

After the injection of the streptavidin beads there is a clear difference in the response of the three types of functionalised cantilevers which is visible in the averaged response shown in Fig. 6.9.b. The test cantilevers functionalised with oligos #930353 (blue) and #930356 (green) deviate from the average response of the Unspec12-functionalised reference cantilevers (red).

The differential response of the cantilevers is shown in Fig. 6.10. Initially the cantilevers coated with oligo #930353 appear to gain more mass while the streptavidin beads are present in the chamber. However, once the rinsing of chamber was complete there was little difference in final mass bound to the surface of the two types of functionalised cantilevers with each showing 1.1 ± 0.2 ng.

The final observed mass uptake due to the binding of the streptavidin beads to the hybridised biotinylated oligos was small. This was unexpected as there was a clear signal from the static mode indicating the hybridisation of the biotinylated oligos on the test cantilevers. The small frequency shift in response to the binding of the beads to the cantilever when compared to similar experiments using the Au NPs could be due to the size of the secondary mass labels used.

6.4 Discussion

It would be expected that the larger mass labels, the 1.87 μm diameter polystyrene beads, despite being less dense ($\rho_{poly} = 1.06 \text{ g/cm}^3$) would give a larger mass uptake on the surface of the cantilever than the 50 nm diameter Au NPs ($\rho_{Au} = 19.3 \text{ g/cm}^3$) for a similar surface coverage. A rough calculation based on the number of spherical particles of the same size as the labels that could fit on one side of the cantilever in a hexagonal close-packed (HCP) formation gives $\sim 60 \text{ ng}$ for the polystyrene beads, $\sim 29 \text{ ng}$ for the 50 nm Au NPs, and $\sim 7.5 \text{ ng}$ for the 12.32 nm Au NPs. Thus for the same area coverage on the surface of the cantilever it would be expected that the mass uptake from the beads would be approximately twice that of the 50 nm NPs, and eight times that of the smaller NPs. However, this is clearly not what is observed in the experiments presented, with the mass gain observed following the opposite trend when the difference in single or double sided functionalisation is taken into account.

The mass calculated by NOSEtools is based on the assumption that the mass uptake on the cantilever is evenly distributed over the entire surface (see Section 1.3.2 for more details). For an individual point mass or a small number of point masses the detection of a mass increase on the surface of the cantilever is dependent on the position of the mass on the surface of the cantilever as is well documented in the work of the Boisen research group [26, 27]. Based on this research it is possible that the masses which are positioned near the nodes of the resonance modes will not result in a frequency shift, and thus will not be detected.

Research by Dorrestijn *et al.* [28] indicates that particles on the surface of the cantilever can form inverted Chladni figures when the cantilever is vibrated in a fluid (i.e. the smaller particles move to the nodes while the larger particles move to the antinodes). They attribute this effect to boundary streaming caused by the vibrating surface in a viscous medium. This effect causes the particles on the surface to be driven towards the nodes or the antinodes depending on their size. Dorrestijn *et al.* define a critical diameter D_c which is based on the Stokes boundary layer thickness, δ , multiplied by a fitting parameter which they determine to be 2.8,

$$\delta = \sqrt{\frac{2\nu}{\omega}} \quad (6.1)$$

where ω is the radial frequency of the vibration, and ν is the kinematic viscosity of the medium ($1.004 \times 10^{-6} \text{ m}^2/\text{s}$ at 20°C). Thus,

$$D_c = 2.8 \sqrt{\frac{\nu}{\pi f_n}} \quad (6.2)$$

where f_n is the resonance frequency of mode n . The D_c can be calculated for the various

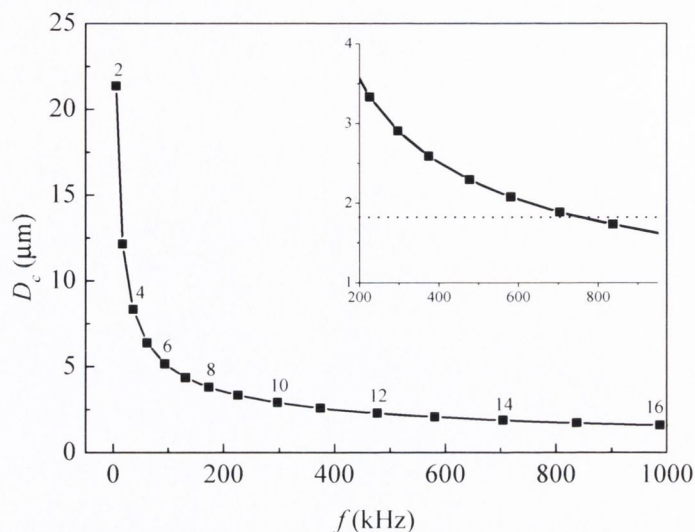


Figure 6.11. The critical bead diameter D_c was calculated for the 1 μm thick cantilevers based on the resonance frequencies measured in Fig. 2.19 and the analysis of particle behaviour on the surface of a cantilever by Dorrestijn *et al.* [28]. Above the D_c particles on the surface will move towards the antinode, while below the D_c the particles will move towards the node. The numbers above the data points indicate the resonance mode and the dashed line in the inset shows the mean diameter of the beads used during the experiment.

resonance modes using the frequencies recorded for the flexural resonance modes 2–19 (Fig. 2.19) and Eq. 6.2 as shown in Fig. 6.11.

Based on these calculations the streptavidin-functionalised beads are below D_c for the 9th resonance mode used in the experiment. In order to ensure that the 1.87 μm diameter beads move towards the antinodes the 15th mode or above would need to be measured (see the inset of Fig. 6.11). Thus, during the experiment it is possible that the beads could move towards the nodes and a smaller frequency shift than expected could be measured.

In the case of the biotin–streptavidin interaction the beads and cantilever interact via molecular recognition. The hybridisation of the oligos occurs before, during the static mode measurement. An additional improvement to the experiment which may increase the probability of bead binding would be the incorporation of an additional spacer and dangling end on the target oligo consisting of a few bases overhang which would protrude further into the liquid and would therefore be more favourable for the biotin–streptavidin interaction.

Dorrestijn *et al.* also observed that smaller particles move about slower on the surface than larger particles, which is likely due to interactions with the surface. The observed speed was 30–50 times slower for a 500 nm diameter particle than a 4 μm

diameter particle. This could explain why the nanoparticles used here showed a larger increase in mass on the cantilever than the beads. The analysis by Dorrestijn *et al.* considered particles as small as 500 nm, and it is expected that the decrease in speed continues as the particle size becomes even smaller. It is postulated that the NPs used here are so small that they either move very slowly and thus stay close to where they bind to the cantilever, or they do not move at all due to the low kinetic energy imparted to them by the cantilever and the slow velocity of the liquid immediately above the surface of the cantilever. Thus, for the smallest NPs the assumption that the mass is evenly distributed is valid, but it may not be the case for the larger micron-scale particles.

The hybridisation bond between the oligos should be strong enough to keep the particles in place once they are hybridised, however the beads and NPs must come within several nanometers of the surface for a period of time before the two strands have the opportunity to find each other and hybridise. It is possible that the streaming effects are occurring before the hybridisation can occur and thus the beads are free to move due to the streaming.

Sweeping the cantilever through several resonance modes may also cause additional forces on the particles as they are first driven towards one position and then another as the modes change. Thus, a multifrequency [29, 30] approach to the actuation of the cantilever where the applied actuation signal is a superposition of several sinusoidal signals with frequencies corresponding to different resonance modes of the cantilever may prove beneficial in future work.

References

- [1] J. Fritz, M. Baller, H. Lang, H. Rothuizen, P. Vettiger, E. Meyer, H. Güntherodt, C. Gerber, and J. Gimzewski, "Translating biomolecular recognition into nanomechanics," *Science*, vol. 288, pp. 316–318, 2000.
- [2] R. McKendry, J. Y. Zhang, Y. Arntz, T. Strunz, M. Hegner, H. P. Lang, M. K. Baller, U. Certa, E. Meyer, H. J. Guntherodt, and C. Gerber, "Multiple label-free biodetection and quantitative dna-binding assays on a nanomechanical cantilever array," *Proceedings of the National Academy of Sciences of the United States of America*, vol. 99, no. 15, pp. 9783–9788, 2002.
- [3] J. Mertens, C. Rogero, M. Calleja, D. Ramos, J. Martín-Gago, C. Briones, and J. Tamayo, "Label-free detection of DNA hybridization based on hydration-induced tension in nucleic acid films," *Nature Nanotechnology*, vol. 3, pp. 301–307, 2008.
- [4] K. Rijal and R. Mutharasan, "Pemc-based method of measuring dna hybridization at femtomolar concentration directly in human serum and in the presence of copious noncomplementary strands," *Analytical Chemistry*, vol. 79, no. 19, pp. 7392–7400, 2007.
- [5] X. Mao, L. Yang, X.-L. Su, and Y. Li, "A nanoparticle amplification based quartz crystal microbalance DNA sensor for detection of *Escherichia coli* O157:H7," *Biosensors & Bioelectronics*, vol. 21, no. 7, pp. 1178–1185, 2006.
- [6] L. B. Nie, Y. Yang, S. Li, and N. Y. He, "Enhanced DNA detection based on the amplification of gold nanoparticles using quartz crystal microbalance." *Nanotechnology*, vol. 18, no. 30, p. 305501, 2007.
- [7] B. H. Cha, S.-M. Lee, J. C. Park, K. S. Hwang, S. K. Kim, Y.-S. Lee, B.-K. Ju, and T. S. Kim, "Detection of Hepatitis B virus (HBV) DNA at femtomolar concentrations using a silica nanoparticle-enhanced microcantilever sensor," *Biosensors & Bioelectronics*, vol. 25, no. 1, pp. 130–135, 2009.
- [8] B. Ilic, H. Craighead, S. Krylov, W. Senaratne, C. Ober, and P. Neuzil, "Attogram detection using nanoelectromechanical oscillators," *Journal of Applied Physics*, vol. 95, no. 7, pp. 3694–3703, 2004.
- [9] J. Chaste, A. Eichler, J. Moser, G. Ceballos, R. Rurali, and A. Bachtold, "A nanomechanical mass sensor with yoctogram resolution," *Nature Nanotechnology*, vol. 7, no. 5, pp. 301–304, 2012.
- [10] M. Varshney, P. S. Waggoner, R. A. Montagna, and H. G. Craighead, "Prion protein detection in serum using micromechanical resonator arrays," *Talanta*, vol. 80, no. 2, pp. 593–599, 2009.
- [11] Q. Chen, W. Tang, D. Wang, X. Wu, N. Li, and F. Liu, "Amplified QCM-D biosensor for protein based on aptamer-functionalized gold nanoparticles,"

- Biosensors & Bioelectronics*, vol. 26, no. 2, pp. 575–579, 2010.
- [12] S.-M. Lee, K. S. Hwang, H.-J. Yoon, D. S. Yoon, S. K. Kim, Y.-S. Lee, and T. S. Kim, “Sensitivity enhancement of a dynamic mode microcantilever by stress inducer and mass inducer to detect PSA at low picogram levels,” *Lab on a Chip*, vol. 9, no. 18, pp. 2683–2690, 2009.
- [13] Q. Chen, X. Wu, D. Wang, W. Tang, N. Li, and F. Liu, “Oligonucleotide-functionalized gold nanoparticles-enhanced QCM-D sensor for mercury(II) ions with high sensitivity and tunable dynamic range,” *Analyst*, vol. 136, no. 12, pp. 2572–2577, 2011.
- [14] Z.-M. Dong and G.-C. Zhao, “Quartz crystal microbalance aptasensor for sensitive detection of mercury(ii) based on signal amplification with gold nanoparticles,” *Sensors*, vol. 12, no. 6, pp. 7080–7094, 2012.
- [15] J. Turkevich, P. C. Stevenson, and J. Hillier, “A study of the nucleation and growth processes in the synthesis of colloidal gold,” *Discussions of the Faraday Society*, vol. 11, pp. 55–75, 1951.
- [16] M.-C. Daniel and D. Astruc, “Gold nanoparticles: Assembly, supramolecular chemistry, quantum-size-related properties, and applications toward biology, catalysis, and nanotechnology,” *Chem Inform*, vol. 35, no. 16, pp. no–no, 2004.
- [17] G. Frens, “Controlled nucleation for the regulation of the particle size in monodisperse gold suspensions,” *Nature Physical Science*, vol. 241, pp. 20–22, 1973.
- [18] F. Mafuné, J.-y. Kohno, Y. Takeda, T. Kondow, and H. Sawabe, “Formation and size control of silver nanoparticles by laser ablation in aqueous solution,” *The Journal of Physical Chemistry B*, vol. 104, no. 39, pp. 9111–9117, 2000.
- [19] S. Barcikowski, A. Menéndez-Manjón, and B. Chichkov, “Generation of nanoparticle colloids by picosecond and femtosecond laser ablations in liquid flow,” *Applied Physics Letters*, vol. 91, p. 083113, 2007.
- [20] S. Peterson and S. Barcikowski, “Tailored nanoparticle-bioconjugates by ultrashort pulsed laser ablation,” *Advanced Functional Materials*, vol. 19, pp. 1167–1172, 2009.
- [21] T. Braun, “Nosetools homepage,” accessed 1st Mar 2010, NOSEtools Version 7.2 (rev 438) is available to download free from the NOSEtools Homepage. The software is copyrighted by Thomas Braun 2008, 2009, University of Basel, Switzerland. [Online]. Available: <http://web.me.com/brunobraun/NOSEtools/Home.html>
- [22] R. Mishra, “Selective gene fishing in complex genomic environments using microcantilevers: Applications in RNAi therapy,” Ph.D. dissertation, Centre for Research on Adaptive Nanostructures and Nanodevices, and the School of Physics, Trinity College Dublin, Dublin, Ireland, 2012.

- [23] S. Smith, Y. Cui, and C. Bustamante, "Overstretching B-DNA: The elastic response of individual double-stranded and single-stranded DNA molecules," *Science*, vol. 271, pp. 795–799, 1996.
- [24] N. Bhatt, P.-J. J. Huang, N. Dave, and J. Liu, "Dissociation and degradation of thiol-modified DNA on gold nanoparticles in aqueous and organic solvents," *Langmuir*, vol. 27, no. 10, pp. 6132–6137, 2011.
- [25] G. Wu, H. Ji, K. Hansen, T. Thundat, R. Datar, R. Cote, M. F. Hagan, A. K. Chakraborty, and A. Majumdar, "Origin of nanomechanical cantilever motion generated from biomolecular interactions," *Proceedings of the National Academy of Sciences*, vol. 98, no. 4, pp. 1560–1564, 2001.
- [26] S. Dohn, R. Sandberg, W. Svendsen, and A. Boisen, "Enhanced functionality of cantilever based mass sensors using higher modes," *Applied Physics Letters*, vol. 86, no. 23, p. 233501, 2005.
- [27] S. Dohn, S. Schmid, F. Amiot, and A. Boisen, "Position and mass determination of multiple particles using cantilever based mass sensors," *Applied Physics Letters*, vol. 97, no. 4, p. 044103, 2010.
- [28] M. Dorrestijn, A. Bietsch, T. Acikalin, A. Raman, M. Hegner, E. Meyer, and C. Gerber, "Chladni figures revisited based on nanomechanics," *Physical Review Letters*, vol. 98, no. 2, p. 026102, 2007.
- [29] R. García and R. Pérez, "Dynamic atomic force microscopy methods," *Surface Science Reports*, vol. 47, pp. 197–301, 2002.
- [30] R. Garcia and E. T. Herruzo, "The emergence of multifrequency force microscopy," *Nature Nanotechnology*, vol. 7, no. 4, pp. 217–226, 2012.

Chapter 7

Antibodies and Magnetic Mass Labels

This chapter will describe a measurement of the binding of anti-biotin antibody-functionalised magnetic beads to a biotin SAM on an Au-coated cantilever array. An average of 3.0 ± 0.3 ng of beads were detected on the surface of the biotin SAM cantilevers. The binding of the beads to the cantilevers was confirmed with SEM analysis of the cantilever array. This work forms the preliminary measurement of an assay designed to use -functionalised magnetic beads and NPs with cantilevers as part of an assay for the detection of inflammation proteins from liquid samples.

7.1 Introduction

To continue on from the preliminary work presented in Chapter 6 and move towards the development of a biological assay magnetic particles were introduced as a mass label. By functionalising the magnetic particles with an antibody that is specific against the antigen of interest it should be possible to fish for the antigen from a liquid sample or perform a preconcentration step prior to detection using an antibody-functionalised cantilever array as depicted in the schematic in Fig. 7.1 in an enzyme-linked immunosorbent assay (ELISA)-like sandwich assay [1].

7.1.1 Magnetic Nanoparticles

Magnetic NPs and microparticles are becoming increasingly popular for work with biological sample separation and DNA extraction [2], in bioassays [3], and as contrast agents in magnetic resonance imaging [4, 5]. Typically the particles are made from iron oxide although other materials may be used and they display superparamagnetism, i.e. they display magnetic properties only when in the presence of a magnetic field, which makes them ideal for use in sample separation applications.

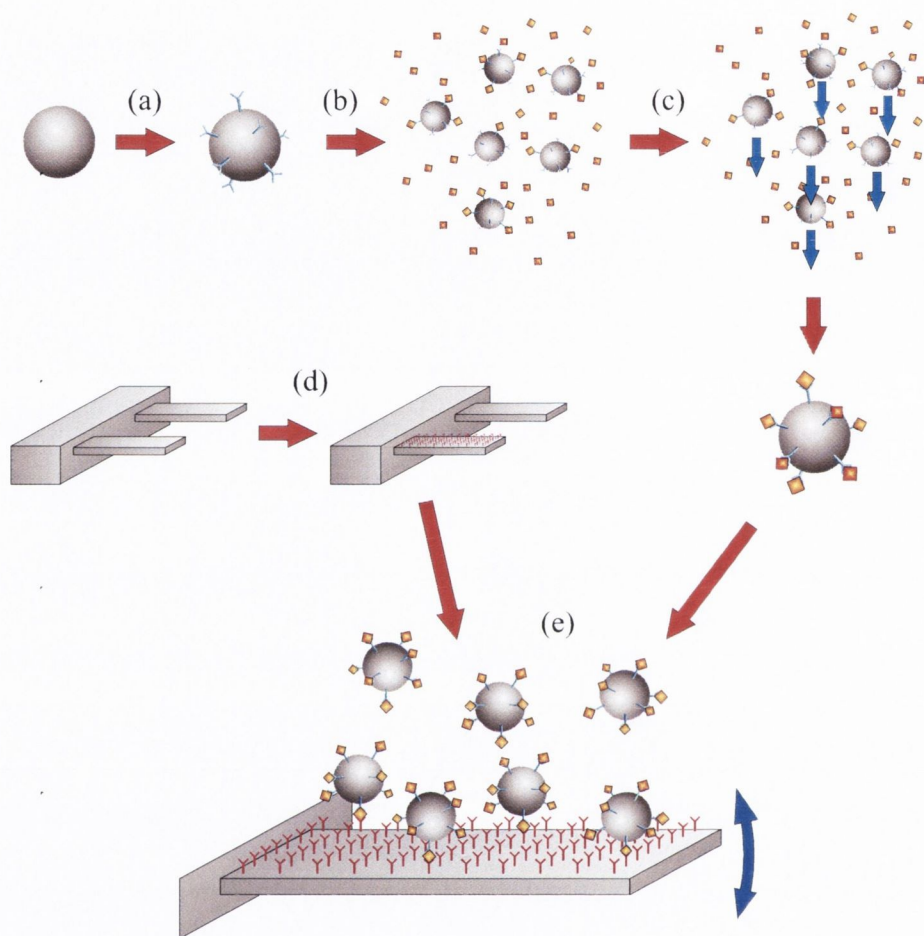


Figure 7.1. Outline of the experiments using nanoparticles as a mass label: **(a)** Magnetic particles will be synthesised with an antibody (blue in the above outline) attached to the surface which binds the target antigen. **(b)** These antibody-coated magnetic particles will then be mixed with the solution containing the target antigen in a low concentration. The target antigen will then bind to the antibody on the surface of the nanoparticle. **(c)** The nanoparticles can then be separated easily from the solution by applying a magnetic field. **(d)** The cantilever array will be functionalised with another (different) antibody (red in the above outline) which also binds the target antigen. **(e)** When the antigen-antibody-particle chain comes in contact with the antibody on the surface of the cantilever it will bind the magnetic particle to the surface. Thus there will be a relatively large mass bound to the surface of the cantilever for every antigen detected, improving the overall sensitivity of antigen detection using the dual-mode device. (Drawings not to scale.)

7.1.2 ELISA

ELISA has become a standard wet-lab technique since its development in the 1960s as a replacement for radioactive labelling techniques [6]. ELISA involves the use of a solid support and antibodies as a recognition element for the detection of a specific antigen. In an indirect ELISA the antigen is fixed to the solid support and an antibody that recognises the antigen is added on top. The antigen is either labelled, which results in a visible signal if the antigen is present, or a secondary antibody with a label is added which causes the visible signal.

Another type of ELISA is the sandwich assay in which an antibody is attached to the solid support (e.g. a 96-well plate). A sample that may contain the antigen is added on top and then rinsed off. An antibody that recognises the antigen is then added followed by a secondary antibody with label which results in a visible signal if the antigen was present in the sample.

7.2 Materials and Methods

Anti-biotin antibody-functionalised magnetic beads were prepared by crosslinking anti-biotin antibodies (ab6643, abcam, 330 Cambridge Science Park, Cambridge, CB4 0FL, UK) with 1 – 2 μm diameter protein G crosslinked magnetic beads (PGMX-10-5, Spherotech) using the protocol described in Appendix B.8. There was a loss of beads of $\sim 25 - 30\%$ during the protocol, and the final stock was diluted by a factor of 150 in PBS to yield a final concentration of 0.0047 % w/v.

A cantilever array was prepared as described in Chapter 3 and the test cantilevers were functionalised with Biotin SAM (as described in Appendix B.9) in ethanol (see Table. 7.1) for one hour. The reference cantilevers were passivated against nonspecific binding using a hydroxyl terminated monolayer. The layer was formed by immersing the cantilevers in a solution of 0.5 mM 11-mercapto-1-undecanol in ethanol for one hour. After functionalisation the array was rinsed in ethanol for 5 minutes followed by rinsing in nanopure water for 5 minutes prior to loading into the fluid chamber.

Following loading of the array into the fluid chamber buffer (PBS, pH 7.4) was caused to flow through the chamber at a rate of 42 $\mu\text{l}/\text{min}$ using the pressure flow system, this flow rate was maintained during equilibration of the system, and was

Table 7.1. Functionalisation of cantilever array for anti-biotin magnetic beads experiment.

| Cantilever | Functionalisation |
|------------|-------------------|
| 1, 2, 5, 6 | 0.5 mM OH SAM |
| 3, 4, 7, 8 | 0.1 mM Biotin SAM |

the flow rate used for the injection of the sample into the fluid chamber during the experiment. The system was allowed to equilibrate for 45 minutes prior to acquisition of a baseline for 50 minutes during which there was no flow of fluid through the chamber. The anti-biotin magnetic beads were injected into the chamber at a concentration of 0.0047 % w/v using a 100 μ l injection loop for 100 seconds and then the flow was stopped. The 100 second injection was timed to ensure that there was sufficient mixing within the fluid chamber and that the concentration of beads within the chamber was stable. After 45 minutes the chamber was rinsed with buffer for 10 minutes prior to obtaining a final baseline with no flow through the chamber. A single resonance mode was recorded once per minute between 800 and 900 kHz (mode 15), with 1,000 data points per frequency sweep (100 Hz frequency resolution).

SEM analysis was performed on the cantilever array following the experiment to confirm the presence of magnetic beads on the surface of the test cantilevers. The array was imaged using a Carl Zeiss Ultra SEM with a voltage of 5 kV and a working distance of 5.8 mm. The array was dried in air prior to imaging.

7.3 Results

The average frequency response and average differential mass uptake from the test cantilevers functionalised with the biotin SAM are shown in Fig. 7.2.a. There is a clear decrease in the average frequency of the test cantilevers upon the injection of the 0.0047 % w/v anti-biotin magnetic beads. There is a small rise in the frequency during the rinsing stage, but this is due to the fluid flowing across the surface of the cantilever and is not due to unbinding of the beads as the frequency returns to the same level once the rinse is finished.

There is an average gain in mass of 3.0 ± 0.3 ng on the surface of the test cantilevers compared to the reference cantilevers upon injection of the 0.0047% w/v anti-biotin magnetic beads as shown in Fig. 7.2.b.

SEM analysis of an array from a similar experiment with identical protocol (shown in Fig. 7.3) indicated that there is significant binding of the anti-biotin magnetic beads towards the tip of the test cantilevers. The beads show up as small white objects on the surface of the cantilevers. The beads are not perfectly spherical and are described as 'granules' with an average diameter in the 1 – 2 μ m range by the manufacturer Spherotech. This is consistent with the particles observed in the SEM images which are imperfect shapes with a diameter in the region of 1 μ m.

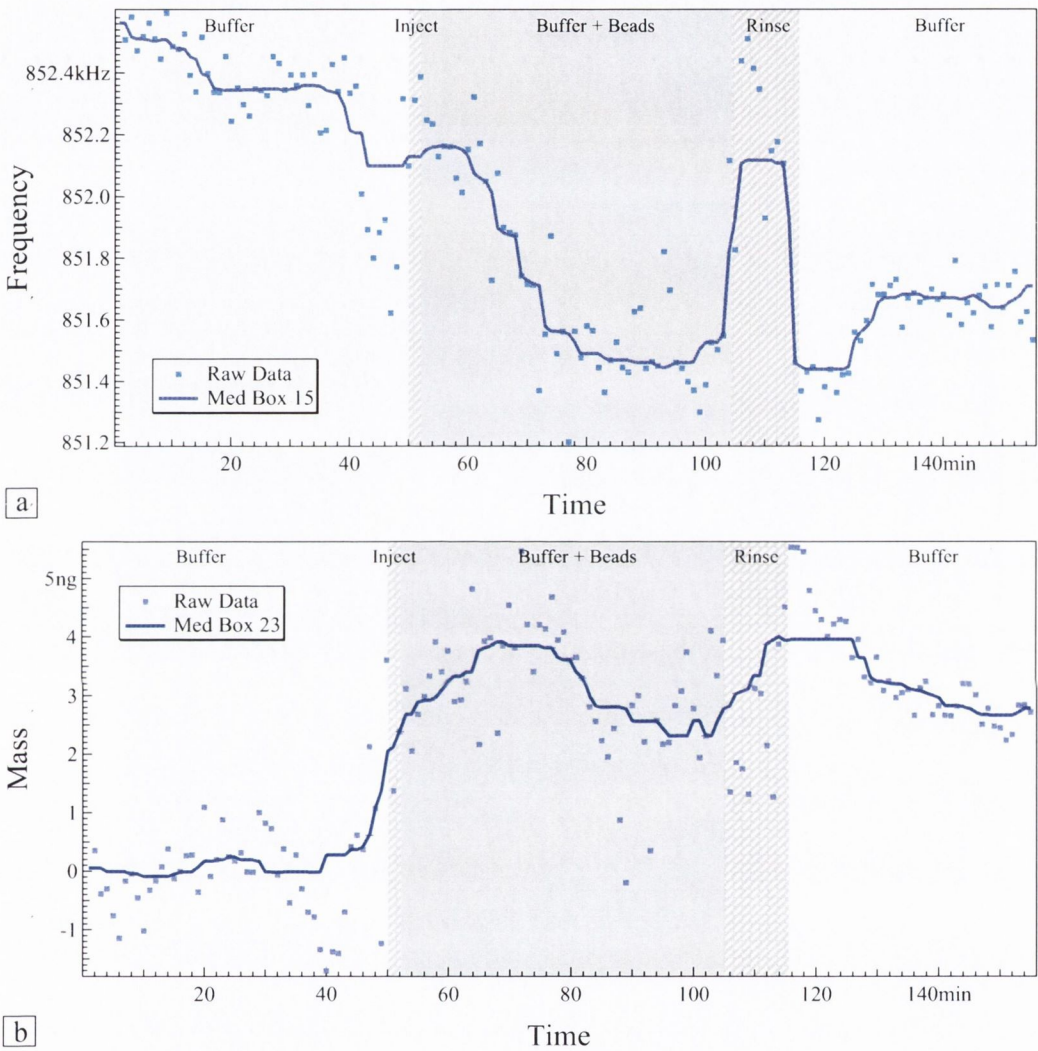


Figure 7.2. **a)** The average frequency response of the test cantilevers during the injection and binding of anti-biotin magnetic beads. There is a clear decrease of the frequency of the test cantilever upon injection of the beads. **b)** The averaged differential mass uptake on the surface of the test cantilevers. There is an average gain of 3.0 ± 0.3 ng following the stabilisation after rinsing. The scatter plot shows the data and the line corresponds to the median box filtered result. The hatched areas indicate the time during which the fluid was flowing through the chamber. The grey area indicates the time in which the beads were present in the chamber. The larger scatter in the shaded region is due to the scattering of the laser beam by the beads.

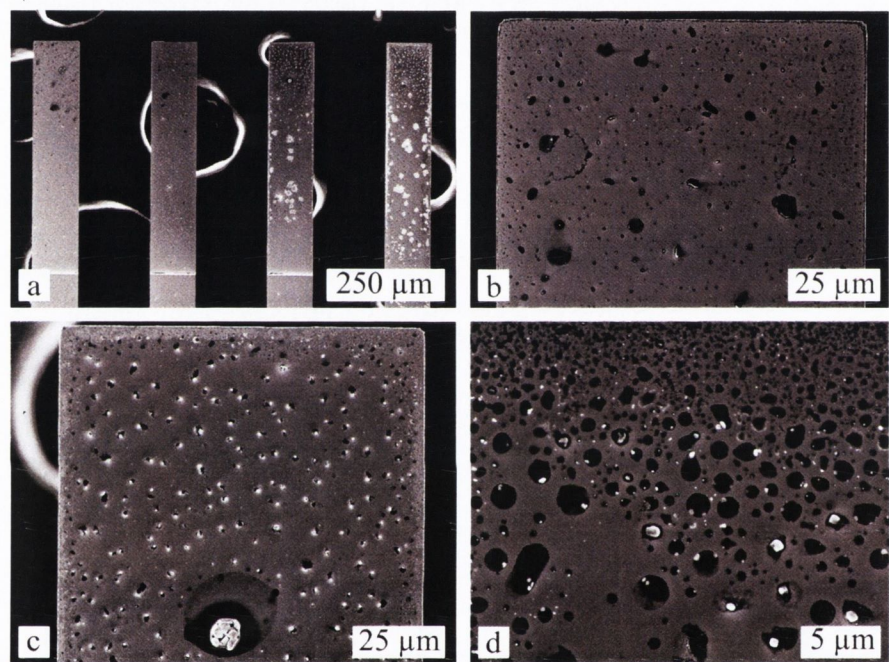


Figure 7.3. SEM images showing the binding of the anti-biotin magnetic beads preferentially to the cantilevers functionalised with the biotin SAM from a similar experiment to the data presented in Fig. 7.2. **a)** Cantilevers 5 – 8 indicating a clear preferences of the binding of the beads (white dots in the image) with cantilevers 7 and 8. **b)** A close up image of the reference cantilever number 6 showing very little binding of beads. **c)** Cantilever 7 showing a lot of beads near the tip of the cantilever. The large white object near the bottom of the image is a salt crystal. **d)** Close up on cantilever 8 showing the size of the particles is in line with the manufacturer description.

7.4 Discussion

There is a average total gain in mass of 3.0 ± 0.3 ng on the test cantilevers compared to the reference cantilevers as shown in Fig. 7.2. The beads are comprised of polystyrene with approximately 12% magnetite (Fe_3O_4). Based on the observed size of the particles being close to 1 μm in diameter there would need to be ~ 110 beads to result in the observed mass shift, which agrees within $\sim 10\%$ of what is observed on the surface of the front 100 μm of the cantilever during SEM analysis (see Fig. 7.3). There is an observed preference of the binding towards the tip of the cantilever. This could be in part due to some of the effects mentioned in Section 6.4. It is also possible that there was incomplete functionalisation of the surface of the cantilever during the capillary functionalisation step as a 1 hour functionalisation step can lead to a significant evaporation of the ethanol in the reservoir which can lead to a receding of the liquid in the capillary tubes.

The experiment presented and the SEM confirmation of binding of the anti-biotin magnetic beads to the cantilevers provides a good proof of principle for future work with a full assay incorporating magnetic beads and antibodies as a preconcentrator and mass label for the detection of inflammation antigens from solution in an ELISA-like sandwich assay with a cantilever.

References

- [1] J. Crowther, *Springer Protocols: Methods in Molecular Biology 516: The ELISA Guidebook*, 2nd ed., J. Walker, Ed. Humana Press, 2009.
- [2] B. Yoza, A. Arakaki, K. Maruyama, H. Takeyama, and T. Matsunaga, "Fully automated dna extraction from blood using magnetic particles modified with a hyperbranched polyamidoamine dendrimer," *Journal of Bioscience and Bioengineering*, vol. 95, no. 1, pp. 21–26, 2003.
- [3] T. Osaka, T. Matsunaga, T. Nakanishi, A. Arakaki, D. Niwa, and H. Iida, "Synthesis of magnetic nanoparticles and their application to bioassays," *Analytical and Bioanalytical Chemistry*, vol. 384, no. 3, pp. 593–600, 2006.
- [4] N. J. Wittenberg and C. L. Haynes, "Using nanoparticles to push the limits of detection," *Wiley Interdisciplinary Reviews: Nanomedicine and Nanobiotechnology*, vol. 1, no. 2, pp. 237–254, 2009.
- [5] J. B. Haun, T.-J. Yoon, H. Lee, and R. Weissleder, "Magnetic nanoparticle biosensors," *Wiley Interdisciplinary Reviews: Nanomedicine and Nanobiotechnology*, vol. 2, no. 3, pp. 291–304, 2010.
- [6] R. M. Lequin, "Enzyme immunoassay (EIA)/enzyme-linked immunosorbent assay (ELISA)," *Clinical Chemistry*, vol. 51, no. 12, pp. 2415–2418, 2005.

Chapter 8

Conclusions and Outlook

8.1 Conclusions

The device presented is capable of rapid and reliable readout of both the static and dynamic response of a cantilever array in a physiological liquid environment. The static-mode resolution of the device is on the order of ~ 2 nm when using a $1\text{ }\mu\text{m}$ thick cantilever. Using the dynamic mode it is possible to readout up to the 19th flexural resonance mode of a $500\text{ }\mu\text{m}$ long and $1\text{ }\mu\text{m}$ thick cantilever. The static and dynamic response of eight cantilevers can be obtained in 30 s with good signal-to-noise levels from the tip of the cantilevers and line scan analysis of the cantilevers is also possible. While the limits of detection and absolute bending measured are dependent on the particular cantilevers chosen for a particular experiment, the device presented here is easily customisable and can provide readout from virtually any 2D array of micron-scale cantilevers with little modification while providing a temperature stable environment with control over fluid flow through the chamber integrated into the user-friendly LabVIEW program.

Using the developed device it was observed that there is at least qualitative agreement with Sader's compressible fluid model for practical microcantilevers with a thickness to length ratio of $\sim 7:500$ and an aspect ratio of 5. The prediction from the scaling analysis of Van Eysden and Sader of a "coincidence point" at mode 3 for the $7\text{ }\mu\text{m}$ thick cantilever is accurate and is clearly observed in the experimental data. The lower than predicted Q factors and resonance frequencies are likely attributed to the geometry and design of the hinge portion of the cantilever. The compressible fluid model should be considered when planning experiments involving the use of higher resonant modes of relatively thick microcantilevers in air.

For the preliminary biological measurements detecting the aggregation of the protein α -synuclein it was possible to quantitatively detect aggregation in a label-free manner on the surface of a cantilever using a concentration of protein that was 50

times less than in comparable fluorescence measurements.

Using the dual-mode device it was possible to detect oligo-functionalised Au nanoparticles from solution using cantilevers functionalised with the complementary strands. It was also possible to observe the tensile stress induced by the hybridisation of biotinylated oligos on the surface of the cantilever. By injecting streptavidin-functionalised polystyrene beads the frequency shift resulting from the binding of the beads to the biotin was observed. The frequency shifts resulting from the binding of the various sized mass labels indicates a trend towards smaller frequency shifts with larger labels was discovered. The trend was explained by the motion of the larger labels away from the sensitive regions of the cantilever induced by boundary streaming on the surface of the vibrating cantilever.

Knowledge gained from the initial experiments using mass labels and oligos was applied to the detection of anti-biotin antibody-functionalised magnetic particles with an average mass uptake of 3.0 ± 0.3 ng on the surface of the cantilevers, which was confirmed with SEM analysis of the cantilever surface. This measurement represents the final step in the preparation for a full assay incorporating magnetic particles and antibodies for the detection of inflammation proteins from liquid samples using the dual mode device.

The measurements presented in this thesis represent state of the art combined-mode measurements of biological interactions measured in liquids at the limit of the microelectromechanical systems technology. The measurements at higher modes (up to the 19th mode), which require a unique design of hardware and software, are uniquely performed at the Nanobiotech lab in CRANN.

8.2 Outlook

8.2.1 Instrumentation

While the new dual-mode device is very stable, with good noise levels and fast performance there are several potential improvements which could be applied to the device or implemented in a newer version of the device. The first and perhaps most pressing improvement would be related to the fluid chamber. As previously mentioned it was not within the scope of the thesis to also develop a new fluid chamber and so the existing fluid chamber was implemented in the dual-mode device.

The existing fluid chamber works well in terms of actuation and providing clean resonance spectra. Idealised flow simulations using Comsol indicate that there is good mixing of fluids and samples within the chamber and the flow is directed uniformly across the cantilevers in the array when arrays without sidebars are used. However, the U-shaped borosilicate glass cover does not form a tight seal with the machined PEEK

body. As such it is possible for the chamber to leak during measurements. This poses a significant hindrance during stop flow experiments where it is the surface tension of the liquid which is preventing a bubble from forming in the chamber and invalidating the experiment. The fluid chamber should be redesigned to incorporate a tight seal of the glass cover to the machined body, while still maintaining the desirable design properties of the existing chamber.

The overall sensitivity and performance of the device in the dynamic mode in liquid is impressive with sub-nanogram sensitivity possible on a routine basis. In order to push the sensitivity lower, higher Q factors of the cantilevers will be necessary. There are several possible methods which could be implemented to achieve better sensitivity. The first and most obvious change could be a move towards smaller sensors as is the trend with most other nanomechanical-sensor-based devices [1], however this would introduce additional problems with unique functionalisation of the individual sensors. Another possibility would be to implement a form of noise squeezing or parametric pumping of the cantilever to potentially increase the Q factor [2].

There has been a lot of interesting work in the field of multifrequency AFM which involves the actuation of the cantilever by applying a superposition of sinusoidal signals with frequencies matching several of the resonance mode frequencies simultaneously [3]. The result is a complex vibration of the cantilever surface corresponding to several resonance modes. By applying the multifrequency actuation to the cantilever when working with the mass labels it should be possible to avoid streaming particles to areas of the cantilever that are less sensitive to mass and instead towards areas that are more sensitive. In addition by choosing the modes actuated carefully it may be possible to remove some of the less sensitive areas that would be associated with resonance at a single mode. A final advantage of this approach would be the faster recording of the response due to a linear sweep of several thousand frequencies being replaced by a single actuation signal. It should be noted that with this multifrequency approach there would be some loss of information which is due to no longer recording the full resonance spectra.

As a final outlook on the instrumentation of the device, the current software is coded in LabVIEW 8.2. A reprogramming of the device in a new version of LabVIEW could provide some small computational performance enhancements and may allow for real-time analysis of the resonance spectra.

8.2.2 Experimental

The experimental work presented in the final two chapters is the foundation for an assay which will utilise magnetic particles functionalised with antibodies in conjunction with the dual-mode device to detect proteins involved in inflammation from a liquid

sample. A collaboration has been established with the research group of Yurii Gun'ko in the School of Chemistry, Trinity College Dublin to provide magnetic nanoparticles which will have a size that is compatible with the boundary streaming effects discussed in Chapter 6. Using these particles the final experiments will be performed for the detection of Interleukin 1 and C Reactive Protein, which are two proteins that play major roles in the inflammation process in the human body [4, 5].

The reproducibility of the cantilever Au surface has a direct effect on the reproducibility of the functionalisation of the cantilever and hence the reproducibility of the experiments performed using the cantilever arrays. Early in the thesis the metal deposition was moved from using the largely manual Edwards evaporation system to the Temescal system which was automatically controlled and promised a more reproducible Au surface. In order for such a tool to provide a reproducible result it must be maintained in a suitable manner. It was found during the course of the experimental work that the batch to batch variation of the quality and thickness of the Au surface was rather large. This had a direct effect on the experimental work performed and made it difficult to achieve consistent results. A move away from metal deposition towards functionalisation schemes that are directed towards the bare silicon could prove to yield more consistent results despite using more complicated chemistry.

During the work presented there were several interesting observations about the effects of fluids on cantilever dynamics. The effect of the changing velocity of the liquid caused by the syringe pump as shown in Chapter 2 indicates a possible relation between the velocity of the fluid flowing across the surface of the cantilever and the resonance frequency of the cantilever. Further investigation into this effect would be interesting from a physics point of view.

During the investigation into the compressibility of the fluid on the cantilever resonance modes there were indications that some of the data could be used for distinguishing between, or the verification of, some other models of cantilever dynamics. With a small time investment some interesting comparisons between theory and experiment could be established.

References

- [1] J. Arlett, E. Myers, and M. Roukes, “Comparative advantages of mechanical biosensors,” *Nature Nanotechnology*, vol. 6, no. 4, pp. 203–215, 2011.
- [2] G. Prakash, A. Raman, J. Rhoads, and R. G. Reifenberger, “Parametric noise squeezing and parametric resonance of microcantilevers in air and liquid environments,” *Rev. Sci. Instrum.*, vol. 83, no. 6, pp. 065 109–12, 2012.
- [3] R. Garcia and E. T. Herruzo, “The emergence of multifrequency force microscopy,” *Nature Nanotechnology*, vol. 7, no. 4, pp. 217–226, 2012.
- [4] C. Dinarello, “Role of pro- and anti-inflammatory cytokines during inflammation: experimental and clinical findings,” *Journal of Biological Regulators and Homeostatic Agents*, vol. 11, no. 3, pp. 91–103, 1997.
- [5] A. Peisajovich, L. Marnell, C. Mold, and T. W. Du Clos, “C-reactive protein at the interface between innate immunity and inflammation,” *Expert Review of Clinical Immunology*, vol. 4, no. 3, pp. 379–390, 2008.

Appendices

Appendix A

Supplementary Information

A.1 Calculation of Phase Shift

The phase shift ϕ of the response of the cantilever as measured on the PSD (R_{PSD}) compared to the driving force applied to the cantilever (F) can be calculated as follows, assuming the frequency of the two signals is the same.

Let

$$F(t) = A_F \cos(\omega t + \phi_F) \quad (\text{A.1})$$

and

$$R_{PSD}(t) = A_{PSD} \cos(\omega t + \phi_{PSD}) \quad (\text{A.2})$$

where A_F and A_{PSD} are the amplitudes; ϕ_F and ϕ_{PSD} are the phase shifts of the signals; and ω is the frequency of the signals.

Multiplying the two signals together gives

$$F(t)R_{PSD}(t) = A_F A_{PSD} \cos(\omega t + \phi_F) \cos(\omega t + \phi_{PSD}) \quad (\text{A.3a})$$

$$= \frac{A_F A_{PSD}}{2} (\cos(2\omega t + \phi_F + \phi_{PSD}) + \cos(\phi_F - \phi_{PSD})) \quad (\text{A.3b})$$

and by low-pass filtering (averaging) the high frequency term is removed and thus

$$\text{Mean}[F(t)R_{PSD}(t)] = \frac{A_F A_{PSD}}{2} \cos(\phi_F - \phi_{PSD}) \quad (\text{A.4})$$

where $\phi = \phi_F - \phi_{PSD}$, and so

$$\phi = \arccos\left(\frac{2 \text{Mean}[F(t)R_{PSD}(t)]}{A_F A_{PSD}}\right). \quad (\text{A.5})$$

A.2 f vs n for Example Spectrum

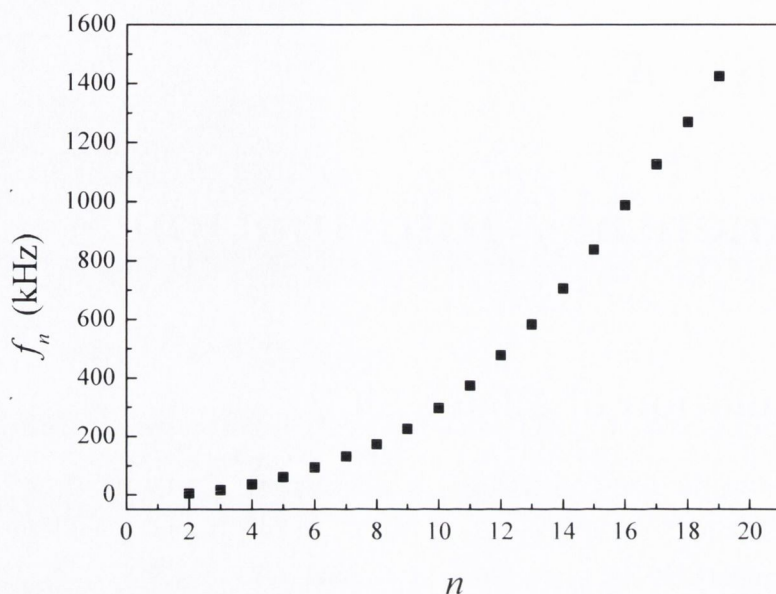


Figure A.1. The frequency, f_n , vs. mode number, n , for modes 2 to 19 in the example spectrum. There is a clear $\sim n^2$ dependence of the frequency which indicates that the modes measured are the flexural modes of resonance and that no torsional modes are observed in the spectrum.

The resonance frequencies of the modes in Fig. 2.19 when plotted against the mode number n display an $\sim n^2$ dependence, as shown in Fig. A.1, which indicates that they are the flexural modes of resonance of the cantilever.

As can be observed from Eq. 1.16 the eigenfrequency of mode n of a cantilever with a distributed mass in the absence of damping, f_{0n} , is proportional to $(n - 0.5)^2$. The flexural resonance frequency obtained from the resonance peak, f_n , can be obtained from f_{0n} by Eq. 1.17.

Thus, a plot of f_n^2 vs. $(n - 0.5)^4$ should yield a straight line. As shown in Fig. A.2 there is a good agreement between the linear fit and the data. There is a slight deviation of the data from the fit due to the fact that the mass of co-moved liquid m_l , upon which f_{0n} and γ both depend, also varies as a function of n as discussed in Section 1.3.3 and reference [2].

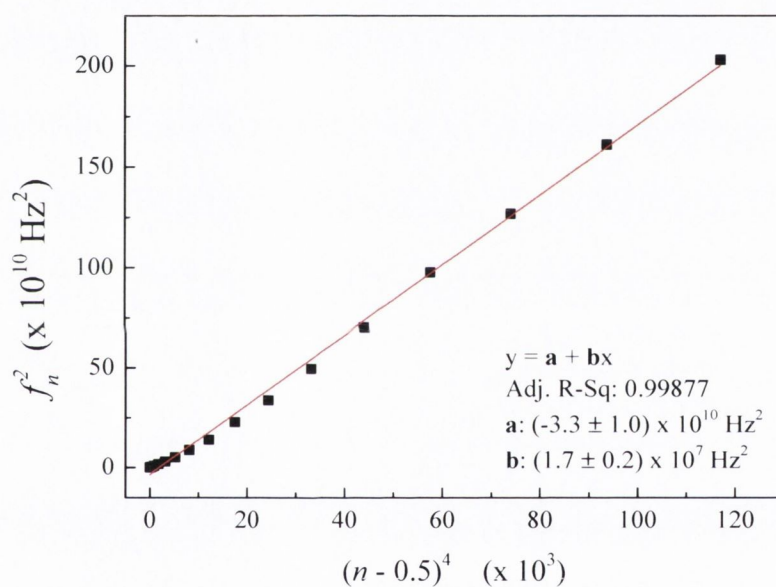


Figure A.2. The frequency, f_n , vs. $(n-0.5)^4$, for modes 2 to 19 in the example spectrum. There is a good agreement between the linear fit and the data, despite the dependence of the mass of co-moved liquid, m_l , also depending on n . This dependence is responsible for the observed slight deviation of the data from a linear trend.

A.3 Heat Pulse

Supplementary graphs showing the individual response of each of the eight cantilever to the heat pulse are contained in this appendix. Fig. A.3 shows the static response of the individual cantilevers to the heat pulse. Cantilever three exhibits a larger response than the rest of the array. During an experiment the heat pulse is used as a calibration technique and the bending response of all eight cantilevers is normalised to the average of the eight.

Fig. A.4 shows the frequency response of the eight cantilevers to the heat pulse. There is around 2% variation in the starting resonance frequency of mode 8 of the cantilevers, which reduces to 0.6% for mode 10. Some of the cantilevers exhibit a larger frequency shift during the pulse, however the trend of the response of the eight cantilevers is similar for each mode. As expected the higher the mode, the larger the frequency shift for each cantilever. Again, normalisation of the response of the cantilevers can be applied if necessary.

Fig. A.5 shows the change in co-moved mass of the cantilevers in the array as calculated by NOSEtools [3]. An average change of $\sim 6.0 \pm 0.5$ ng is observed. It should be noted that this analysis assumes that the spring constant of the cantilever remains unchanged during the experiment, which may not be true [4, 5].

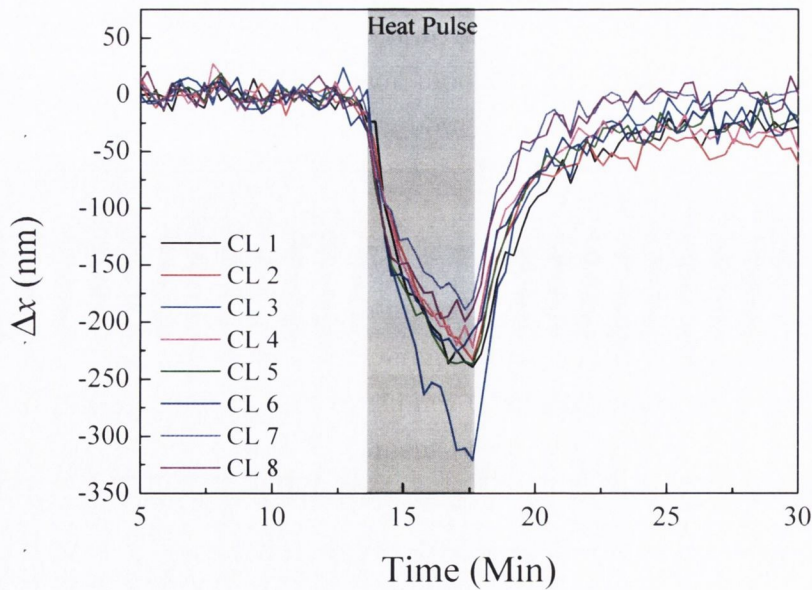


Figure A.3. Individual static bending response of the eight cantilevers in the array to the heat pulse. Cantilever three shows a significantly larger response to the heat pulse than the cantilevers in the rest of the array, with the rest of the cantilevers bunching within 40 nm of each other at their maximum deflection.

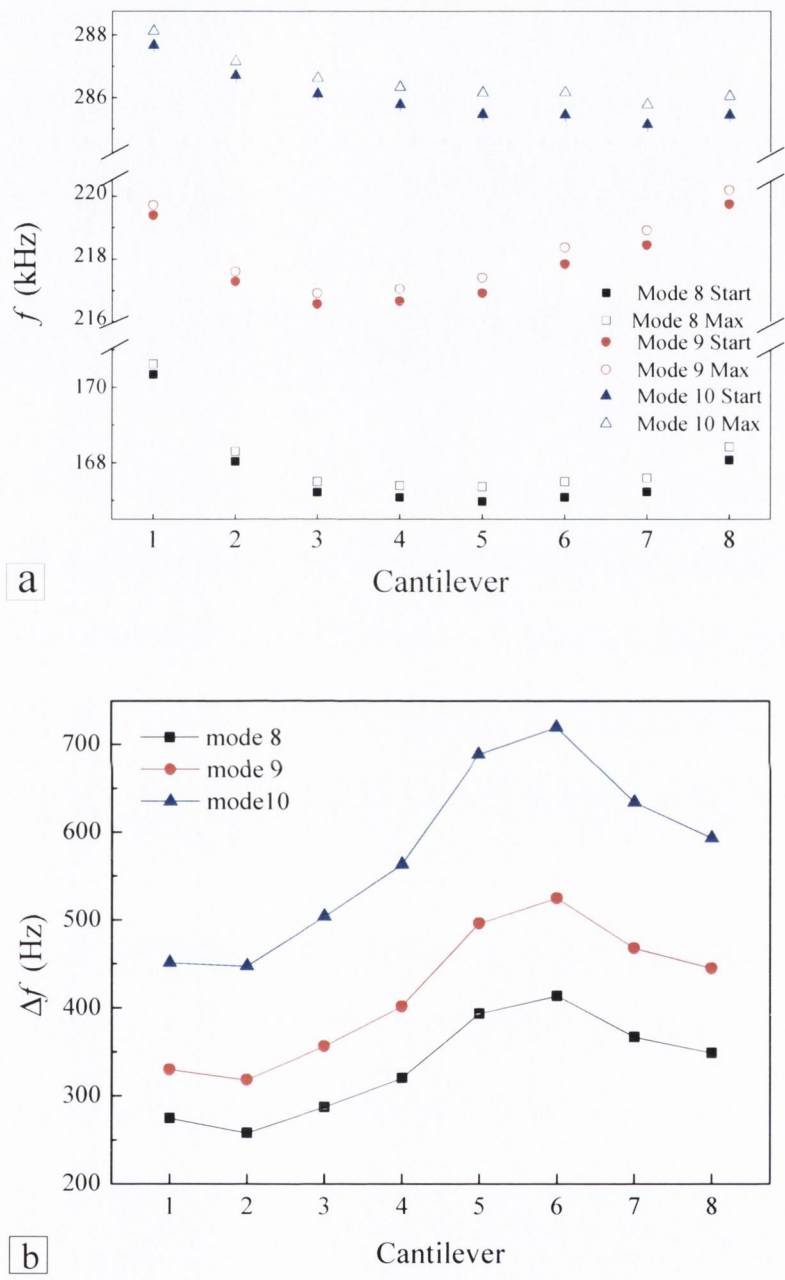


Figure A.4. The frequency response of modes 8, 9, and 10 to the heat pulse. **a)** Start frequency and maximum frequency for each of the eight cantilevers in the array for the three modes. There is a small variation in the start frequency of each of the cantilevers, around 2% for mode 8 reducing to 0.6% for mode 10. **b)** Maximum frequency change of the resonance modes for each of the cantilevers in the array. Some of the cantilevers exhibit a larger response to the heat pulse, however the trend of the magnitude of the response of the eight cantilevers is similar for each mode. The joining lines are intended as a guide for the eye only.

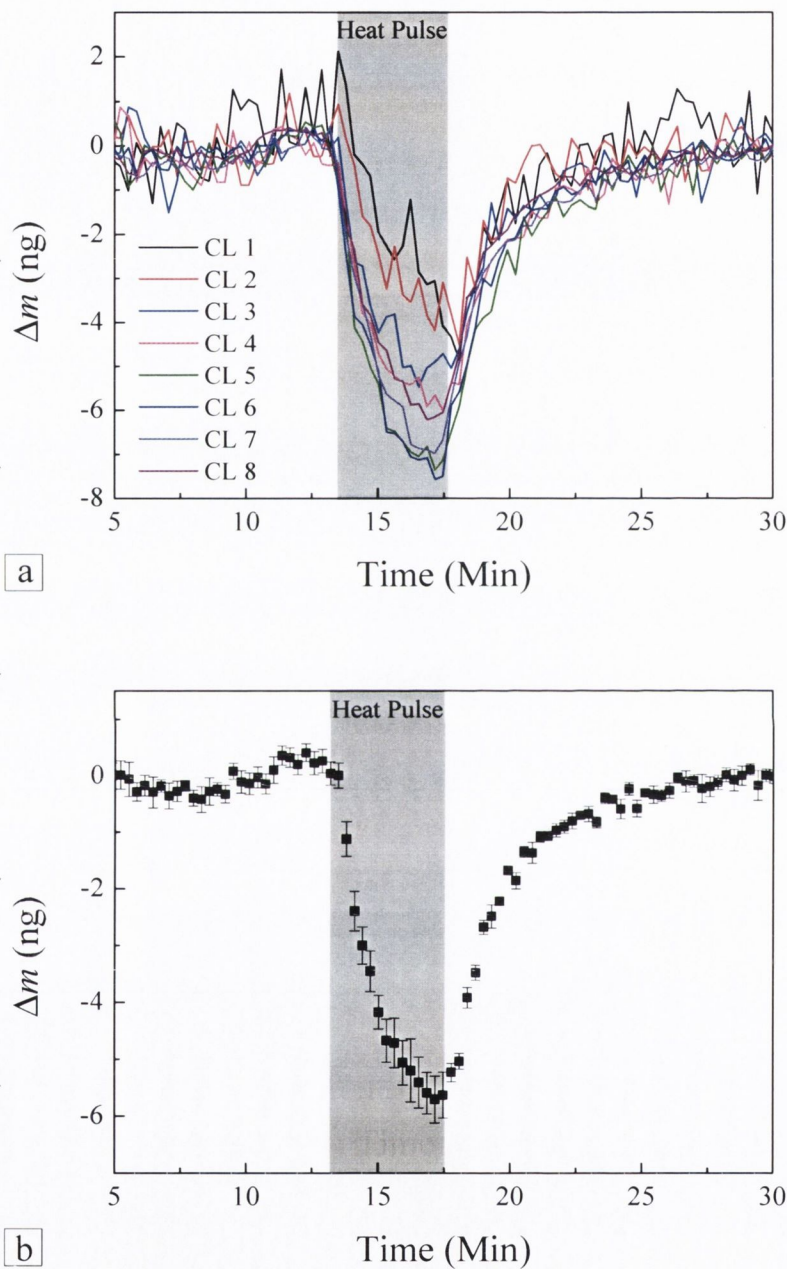


Figure A.5. The change in co-moved mass during the heat pulse as calculated by NOSEtools [3]. **a)** The change in mass for the individual cantilevers. The average noise in the experiment is < 1 ng for most of the cantilevers, with cantilevers 1 and 2 being more noisy. **b)** The mean response of the eight cantilevers to the heat pulse shows an average change in mass of $\sim 6.0 \pm 0.5$ ng. The error bars correspond to the standard error of the mean of the eight samples.

A.4 Protein Aggregation Cantilever Measurements

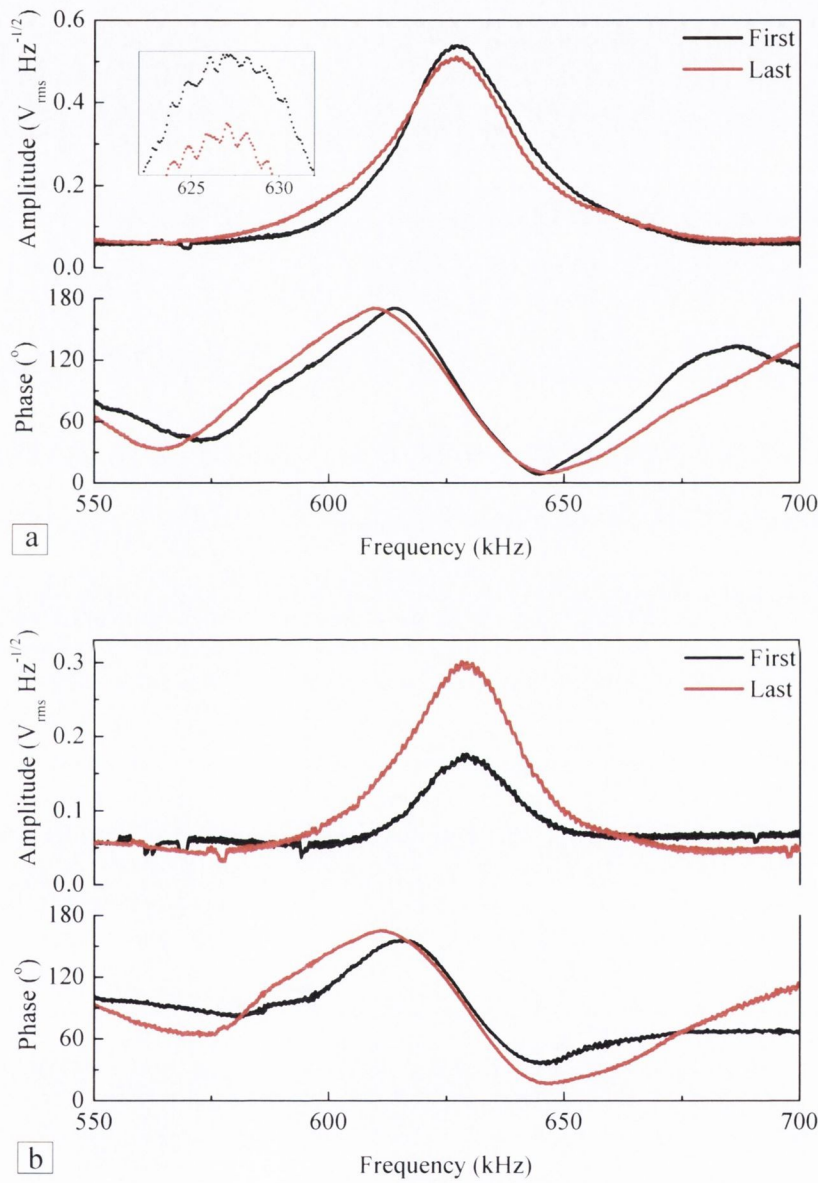


Figure A.6. The amplitude and phase spectra for the 14th flexural resonance mode for **a)** the test cantilever functionalised with α -synuclein and **b)** the reference cantilever functionalised with an OH SAM. The black spectra correspond to the first measurement and the red spectra correspond to the last measurement. The inset in a) shows the small frequency change in the resonance frequency of the test cantilever.

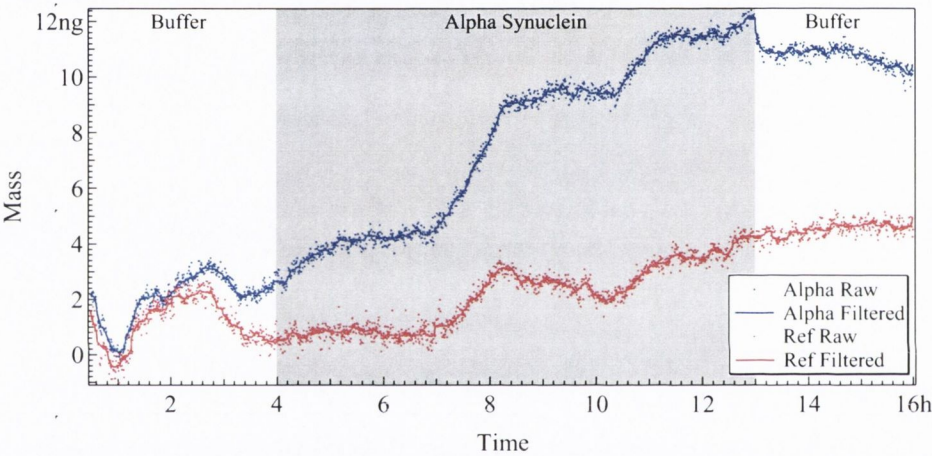


Figure A.7. Graph of bound mass on the surface of the cantilever vs. time. The frequency spectra recorded during the experiment were post processed using NOSEtools software to obtain the resulting plot of bound mass vs. time. The blue plots show the data from the cantilever functionalised with α -synuclein monomers and the red plots show the data from the OH-functionalised reference cantilever. The scatter plots show the raw data and the line corresponds to the median box filtered data (box size 23). The grey area indicates the period that 10 $\mu\text{g}/\text{ml}$ α -synuclein in 20 mM sodium phosphate buffer was flowing through the fluidic chamber at a rate of 3.3 $\mu\text{l}/\text{min}$.

A.5 Oligo-Functionalised Au Nanoparticles Measurements

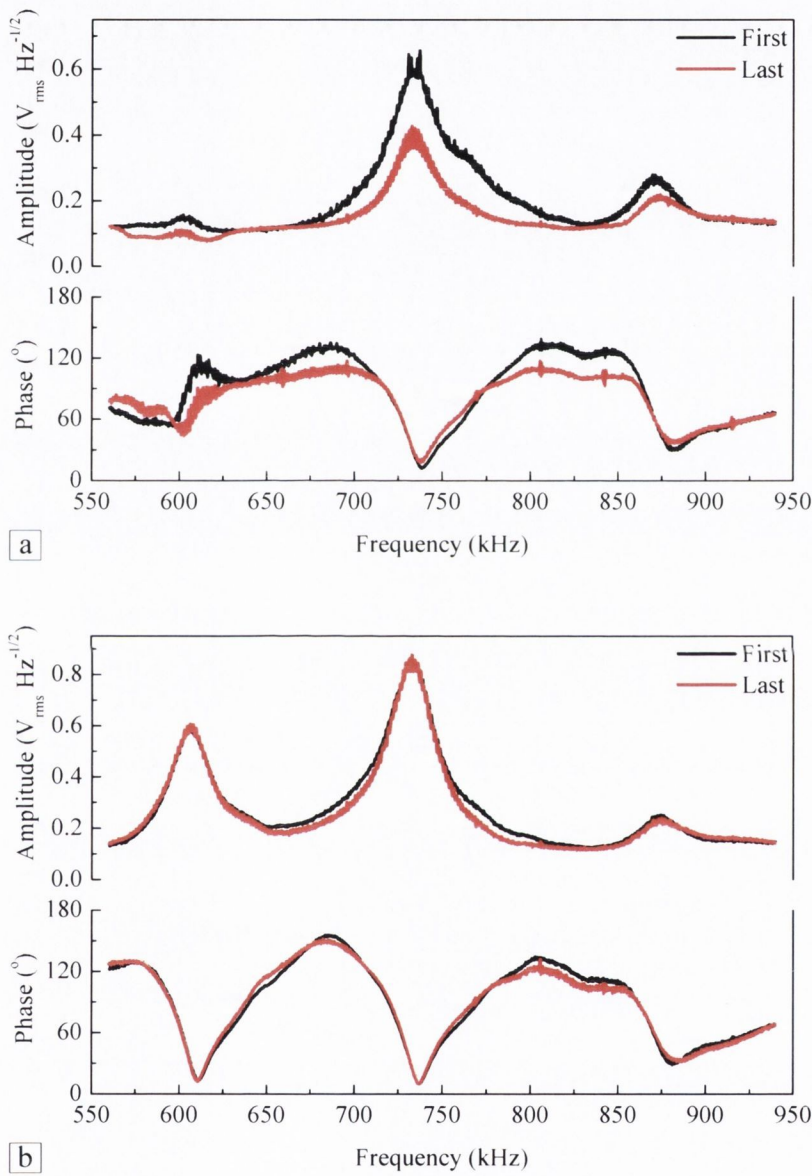


Figure A.8. The amplitude and phase spectra for the 14–16th flexural resonance modes for **a)** the test cantilever functionalised with the complementary strand # 930353 and **b)** the reference cantilever functionalised with an unspecific 12 mer. The black spectra correspond to the first measurement and the red spectra correspond to the last measurement.

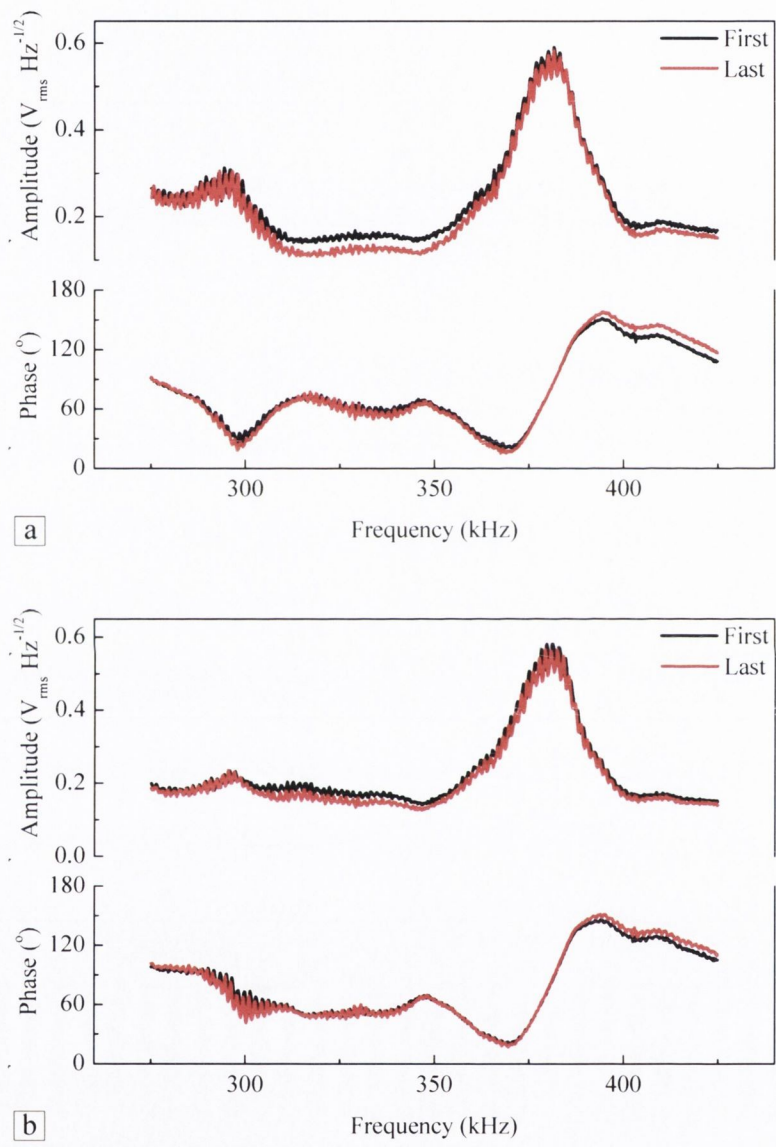


Figure A.9. The amplitude and phase spectra for the 10th and 11th flexural resonance modes for **a)** the test cantilever functionalised with the complementary strand # 930352 and **b)** the reference cantilever functionalised with Unspec12. The black spectra correspond to the first measurement and the red spectra correspond to the last measurement.

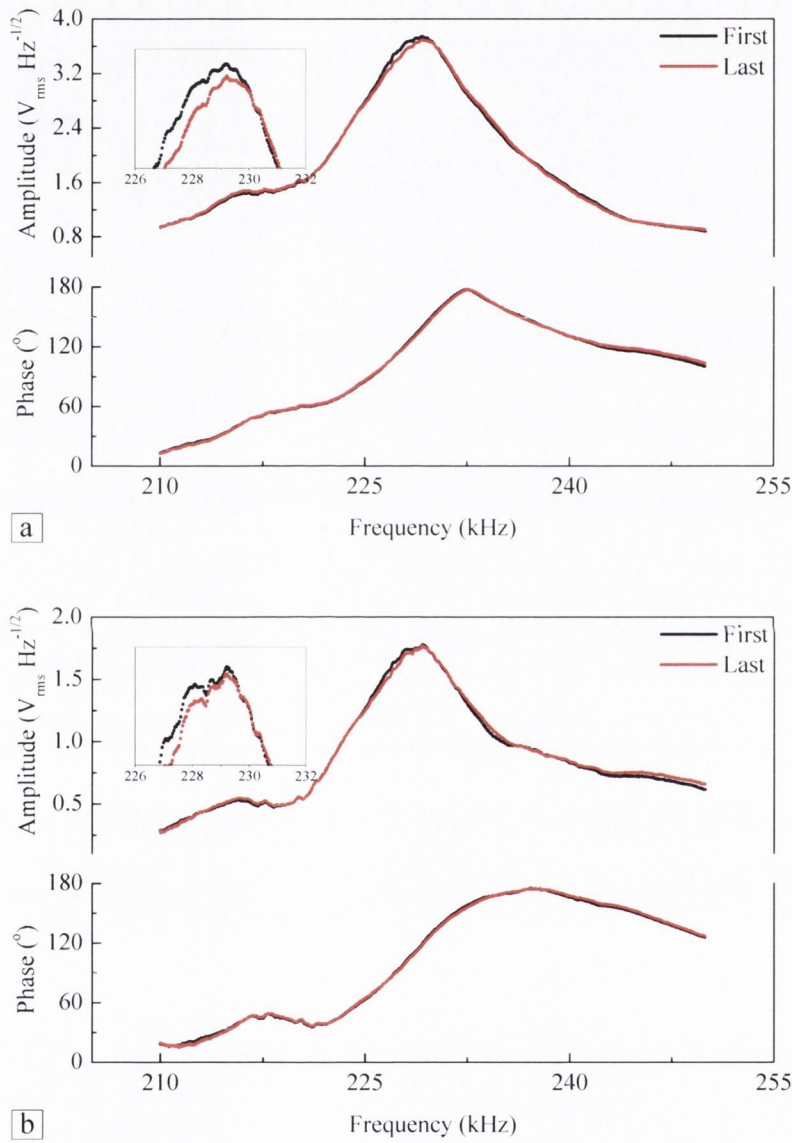


Figure A.10. The amplitude and phase spectra for the 9th flexural resonance mode for **a)** a test cantilever functionalised with the complementary strand # 930353 and **b)** the reference cantilever functionalised with Unspec12. The black spectra correspond to the first measurement and the red spectra correspond to the last measurement.

A.6 Dulbecco's PBS

Dulbecco's phosphate-buffered saline (DPBS) is a variation of PBS first described by Dulbecco in 1954 [6] which is typically used in a range of cell culturing applications. The DPBS used in the oligonucleotide experiments is obtained from Gibco (®) and contains additional calcium and magnesium which improves the bending signal obtained during hybridisation of the two oligonucleotide strands. The formulation of the buffer is given in Table A.1 [7].

Table A.1. The formulation of Gibco (®) DPBS as described in Reference [7].

| Inorganic Salts | Molecular Weight | Conc. mg/L | Conc. mM |
|---|------------------|---------------|-------------|
| Calcium Chloride (CaCl ₂) | 111 | 100 | 0.901 |
| Magnesium Chloride (MgCl ₂ –6H ₂ O) | 203 | 100 | 0.493 |
| Potassium Chloride (KCl) | 75 | 200 | 2.67 |
| Potassium Phosphate monobasic (KH ₂ PO ₄) | 136 | 200 | 1.47 |
| Sodium Chloride (NaCl) | 58 | 8000 | 137.93 |
| Sodium Phosphate dibasic (Na ₂ HPO ₄ –7H ₂ O) | 268 | 2160 | 8.06 |

A.7 SEM Images of Au Nanoparticles on Cantilever Surface

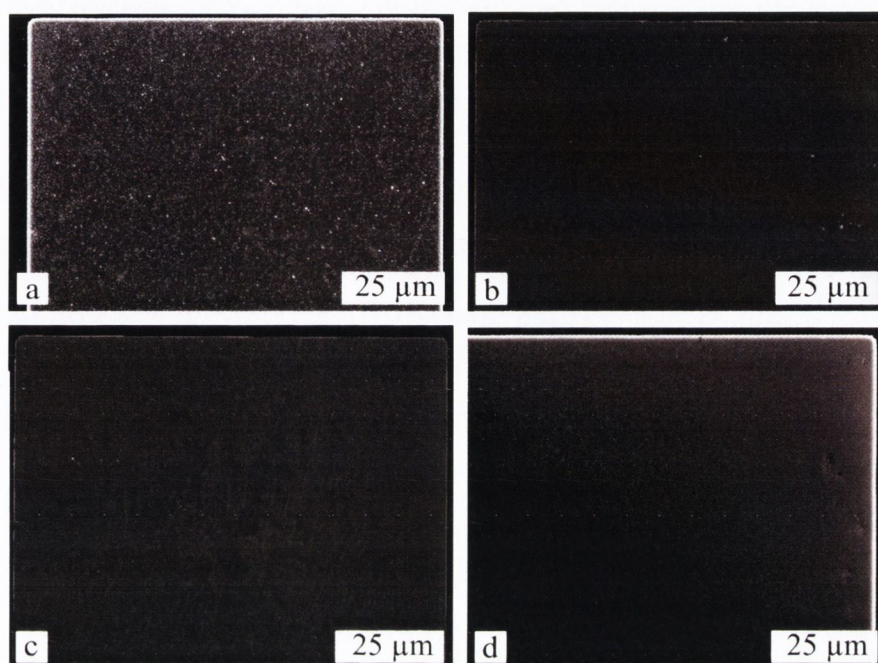


Figure A.11. SEM images showing the binding of the oligo-functionalised Au NPs preferentially to the cantilevers functionalised with the complementary oligo strand (faint white dots in the images). The number of NPs bound to the surface of the functionalised cantilevers was lower than expected due to the decreased melting temperature of the oligo hybridisation in the lower salt concentration buffer. **a)** Unfunctionalised Au NPs unspecifically bound to surface of bare Au coated cantilever. **b)** BioB2-functionalised Au NPs bound to BioB2c-functionalised Au coated cantilever surface. **c)** BioB3-functionalised Au NPs bound to BioB3c-functionalised Au coated cantilever surface. **d)** BioB4-functionalised Au NPs bound to BioB4c-functionalised Au coated cantilever surface.

A.8 Heat Pulse for Calibration of Static-Mode Oligo Hybridisation Test

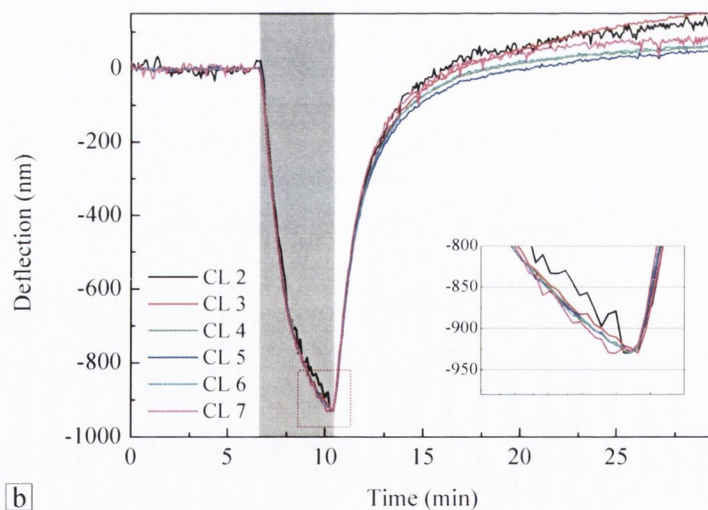
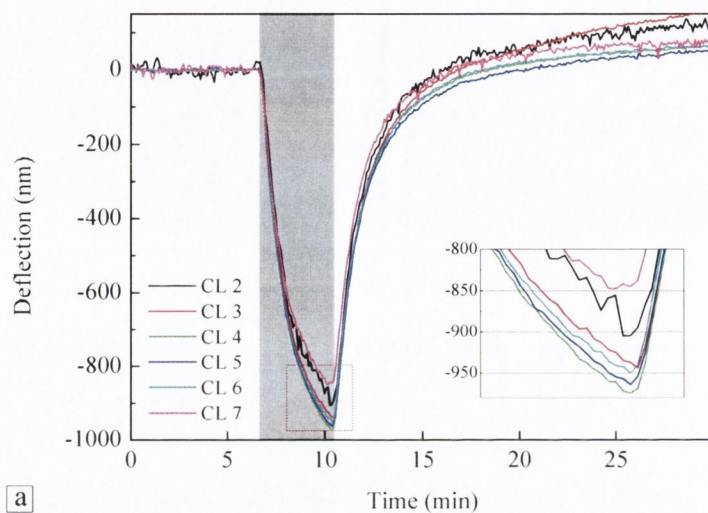


Figure A.12. **a)** The baseline corrected change in deflection of six cantilevers. There is a difference of ~ 120 nm between the total deflection of the cantilevers as shown in the inset. **b)** The response of the cantilevers is calibrated by scaling the response of each of the cantilevers to the mean of their maximum deflection using NOSEtools [3]. The grey area corresponds to the time when the heat pulse is being applied to the chamber.

A.9 Biotinylated Oligos with Streptavidin Beads

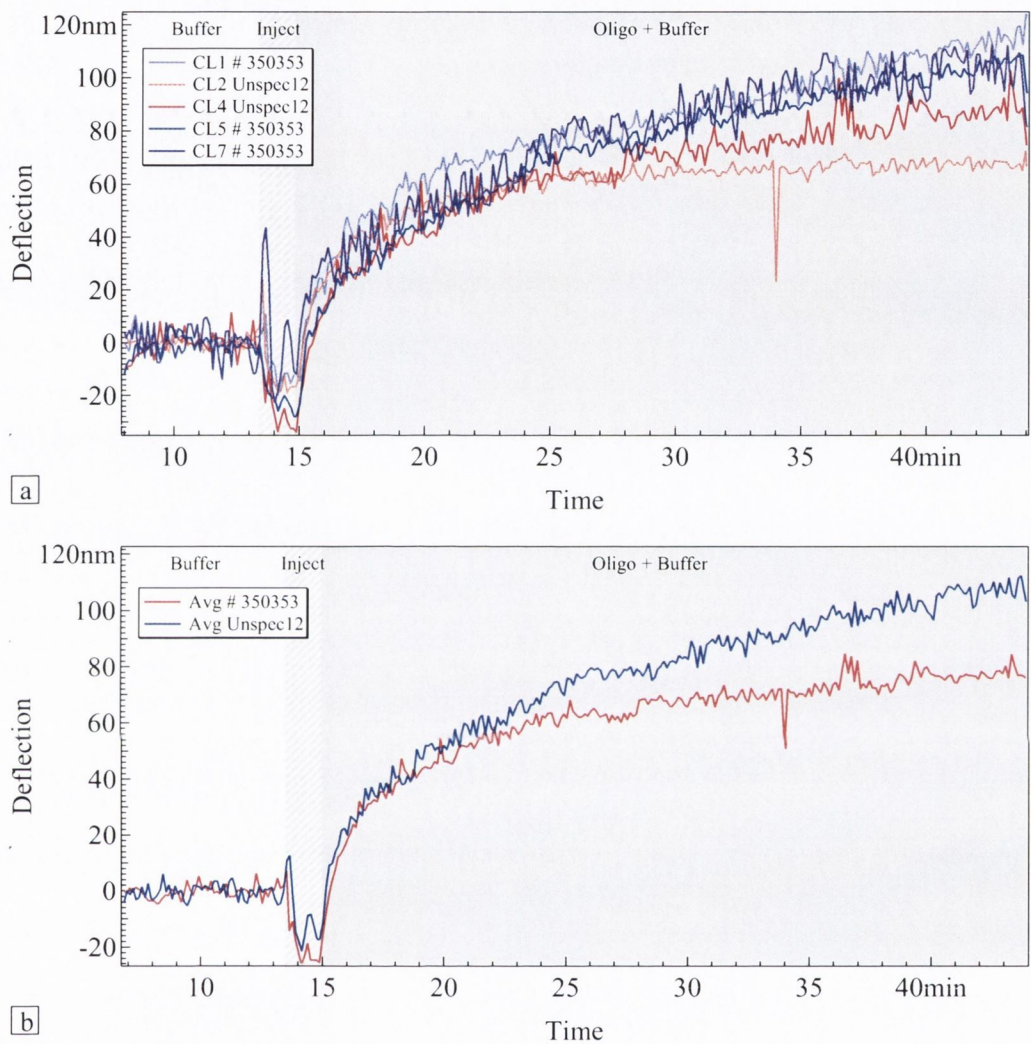


Figure A.13. **a)** The calibrated and baseline corrected data from the injection of 20 nM oligo #1234760. The test cantilevers functionalised with oligo #350353 are shown in shades of blue and the reference cantilevers functionalised with Unspec12 are shown in shades of red. **b)** The averaged response of the test and reference cantilevers. The hatched area corresponds to the time when the liquid was flowing through the chamber for the injection of the biotinylated oligos and the shaded area corresponds to the time when the biotinylated oligos were present in the chamber.

References

- [1] T. Braun, V. Barwich, M. Ghatkesar, A. Bredekamp, C. Gerber, M. Hegner, and H. Lang, "Micromechanical mass sensors for biomolecular detection in a physiological environment," *Physical Review E*, vol. 72, no. 031907, p. 031907, 2005.
- [2] M. K. Ghatkesar, T. Braun, V. Barwich, C. Gerber, M. Hegner, and H.-P. Lang, "Resonating modes of vibrating microcantilevers in liquid," *Applied Physics Letters*, vol. 92, p. 043106, 2008.
- [3] T. Braun, "Nose tools homepage," accessed 1st Mar 2010, NOSEtools Version 7.2 (rev 438) is available to download free from the NOSEtools Homepage. The software is copyrighted by Thomas Braun 2008, 2009, University of Basel, Switzerland. [Online]. Available: <http://web.me.com/brunobraun/NOSEtools/Home.html>
- [4] M. J. Lachut and J. E. Sader, "Effect of surface stress on the stiffness of cantilever plates," *Physical Review Letters*, vol. 99, no. 20, p. 085440, 2007.
- [5] M. J. Lachut and J. E. Sader, "Effect of surface stress on the stiffness of thin elastic plates and beams," *Physical Review B*, vol. 85, no. 8, pp. 085440–, 2012.
- [6] R. Dulbecco and M. Vogt, "Plaque formation and isolation of pure lines with poliomyelitis viruses," *The Journal of Experimental Medicine*, vol. 99, no. 2, pp. 167–182, 1954.
- [7] Technical resources - media formulations. Invitrogen. [Online]. Available: http://www.invitrogen.com/site/us/en/home/support/Product-Technical-Resources/media_formulation.144.html

Appendix B

Protocols

B.1 Piranha Cleaning of Cantilever Arrays

This protocol is used for the cleaning of the cantilever arrays prior to metal deposition. Piranha cleaning removes organic contaminants from the surface of the cantilevers and leaves them hydrophilic.

Precautions Extreme care must be taken when working with piranha solution and full PPE including face shield, lab coat, and suitable gloves must be worn. The piranha solutions should be prepared in minimal amounts and all work should be performed in a fume hood due to gasses produced by the solution. Due to its violent reaction upon contact with organic materials, and the high temperatures reached during reactions ($>100\text{ }^{\circ}\text{C}$), piranha solution should not be stored. It should always be prepared fresh before use and disposed of in an appropriate manner immediately after use to avoid risk of explosion.

Materials

- Sulphuric Acid (H_2SO_4), 99.99%
- Hydrogen Peroxide (H_2O_2), 30%
- RBS detergent solution, 2% in nanopure water
- Sodium Chloride (NaCl), 1 M
- Ethanol ($\text{C}_2\text{H}_6\text{O}$), HPLC Grade
- Isopropanol ($\text{C}_3\text{H}_8\text{O}$), HPLC Grade
- Nanopure water, 18 M Ω
- Teflon beakers and teflon coated tweezers

- Large beaker of water (e.g. 2 L) for quenching solution after use

Method

1. Preclean:

Wash array in 2% RBS detergent solution for 2 minutes.

Rinse in 1 M NaCl for 30 seconds.

Rinse in nanopure water for 30 seconds.

2. Bath 1:

Prepare 5-10 ml piranha solution ($\text{H}_2\text{SO}_4:\text{H}_2\text{O}_2 = 1:1$) by slowly adding the H_2O_2 to the H_2SO_4 .

Dip the cantilever array in the piranha solution for 30 seconds.

Rinse in 1 M NaCl for 30 seconds.

Rinse in nanopure water for 30 seconds.

3. Bath 2:

Prepare 5-10 ml piranha solution.

Bathe in piranha solution for 20 minutes.

Bathe in 1 M NaCl for 5 minutes.

Bathe in ethanol/nanopure water ($\text{C}_2\text{H}_6\text{O}:\text{H}_2\text{O} = 1:1$) for 5 minutes.

Rinse in nanopure water for 30 seconds.

4. Bath 3:

Prepare 5-10 ml piranha solution.

Bathe in piranha solution for 10 minutes.

Bathe in 1 M NaCl for 5 minutes.

2 × Bathe in ethanol/nanopure water ($\text{C}_2\text{H}_6\text{O}:\text{H}_2\text{O} = 1:1$) for 5 minutes.

Bathe in isopropanol for 2 minutes.

5. Dry on filter paper and store in vacuum.

Note If adequate rinsing is not performed after the RBS detergent wash and the NaCl rinse steps residue may be left on the cantilever surface. These steps can be omitted from the protocol if desired and a clean cantilever surface will still be obtained.

B.2 Plasma Cleaning of Cantilever Arrays

This protocol is designed to clean the cantilever surface prior to metal deposition. Plasma cleaning removes organic contaminants from the surface of the cantilever arrays. The plasma cleaning is performed in a Diener PICO Barrel Asher (Diener Electronic GmbH & Co. KG, Nagolder Str. 61, D-72224 Ebhausen, Germany). The Ti/Au deposition should be performed immediately after the plasma cleaning.

Materials

- Acetone ($\text{C}_3\text{H}_6\text{O}$), HPLC Grade
- Ethanol ($\text{C}_2\text{H}_6\text{O}$), HPLC Grade

Method

1. Bathe in HPLC grade acetone (Sigma-Aldrich) (minimum of 15 min). Dry on filter paper.
2. 5 minute exposure to O_2 plasma, O_2 at 0.3 mbar, 160 W, 40 kHz.
3. Bathe in HPLC grade ethanol (2 min).

B.3 UV Cleaning of Cantilever Arrays

This protocol is used to regenerate the surface of the Ti/Au-coated cantilever arrays prior to functionalisation. The UV/ozone cleaning is performed using a Boekel UV Cleaner (UV Clean 135500, Boekel, 855 Pennsylvania Blvd, Feasterville, PA. 1905, USA).

Materials

- Ethanol ($\text{C}_2\text{H}_6\text{O}$), HPLC Grade

Method

1. 5 minute exposure to UV in air.
2. 5 minute bath in HPLC grade ethanol.
3. Dry on filter paper.

B.4 PEG Silane Functionalisation

This protocol is used to coat the bare silicon cantilever array with PEG prior to metal deposition on one side only. The PEG prevents unspecific binding of material to the bare silicon surface during measurements.

Materials

- 4,900 μl Ethanol ($\text{C}_2\text{H}_6\text{O}$), HPLC Grade
- 50 μl Hunig's Base (N-Ethyldiisopropylamine) ($\text{C}_8\text{H}_{19}\text{N}$) (Fluka)
- 50 μl (Hydroxy(polyethyleneoxy)propyl)triethoxy silane (8-12 EO) (ABCR GmbH & Co. KG)

Method

1. Mix the materials in a 10 ml beaker and carefully place the clean bare silicon cantilever array inside.
2. Leave on shaker at 150 RPM for 2 hours.

B.5 Oligonucleotide Preparation

This protocol is designed to remove dithiothreitol (DTT) ($C_4H_{10}O_2S_2$) from the thiolated oligo solutions obtained from Microsynth. DTT is used a protective agent with thiolated DNA to prevent dimerisation of the terminal sulphur atoms in the presence of oxygen [1]. The DTT is removed from the solution by a series of extractions using diethylether which is very weakly soluble in water and is less dense and so form a layer above the water after mixing. The DTT is soluble in the diethylether and is thus removed with the diethylether.

Materials

- Thiolated oligonucleotide solution protected with DTT (1 μ M)
- Diethylether ($(C_2H_5)_2O$)
- Nanopure H_2O

Method

1. Depending on the final concentration of oligonucleotide required, mix the oligo solution with the nanopure H_2O to obtain 100 μ l total volume in a 1 ml eppendorf tube.
2. Add 500 μ l of diethylether and shake.
3. Allow the solution to separate into two layers (the diethylether will be on top) and then carefully pipette the diethylether out.
4. Repeat the previous two steps 5 times.
5. After the last extraction ensure that all of the diethylether is removed from the eppendorf by removing the bottom layer (containing the oligos) using a pipette and place in a new eppendorf tube.
6. Place in SpeedVac on low setting for 10 minutes.
7. Measure concentration in Nanodrop and resuspend in buffer if required. Aliquot as necessary. Store at $-20\text{ }^{\circ}\text{C}$.

B.6 Functionalised Au Nanoparticle Buffer Transfer Protocol

This protocol is based on a protocol recommended by Particular GmbH for the addition of salt to their oligo-functionalised Au nanoparticles. The aim is to transfer the nanoparticles from water to a buffer. The final buffer required is 10 mM sodium phosphate and 150 mM NaCl. After each step the solution should be mixed fully and placed on a linear shaker at 275 RPM while incubating. The centrifuge speed depends on the size of the nanoparticles used. The speed stated is for 12 nm diameter nanoparticles.

Materials

- Oligonucleotide-functionalised Au nanoparticles
- 100 mM sodium phosphate buffer, pH 7.4 ($\text{NaH}_2\text{PO}_4/\text{Na}_2\text{HPO}_4$)
- 2 M NaCl
- 10 mM sodium phosphate, 150 mM NaCl buffer

Method

1. For a 400 μl starting volume of functionalised nanoparticles in water, add 44.4 μl 100 mM sodium phosphate buffer to raise the concentration to 10 mM. Mix and place on linear shaker for 24 hrs.
2. Add 5.6 μl 2 M NaCl to raise the NaCl concentration to 25 mM. Mix and leave on shaker for 3 hrs.
3. Add 5.7 μl 2 M NaCl to raise the NaCl concentration to 50 mM. Mix and leave on shaker for 13 hrs.
4. Repeat the above two steps twice adding 5.8, 5.85, 5.9 and 6.0 μl of 2 M NaCl each time to raise the concentration of NaCl to 150 mM total. The total time for all steps is 72 hrs.
5. Centrifuge at 14,000 g for 15 mins, replace buffer and resuspend. Store at 4 °C.

Note A glass vial (e.g. 1 ml) should be used for the buffer transfer protocol salt addition steps. When normal or low binding eppendorf plastic tubes were used a lot of binding of the nanoparticles to the walls of the tubes occurred. After each additional step the colour of the suspension would fade and more binding to the walls

was observed. Losses when using the plastic tubes were too high (around 90%) to provide useful samples.

B.7 Au Nanoparticle-DNA Conjugation

This protocol is based on the Mirkin protocol [2, 3] for conjugating thiolated oligos with Au nanoparticles which is presented in a longer form in Current Protocols in Nucleic Acid Chemistry [4].

Materials

- Thiolated oligonucleotide 1 mM dissolved in water
- Au Nanoparticle Colloid, 50 nm Diameter (BBI Life Sciences)
- 2 M NaCl
- 100 mM sodium phosphate buffer, pH 7 (0.0584 % w/v NaH_2PO_4 , 0.1547 % w/v Na_2HPO_4)
- 10 mM sodium phosphate/100 mM NaCl buffer, pH 7

Method

1. Calculate number of moles of oligo needed for functionalisation using the following formula [4]

$$\text{Number of Moles} = 4\pi r^2 \times c_n \times 35 \text{ pmol/cm}^2 \times V \quad (\text{B.1})$$

where r is the radius of the nanoparticles (25 nm), c_n is the concentration of the nanoparticles ($4.5 \times 10^{10} \text{ ml}^{-1}$), and V is the volume of nanoparticles in litres. Using the above formula gives 0.12 nmol of oligos for 1 ml of nanoparticles.

2. Add 1.5 times the number of moles calculated to the solution of Au nanoparticles.
3. Leave for 16 hrs on a linear shaker at 75 RPM in a covered glass vial.
4. Add 2 M NaCl and 100 mM sodium phosphate buffer to bring the final concentration to 10 mM sodium phosphate and 100 mM NaCl. Split the addition into 5 steps separated by 1 hour covered on the shaker at 75 RPM. The salt addition steps follow the protocol presented in B.6, but at a reduced waiting time.
5. After the final salt addition leave the suspension covered on linear shaker for 24 hours at 75 RPM.
6. Split into 200 μl batches and centrifuge at 4000 g for 15 minutes to obtain a crimson oil at bottom of tube.

7. Resuspend in 10 mM sodium phosphate/100 mM NaCl buffer.
8. Repeat centrifugation and resuspension 5 times.
9. Store at 4 °C.

Note It was found that during the addition of salt to the nanoparticle/oligo conjugate suspension that the colour of the solution became paler with each additional step, eventually resulting in the majority of the nanoparticles becoming irreversibly coagulated at the bottom of the tube. Decreasing the size of the increase of salt concentration step and increasing the incubation time did not fix this problem. The larger nanoparticle/oligo conjugates appear to be unstable at the higher salt concentration. Finally the addition of the 100 mM NaCl was removed from the protocol (i.e. conjugates suspended in 10 mM sodium phosphate only) which resulted in a better yield of nanoparticle/oligo conjugates.

B.8 Antibody Binding to Protein G Magnetic Beads

This protocol is designed to bind the Fc region of the antibodies to the protein G on the surface of the magnetic beads. The antibodies are then then cross linked to the beads in the second half of the protocol to improve the strength of the bond between the antibody and the beads.

Materials

- 0.05 M Sodium Tetraborate ($\text{B}_4\text{Na}_2\text{O}_7$) pH 8.2
- 0.1 M Ethanolamine ($\text{C}_2\text{H}_7\text{NO}$) pH 8.2
- 0.2 M Triethanolamine ($\text{C}_6\text{H}_{15}\text{NO}_3\text{HCl}$) pH 8.2
- 0.1 M Glycine ($\text{C}_2\text{H}_5\text{NO}_2$) pH 2.8
- PBS 1X pH 7.4
- Protein G magnetic beads: 1 - 2 μm granules (PGMX-10-5, Spherotech)
- Antibody¹
- DMP (Dimethyl pimelimidate 2 HCl) crosslinker (Pierce 21667)²

Method

1. 3 \times Wash beads in PBS buffer: Using 500 μl of magnetic bead stock, apply magnet to pellet beads, remove stock buffer, resuspend in PBS.
2. Bind antibody: Use sufficient antibody solution to contain twice the binding capacity of the beads. Add PBS to the antibody solution so that have 500 μl total volume and resuspend the pellet. Incubate for 1 hour with agitation (linear shaker at 360 RPM) at room temperature.
3. Remove unbound antibody: Pellet using magnet, remove liquid, resuspend in 0.05 M Sodium Tetraborate pH 8.2 and pellet again.

¹When using new antibodies always aliquot them so they do not undergo too many freeze/thaw events (do the aliquoting on ice).

²Do not use buffers that contain primary amines (e.g., Tris, glycine, etc.), as these buffers will compete with the crosslinking reaction.

4. 3× Cross-link antibody to beads: Resuspend pellet in DMP (500 μ l, DMP 10 mg/ml in 0.2 M Triethanolamine pH 8.2). Leave for 30 minutes with agitation (linear shaker at 360 RPM) at room temperature. Pellet with magnet and remove liquid. Resuspend in 0.05 M Sodium Tetraborate pH 8.2 (500 μ l). Leave for 5 minutes.
5. 2× Quench and wash: Pellet with magnet and remove liquid. Resuspend in 500 μ l 0.1 M Ethanolamine pH 8.2. Leave for 5 minutes. Pellet with magnet and remove liquid.
6. Resuspend in 500 μ l 0.05 M Sodium Tetraborate pH 8.2. Leave for 5 minutes.
7. 2× Remove antibody not cross-linked: Pellet with magnet and remove liquid. Resuspend in 500 μ l 0.1 M Glycine pH 2.8. Leave for 5 minutes.
8. 3× Final Wash: Pellet with magnet and remove liquid. Resuspend in 500 μ l PBS.
9. Store in 500 μ l PBS (+ 0.05% sodium azide and 0.1% Tween 20 for long term storage).

B.9 Biotin SAM Formation

This protocol is taken from the manufacturer recommendations and is designed to form a biotin SAM on an Au surface [5].

Materials

- 1 tube of 1 μmol Biotin SAM Formation Reagent (B564-10, Dojindo)
- Ethanol ($\text{C}_2\text{H}_6\text{O}$), HPLC Grade
- Nanopure water, 18 M Ω
- Clean Au coated cantilever array

Method

1. Add 1 ml of ethanol to the tube and pipette to dissolve the reagent to yield a 1 mmol/l Biotin SAM solution.
2. Dilute the solution by a factor of 10 using ethanol.
3. Immerse the Au coated cantilever array in the solution using the capillary functionalisation technique (Section 3.4) for 1 hour.
4. Rinse the array several times in ethanol and water.

References

- [1] W. W. Cleland, "Dithiothreitol, a new protective reagent for SH groups*," *Biochemistry*, vol. 3, no. 4, pp. 480–482, 1964.
- [2] C. A. Mirkin, R. L. Letsinger, R. C. Mucic, and J. J. Storhoff, "A dna-based method for rationally assembling nanoparticles into macroscopic materials," *Nature*, vol. 382, no. 6592, pp. 607–609, 1996.
- [3] J. J. Storhoff, R. Elghanian, R. C. Mucic, C. A. Mirkin, and R. L. Letsinger, "One-pot colorimetric differentiation of polynucleotides with single base imperfections using gold nanoparticle probes," *J. Am. Chem. Soc.*, vol. 120, no. 9, pp. 1959–1964, 1998.
- [4] T. A. Taton, *Current Protocols in Nucleic Acid Chemistry*. John Wiley & Sons, Inc., 2001, ch. Preparation of Gold Nanoparticle-DNA Conjugates, pp. 12.2.1–12.2.12.
- [5] "Technical manual - biotin SAM formation reagent," Dojindo Molecular Technologies, Inc., Tech. Rep., 2011. [Online]. Available: http://www.dojindo.com/TechnicalManual/Manual_B564.pdf

Mathematica Source Code

This code was used to determine the matrix size that provided sufficient convergence of the resonance frequencies and Q factors predicted by the models.

167


```

aa = Array[z, M];
mm = Array[z, 1];

QQ = mm;
FF = mm;
BB = mm;

CCC[n_] := xx /. FindRoot[Cos[xx] Cosh[xx] ==
-1, {xx, (n - 1/2) *  $\pi$ }, WorkingPrecision -> 200];
(* nth positive root of the equation *)
(*Eqn3SaderJApplPhys106 094904(2009)*)
 $\omega = ((CCC[n]^2) * t / (L^2)) * \text{Sqrt}[(EE) / (12 * \rho c)];$ 
(*Eqn2SaderJApplPhys106 094904(2009)*)
 $f = \omega / (2 * \pi);$ 
(* vacuum frequency *)
 $\text{Rey} = \rho_{\text{air}} * \omega * (b^2) / \eta;$ 
(* Reynolds number *) (*Eqn5SaderJApplPhys106 094904(2009)*)
 $\kappa = CCC[n] * b / L;$ 
(* normalised mode number *) (*Eqn5SaderJApplPhys106 094904(2009)*)
 $\zeta = \omega * b / c;$ 
(* normalised wave number *) (*Eqn5SaderJApplPhys106 094904(2009)*)
 $\text{ppp} = (\kappa^2 - \zeta^2) / 16;$ 
(* Terms for A below *)
 $\text{rrr} = (\kappa^2 - I * \text{Rey}) / 16;$ 

For[iii = 2, iii ≤ maxsize, iii = iii + 2,
  M = iii;
  Parallelize[A[q_, m_] =
     $(-4^{((2 * q) - 1)} / \text{Sqrt}[\pi]) * \text{MeijerG}[\{\{3/2\}, \{\}\}, \{\{0, (-1 + q + m)\}, \{(1 + q - m)\}\}, \text{ppp}]$ 
     $- ((\kappa^2) * (2^{((4 * q) - 5)} / \text{Sqrt}[\pi])) *$ 

```

```
MeijerG[{{1/2}, {}}, {{0, (-2 + q + m)}, {(0 + q - m)}}, rrr]
- (2^((4 * q) - 1)/Sqrt[π])*
MeijerG[{{1/2}, {}}, {{0, (-1 + q + m)}, {(1 + q - m)}}, rrr];
```

```
Parallelize[AA = Table[A[q, m], {q, M}, {m, M}]];
Parallelize[a1 = LinearSolve[N[AA, 200], N[aa, 200]][[1]]];
Γ = 8 * a1; (*Eqn6SaderJApplPhys106 094904(2009)*)
factor = 1/Sqrt[1 + ((π * ρair * b)/(4 * ρc * t)) * Re[Γ]];
fr = f * factor; (* resonant frequency in medium *)
1 - factor; (* Normalised resonant frequency *)
Q = ((4 * ρc * t)/(π * ρair * b) + Re[Γ])/Im[Γ];
Print["Matrix Size = ", M]
Print["Mode Number = ", n];
Print["Resonant Frequency in Air = ", fr, " Hz"];
Print["Q Value = ", Q];
Print["Re a1 = ", Re[a1]];
Print["Im a1 = ", Im[a1]];
AppendTo[FF, fr];
AppendTo[QQ, Q];
AppendTo[BB, a1];
]

QQ2 = Rest[QQ];
FF2 = Rest[FF];

Export["ConvergenceQ.xls", QQ2]
Export["ConvergenceF.xls", FF2]
```


C.2 Compressible Fluid Model

The code below was used to calculate the resonance frequencies and Q factors predicted by the compressible fluid model [1]. The thickness of the cantilever was changed to obtain the different curves presented.

```
Clear[QQ, QQ1, FF, FF1, M, maxmode, um, t, L, b, EE, ρc, ρpair, η, c, z, aa]

M = 36;

maxmode = 6;

$MinPrecision = 200;

um = 10^-6; (*micro*)

t = 6.72300000000000000000 * um; (*thickness*)

L = 500.00000000000000000000 * um; (*length*)

b = 100.00000000000000000000 * um; (*width*)

EE = 169.00000000000000000000 * 10^9; (*Young's Modulus SiPa*)

ρc = 2330.00000000000000000000; (* Density Silicon *)

ρpair = 1.18390000000000000000; (*densityofairkgm^(-3)at25degreescelsius*)

η = 1.78000000000000000000 * (10^(-5)); (*viscosityofairkg/(ms)*)

c = 346.18000000000000000000;

(*speedofsoundm/sat25degreescelsius346.18*)

z[i_] = If[i == 1, 1, 0];

aa = Array[z, M];

mm = Array[z, 1];

QQ = mm;

FF = mm;

For[iii = 1, iii ≤ maxmode, iii++,

Clear[n, f, ω, κ, ζ, A, AA, q, m, Rey, Q, xx, ppp, rrr, a1, Γ, factor];

n = iii;

CCC[n_] := xx /. FindRoot[Cos[xx] Cosh[xx] ==

-1, {xx, (n - 1/2) * π}, WorkingPrecision → 200];

(* nth positive root of the equation *) (*Eqn3SaderJApplPhys106 094904(2009)*)
```

```

 $\omega = ((CCC[n]^2) * t / (L^2)) * \text{Sqrt}[(EE) / (12 * \rho c)];$ 
(*Eqn2SaderJApplPhys106 094904(2009)*)

 $f = \omega / (2 * \pi);$ 
(* vacuum frequency *)

 $\text{Rey} = \rho_{\text{air}} * \omega * (b^2) / \eta;$ 
(* Reynolds number *) (*Eqn5SaderJApplPhys106 094904(2009)*)

 $\kappa = CCC[n] * b / L;$ 
(* normalised mode number *) (*Eqn5SaderJApplPhys106 094904(2009)*)

 $\zeta = \omega * b / c;$ 
(* normalised wave number *) (*Eqn5SaderJApplPhys106 094904(2009)*)

 $\text{ppp} = (\kappa^2 - \zeta^2 * (\text{Rey} / (\text{Rey} - ((4/3) * (\zeta^2) * I)))) / 16;$ 

 $\text{rrr} = (\kappa^2 - I * \text{Rey}) / 16;$ 

Parallelize[A[q_, m_] =
  (-4^((2 * q) - 1) / Sqrt[ $\pi$ ]) *
    MeijerG[{{3/2}, {}}, {{0, (-1 + q + m)}, {(1 + q - m)}}], ppp]
    - (( $\kappa^2$ ) * (2^((4 * q) - 5) / Sqrt[ $\pi$ ])) *
    MeijerG[{{1/2}, {}}, {{0, (-2 + q + m)}, {(0 + q - m)}}], rrr]
    - (2^((4 * q) - 1) / Sqrt[ $\pi$ ]) *
    MeijerG[{{1/2}, {}}, {{0, (-1 + q + m)}, {(1 + q - m)}}], rrr];

Parallelize[AA = Table[A[q, m], {q, M}, {m, M}]];
Parallelize[a1 = LinearSolve[N[AA, 200], N[aa, 200]]][[1]];

 $\Gamma = 8 * a1;$  (*Eqn6SaderJApplPhys106 094904(2009)*)

 $\text{factor} = 1 / \text{Sqrt}[1 + ((\pi * \rho_{\text{air}} * b) / (4 * \rho c * t)) * \text{Re}[\Gamma]];$ 

 $\text{fr} = f * \text{factor};$  (* resonant frequency in medium *)

1 - factor; (* Normalised resonant frequency *)

 $Q = ((4 * \rho c * t) / (\pi * \rho_{\text{air}} * b) + \text{Re}[\Gamma]) / \text{Im}[\Gamma];$ 

Print["Mode Number = ", n];

```



```
Print["Resonant Frequency in Air = ", fr, " Hz"];
```

```
Print["Q Value = ", Q];
```

```
AppendTo[FF, fr];
```

```
AppendTo[QQ, Q];
```

```
]
```

Below is the Mathematica source code for the calculations of resonance frequency and Q factor predicted by the extended viscous model [2]. The thickness of the cantilever was changed to obtain the different curves presented.

```
Clear[QQ, QQ1, FF, FF1, M, maxmode, um, t, L, b, EE, ρc, ρpair, η, c, z, aa]

M = 36;

maxmode = 6;

$MinPrecision = 200;

um = 10^-6; (*micro*)

t = 6.723000000000000000 * um; (*thickness*)

L = 500.000000000000000000 * um; (*length*)

b = 100.000000000000000000 * um; (*width*)

EE = 130.000000000000000000 * 10^9; (*Young'sModulusSiPa*)

ρc = 2330.000000000000000000; (* Density Silicon *)

ρpair = 1.18390000000000000000; (*densityofairkgm^(-3)at25degreescelsius*)

η = 1.78000000000000000000 * (10^(-5)); (*viscosityofairkg/(ms)*)

c = 346.180000000000000000;

(*speedofsoundm/sat25degreescelsius346.18*)

z[i_] = If[i == 1, 1, 0];

aa = Array[z, M];

mm = Array[z, 1];

QQ = mm;

FF = mm;

For[iii = 1, iii ≤ maxmode, iii++,

Clear[n, f, ω, κ, ζ, A, AA, q, m, Rey, Q, xx, ppp, rrr, a1, Γ, factor];

n = iii;

CCC[n_] := xx /. FindRoot[Cos[xx] Cosh[xx] ==

-1, {xx, (n - 1/2) * π}, WorkingPrecision → 200]; (* nth positive root of the equation *)
```



```

 $\omega = ((CCC[n]^2) * t / (L^2)) * \text{Sqrt}[(EE) / (12 * \rho c)];$ 
 $f = \omega / (2 * \pi);$  (* vacuum frequency *)
 $\text{Rey} = \rho_{\text{air}} * \omega * (b^2) / \eta;$  (* Reynolds number *)
 $\kappa = CCC[n] * b / L;$  (* normalised mode number *)
 $\zeta = \omega * b / c;$  (* normalised wave number *)
 $\text{ppp} = (\kappa^2) / 16;$ 
 $\text{rrr} = (\kappa^2 - I * \text{Rey}) / 16;$ 

Parallelize[A[q_, m_] =
   $(-4^{((2 * q) - 1)} / \text{Sqrt}[\pi]) * \text{MeijerG}[\{\{3/2\}, \{\}\}, \{\{0, (-1 + q + m)\}, \{(1 + q - m)\}\}, \text{ppp}]$ 
     $- ((\kappa^2) * (2^{((4 * q) - 5)} / \text{Sqrt}[\pi])) * \text{MeijerG}[\{\{1/2\}, \{\}\}, \{\{0, (-2 + q + m)\}, \{(0 + q - m)\}\}, \text{rrr}]$ 
     $- (2^{((4 * q) - 1)} / \text{Sqrt}[\pi]) * \text{MeijerG}[\{\{1/2\}, \{\}\}, \{\{0, (-1 + q + m)\}, \{(1 + q - m)\}\}, \text{rrr}];$ 

Parallelize[AA = Table[A[q, m], {q, M}, {m, M}]];
Parallelize[a1 = LinearSolve[N[AA, 200], N[aa, 200]][[1]]];
 $\Gamma = 8 * a1;$ 
 $\text{factor} = 1 / \text{Sqrt}[1 + ((\pi * \rho_{\text{air}} * b) / (4 * \rho c * t)) * \text{Re}[\Gamma]];$ 
 $\text{fr} = f * \text{factor};$  (* resonant frequency in medium *)
 $1 - \text{factor};$  (* Normalised resonant frequency *)
 $Q = ((4 * \rho c * t) / (\pi * \rho_{\text{air}} * b) + \text{Re}[\Gamma]) / \text{Im}[\Gamma];$ 
Print["Mode Number = ", n];
Print["Resonant Frequency in Air = ", fr, " Hz"];
Print["Q Value = ", Q];
AppendTo[FF, fr];
AppendTo[QQ, Q];

```

]

QQ1 = Rest[QQ]

FF1 = Rest[FF]

ListLinePlot[QQ1, AxesLabel →

{ "Matrix Dimension (n x n)", "Q Value" },

AxesOrigin → {0, 0}, PlotRange → Full, PlotRangePadding → 1]

ListLinePlot[FF1, AxesLabel →

{ "Matrix Dimension (n x n)", "Frequency (Hz)" },

AxesOrigin → {0, 0}, PlotRange → Full, PlotRangePadding → 1]

Export["Qvalue_6.723um_130Gpa_ext.xls", {"Q value" → QQ1, "Frequency" → FF1}]

References

- [1] C. A. Van Eysden and J. E. Sader, "Frequency response of cantilever beams immersed in compressible fluids with applications to the atomic force microscope," *Journal of Applied Physics*, vol. 106, p. 094904, 2009.
- [2] C. A. Van Eysden and J. E. Sader, "Frequency response of cantilever beams immersed in viscous fluids with applications to the atomic force microscope: Arbitrary mode order," *Journal of Applied Physics*, vol. 101, p. 044908, 2007.

Appendix D

List of Publications and Presentations

Publications

- Jason Jensen, Niall Maloney, and Martin Hegner. A Multi-Mode Platform for Cantilever Arrays Operated in Liquid. *Submitted*, 2013.
- Jason Jensen, Margherita Farina, Giampaolo Zuccheri, Wilfried Grange, and Martin Hegner. Quantitative, Label-Free Detection of the Aggregation of α -Synuclein Using Microcantilever Arrays Operated in a Liquid Environment. *Journal of Sensors* **2012**: 874086, 2011. DOI:10.1155/2012/874086
- Jason Jensen and Martin Hegner. Predictions of the Compressible Fluid Model and its Comparison to Experimental Measurements of Q Factors and Flexural Resonance Frequencies for Microcantilevers. *Journal of Sensors* **2012**: 258381, 2011. DOI:10.1155/2012/258381
- N. Maloney, G. Lukacs, N. Nugaeva, W. Grange, J. P. Ramseyer, J. Jensen, and M. Hegner. Fibre Optic Readout of Microcantilever Arrays for Fast Microorganism Growth Detection. *Journal of Sensors* **2012**: 405281, 2011. DOI:10.1155/2012/405281
- Casper Hyttel Clausen, Jason Jensen, Jaime Castillo, Maria Dimaki and Winnie Edith Svendsen. Qualitative mapping of structurally different dipeptide nanotubes. *Nano Letters* **8**(11): 4066-4069, 2008. DOI:10.1021/nl801037k

Presentations

Oral

- 4th Multifrequency AFM Conference. Madrid, Spain; October 2012.

- CSET Wide Thesis in Three Competition: Dublin Ireland, November 2011, Winner: Audience voted Best Presentation.
- CRANN Thesis in Three Competition: Dublin Ireland, October 2011, Winner: 1st Place.
- 8th *International Workshop on Nanomechanical Cantilever Sensors*. Dublin, Ireland; May 2011.
- 7th *International Workshop on Nanomechanical Cantilever Sensors*. Banff, Canada; May 2010.

Poster

- Jason Jensen, Niall McLaughlin, Margherita Farina, Giampaolo Zuccheri and Martin Hegner. A Microcantilever Based Quantitative Sensing Platform for the Investigation of Biological Interactions. 8th *International Workshop on Nanomechanical Cantilever Sensors*. Dublin, Ireland; May 2011.
- Jason Jensen, Margherita Farina, Giampaolo Zuccheri and Martin Hegner. A label-free, real-time technique for investigating the early stage fibril formation involved in Parkinson's Disease. *Inspire BioNano Conference*. Dublin, Ireland; October 2009. Winner: Best Poster
- Jason Jensen, Margherita Farina, Giampaolo Zuccheri and Martin Hegner. A label-free, real-time technique for investigating the early stage fibril formation involved in Parkinson's Disease. *Trinity College Dublin Nanomedicine Seminar and Workshop*. Dublin, Ireland; June 2009.
- Various poster presentations for CRANN internal and outreach events

List of Figures

| | | |
|------|--|----|
| 1.1 | SEM image of a cantilever array | 2 |
| 1.2 | Schematic of static bending readout | 6 |
| 1.3 | Schematic of static bending line profile readout | 8 |
| 1.4 | Schematic of dynamic mode readout | 14 |
| 2.1 | The fluid chamber | 26 |
| 2.2 | Contribution of piezoelectric actuation to amplitude spectrum | 27 |
| 2.3 | Optic cage and laser positioning system | 29 |
| 2.4 | Laser spot position on cantilever | 31 |
| 2.5 | Movement of laser spot between cantilevers | 32 |
| 2.6 | Example of a PSD structure and PSD holder | 33 |
| 2.7 | Thermocouple calibration | 35 |
| 2.8 | Various components of the fluidic system | 37 |
| 2.9 | Pressure sensor and flow calibration | 38 |
| 2.10 | Assembled dual-mode device optical deflection system | 39 |
| 2.11 | Photograph of the dual-mode device including peripheral components | 40 |
| 2.12 | Schematic of dual-mode device control and measurement procedure | 42 |
| 2.13 | LabVIEW dual-mode device VI front panel | 43 |
| 2.14 | LabVIEW dual-mode device VI block diagram | 44 |
| 2.15 | LabVIEW sub VI for measurement procedure | 46 |
| 2.16 | LabVIEW sub VI for movement of stages | 47 |
| 2.17 | LabVIEW sub VI for dynamic mode | 48 |
| 2.18 | LabVIEW sub VI for static mode | 50 |
| 2.19 | Typical Amplitude and Phase spectra of a 1 μm thick cantilever in water | 51 |
| 2.20 | Line scan of cantilever | 53 |
| 2.21 | Static response to heat pulse | 54 |
| 2.22 | Dynamic response to heat pulse | 54 |
| 2.23 | Syringe pump frequency response | 56 |
| 2.24 | Pressure pump frequency response | 57 |
| 2.25 | Syringe pump frequency response, FFT and frequency vs. pump speed | 58 |

| | | |
|------|---|-----|
| 3.1 | Capillary Functionalisation | 65 |
| 4.1 | Critical frequency and mode vs cantilever thickness | 68 |
| 4.2 | SEM images of cantilever hinge end | 69 |
| 4.3 | Resonance modes and SHO fit for 7 μm thick cantilever | 70 |
| 4.4 | Resonance modes and SHO fit for 2 μm thick cantilever | 71 |
| 4.5 | Convergence of output based on matrix size | 73 |
| 4.6 | Resonance frequencies and Q factors of 7 μm thick cantilevers | 74 |
| 4.7 | Q factor 7 μm thick one clamp position | 75 |
| 4.8 | Resonance frequencies and Q factors of 2 μm thick cantilevers | 76 |
| 5.1 | Possible disease pathways for Parkinson's disease | 83 |
| 5.2 | Functionalisation of cantilever surface with α -synuclein | 86 |
| 5.3 | Cantilever measurement of α -synuclein aggregation | 89 |
| 5.4 | Fluorescence measurement of α -synuclein aggregation | 90 |
| 6.1 | Bound mass vs. time for laser-ablated oligo functionalised nanoparticles hybridising on cantilever surface | 105 |
| 6.2 | Oligo-functionalised laser-ablated Au nanoparticle binding | 105 |
| 6.3 | DLS comparison between bare and functionalised Au nanoparticles | 107 |
| 6.4 | Oligo functionalised 50 nm Au nanoparticle binding | 108 |
| 6.5 | DLS comparison between bare and functionalised Au nanoparticles after one week of storage | 109 |
| 6.6 | Baseline corrected scaled data and averaged data for oligo experiment | 110 |
| 6.7 | Differential deflection for oligo experiments | 111 |
| 6.8 | Differential deflection change for oligo bead experiment | 112 |
| 6.9 | Baseline corrected data and averaged data for oligo beads experiment | 113 |
| 6.10 | Differential mass change for oligo bead experiment | 114 |
| 6.11 | Critical diameter for particle movement on cantilever surface | 116 |
| 7.1 | Schematic of magnetic particle experiments | 122 |
| 7.2 | Anti-biotin magnetic beads binding to biotin SAM | 125 |
| 7.3 | SEM of magnetic beads on cantilevers | 126 |
| A.1 | f vs n for example spectrum | 138 |
| A.2 | f_n^2 vs $(n - 0.5)^4$ for example spectrum | 139 |
| A.3 | Static response of each cantilever to heat pulse | 140 |
| A.4 | Individual cantilever frequency response to heat pulse | 141 |
| A.5 | Change in co-moved mass during heat pulse | 142 |
| A.6 | Amplitude and phase spectra from α -synuclein experiment | 143 |

| | |
|---|-----|
| A.7 Cantilever measurement of α -synuclein aggregation pre reference subtraction | 144 |
| A.8 Amplitude and phase spectra from oligo functionalised Au nanoparticles experiment | 145 |
| A.9 Amplitude and phase spectra from oligo functionalised 50 nm Au nanoparticles experiment | 146 |
| A.10 Amplitude and phase spectra from biotinylated oligo with streptavidin beads experiment | 147 |
| A.11 SEM Images of Au Nanoparticles on Cantilever Surface | 149 |
| A.12 Heat pulse and calibration for oligo experiment | 150 |
| A.13 Baseline corrected data and averaged data for static oligo beads experiment | 151 |

List of Tables

| | | |
|-----|--|-----|
| 2.1 | Constants for thermocouple calibration | 35 |
| 3.1 | BOC Edwards metal coating settings | 63 |
| 3.2 | Temescal metal coating settings | 63 |
| 6.1 | Information about the oligos used during experiments | 99 |
| 6.2 | Functionalisation of cantilever array for laser-ablated nanoparticles experiment | 100 |
| 6.3 | Functionalisation of cantilever array for #930356-functionalised nanoparticles experiment | 101 |
| 6.4 | Functionalisation of cantilever array for static biotinylated oligos experiment | 102 |
| 6.5 | Functionalisation of cantilever array for two-step biotinylated oligos with streptavidin beads experiment | 103 |
| 7.1 | Antibody Beads Cantilever Functionalisation | 123 |
| A.1 | Dulbecco's PBS formulation | 148 |

Glossary

α -synuclein a natively unfolded protein which can aggregate to form fibrils in conditions characterised by Lewy bodies, e.g. Parkinson's disease.

achromatic doublet a lens designed to limit chromatic and spherical aberration. It is normally comprised of two separate lenses, one concave and one convex, each with different dispersions.

amyloid an insoluble fibrous protein aggregate formed from misfolded versions of proteins found naturally in the body.

antibody also known as immunoglobulin.

primary antibody an antibody raised against an antigenic target and binds the antigen.

secondary antibody an antibody which binds a primary antibody or antibody fragment.

antigen a substance that causes the production of one or more antibodies. Also the target of an antibody.

biotin $C_{10}H_{16}N_2O_3S$, is a water soluble vitamin (B7 *or* H) commonly used in biotechnology for protein conjugation during assays. Biotin forms a highly stable bond with streptavidin.

block diagram contains the source code of any LabVIEW program, and determines the execution of the program.

bradykinesia generalised slowness of movement.

cytoplasm the substance within a cell containing all of the cell's organelles except the nucleus.

dopamine a common neurotransmitter in animals.

dopaminergic neurons neurons that contain or synthesise dopamine.

Drosophila a small genus of fly often called the fruit fly, which is commonly used as a model organism.

festinating gait short jerky steps, also difficulty initiating and stopping movement.

front panel provides the inputs and outputs to the LabVIEW program.

functionalisation the process of adding a functional group to a material surface by chemical synthesis methods.

functional group a specific group of atoms or bonds within molecules that are responsible for the characteristic chemical reactions of those molecules.

immunoglobulin a Y shaped protein produced by the immune system capable of identifying and binding to a specific target.

Lewy body an aggregate of protein that forms in the nerve cells during Parkinson's disease.

lyophilisation a.k.a freeze-drying. The material is frozen and then the pressure is dropped to sublime the remaining frozen water in the material.

NOSetools a data analysis package for the handling of cantilever array data written by T. Braun implemented in the IGOR Pro environment.

oligonucleotide (oligo) a short nucleic acid polymer with fifty or fewer bases.

Parkinson's disease a degenerative disorder affecting the central nervous system.

pathogenesis the mechanism by which a disease is caused.

protein G an immunoglobulin-binding protein.

streptavidin is a small protein (60 kDa) which is purified from *Streptomyces avidinii*. Streptavidin binds biotin with a high affinity and specificity. The bond formed between streptavidin and biotin is highly stable and is one of the strongest non-covalent bonds in nature. Due to the strong bond, streptavidin is used in biotechnology during the purification of biotinylated proteins.

Thioflavin T a dye used to visualise amyloid protein aggregates.

thiol an organic compound that contains a carbon bonded sulfhydryl (SH) group. Thiols form a strong bond with noble metals and can be used to form a SAM. The sulphur gold bond is semi covalent with a strength of ~ 45 kcal/mol.

virtual instrument a LabVIEW program.